VILNIUS UNIVERSITY

Tomas
ŠNEIDERIS

Towards Understanding Amyloid Fibril Formation and Self-replication

DOCTORAL DISSERTATION

Natural Sciences,
Biochemistry (N 004)

VILNIUS 2020

This dissertation was written between 2015 and 2019 at Vilnius University and Cambridge University.
The research was supported by Research Council of Lithuania.

Scientific supervisor – Dr. Vytautas Smirnovas (Vilnius University, Natural Sciences, Biochemistry – N 004).

This doctoral dissertation will be defended in a public meeting of the Dissertation Defence Panel:
Chairman – **Prof. Dr. Jolanta Sereikaitė** (Vilnius Gediminas Technical University, Natural Sciences, Biochemistry – N 004).
Members:
Prof. Dr. Kristaps Jaudzems (University of Latvia, Latvia, Natural Sciences, Chemistry – N 003);
Dr. Vytautas Petrauskas (Vilnius University, Natural Sciences, Biophysics – N 011);
Prof. Dr. Ludmilla A. Morozova-Roche (Umeå University, Sweden, Natural Sciences, Biochemistry – N 004);
Dr. Gintautas Tamulaitis (Vilnius University, Natural Sciences, Biochemistry – N 004).

The dissertation shall be defended at a public meeting of the Dissertation Defence Panel at 3 PM on 16 March 2020 in room R-401 of the Life Sciences Centre, Vilnius University.

The text of this dissertation can be accessed at the library of Vilnius University, as well as on the website of Vilnius University: www.vu.lt/lt/naujienos/ivykiu-kalendorius

VILNIAUS UNIVERSITETAS

Tomas
ŠNEIDERIS

Baltymų amiloidinių fibrilių susidarymo ir savireplikacijos savybių tyrimas

DAKTARO DISERTACIJA

Gamtos mokslai,
Biochemija (N 004)

VILNIUS 2020

Disertacija rengta 2015–2019 metais Vilniaus universitete ir Kembridžo universitete.
Mokslinius tyrimus rėmė Lietuvos mokslo taryba.

Mokslinis vadovas – dr. Vytautas Smirnovas (Vilniaus universitetas, gamtos mokslai, biochemija – N 004).

Gynimo taryba:
Pirmininkė – **prof. dr. Jolanta Sereikaitė** (Vilniaus Gedimino technikos universitetas, gamtos mokslai, biochemija – N 004).
Nariai:
prof. dr. Kristaps Jaudzems (Latvijos universitetas, Latvija, gamtos mokslai, chemija – N 003);
dr. Vytautas Petrauskas (Vilniaus universitetas, gamtos mokslai, biofizika – N 011);
prof. dr. Ludmilla A. Morozova-Roche (Umėjos universitetas, Švedija, gamtos mokslai biochemija – N 004);
dr. Gintautas Tamulaitis (Vilniaus universitetas, gamtos mokslai, biochemija – N 004).

Disertacija ginama viešame Gynimo tarybos posėdyje 2020 m. kovo mėn. 16 d. 15 val. Vilniaus universiteto Gyvybės mokslų, centro R-401 auditorijoje. Adresas: Saulėtekio al. 7, LT-10257 Vilnius, Lietuva.

Disertaciją galima peržiūrėti Vilniaus universiteto bibliotekoje ir VU interneto svetainėje: https://www.vu.lt/naujienos/ivykiu-kalendorius

Abstract

Towards Understanding Amyloid Fibril Formation and Self-replication

Millions of people around the world suffer from amyloid-related disorders. Alzheimer's and Parkinson's diseases alone afflict more than 50 million patients worldwide. Despite continuous efforts, there are still no disease modifying drugs available for the majority of amyloid-related disorders and the overall failure rate in clinical trials is very high. One of the main reasons for this is a lack of fundamental knowledge of amyloid fibril formation process.

In the present work, new mechanistic insights into the processes of amyloid fibril formation and self-replication are provided. In particular, herein it is demonstrated that monomer-oligomer equilibrium is the fundamental factor governing the formation of distinct insulin fibril strains. Moreover, evidence of the possible direct role of off-pathway oligomeric insulin forms in the amyloid fibril formation mechanism is provided. Also, in this work it is shown that environmental conditions define the inhibitory efficiency of anti-amyloid compounds in a very sensitive manner. Furthermore, new mechanistic insights into the processes of prion self-replication are presented. In particular, the fundamental role of secondary nucleation in the "strain switching" is demonstrated, and a new phenomenon, which emerges during self-propagation reaction of distinct prion strains under different environmental conditions, is described. Finally, herein it is demonstrated that high-resolution atomic force microscopy combined with microfluidic sample deposition platform enables the possibility to image all molecular species present during the aggregation time-course, and allows to acquire single-molecule quantitative data.

Acknowledgements

I would like to convey my appreciation to all people who have helped and motivated me throughout my PhD studies.

First, I would like to thank my supervisor Dr. Vytautas Smirnovas for giving me a wonderful opportunity to start my journey into the world of amyloids. All the years I spent in Vytautas lab greatly contributed to my professional and personal growth. I am most grateful for his kindness, guidance, personal support, and for sharing his experience and knowledge.

I am thankful to all my colleagues for useful advice and personal support, especially Mantas Žiaunys, Andrius Sakalauskas, Akvilė Botyriūtė, and Katažyna Milto for fundamental collaborations and scientific discussions that resulted in several joint publications, and most importantly for their friendship and shared great time. I would like also to thank Martynas Grigaliūnas, Domantas Dargužis, Romuald Stanilko and Elžbieta Kulicka for collaboration and great time in the lab. For the friendly atmosphere I am sincerely thankful to all members of our lab and the Department of Biothermodynamics and Drug Design.

I would like to thank Vilma Michailovienė for improving my protein purification skills, Dr. Marija Jankunec for introducing me to the basics of atomic force microscopy and for the access to the atomic force microscope, Prof. Gediminas Niaura, Dr. Ilja Ignatjev, and Martynas Talaikis for the possibility to use Fourier-Transform infrared spectrometer, Dr. Lina Baranauskienė for her advice and personal support.

I am sincerely grateful to Prof. Michele Vendruscolo (University of Cambridge) for the hospitality and possibility to improve my professional skills and for significant contribution to joint publications. Thank you for trusting me.

I am most grateful to Dr. Francesco Simone Ruggeri (University of Cambridge) for introducing me to the advanced atomic force microscopy, sharing his experience and knowledge, and for the extremely interesting work which resulted in several joint publications. It was a great pleasure and honour to work with you.

I would like also to thank Prof. Tuomas Knowles (University of Cambridge) for significant contribution to joint publications, the hospitality and the possibility to join his group meetings and lab activities.

For the friendly atmosphere, effective lab work and significant contribution to joint publications I am sincerely thankful to all members of these groups, especially Dr. Tadas Kartanas, Dr. Sean Chia, Dr. Ryan Limbocker, Tuuli Hakala, Rodrigo Cataldi, Tom Scheidt, Dr. Benedetta Mannini, Zenon Toprakcioglu, Dr. Magdalena Czekalska, Yufan Xu, and Ella Feng.

I would like to thank all internal and external collaborators: Rebecca Sternke-Hoffmann, Alessia Peduzzo, Dr. Alexander K. Buell, Dr. Jonathan Cannon, Dr. Rasa Rutkienė, Dr. Rolandas Meškys and Prof. Roland Winter.

For the financial support I am grateful to Lithuanian Research Council and Vilnius University, COST action BM1405, and EBSA.

Finally, my deepest gratitude goes to Greta and my family for the endless patience, support and the unconditional belief in me.

Tomas

Contents

List of Figures

List of Tables

List of Abbreviations

α-syn	α-synuclein
Aβ	Amyloid beta
AD	Alzheimer's disease
AFM	Atomic force microscopy
CJD	Creutzfeldt-Jakob disease
CR	Congo red
Cryo-EM	Cryo-electron microscopy
DMSO	Dimethyl sulfoxide
EM	Electron microscopy
FTIR	Fourier-transform infrared spectroscopy
Htt	Huntingtin
IAPP	Islet amyloid polypeptide
iCJD	Iatrogenic Creutzfeldt-Jakob disease
IDP	Intrinsically disordered peptide or protein
NFT	Neurofibrillary tangles
PD	Parkinson's disease
PrP^{Sc}	Scrapie prion protein
PrP^{C}	Cellular prion protein
SOD1	Superoxide dismutase 1
ThT	Thioflavin-T
TSE	Transmissible spongiform encephalopathy
TTR	Transthyretin
vCJD	Variant Creutzfeldt-Jakob disease

Chapter 1

Introduction

The onset and progression of more than 50 human disorders (Table 2.1), including Alzheimer's disease (AD) [1], Parkinson's disease (PD) [2], type II diabetes [3], and prion diseases [4], are associated with the failure of a specific peptide or protein to adopt or remain in its native functional conformational state, and their subsequent conversion into insoluble fibrillar aggregates, termed amyloids. In recent years, the process of amyloid formation has emerged as a subject of fundamental importance as it was recognised that many disorders associated with amyloid formation are no longer rare and are rapidly becoming some of the most common medical conditions in the ageing society [5]. Millions of people around the world suffer from amyloid-related diseases, AD and PD alone afflict more than 50 million patients worldwide [1, 2, 6]. Despite significant and sustained efforts, however, the molecular and mechanistic links between protein aggregation and toxicity remain challenging to characterise. In addition, there are still no effective disease modifying drugs or treatment modalities available for amyloid-related disorders [7, 8]. The main reasons for this are the complex nature of the peptide and protein aggregation and self-replication, and relatively poor understanding of this process [8, 9]. The complete elucidation of amyloid fibril formation process is possible only if all conformational states, and oligomeric structures adopted by the polypeptide chain during the process, as well as the thermodynamics and kinetics of all conformational changes are known [10].

The formation of amyloid fibrils is a complex process, which involves several microscopic events, including primary and secondary nucleation, elongation, and fragmentation [5, 11–13]. The alterations in environmental conditions can modulate these events resulting in the emergence of different pathways of amyloid fibril formation, leading to

the formation of structurally distinct amyloid aggregates, termed strains [5, 9, 11, 14–27]. Such conformational variability, also referred to as polymorphism phenomena, is thought to be the generic property of amyloid proteins [11, 28, 29]. Conformational variability of amyloid fibrils can be viewed as another major reason for failure of anti-amyloid treatment modalities, as compounds that are effective against one fibril strain, which causes a particular phenotype of amyloid-related disorder, may be ineffective against others [9]. Thus, studies of amyloid fibril polymorphism phenomena are fundamental for development of effective anti-amyloid treatment modalities.

The goal of the study

To study amyloid protein fibril formation and self-replication, and to obtain new insights about these processes.

Objectives

- To study the effects of different factors on insulin fibril formation.
- To study self-replication of different prion protein amyloid strains.
- To study time-course of amyloid beta 42 aggregation via high-resolution atomic force microscopy by applying microfluidic spray device for sample deposition.

Scientific novelty

In this study, new mechanistic insights into the process of distinct insulin strain formation are provided. In particular, investigation of the effects of distinct factors on insulin aggregation enabled to determine that monomer-oligomer equilibrium is the fundamental factor governing the formation of distinct insulin strains. Moreover, for the first time, evidence of possible direct role of oligomeric insulin forms in the amyloid formation pathway is provided. The results add one more piece to the global picture of the insulin aggregation mechanism, and brings us one step closer to the complete elucidation of this pathway. Multiple studies have screened numerous compounds in search of effective anti-amyloid compounds, however, no anti-amyloid drugs are present

to date. In this study, a new insights into the process of assessment of effects of anti-amyloid compounds are provided. In particular, herein it is demonstrated that the inhibitory efficiency of compounds depends on the environmental conditions, under which amyloid aggregation reaction is performed, as well as the methods used for assessment of effects.

Furthermore, new mechanistic insights into the process of prion self-replication are provided in this study. In particular, for the first time, it is demonstrated that polymorphism of amyloid fibrils can be defined by the concentration of seeds. Moreover, a new phenomenon, which emerges during self-propagation reaction of distinct prion strains under different environmental conditions, is described. The results suggest that abnormalities in the kinetics of seed-induced aggregation reactions may be related to artefacts / anomalies of the secondary nucleation process.

Finally, the application of novel microfluidic spray device for deposition of heterogeneous amyloid samples for analysis via atomic force microscopy is demonstrated. In particular, application of such approach enabled the possibility to image all molecular species present during amyloid beta 42 (Aβ42) aggregation time-course via high-resolution AFM, and allowed for the first time to acquire single-molecule quantitative data that is fundamental for complete elucidation of amyloid aggregation mechanisms.

Defending statements

- Monomer-oligomer equilibrium is one of the main factors governing the formation of distinct insulin strains.
- Insulin amyloid aggregation may be inhibited by insulin oligomers.
- Environment is an important factor in determining the anti-amyloid efficacy of epigallocatechin-3-gallate (EGCG).
- Self-replication of amyloid fibril conformational template can proceed only via fibril elongation.

- The abnormalities in ThT signal during seed-induced aggregation reactions can be explained by the events related to secondary nucleation process.
- High-resolution atomic force microscopy in combination with microfluidic sample deposition technique enables the possibility to image all molecular species present during Aβ42 aggregation time-course, and allows to acquire single-molecule quantitative data.

Chapter 2

Literature overview

2.1 Amyloids and amyloid-related disorders

2.1.1 Brief history of amyloids

The term amyloid was introduced by German scientist Rudolph Virchow in 1854 to denote macroscopic tissue abnormalities found in the human brain [30]. Using the most advanced methodology and medical knowledge of that time, Virchow stained cerebral *corpora amylacea* (meaning "starch-like bodies" in Latin), which had an abnormal macroscopic appearance, with iodine. He found that the macroscopic brain tissue abnormality exhibited a positive iodine staining reaction: it stained pale blue on treatment with iodine, and violet upon subsequent addition of sulfuric acid. Based on these results, Virchow concluded that the fundamental component of the evident macroscopic abnormality was starch and gave it the name amyloid (derived from *amylum* and *amylon*, the Latin and Greek words for starch, respectively) [30, 31]. Just 5 years after this finding, Friedreich and Kekule demonstrated that amyloid deposits are predominantly proteinaceous particles, with carbohydrates, in particular glycosaminoglycans, being associated ubiquitously. Despite proteinaceous nature, the term amyloid has remained [30, 31].

Congo red (CR) staining was introduced in 1922 by Bennhold as an alternative histopathological method for detection of amyloid plaques [32, 33]. Bennhold intravenously injected CR solutions into 21 healthy subjects and 21 patients with different diseases. The *post-mortem* examination of tissue samples of a patient who was diagnosed with amyloidosis, revealed that liver and spleen appeared to be stained by CR. Since

its introduction, the CR staining method has undergone several modifications in order to increase the specificity and reduce the number of false-positives [32]. It was demonstrated in multiple studies that CR-stained amyloid deposits have orange-red appearance when examined under light microscopy, and exhibit positive apple-green birefringence when examined under cross-polarised light [30, 32]. The unique tinctorial properties of amyloid plaques in the presence of CR suggested that amyloid deposits are composed of highly organised protein units in the form of fibrils [31]. The identification of unique staining properties of amyloid deposits provided a basis upon which amyloid fibrils could be isolated from tissues [30]. Congophilia with apple-green birefringence became the first criterion used for identification of amyloid plaques.

The subsequent studies of amyloid deposits of diverse origin in humans and animals using electron microscopy confirmed that all forms of amyloids exhibit a comparable submicroscopic fibillar ultrastructure [30, 34]. This structure became the second criterion.

Possibility to isolate amyloid deposits of distinct origin allowed to determine amino acid sequence of fibrils isolated from tissue of patients. This enabled to discover biochemical heterogeneity of amyloids, and identify Amyloid A [35], antibody light chains [36], and transthyretin (TTR) [37, 38] as the fundamental protein components of fibrils in amyloid plaques of distinct origin. These findings suggested that an individual peptide or protein precursor is associated with a particular amyloid-related disorder [31, 39]. To date, 37 peptides and proteins have been found to form extracellular and/or intracellular nanoamyloid deposits in human diseases [8].

X-ray diffraction studies of amyloid fibrils revealed that all fibrils possess ordered secondary structure, containing a specific diffraction pattern known as cross-β pattern, which is thought to arise from arrays of β-sheets running parallel to the long axis of the fibril, while β-strands in an individual sheet are arranged perpendicularly. [29, 40, 41]. The universal cross-β structure became the third criterion.

The amyloid fibrils possess specific properties such as proteolytic resistance, flexibility and intrinsic Young's modulus in the order of giga-Pascals, making them an attractive biomaterial in medicine and

nanotechnology [7, 13, 42–48]. Indeed, despite their pathological roles, amyloid fibrils have been found to be involved in many physiologically beneficial roles, including adhesives, catalytic scaffolds, bacterial coatings, and structures for peptide hormone storage [13, 49–52]. Such fibrils are termed functional amyloids. Such type of structures have no link to protein deposition diseases, however, fibrillar aggregates formed *in vitro* exhibit similar morphological, structural and tinctorial properties, enabling them to be classified as amyloid fibrils [10].

2.1.2 Amyloid-related disorders

The formation and accumulation of extracellular amyloid deposits or intracellular inclusions is associated with a range of debilitating medical disorders (Table 2.1), including Alzheimer's, Parkinson's and prion diseases [8]. Most of these disorders are sporadic or arise from specific mutations and are hereditary. In rare cases, however, they can be transmitted from one host to another, the best-studied example being transmissible spongiform encephalopathies [8, 10, 26, 53].

The principal component of extracellular amyloid deposits is a specific peptide or protein that forms the core. Non-fibrillar constituents of amyloid deposits, including metal ions, glycosaminoglycans, the serum amyloid P component, apolipoprotein E, collagen, and many others, also play an important role in fibrilogenesis [54, 55]. Amyloid fibrils, similar to the ones isolated form patients, can also be produced *in vitro* by altering environmental conditions (*e.g.* using mildly denaturing conditions) [10]. Interestingly, the peptides and proteins found as intractable aggregates in patients with a particular amyloid-related disorder, do not share any obvious amino acid sequence identity, structural homology, or function to each other.

Despite the fact that the appearance of amyloid deposits is closely associated with the onset of amyloid-related disorders, the mechanisms and events underlying amyloid formation and toxicity remain challenging to characterise. In case of systemic or localised amyloidoses, the impairment and disruption of tissue architecture in vital organs are mainly associated with the accumulation of large quantities of amyloid deposits

[5, 8, 10], whereas in case of neurodegenerative disorders, including Alzheimer's and Parkinson's disease, the on-pathway oligomers and protofibrils are thought to be the primary pathogenic and most toxic species [5, 8, 56–58]. The exposure of hydrophobic groups, that under normal physiological conditions would be inaccessible within the cellular environment, on the oligomer surface appears to be a major determinant of oligomer-mediated toxicity [5, 8]. Although considered less toxic, the mature amyloid fibrils are equally important pathogenic species, as they can interfere with protein homeostasis network, serve as a reservoir of protein oligomers that can be released, act as catalytic surface for the generation of toxic oligomers through secondary nucleation, and spread within organs of the host and even between individuals [5, 8, 28, 53, 59–63]. Prevention and treatment of a given disease generally require a deep understanding of its underlying causes, thus elucidation of the mechanisms of amyloid aggregate formation, indication of all species present during this process and understanding the cause of neurotoxic effects of these species is fundamental to the development of therapeutic approaches.

TABLE 2.1: Some of amyloid-related human disorders. Adapted from [8].

Disease	**Aggregating peptide or protein**
Alzheimer's disease	Aβ40 and/or Aβ42 peptide
Transmissible spongiform encephalopathies	Prion protein or its fragments
Parkinson's disease	α-Synuclein
Dementia with Lewy bodies	α-Synuclein
Frontotemporal dementia with Parkinsonism	Tau
Pick disease	Tau
Huntington's disease	Huntingtin with polyQ expansion
Senile systemic amyloidosis	Transthyretin
Dialysis-related amyloidosis	β_2-microglobulin
AL amyloidosis	Immunoglobulin light chains or fragments
AA amyloidosis	Fragments of serum amyloid A protein
Lysozyme amyloidosis	Mutants of lysozyme
Type II diabetes	Islet amyloid polypeptide
Injection-localised amyloidosis	Insulin
Prostate cancer	Proteins 100A8/A9

Alzheimer's disease

Alzheimer's disease is a neurodegenerative disorder first described over 100 years ago by Alois Alzheimer. To date AD is most prevalent form of dementia, which affects approximately 40 million patients worldwide and this number is projected to rise steadily to afflict 135 million people by 2050 [1, 6]. AD is a complex neurodegenerative disorder characterised clinically by a progressive loss of memory and cognitive functions. The two pathological hallmarks of AD are the extracellular amyloid deposits and intracellular neurofibrillary tangles (NFTs), which are composed of (Aβ) peptide and the microtubule-associated protein tau, respectively [1, 6, 57, 64]. AD is an age-related disorder and in most cases it occurs late in life, with the incidence increasing from 1 in 10 of those over 65 years old to 1 in 2 of individuals over 85 years old [64]. The principle causative agent of AD is thought to be Aβ aggregates, in particular oligomeric forms of the peptide, which cause neuronal toxicity and triggers downstream signaling events that result in hyperphosphorylation of tau protein and subsequent development of NFTs [6, 57, 64]. Aβ is a ~4 kDa intrinsically disordered peptide, produced by proteolytic cleavage of amyloid β-protein precursor (AβPP) first by β-secretase and subsequently by γ-secretase. In humans, there are two predominant cleavage products: Aβ40 and Aβ42, which are 40 or 42 amino acids long, respectively [57, 64, 65]. Aβ40 is the most abundant form (constitutes to ~90% of the secreted Aβ), whereas Aβ42 is less abundant (comprises ~10% of the secreted Aβ), however, the latter is more aggregation prone and forms fibrils more rapidly. Although the biological role of Aβ is unclear, it is thought that soluble Aβ plays an important role in the facilitation of neuronal growth, cellular survival, modulation of synaptic function and defence against oxidative stress [65]. Age and gene mutations, in particular in gene encoding apolipoprotein E, genes for AβPP and presenilin 1 and 2, are the main risk factors of AD. Additional factors, including oxidative stress or ischemia, may also cause upregulation of AβPP processing, hence resulting in an increase in Aβ levels in the brain [57, 64]. Although still under debate, the oligomeric assemblies of

Aβ are considered as primary, whereas fibrils are the secondary toxic species [1, 6, 57, 64]. Thus aggregated rather than monomeric Aβ are the pathogenic forms. However, the molecular and mechanistic links between Aβ aggregation and toxicity are still unclear.

Prion diseases

Prion diseases also known as transmissible spongiform encephalopathies (TSEs) is a group of neurodegenerative disorders affecting humans and other mammals (Table 2.2). TSEs can be sporadic, heritable or acquired by infectious route. Although in humans infectious forms of TSEs occur less frequently than heritable or sporadic forms (accounting for approximately 5, 10 and 85% of all cases, respectively) they are most well known for the general public [4, 20]. Unlike in humans, TSEs in animals mainly occur as infectious disorders [20]. The agent that causes these diseases was termed "prion" by Stanley B. Prusiner and is defined as "proteinaceous infectious particle" [53, 66]. According to the protein-only hypothesis, the infectious disease-causing agent is the misfolded, aggregated form PrP^{Sc} of the cellular prion protein PrP^{C}. PrP^{Sc} can self-replicate by recruiting PrP^{C} as a substrate. Even though PrP^{C} and PrP^{Sc} share the same amino acid sequence, the secondary structures of these conformers are distinct. PrP^{C} consists of three α-helices and two short antiparallel β-strands, whereas PrP^{Sc} has a β-sheet-rich structure, which consists of β-strands and relatively short turns and/or loops, with no native α-helices present [20, 67]. Physiological roles of PrP^{C} are unclear, however, several potential functions, including regulation of synaptic transmission and plasticity, sleep homeostasis and continuity, cellular transport and localisation of its binding partners, modulation of the functionality of ion channels and ionotropic glutamate receptors, transmembrane signaling, and scavenging for amyloid aggregates of Aβ, have been suggested [68].

One of the most interesting aspects of prion diseases is the existence of multiple “strains”, which leads to different disease phenotypes that are distinguished by distinct clinical signs, incubation time and neuropathology [4, 17, 20]. To date there is still no clear understanding

TABLE 2.2: Prion diseases. Adapted from [4].

Disease	**Host**	**Route of transmission or disease-induction mechanism**
Sporadic CJD	Humans	Unknown
Iatrogenic CJD	Humans	Accidental medical exposure to CJD-contaminated tissues, hormones or blood derivatives
Iatrogenic CJD	Humans	Genetic (germline PRNP mutations)
Variant CJD	Humans	Genetic (germline PRNP mutations)
Kuru	Humans	Ritualistic cannibalism
Fatal familial insomnia	Humans	Genetic (germline PRNP mutations)
Sporadic fatal insomnia	Humans	Unknown
Gerstmann–Sträussler–Scheinker syndrome	Humans	Unknown
Scrapie	Sheep, goat and mouflon	Horizontal and possibly vertical
Atypical scrapie	Sheep and goat	Unknown
Chronic wasting disease	Mule deer, white-tailed deer, Rocky Mountain elk and moose	Horizontal and possibly vertical
Bovine spongiform encephalopathy (BSE)	Cattle	Ingestion of BSE-contaminated food
Atypical BSE	Cattle	Unknown
Feline spongiform encephalopathy	Zoological and domestic felids	Ingestion of BSE-contaminated food
Transmissible mink spongiform encephalopathy	Farmed mink	Ingestion of BSE-contaminated food
Spongiform encephalopathy of zoo animals	Zoological ungulates and bovids	Ingestion of BSE-contaminated food

what leads to formation of a wide variety of strains, or how many different strains can be formed. Understanding this phenomena is of fundamental importance for development of therapeutic treatment modalities, since approaches effective against one particular phenotype of disease, may be ineffective against other.

2.1.3 Insulin as a model protein to study amyloid aggregation

Insulin is a 5.8 kDa peptide hormone involved in regulation of carbohydrate, fat and protein metabolism [69–72]. Insulin consists of two polypeptide chains (A and B) linked by two disulfide bonds. The A chain consists of 21 amino acids with an additional disulfide bond between residues 6 and 11, whereas the B chain is longer and consists of 30 amino acids. The secondary structure of insulin is predominantly α-helical [73]. Under native conditions the dominant form of insulin is a zinc-coordinated hexamer. Over the pH 2-8 range the predominant form of zinc-free insulin can vary from dimer (insulin concentration $<$ 1.5 mg/ml) to tetramer (insulin concentration $>$ 1.5 mg/ml). Monomer is the dominant form of insulin in 20% acetic acid solution [74].

Biosynthetic human insulin is generally used as a protein-based medicine in the treatment of diabetes [74–76]. Despite its main application in medicine, recombinant human insulin is also extensively used as a model protein to study mechanisms and properties of amyloid fibril formation *in vitro* [69, 74, 76–88]. Under specific conditions insulin is prone to aggregate and can form amyloid aggregates that share common structural features with those that are found in neurodegenerative pathologies such as AD, PD, TSEs and other. Studies of insulin aggregation provided new fundamental insights into the process of amyloid formation and the polymorphism phenomena [74, 81–89]. Fibrillation of insulin itself is associated with the clinical syndrome injection-localised amyloidosis, which was observed in diabetes patients after continuous subcutaneous injections of insulin [71, 77, 90], however, such incidents are relatively rare [72].

2.1.4 The mechanisms of amyloid fibril formation

Peptides and proteins are very important biomolecules that are involved in almost every biological process. In order to function, these biomolecules have to acquire their native structural conformation [8, 29]. Protein molecules can adopt multiple distinct conformational states within a living system, starting from its synthesis in the ribosome and ending with degradation through proteolysis (Fig. 2.1) [8, 29]. Most newly synthesised peptides or proteins adopt a folded conformational state through the formation of one or more partially folded states (Fig. 2.1). Some peptides and proteins, including α-synuclein (α-syn), tau, islet amyloid polypeptide (IAPP) and Aβ are largely unstructured in solution and are often described as intrinsically disordered peptides and proteins (IDPs) [8, 91]. Although it was demonstrated that some IDPs can adopt more well-defined structures upon binding to specific partners [91, 92]. Under certain circumstances, however, peptides and proteins can fail to adopt, or remain, in their native functional conformation, and can acquire misfolded conformations that are susceptible to form nonfunctional and potentially harmful aggregates (Fig. 2.1) [8, 29]. Both globular proteins and IDPs have been found to be involved in protein aggregation linked to disease [8, 93–99].

The development and application of robust experimental and mathematical techniques that allow deciphering the mechanistic details of the protein aggregation process, in combination with fundamental biophysical techniques, used to study protein aggregation and amyloid formation, enabled to acquire mechanistic insight into the amyloid aggregation process [12, 13, 61]. When the quantity of fibrils formed during protein aggregation process is measured as a function of time by monitoring thioflavin-T fluorescence (ThT) intensity or light scattering, sigmoidal kinetics, reflecting three distinct phases, generally described as a lag, growth and plateau phase, are frequently observed (Fig. 2.2) [8, 29].

The process of amyloid fibril formation can be imagined as a nucleation dependent polymerisation reaction, where an initial nucleation step (*i.e.* primary nucleation) is followed by a rapid growth

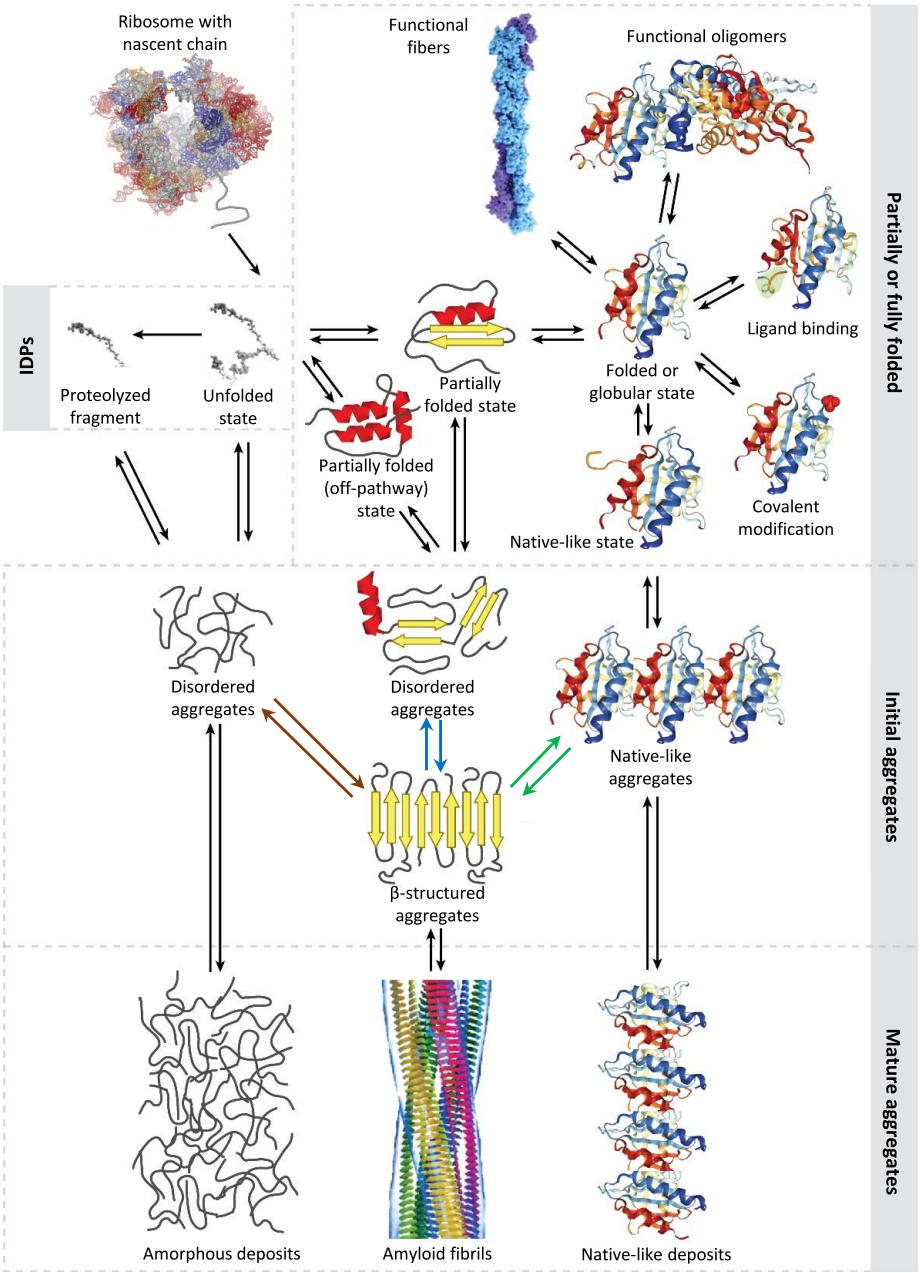

FIGURE 2.1: Schematic illustration of possible pathways of amyloid fibril formation. The brown, blue and green arrows represent three possible mechanisms of nuclei formation: nucleated polymerisation, nucleated conformational conversion and native-like aggregation, respectively. Adapted from [8].

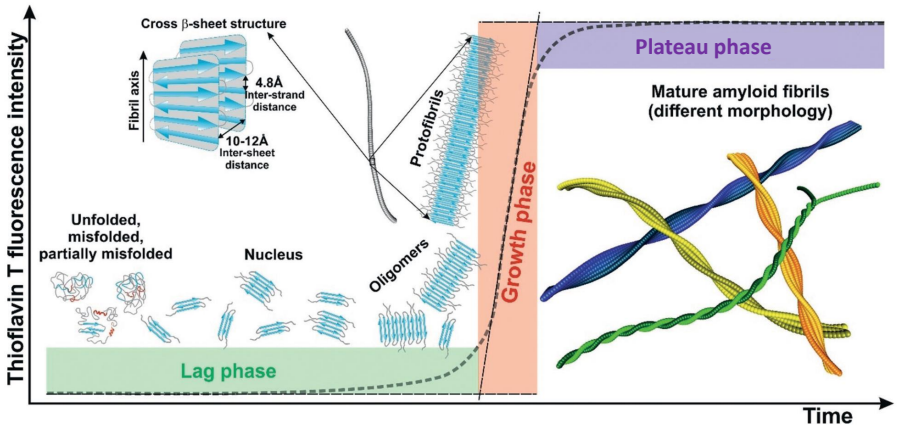

FIGURE 2.2: Schematic representation of the amyloid aggregation process monitored by measuring ThT fluorescence intensity. The lag phase corresponds to the assembly of peptides or proteins into the nuclei, which can grow into larger oligomeric species. In the growth phase nuclei and oligomers continue to grow and proliferate, assembling into prefibrillar structures that rapidly elongate to form ordered fibrillar structures known as protofibrils. The plateau phase corresponds to the assembly of protofilaments into mature amyloid fibrils. Adapted from [29].

through association and elongation and, in certain cases, through a secondary pathway (*e.g.* fibril-surface catalysed nucleation, termed secondary nucleation [61], and fibril fragmentation) [8, 100] (Fig. 2.3). Partially or completely disordered peptide and protein monomers can spontaneously convert into growth-competent structures, termed nuclei, through a thermodynamically unfavourable process, which takes place in the initial stages, also referred to as the lag phase, of aggregation process (Fig. 2.2). The nuclei can be considered as the smallest structures that are able to grow further through the addition of monomers to form intermediate species and amyloid fibrils [8, 100]. The aggregation process of a wide range of systems including Aβ [101], α-syn [97], prion proteins [102], insulin [98] and others [8], have been described using the nucleated polymerisation model.

In specific cases, however, monomers have been found to convert into misfolded aggregated species, which lack the structural characteristics necessary to grow into well organised amyloid fibrils (Fig. 2.1)

[8, 103]. These growth-incompetent species, however, can undergo structural reorganisation to generate nuclei on which other disorganised oligomeric species acquire the amyloid conformation through templating, leading eventually to the formation of intermediate and fibrillar amyloid species (Fig. 2.1) [8, 103]. Aforementioned type of aggregation mechanism, termed nucleated conformational conversion model, has been used to describe mechanism of amyloid formation of Aβ_{40} [94], α-syn [93], huntingtin (Htt) exon 1 [99] and others [8].

Most of aggregation prone regions in globular proteins are normally buried within the core of the protein, which means that in order to aggregate, fully folded proteins must first rearrange into partially unstructured states that are prone to aggregate. Latter structures can self-assemble into intermediate species and through one of the aforementioned mechanisms proceed to fibrillization stage (Fig. 2.1) [11, 104]. It was demonstrated that natively folded globular proteins possess small but significant tendency to rearrange into the amyloid state without crossing a major energy barrier for unfolding, by generating native-like conformations as a consequence of ligand release, local unfolding, or thermal fluctuations. Aggregation prone segments that are normally buried or highly structured in the fully folded state gain flexibility or become exposed to the solvent , triggering the formation of native-like aggregates that then rearrange into amyloid-like oligomers and fibrils (Fig. 2.1) [5, 8, 10, 104].

The molecular-level events, which contribute to the overall formation of amyloid aggregates can be divided into two general categories: events that lead to an increase in aggregate mass and events that modify the total number of aggregates [8, 13, 61, 62] (Fig. 2.3). Fibril elongation (addition of individual monomers to nuclei/fibril ends) is the main event that contributes to the growth of aggregate mass (Fig. 2.3). Typically, fibril elongation is much faster than their dissociation into monomers, thus the latter event is often neglected in descriptions of amyloid formation kinetics [13, 105]. The events involved in formation

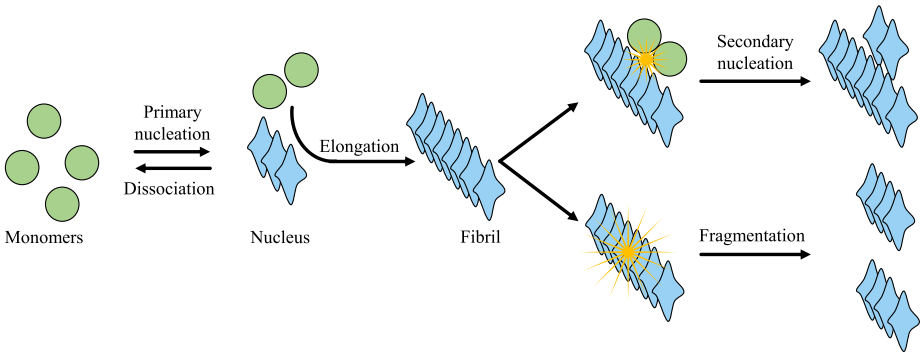

FIGURE 2.3: The molecular-level events involved in the amyloid aggregation process.

of new fibrils are primary nucleation, fragmentation and secondary nucleation (Fig. 2.3) [13, 88]. In the absence of preformed aggregates, primary (*i.e.* spontaneous) nucleation is always the first event in the protein aggregation process [13, 88]. Fibril fragmentation and secondary nucleation are fibril formation events that depend on the population of existing aggregates and are referred to as secondary processes to distinguish them from primary pathways that depend only on the concentration of monomers (*e.g.* primary nucleation) [13, 88]. Fragmentation generates new growth-competent fibril ends through breakage of existing fibrils, whereas secondary nucleation refers the formation of aggregation-competent nuclei from monomeric protein molecules on the fibril surface [13, 88]. During the secondary nucleation the formation of new aggregates takes place specifically on the surface of existing fibril, thus the amount of catalytic surface is not constant and it will alter with the amount of aggregates present [13, 88].

2.1.5 Structure of amyloid fibrils

Amyloid fibrils, formed by different peptides or proteins, seem to be remarkably similar at the angstrom length scale [5, 8, 29]. X-ray diffraction studies of distinct amyloid aggregates revealed a common β-sheet-rich structure, termed "cross-β", in which β-sheets run parallel to the long

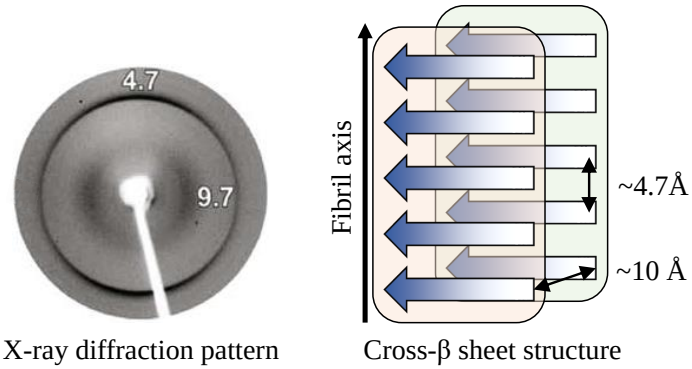

FIGURE 2.4: Cross-β pattern of amyloid fibrils. X ray diffraction pattern of amyloid fibrils (left) show a meridional reflection at 4.7-4.8 Å and an equatorial reflection at 10-12 Å. This diffraction pattern originates from cross-β structure, in which β-sheets run parallel to the long axis of the fibrils, while β-strands are arranged perpendicularly (right). Adapted from [108].

axis of the fibrils, while β-strands are arranged perpendicular to the fibril axis (Fig. 2.4) [29, 41]. The separation between β-sheets is 10-12 Å, while the distance between β-strands is 4.7-4.8 Å [29, 41, 106, 107].

Whether extracted from organisms or generated *in vitro* amyloid fibrils typically appear as unbranched, elongated, thread-like structures 6-13 nm in height and up to few micrometres in length, as observed by electron microscopy (EM) or atomic force microscopy (AFM) techniques [7, 8, 29]. Mature amyloid fibrils are typically composed from 2-6 protofilaments, that often twist around each other or associate laterally through specific side chain interactions [7, 8, 29, 44, 109]. Distinct three-dimensional arrangement of protofilaments, termed morphological polymorphism, has been observed by EM and AFM (Fig. 2.5) [29]. Unlike conformational polymorphism, which is caused by the different conformations of protofilaments themselves, morphological polymorphism is the different packing of protofilaments into amyloid fibrils. These morphological polymorphs can be divided into four types: crystals, twisted ribbons, helical ribbons and nanotubes (Fig. 2.5) [29, 44, 110, 111]. Crystals are tape-like aggregates, which possess no macroscopic chirality. Twisted ribbons are defined by undergoing pure torsion

around the fibril axis, leading to the saddle-like curvature, whereas helical ribbons are characterised by winding around a hypothetical cylinder of a finite radius, both polymorphs can be either right-handed or left-handed twisted. Finally, nanotubes are observed as elongated structures with no evident cross-sectional height periodicity along fibril axis [29, 44, 110, 111].

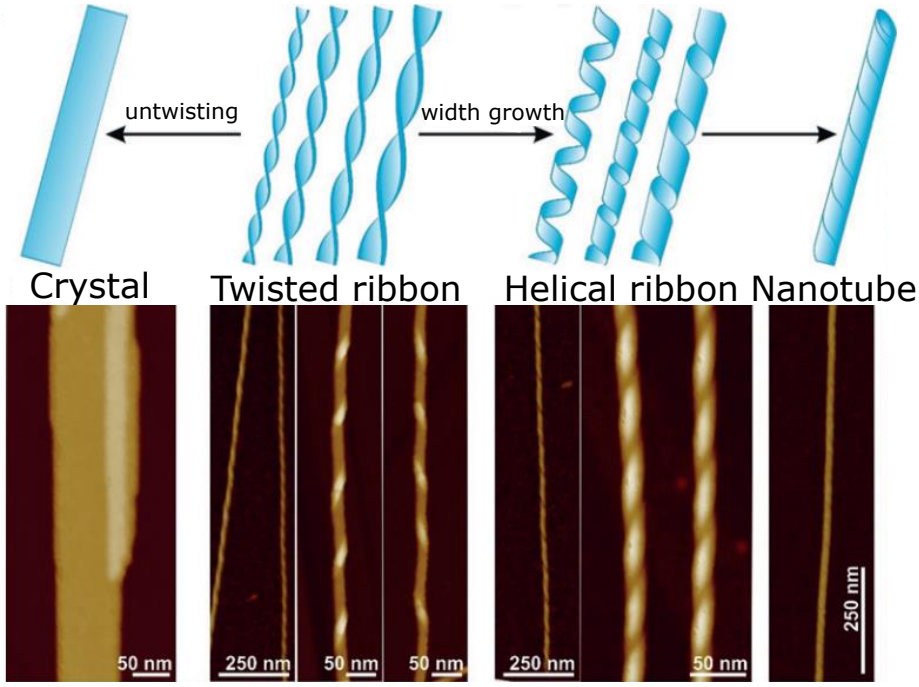

FIGURE 2.5: Morphological polymorphism of amyloid fibrils and order-order transitions among distinct polymorphs. Amyloid fibrils, possessing twisted ribbon structure can evolve into crystal or helical ribbon structure through untwisting or lateral aggregation, respectively. Amyloid fibrils, possessing helical ribbon structure can evolve into nanotubes through closure of the edges at constant mean curvature. Adapted from [29].

Order-order transitions have been observed among aforementioned polymorphs [29]. For instance, morphological transition sequence from

twisted ribbon to helical ribbon and finally nanotube was observed during detailed study of the heptapeptide aggregation process using high-resolution time-lapse AFM [111]. Transition from twisted ribbon to crystal fibrils was also observed [110]. The latter process is thought to proceed through progressive untwisting of twisted ribbon fibrils, whereas transition from twisted to helical ribbon fibril proceeds through progressive growth in width trough the lateral addition of protofilaments. The transition from helical ribbon to nanotube-like fibrils is thought to proceed through progressive closure of the helical ribbons, which enables to reduce the line tension associated with the external protofilaments while preserving identical curvature and hence bending energy [29].

The application of solid state nuclear magnetic resonance (ssNMR) spectroscopy, cryo-electron microscopy (cryo-EM), and X-ray crystallography to study structures of amyloid fibrils enabled to determine detailed three-dimensional structures of amyloid fibrils formed by distinct peptides and proteins, and has generated a dramatic increase in our knowledge of quaternary structure of fibrillar aggregates [8]. For instance, structural models of Aβ40 protofilaments formed under quiescent or agitated conditions, revealed not only differences between these polymorphs but also overall similarities (Fig. 2.6A, B) [112, 113]. Under agitated conditions Aβ40 forms protofilaments, which are 6 nm in width and associate laterally to form striated ribbons [112], whereas protofilamets formed under quiescent conditions are 7 nm in width and do not associate laterally [113]. Both models revealed that each Aβ40 peptide chain has a flexible N-terminal segment and a pair of β-strands at residues 10-22 and 30-40 [8, 112, 113]. In protofilaments, both β-strands are incorporated into stacked β-sheets, running parallel to the long axis of the protofilaments. All β-strands are arranged in a parallel, in-register fashion, and have multiple intermolecular side chain contacts [8]. However, the protofilaments formed under agitated conditions consist of four β-sheets and has a two-fold symmetry (Fig. 2.6A), whereas the ones formed under quiescent conditions consist of six β-sheets arranged in thee-fold symmetry (Fig. 2.6B). Another interesting example is fibril structure determined for the prion domain of HET-s from the filamentous fungus *Podospora anserina* (Fig. 2.6C) [114, 115].

HET forms fibrils consisting of a left-handed or right-handed β-solenoid structure in which each molecule contributes to two windings of the β-solenoid and eight β-strands [114, 115].

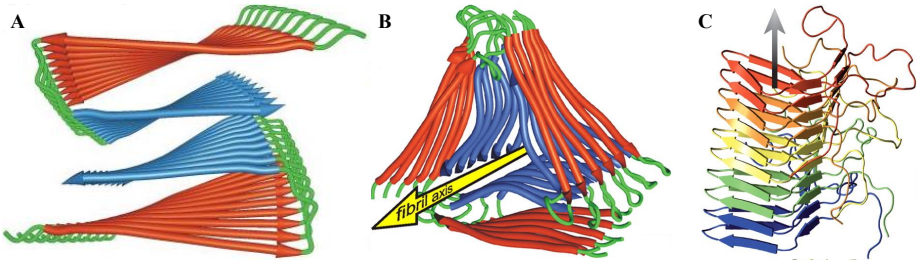

FIGURE 2.6: Three-dimensional structures of amyloid fibrils. Structural models of Aβ40 protofilaments formed under agitated (A) and quiescent (B) conditions. (C) Left-handed β-solenoid structure of the fibril of the HET-s prion domain. Adapted from [112] (A), [113] (B, Copyright (2008) National Academy of Sciences), [114] (C).

2.1.6 Polymorphism of amyloid aggregates

One of the most fascinating properties common among amyloidogenic proteins is their ability to form conformationally diverse fibrils, termed "strains", the best-studied example being prions [8, 10, 20, 21, 28, 29, 53, 116]. The prion strains are defined as conformationally different infectious aggregates that, when transmitted to identical hosts, exhibit distinct prion-disease phenotype, which is characterised by diverse patterns of protein aggregate deposition, incubation times, histopathological lesion profiles, and specific neuronal target areas [4, 9, 20, 28, 53]. Most of these traits are relatively stable across serial passage, however, formation of new distinct strains upon transmission of prions into a different host or into the same host expressing different polymorphisms of the prion gene, has also been observed [9, 53, 117, 118]. Latter phenomena is sometimes referred to as a "strain mutation" or "conformational switching".

"Strain mutation" or "conformational switching" is the ability of prions to adapt to specific environment through a Darwinian evolution:

the most "aggressive" strains that self-replicate fastest generally dominate [17, 19] (Fig. 2.7). This phenomena is frequently observed when prions are transmitted to different host species [119]. Although the origin of this phenomena is not clear, two hypotheses have been suggested. First, "cloud" hypothesis, which suggest that pools of infectious form of prion protein (PrP^{Sc}) within individual isolates are intrinsically heterogeneous (Fig. 2.7A). Upon the alteration in the environment, the strains that fit the best to replicate in the new environment gain selective advantages, which results in transformation of the strain population. Alternative to the "cloud" hypothesis is the deformed templating model, which suggests that alterations in the environment result in generation of new PrP^{Sc} variants and hence strains, which are the best fit for self-replication in a new environment [17–19] (Fig. 2.7B).

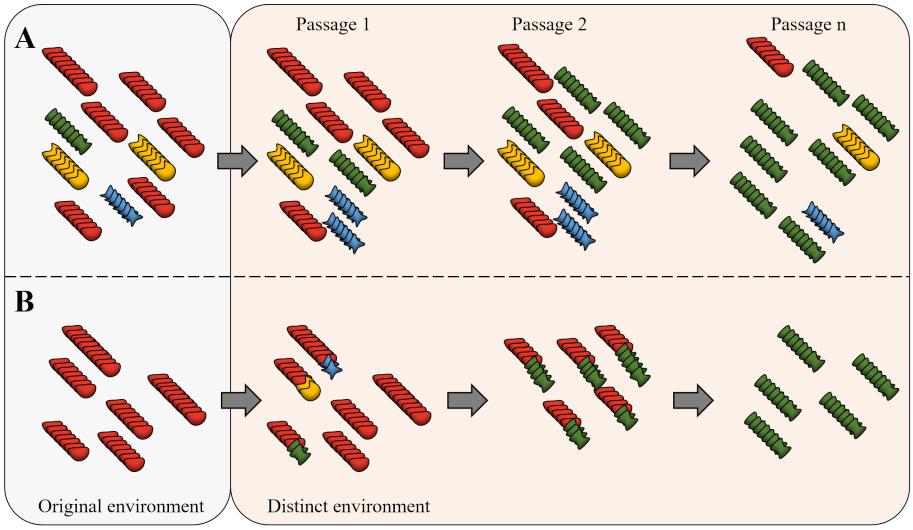

FIGURE 2.7: Schematic illustration of "cloud" (A) and deformed templating (B) hypotheses describing the origin of prion mutation phenomena. Adapted from [18].

The conformational diversity in prions initially was noted in goats [120]. Healthy goats inoculated with scrapie isolates (*i.e.* strains) from goats with scratching or nervous syndrome developed scrapie disease with similar symptoms to scratching or nervous syndrome, respectively. Later, two biologically distinct strains, termed "hyper" and "drowsy",

of transmissible mink encephalopathy agent has been isolated by serial passage in outbread Syrian golden hamsters [121]. Studies in mice have also demonstrated the existence of diverse prion strains, which produce characteristic phenotype in inoculated recipients [20, 53, 122, 123]. Subsequently, numerous prion strains have been identified in human and other mammal prion diseases [4, 9, 20, 53]. Biochemical analysis of prion aggregates, obtained from infected mammals, enabled to determine structural variations, including differences in glycosylation patterns, extent of protease resistance, electrophoretic mobility of proteolytic fragments and conformational stability, that make up different strains [26].

De novo formation of prion strains under distinct environmental conditions *in vitro* was demonstrated in multiple studies [17, 20–27]. The possibility to *in vitro* generate prion strains, which behave similar to the ones in live organisms, is of fundamental importance to elucidation of prion aggregation process. For instance, distinct prion strains, possessing different conformational stabilities, were generated from mouse recPrP by altering environmental conditions, including pH, temperature, and urea concentration. Subsequently, these strains were inoculated into transgenic mice (Tg9949). The animals inoculated with the most stable prion strains exhibited the longest incubation periods, while mice inoculated with the less stable aggregates developed prion disease sooner (Fig. 2.8) [124]. Interestingly, the opposite correlation was observed in case of hamster prions. Syrian golden hamsters inoculated with more stable strains exhibited shorter incubation periods, while hamsters inoculated with less stable strains developed prion disease later [125]. Even though conflicting, both results suggest that conformational stability of the aggregates and the duration of incubation time after inoculation in susceptible animals are directly correlated. This concept has been proven to be of fundamental importance for developing therapeutic strategies to fight prion diseases and their transmission. Despite persistent and sustained efforts there are no effective anti-prion drugs, and it seems that the effects of tested potential inhibitors is closely related to particular prion strains, as no universal inhibitor for all strains exists [17, 126]. It is worth to notice that even though most of the

artificial prion strains can self-replicate *in vitro*, only some of them are infectious and capable to self-propagate *in vivo* [17, 26, 27, 124]. Thus, the mechanisms of prion infectivity remain to be established.

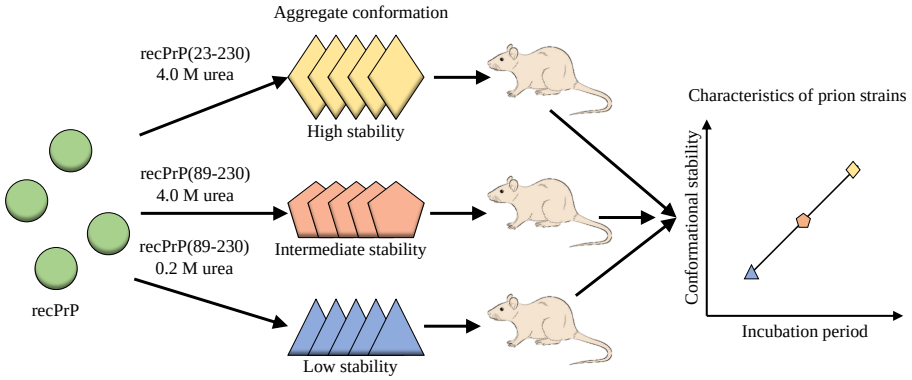

FIGURE 2.8: Schematic illustration of correlation between conformational stability of the aggregates and the length of incubation time after inoculation in susceptible animals. Mice inoculated with less stable strains develop prion disease faster when compared to the ones inoculated with the more stable aggregates. Adapted from [26].

Prion-like conformational variability has also been observed in fibrils formed by other amyloid proteins [8, 10, 28]. Multiple studies have shown that Aβ fibrils are highly polymorphic, with molecular structures that depend on aggregation conditions [127–131]. For instance, under quiescent and agitated conditions Aβ_{40} forms twisted fibrils and striated ribbons, respectively. Both of these strains could self-propagate even under distinct environmental conditions. In addition, these strains display significantly different toxicities in neuronal cell cultures [127]. Several discrete sub-populations of brain Aβ42 conformers, that have distinct conformational characteristics, different toxicity and propagation rates in AD, have been identified in brain samples of patients diagnosed with rapidly progressive sporadic AD [132, 133]. Similarly, Aβ40 fibrils, extracted from two patients with distinct clinical histories of AD, were structurally different from one another [129]. These findings suggest that AD exhibits a wide spectrum of Aβ conformers, with distinct structural characteristics, that may play an important role in the onset

and progression of distinct AD phenotypes. It was demonstrated that α-syn can form strains with different structures, levels of toxicity, *in vitro* and *in vivo* self-propagation properties, which cause distinct synucleinopathies [134–138]. Similarly, tau fibril strains, which target different brain regions and propagate pathology at unique rates, are thought to be responsible for the heterogeneity of human tauopathies [139–141]. Insulin was also found to form structurally different amyloid fibrils *in vitro* [74, 81–84, 86, 142]. Moreover, distinct strains of SOD1 aggregates with different structural architectures, molecular properties, distribution, end-stage aggregate levels, and histopathology were also reported by multiple studies [143, 144].

It is evident that structural polymorphism is common among amyloidogenic proteins. Studies of this phenomena are highly important for development of effective anti-prion therapeutic strategies.

Conformational polymorphism can be encountered at all levels of aggregation, and can be seen to originate due to rugged energy landscape that underlies misfolding and aggregation (Fig. 2.9) [29]. Peptide and protein folding into native conformation state can be described by an energy landscape that represents the energy of the amino acid sequence as a function of all possible conformations, and it can be seen as funnel-like landscape (Fig. 2.9) [29]. The newly synthesised polypeptide chain needs to run through several folding intermediates in order to acquire the native folded state. The energy landscape towards the thermodynamically favourable native conformational state is often rugged, meaning that the molecules have to cross substantial kinetic energy barriers [29, 145]. In the case of folding routes leading towards aggregate formation, the configuration of the energy landscape is similar to that of leading to the formation of native conformational state as far as funnel-like shape is concerned, however, due to the appearance of intermolecular interactions and their competition with intramolecular interactions, the ruggedness of the aggregation landscape is much larger [29, 146]. Newly synthesised polypeptide chains have a high degree of entropy and free energy. During the folding process the conformational states, and hence the entropy and free energy, decrease towards the state occupying the lowest absolute energy minimum, which represents the

conformation of natively folded proteins [28, 29, 146–148]. In case of folding routes leading towards aggregate formation, the amyloid fibrils have been postulated to be the most stable thermodynamic state occupying the lowest absolute energy minimum in the energy landscape [29, 149, 150]. The energy landscape of polypeptide chain folding into native state resembles a funnel with a global minimum that corresponds to the native state, whereas the energy landscape of amyloid fibrils can be characterised with numerous local minima peaks corresponding to different strains of fibrils [28, 29, 150] (Fig. 2.9). Theoretically, multiple strains could emerge in one fibrillization event, but the exact environmental conditions may favour the generation and propagation of one strain over the others [28]. In order to prevent formation of misfolded and non-functional conformational states of peptides and proteins, evolution has provided living systems with strategies to maintain peptides and proteins in their soluble states. Molecular chaperones are fundamental biomolecules which assist the folding of individual polypeptide chains into their native state by lowering the energy barriers separating folding intermediates. Chaperones also prevent intermolecular interactions between misfolded molecules, which otherwise could lead to the aggregate formation [8, 29].

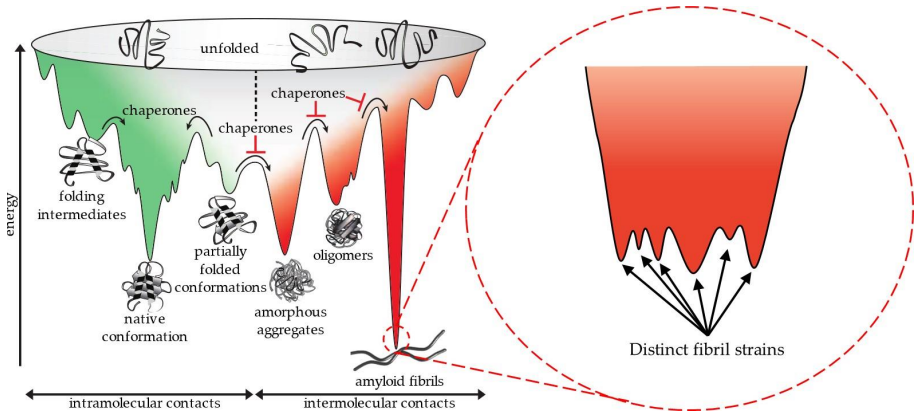

FIGURE 2.9: The energy landscape of polypeptide chain folding into native state (green) and the amyloid fibrils (red). The energy landscape of amyloid fibrils can have numerous local minima peaks corresponding to different strains of fibrils. Adapted from [29, 59].

2.1.7 Self-propagation and spreading of amyloid aggregates

A key pathogenic event in TSEs is conformational conversion of native, protease-sensitive, cell-surface localised prion protein PrP^{C} into a misfolded, aggregation-prone and protease-resistant pathogenic conformer, PrP^{Sc}. One of the most fascinating and also frightening features of TSEs is that they can be transmitted among individuals of the same and other species [9, 20, 28, 53, 151–153]. In humans, infectious forms of prion diseases include kuru, iatrogenic (iCJD) and variant Creutzfeldt-Jakob disease (vCJD). Kuru was transmitted among the Fore people of Papua New Guinea by ritualistic cannibalism during which they ate the brains of their relatives in an attempt to immortalise them [20, 154, 155]. iCJD was caused by prion-contaminated human growth hormone and gonadotropin, *dura mater* grafts, and transplants of corneas obtained from people who died of Creutzfeldt-Jakob disease (CJD) [20, 156, 157]. vCJD caused death of more than 200 people, mostly in United Kingdom. vCJD resulted from prions being transmitted from cattle with bovine spongiform encephalopathy (BSE) to humans through consumption of prion-tainted beef products [20, 158–160].

It is believed that stable, aggregation-prone nuclei (oligomers) or fibrillar aggregates (*i.e.* PrP^{Sc}), formed from misfolded PrP^{C}, can be transmitted between cells and even organisms where then they act as a "seed" that induces conformational change of PrP^{C}, located in host organism, into PrP^{Sc}, which eventually results in onset and progression of disease [4, 9, 20, 28, 151, 152, 161]. As an infectious agent, PrP^{Sc} can replicate itself by imprinting its pathogenic conformation on host PrP^{C} molecules. Although the molecular mechanisms underlying the *in vivo* PrP^{C}-to-PrP^{Sc} conversion are poorly understood, it is thought that it proceeds through one of the previously mentioned mechanisms, likely by nucleated-polymerisation reaction (Section 2.1.4) (Fig. 2.3 and Fig. 2.10) [9, 20, 161]. Briefly, the spontaneous formation of stable aggregation-prone oligomeric nucleus is thermodinamically unfavourable, however, once the nucleus has formed it acts as a template that induces conformational change of PrP^{C} into PrP^{Sc}. Thus the rate-limiting step is not the conformational conversion itself, but the

nucleation step [9, 161]. It is unlikely that a stable aggregation-prone nucleus will ever form in healthy individuals, who do not have gene mutations, which could result in the onset of prion disease, and whose biological clearance mechanisms function correctly. However, the nucleation step can be bypassed by exposure to exogenous "seed" (*i.e.* aggregation-prone nuclei (oligomers) or fibrillar aggregates) (Fig. 2.10) through ingestion (oral exposure), blood transfusion, *corneal* and *dura mater* transplantations from diseased cadaveric donors, through the use of prion-contaminated electroencephalography electrodes and neurosurgical instruments, and through the intramuscular administration of contaminated pituitary-derived hormones [4, 161]. The continuous fragmentation of existing fibrils and secondary nucleation are considered as one of the key processes that facilitate propagation of prion and also other amyloid aggregates [8, 161]. For instance, it was demonstrated that these secondary pathways play an important role in proliferation of SUP35 [162–164], IAPP [165], tau [166], Aβ [62, 63], α-syn [167] aggregates.

Recent collection of studies has provided convincing evidence that "prion-like" self-propagation may be a key phenomenon in all forms of amyloid, including Aβ, α-syn, tau, Htt, TTR, superoxide dismutase 1 (SOD1) and TDP-43. And it is most likely to be the mechanism by which amyloid deposits spread [151, 168–178].

Several mechanisms of cell-to-cell transmission have been proposed (Fig. 2.11) [28, 153]. Intracellular aggregates can be released from the host cell into extracellular space in the "naked" form via exocytosis [28, 153, 179, 180], or via membrane-bound vesicles such as exosomes [28, 181, 182] (Fig. 2.11 a, b, respectively). Aggregates free-floating in extracellular space may directly penetrate the plasma membrane of the recipient cells [179, 183] (Fig. 2.11 c), or enter by fluid phase endocytosis (Fig. 2.11 d) [177, 184–186] or receptor-mediated endocytosis (Fig. 2.11 e) [187, 188]. Exosomes containing aggregates can fuse with the membrane of recipient cell, and release aggregates into cytoplasm [181, 182, 189, 190]. Intercellular seeds may also be transferred via tunneling nanotubes [191, 192] (Fig. 2.11 f), that directly connect the cytoplasm of two cells. Internalised seeds then nucleate the fibrillisation of native

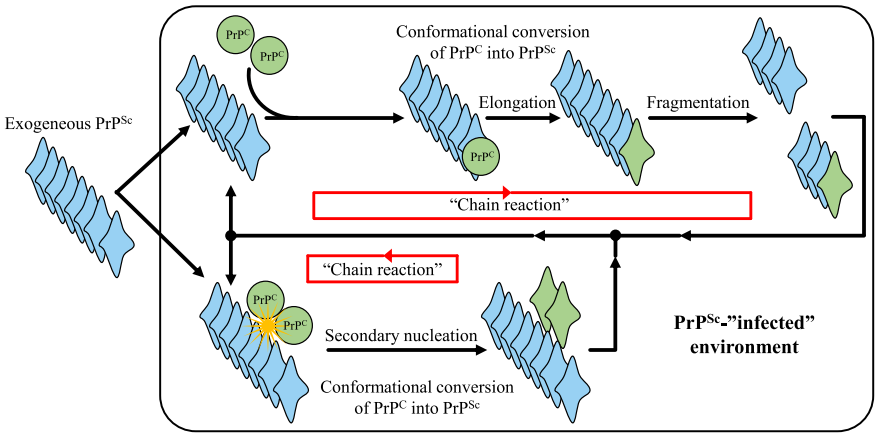

FIGURE 2.10: Schematic representation of PrP^C aggregation process induced by exposure to exogenous infectious agent. Spontaneous formation of aggregation-prone nuclei is a very slow process, which is unlikely to happen in healthy individuals. However, this step is bypassed upon exposure to exogenous "seed". Exogeneous PrP^{Sc} self-propagate by inducing conformational conversion of PrP^C into PrP^{Sc}. The continuous fragmentation of existing aggregates and secondary nucleation results in generation of new infectious agents. The overall process of self-replication can be imagined as a "chain-reaction" which is continuous until all monomeric species are depleted.

monomers in the cytoplasm of the recipient cell. It is evident that multiple pathways may be involved in cell-to-cell spreading of amyloid aggregates.

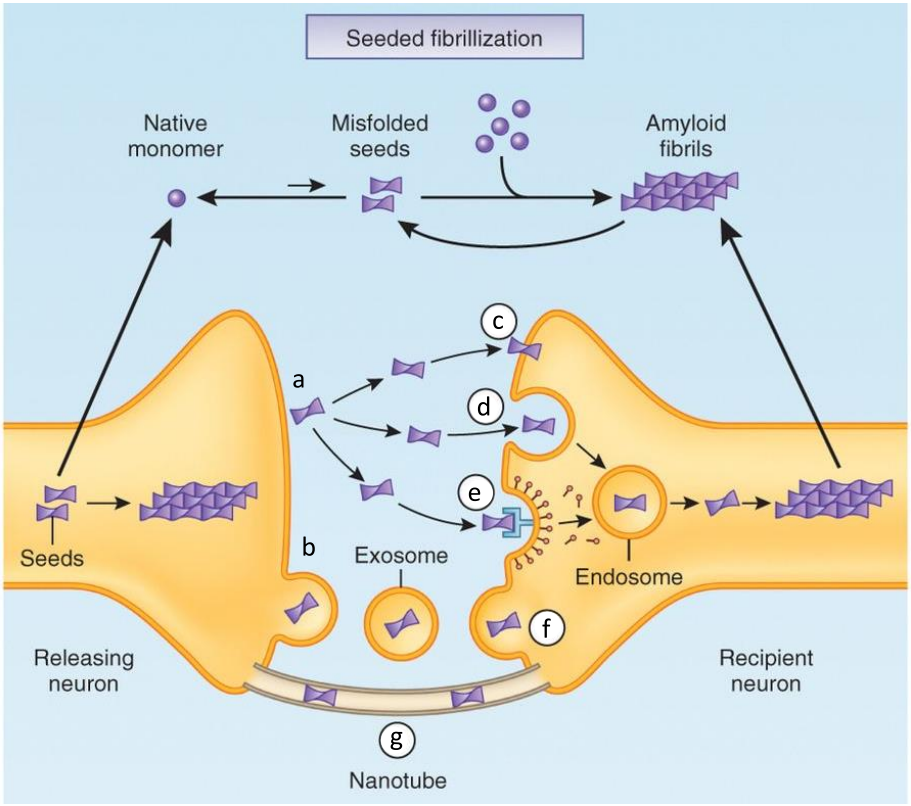

FIGURE 2.11: Schematic illustration of potential pathways of cell-to-cell spreading of amyloid aggregates. Cellular amyloid aggregates can be released from cell in "naked" form (a) or inside exosomes (b). Free-floating aggregates can enter recipient cell by direct penetration of the plasma membrane (c), fluid phase endocytosis (d), or receptor-mediated endocytosis (e). Exosomes containing aggregates may fuse with the membrane of recipient cell (f) and release aggregates into cytoplasm of recipient cell. Intracellular aggregate transfer may also occur via nanotubes (g), which directly connects the cytoplasm of two cells. Adapted from [28].

2.2 Biophysical techniques used to study amyloid aggregation.

2.2.1 Thioflavin-T assay

The benzothiazole dye Thioflavin-T (ThT) was first introduced as a fluorescent marker for amyloid fibrils in 1965 by Vassar and Culling. Upon binding to amyloid fibrils ThT displays a dramatic shift of excitation maximum (from 385 nm to 450 nm) and the emission maximum (from 445 nm to 482 nm), and exhibits a strong increase in fluorescence emission. It is thought that ThT behaves as a molecular rotor [193]. The ThT molecule consists of benzylamine and benzothiazole rings connected through a C-C bond. In solution, a low energy barrier enables these rings to rotate freely about their shared C-C bond, which quenches excited states generated by photon excitation, causing low fluorescence emission for free ThT. Upon binding to amyloid fibris, however, the rotation about C-C is restricted, resulting in a high quantum yield of fluorescence [193, 194].

Because of simplicity, ThT fluorescence assay has become a standard technique to monitor amyloid fibril formation *in vitro*. When the quantity of fibrils formed during amyloid aggregation process is measured as a function of time by monitoring ThT fluorescence emission intensity, sigmoidal kinetics are frequently observed (Fig. 2.12) [8, 29]. The phenomenological parameters describing aggregation process are: reaction half-time (t_{50}); maximal growth rate (k_{app}); and the lag time ($t_{lag} = t_{50} - 2/k_{app}$). These parameters can be extracted by fitting data with the following sigmoidal equation:

$$Y = y_i + m_i t + \frac{y_f + m_f t}{1 + e^{-((t-t_{50})\times k_{app})}} \tag{2.1}$$

where Y is ThT fluorescence emission intensity, t is time and t_{50} is the time point when 50% of maximum ThT fluorescence intensity is reached. The initial baseline is described by $y_i + m_i t$ and the final baseline is described by $y_f + m_f t$.

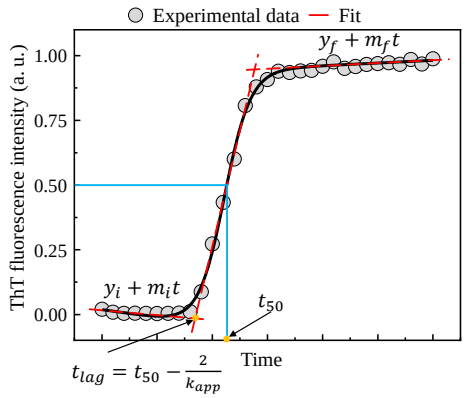

FIGURE 2.12: Schematic illustration of the sigmoidal increase in ThT fluorescence intensity upon amyloid fibril formation.

2.2.2 Chemical kinetics

Development and application of robust experimental and mathematical techniques to analyse the kinetics of amyloid fibril formation enabled to relate the commonly available bulk experimental measurements to the microscopic steps in the mechanism of aggregation and has brought new mechanistic insights into amyloid formation process [12, 13, 61, 195]. Distinct elementary molecular-level events, including primary nucleation, elongation, secondary nucleation and fragmentation, contribute to the overall formation of amyloid aggregates. One of the main goals in molecular-self assembly of amyloids is to determine importance and contribution of these microscopic steps to the overall reaction [61]. The investigation of the amyloid fibril formation mechanisms starts from the formulation of a differential rate law (*i.e.* master equation) for the aggregation kinetics. A full kinetic description of amyloid aggregation in terms of a master equation is complex, involving infinitely many non-linear coupled differential equations describing time evolution of the concentrations of each species (*i.e.* monomers, oligomers and fibrils). However, these equations can be simplified by considering only the total number and mass concentration of aggregates of any size instead of taking into account the concentrations of all aggregates sizes individually [12, 13]. In this

description, three quantities: the monomer concentration, the fibril number concentration, and the fibril mass concentration, define the state of aggregating system [12, 13]. For instance, aggregating system, in which all previously mentioned microscopic steps are present, can be described by following equations

$$\frac{dP}{dt} = k_n m(t)^{n_c} + k_- M(t) + k_2 M(t) \frac{m(t)^{n_2}}{(1 + m(t)/K_M)^{n_2}} \tag{2.2}$$

$$\frac{dM}{dt} = 2k_+ P(t) \frac{m(t)}{1 + m(t)/K_E} \tag{2.3}$$

where m(t) is the monomer concentration; P(t) is the the fibril number concentration; M(t) is the fibril mass concentration; n_c and n_2 are the reaction order for primary and secondary nucleation, respectively; k_n, k_+, k_- and k_2 are the primary nucleation, elongation, fragmentation and secondary nucleation rate constants, respectively; K_M is Michaelis constant for secondary nucleation. K_M has units of concentration^{n2}, and $K_M{}^{1/n2}$ gives monomer concentration at which secondary nucleation is half saturated. K_E is Michaelis constant for elongation. K_E has units of concentration, and it gives monomer concentration at which elongation is half saturated.

Because of the complexity of the aggregation process the selection of a suitable models for global fitting to the experimental data is difficult, however, the number of model choices can be narrowed down by applying constraints on possible mechanisms [12, 13]. In particular, the curvature of double logarithmic plots of the half-time versus monomer concentrations, and their slopes can provide insights into which aggregation mechanisms are dominant. For instance, linear plots suggest that the dominant mechanism does not change at different monomer concentrations, whereas positive curvature points towards the presence of saturation effects in the dominant mechanism and negative curvature indicates that competition of processes in parallel is present (Fig. 2.13). The scaling exponent γ, defined by the relationship $t_{50} \propto m(0)^{\gamma}$ can also provide insights into the underlying mechanism of amyloid formation. The γ expected for different dominant mechanisms of aggregation are

summarised at Table 2.3.

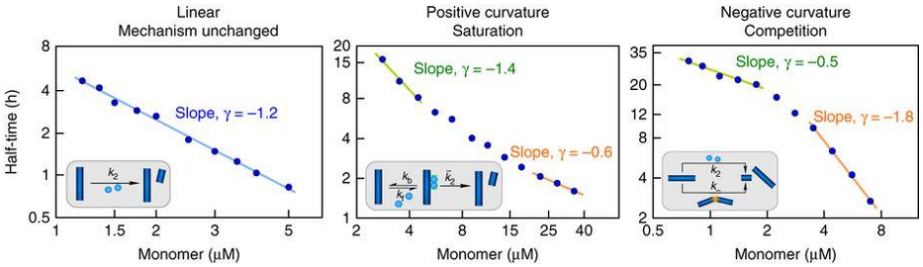

FIGURE 2.13: Schematic illustration of double logarithmic plots with different curvatures. Adapted from [12].

Application of this approach to study protein fibrillization has brought new mechanistic insights into aggregation process of distinct amyloid proteins, including Aβ40, Aβ42 and insulin [62, 88], and tremendously increased our knowledge of this complex process. Moreover, this approach has proven to be extremely useful in drug-discovery, as it enables to determine mechanisms of action of potential therapeutic molecules [42, 196–199].

TABLE 2.3: The scaling exponents expected for different dominant mechanisms of aggregation. Adapted from [12].

Dominant pathway	**Approximate γ**
Primary nucleation only	$-\frac{n_c}{2}$
Fragmentation	$-\frac{1}{2}$
Secondary nucleation	$-\frac{1+n_2}{2}$
Dominant pathway	**Change in γ**
Saturating secondary nucleation	$+\frac{n_2}{2}$
Saturating elongation	$+\frac{1}{2}$
Competing secondary processes	$-\frac{n_2}{2}$
Competing primary and secondary process	$-\frac{n_2+1-n_c}{2}$

2.2.3 Fourier-transform infrared spectroscopy (FTIR)

Infrared (IR) spectroscopy is one of the most important and well established analytical techniques for secondary structure determination of polypeptides, proteins and their aggregates [200–204]. The working principle of IR spectroscopy is based on the measurements of absorbed infrared radiation at a particular energy by a sample under investigation. The IR spectra of polypeptides display absorption bands associated with their characteristic amide group. There are nine such bands, termed amide A, amide B and amides I-VII. The amide I and II bands are the two most prominent vibrational bands of the protein backbone and therefore are frequently used to study structural properties of polypeptides.

The amide II band (1575-1480 cm^{-1}) derives mainly from in-plane N-H bending (60% of the potential energy) and from C-N stretching vibration (40% of the potential energy). Although the amide II band of deuterated polypeptide overlaps with the H-O-D bending vibration making it difficult to obtain information about the conformation of this band, the remainder of this band at 1550 cm^{-1} can provide information about the accessibility of solvent to the polypeptide backbone [200, 201, 203].

The amide I band (1700-1600 cm^{-1}) is the most useful infrared band for the analysis of secondary structure of polypeptides in aqueous environment. The amide I band derives mainly form C=O stretching vibration of the amide group coupled to the in plane N-H bending and C-N stretching modes. The exact frequency (*i.e.* wavenumber) of this vibration depends on the nature of hydrogen bonding involving the C=O and N-H groups, which is determined by the secondary structure of protein under investigation (Table 2.4) [200, 201, 203]. Since proteins can have a variety of domains containing polypeptide fragments in different conformations, the observed amide I band is typically a complex composite consisting of a number of overlapping component bands representing α-helices, β-sheets, turns and random structures [200, 201, 203]. To avoid overlapping of protein amide I and water bands, D_2O is used as solvent

TABLE 2.4: Assignment of amide I band positions to secondary structure of polypeptide chain. Adapted from [42, 200, 203, 207].

Secondary structure	**Band position in H_2O**	**Band position in D_2O**
α-helix	1657-1648 cm^{-1}	1660-1642 cm^{-1}
'3-turn' helix	1666-1659 cm^{-1}	1643-1639 cm^{-1}
β-sheet (characteristic for native β-sheet proteins)	1641-1623 cm^{-1}	1660-1642 cm^{-1}
β-sheet (characteristic for amyloid fibrils)	1630-1610 cm^{-1}	
Antiparallel β-sheet	1695-1674 cm^{-1}	1694-1672 cm^{-1}
β-turn	1686-1662 cm^{-1}	1694-1672 cm^{-1}
Random coil	1657-1642 cm^{-1}	1654-1639 cm^{-1}

in FTIR measurements. At equal concentrations of D^+ and H^+, respectively, the pH-meter reading with a glass electrode is 0.4 pH units lower in D_2O than in H_2O [205]. However, isotopes affect the pKa of protein ionizable groups, and for solutions of globular proteins the ΔpKa was found to be 0.4 pH units in the acidic range, thus the isotope effect on the glass electrode and the ionization constant cancel each other, so that an identical pH-meter reading (in the acidic range) refers to an identical ionization state of the biopolymer in D_2O and H_2O solutions [206].

FTIR has been extensively employed in the amyloid aggregation studies to monitor conformational transition from monomers to β-sheet rich fibrilar structures, as well as to determine structural properties of these aggregates [42, 81–86, 142, 204, 207].

2.2.4 Atomic force microscopy

Since introduction in 1986 by Binnig, Quate and Gerber, atomic force microscopy has emerged as one of the most powerful and versatile single-molecule techniques used for imaging and characterisation of biomolecules [7, 42, 208, 209]. AFM is a high precision technique which enables to acquire three-dimensional image of a sample, deposited on an atomically flat surface. Substrates, typically used for sample

deposition, are atomically flat mica, highly ordered pyrolytic graphite, glass, and gold [7, 42, 208]. The sample morphology is reconstructed by probing distance-dependent tip-sample interaction forces. The AFM probe is a microfabricated sharp tip, attached to a flexible cantilever at its free end (Fig. 2.14). Typically probes are made of silicon or silicon nitride and can be pyramidal or conical shaped, with tip radius of curvature between 1 and 50 nm. Conventional cantilevers are triangular or rectangular levers typically 10-200 μm in length [7, 42, 208, 209]. The sample can be moved in respect to the probe, horizontally (X, Y) and vertically (Z) using piezoelectric scanners (Fig. 2.14). The tip probes sample surface in a raster way, moving sequentially along parallel lines. All lines are divided in a fixed number of pixels, each of which stores a value of recorded tip-sample interaction force. Once the scan is completed the data acquired is used to reconstruct a three-dimensional representation of the sample surface, which is typically represented as a two-dimensional (XY) image associated with a height scale (Z) of the morphology of the sample [7, 42, 44, 208, 210].

Most of conventional AFMs can operate in two general modes: static or dynamic mode (DM) [7, 42, 208, 209]. In the static mode, also known as contact mode, the probe is brought into close contact with the sample and scanned across its surface. The elastic deformation (*i.e.* deflection) of the cantilever, caused by tip-sample repulsion forces, can be directly measured. Typically, optical lever method is used. A laser beam is focused on the back of the cantilever and the position of the reflected beam is detected by a position-sensitive four-quadrant photodiode (PSPD) (Fig. 2.14)[7, 42, 208, 209]. Three-dimensional images of the sample surface are obtained by maintaining a constant deflection of the cantilever, and hence tip-sample interaction force, during the scanning. The deflection Δz of the cantilever is proportional to the tip-sample interaction force F, as described by the Hooke's law $F = k \times \Delta z$, where k is the cantilever's spring constant [7, 42, 208, 209]. When the position of the laser spot on the PSPD changes, the feedback system including a proportional, integral, and differential (PID) controller (Fig. 2.14), reacts by extending or retracting the piezo actuator along the Z axis to compensate deviation of the cantilever deflection from the chosen set point

value. The vertical displacement ΔZ of the scanner is registered for each pixel and the obtained ΔZ map corresponds to the topograpy of the sample surface. In most of conventional AFMs the measured deflection of the cantilever ranges typically between 0.1 nm to a few micrometres, which enables to routinely measure forces ranging from 10^{-13} N to 10^{-5} N [7, 42, 208, 209].

Although static (*i.e.* contact) mode AFM is widely used to characterise solid substrates, its application to soft biological samples was found to be limited by a large lateral tip-sample frictional forces that are present during imaging, and which may cause sample damage and introduce artefacts in the measurements of soft biological samples [7, 42, 208, 209]. In order to avoid this issue, the dynamic mode of AFM was introduced [211]. In this mode the cantilever is driven into oscillation at a fixed excitation frequency, and scanned over the surface of the sample. Depending on the mechanism of how the cantilever is driven into oscillation, two modes of DM-AFM can be considered: amplitude-modulation (AM) mode and frequency-modulation (FM) mode [208]. In AM mode the cantilever is driven into oscillation using an external frequency generator (Fig. 2.14), whereas in FM mode a self-driven oscillator, which uses the signal of cantilever deflection as drive signal (Fig. 2.14), is used. Same as in static mode, the deflection of the cantilever in dynamic mode is typically measured using an optical lever method. In AM-AFM mode, the system is typically operating in tapping mode where the tip is intermittently brought in contact with the sample [7, 42, 208, 209]. However, if more complex feedback mechanisms are used, AM-AFM can also work in a non-contact mode, both in air and in liquid [7, 42]. The oscillation amplitude of the cantilever and its phase shift are used as a feedback parameters to measure the topography of the sample surface. When the distance between the tip and sample changes, the oscillation amplitude of the cantilever is modified, the feedback loop will adjust the tip-sample distance (ΔZ) by extending or retracting the piezo actuator along the Z axis in order to maintain amplitude constant [7, 42, 208, 209]. ΔZ value is recorded for each pixel and is subsequently used to retrieve the topography of the sample surface. Although FM-AFM has been implemented to reach atomic resolution

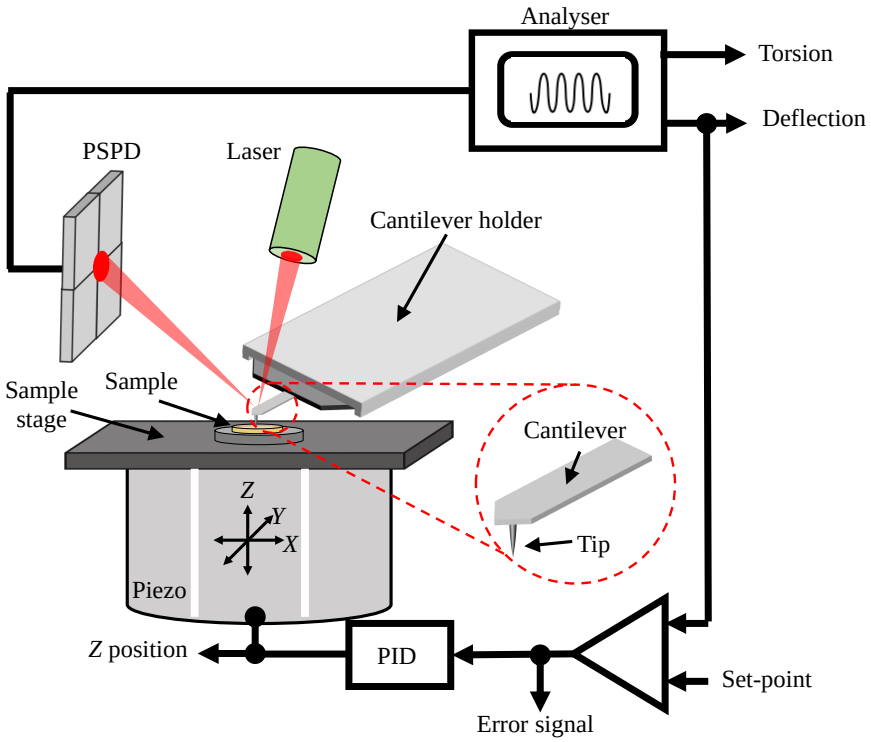

FIGURE 2.14: Simplified schematic depiction of an atomic force microscope operated in dynamic mode where the driving of the cantilever can be switched between amplitude modulation (solid lines) and frequency modulation (dashed lines) modes. In the AM-AFM mode the cantilever is driven into oscillation using an external frequency generator, while in the FM-AFM a feedback loop consisting of a time ("phase") shifter and amplifier is used to drive the oscillations of the cantilever. The cantilever oscillates between the nearest tip-sample position D and D+2A, where the equilibrium position of the tip is denoted as d. Adapted from [208].

in ultra-high vacuum environment, the more complex feedback mechanisms, and the low thermal stability of resonant cantilever frequency in air have limited its spreading for common applications [7, 42, 208, 209]. For all the reasons mentioned above, AM-AFM is the most commonly used modality of AFM to study biological specimen in liquid and air, and has been widely applied to investigate structures from the single protein to the cellular scale [7, 212, 213].

The AFM is often employed to study amyloid aggregation process [7, 42, 44, 214–217]. In particular, AFM enables to visualise and statistically characterise morphological properties (*e.g.* height, width, length) of the polymorphic and heterogeneous species, including monomers, oligomers, protofibrillar structures and mature amyloid fibrils, present during the process of amyloid aggregation [7, 44, 214–223]. This possibility has been essential for the elucidation of mature fibril structure and mechanisms of formation. For instance, based on statistical analysis of fibrillar species dimensions, including cross-sectional height, persistence length and periodicity, several studies have demonstrated that mature amyloid fibrils are formed by the hierarchical self-assembly of protofilaments twisting together through specific side chain interactions [41, 217, 224–228]. Moreover, studies of Aβ aggregation process using high-resolution AFM brought new mechanistic insights into the process of fibril formation and the molecular basis for the different structural transitions in the amyloid pathway [128, 131, 229–234] and for the first time provided visual evidence for secondary-nucleation sites on the surfaces of Aβ42 fibrils [131]. Imaging amyloid assembly process using AFM enables not only to monitor fibril formation but also allows to assess the effects of various internal and external factors on the aggregation process and the morphology of the final fibrillar products [235–239].

Chapter 3

Materials and Methods

Materials and methods of section 4.1.1

Formation of insulin aggregates

Recombinant human insulin was purchased from Sigma Aldrich (#91077C). Insulin amyloid fibrils were formed by incubating fresh 1 mM insulin solution in 100 mM phosphate buffer (PB), at different pH (in H_2O) and pH* (in D_2O, where pH* is the pH-meter readout uncorrected for isotopic effects [206]) values at 60 °C for 24 hours with 300 RPM agitation (using a MHR 23 thermomixer, Ditabis, Germany).

For seeding experiments 1 ml of insulin fibril solution was sonicated for 10 minutes using a Bandelin Sonopuls 3100 ultrasonic homogeniser equipped with a MS73 tip (using 50% of the power, cycles of 30 s/30 s sonication/rest, total energy applied to the sample per cycle, 0.56 kJ). The sample was kept on ice during the sonication procedure. Right after the treatment, one part of the fibrils was mixed with 9 parts of the fresh 1 mM insulin solution in the appropriate buffer and incubated at 37 °C for 24 hours without agitation. The secondary structures and morphological signatures of the aggregates obtained were determined using FTIR spectroscopy and AFM.

Measurements of seed-induced aggregation reaction kinetics

Samples were prepared as described above, with addition of 50 μM ThT. Right after mixing the fresh insulin solution with seeds, samples were divided into 200 μl aliquots, in 96-well plates. The plates were sealed using clear polyolefin sealing tape. The aggregation kinetics were followed under quiescent conditions at 37 °C using a Biotek Synergy H4 plate reader. Formation of insulin fibrils was monitored by measuring

ThT fluorescence intensity through the bottom of the plate every 2 min (with excitation filter 440 nm and emission filter 482 nm), simultaneously formation of fibrils was monitored by measuring absorbance at 600 nm, which changes together with the increasing size of aggregates due to light scattering.

Initial kinetic parameters of aggregation were obtained as described by [74], using Equation 2.1.

Fourier-Transform Infrared Spectroscopy

To avoid overlapping of protein amide I and water bands, 1 ml of insulin fibrils prepared in H_2O were separated from water by centrifugation at 20 000 $\times$ g for 30 min and subsequently resuspended in 1 ml of D_2O, the procedure was repeated three times.

Fibrils originally prepared in D_2O, or resuspended in D_2O, were sonicated for 1 minute using a Bandelin Sonopuls 3100 ultrasonic homogeniser equipped with a MS73 tip. The FTIR spectra were recorded using a Nicolet 5700 spectrometer from Thermo Scientific equipped with a liquid-nitrogen-cooled mercury-cadmium-telluride detector. For all measurements, CaF_2 transmission windows and 0.05 mm Mylar spacers were used. Spectra were recorded at room temperature. For each spectrum, 256 interferograms of 2 cm^{-1} resolution were co-added. A corresponding buffer spectrum was subtracted from each sample spectrum. All the spectra were baseline-corrected and normalised before further data processing. All data processing was performed using GRAMS software.

Atomic force microscopy

For AFM experiments, 1 mM insulin was diluted 100 times with deionized water, 30 μl of the sample were deposited on freshly cleaved mica and left to adsorb for 1 min, the sample was rinsed with 1 ml of water and dried gently using airflow. AFM images were recorded in the Tapping-in-Air mode at a drive frequency of approximately 300 kHz, using a MultiMode SPM microscope equipped with a NanoScope IIIa controller. PointProbe NCHR aluminium-coated silicon tips from

Nanosensors were used as a probe. AFM images were flattened using SPIP (Image Metrology) software.

Materials and methods of section 4.1.2

Formation of insulin aggregates

Recombinant human insulin was purchased from Sigma Aldrich (#91077C). Insulin amyloid-like fibrils were prepared by incubation of fresh insulin solution in 100 mM phosphate buffer pH 2.4 (with and without NaCl) at 60 °C for 24 hours in quiescent conditions. To follow aggregation kinetics, (0.5–5.0 mg/ml) samples were prepared as described above, with addition of 100 μM Thioflavin T (ThT). Aggregation kinetics were recorded at constant 60 °C temperature using QIAGEN Rotor-Gene Q real-time analyser. Increase of ThT fluorescence intensity upon fibril formation was observed using green channel (excitation 470 nm; emission 510 nm).

Determination of kinetic parmetes

Initial kinetic parameters of aggregation were obtained as described by [74], using Equation 2.1.

ThT maximum intensities showed linear increase upon rising protein concentration. Fibril concentration was estimated by matching maximum ThT fluorescence intensity to the respective initial insulin concentration for each experimental curve (assuming that aggregation efficiency is 100%) using the following equation:

$$\text{Fibril concentration} = \frac{(y_x - y_{min}) \times c}{y_{max} - y_{min}} \tag{3.1}$$

where y_x is ThT fluorescence intensity at time x, y_{min} and y_{max} are the minimal and maximal fluorescence intensities, respectively, and c is initial insulin concentration.

Data analysis

Insulin aggregation models and experimental data fitting were done

using rModeler (Ubicalc Software). Fitting was performed using "Classic", "Saturated elongation", "Classic + Tetramers" and "Classic + Capping" models (Fig. 3.1) on experimental results from insulin aggregation with and without NaCl. Steps of amyloid aggregation were described using the following equations:

Primary nucleation, a process in which native protein molecules (M) change their secondary structure and become aggregation centers (A) with rate constant k_n:

$$\frac{d[A]}{dt} = k_n[M]^2 \tag{3.2}$$

Elongation (3.3) or saturated elongation (3.4), responsible for fibril growth (F), during which amyloidogenic proteins are added to aggregation centers (A) with rate constant k_+, where K_M determines the monomer concentration at which this process saturates:

$$\frac{d[F]}{dt} = k_+[M][A] \tag{3.3}$$

$$\frac{d[F]}{dt} = \frac{k_+[M][A]}{1 + \frac{[M]}{K_M}} \tag{3.4}$$

Secondary nucleation, the process of aggregation center (A) formation on the surface of fibrils (F) with rate constant k_2, using the surface as a catalyst:

$$\frac{d[A]}{dt} = k_2[M]^2[F] \tag{3.5}$$

Fibril fragmentation, resulting in the creation of new aggregation centers (A) due to breaks in the fibrils (F) with rate constant k_-:

$$\frac{d[A]}{dt} = k_-[F] \tag{3.6}$$

Equilibrium between monomers (M) and tetramers (T), where k_t and k_m are the tetramer and monomer formation rate constants:

$$\frac{d[T]}{dt} = k_t[M]^4 \tag{3.7}$$

$$\frac{d[M]}{dt} = -k_m[A][T] \tag{3.8}$$

"Capping" of aggregation centers (A) by tetramers (T) with rate constant k_c:

$$\frac{d[A]}{dt} = -k_c[A][T] \tag{3.9}$$

	1° Nucleation	Elongation	Saturated elongation	2° Nucleation	Fragmentation	Monomer-Tetramer Equilibrium	"Capping"
	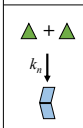	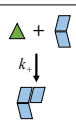	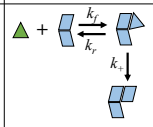	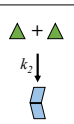	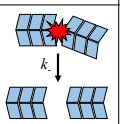	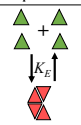	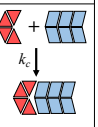
Increase in *[A]* Increase in *[F]*	$k_n M(t)^2$ *negligible*	- $k_+ M(t)A(t)$	- $\frac{k_+ M(t)A(t)}{1+\frac{M(t)}{K_M}}$	$k_2 M(t)^2 F(t)$ *negligible*	$k_- F(t)$ -	- -	$-k_c A(t)T(t)$ -
"Classic" model	+	+		+	+		
"Saturated elongation"	+		+	+	+		
"Classic + Tetramers"	+	+		+	+	+	
"Classic + Capping"	+	+		+	+	+	+

FIGURE 3.1: A schematic representation of microscopic events involved amyloid fibril formation process described by four different models. The rate constants are k_n (primary nucleation), k_+ (elongation), k_2 (secondary nucleation), k_- (fragmentation), and k_f and k_r (intermediate association and dissociation) as well as two additional steps, which include K_E (monomer–tetramer equilibrium) and k_c (aggregation center "capping").

Dynamic light scattering (DLS)

For DLS experiments, freshly prepared 0.5-5.0 mg/ml insulin solutions at different NaCl concentrations were filtered through 0.45 μm syringe filters. The size measurements were performed at 60 °C using Malvern Zetasizer μV. For each sample 3 repeats of 10 scans were recorded.

Circular dichroism (CD)

For CD experiments, 5 mg/ml insulin samples, with and without 100 mM NaCl, were filtered through 0.45 μm syringe filters. The samples were incubated at 60 °C and CD spectra were measured every 15

minutes in the 190-280 nm wavelength region using a Jasco J-815 Spectropolarimeter with a 0.1 mm path length cuvette. Each measurement was repeated 3 times.

Atomic force microscopy

For AFM experiments 30 μl of the 5.0 mg/ml (diluted 10 times) insulin fibril solutions, containing 0, 25, 50, 75 and 100 mM NaCl, were deposited on freshly cleaved mica and left to adsorb for 1 min, the samples were gently rinsed with water and dried using airflow. AFM images were recorded in the Tapping-in-Air mode at a drive frequency of approximately 300 kHz, using Bruker Dimension Icon scanning probe microscope system and aluminium-coated silicon tips RTESPA-300 as a probe. AFM images were flattened using SPIP (Image Metrology) software.

Fourier-transform infrared spectrometry

To prepare monomer samples, 5.0 mg of insulin were dissolved in 100 mM phosphate buffer pD 2.4 (in D_2O) with and without 100 mM NaCl. To prepare fibril samples, insulin fibrils were separated from buffer solution by centrifugation at 20 000 $\times$ g for 30 min and later resuspended in D_2O, the procedure was repeated three times. All samples were sonicated for 1 min using Bandelin Sonopuls 3100 ultrasonic homogeniser equipped with MS73 tip (using 50% of the power, total energy applied to the sample - 1.12 kJ). The FTIR spectra were recorded using Bruker Vertex 80v IR spectrometer equipped with mercury cadmium telluride (MCT) detector. For all measurements, CaF_2 transmission windows and 0.05 mm Teflon spacers were used. Spectra were recorded at room temperature under vacuum conditions ($\approx$2 mBar). For each spectrum, 256 interferograms of 2 cm^{-1} resolution were co-added. A corresponding buffer spectrum was subtracted from each sample spectrum. All the spectra were normalised to the same area of amide I/I' band (1700-1595 cm^{-1}). All data processing was performed using GRAMS software.

Materials and methods of section 4.1.3

Preparation of initial solutions

Initial solutions of insulin (Sigma Aldrich #91077C) were prepared by dissolving 2 mg of dry insulin powder in 0.5 ml of 100 mM sodium phosphate buffer pH 2.4, supplemented with 100 mM NaCl (PB) or 20% acetic acid, supplemented with 100 mM NaCl (AC). Concentration of insulin (M.W. - 5808 Da, ε_{280} - 6335 M^{-1} cm^{-1}) was determined by measuring UV-absorption at 280 nm using NanoDrop 2000 (Thermo Fisher Scientific). Subsequently, insulin solutions were diluted to a final concentration of 2 mg/ml (344 μM) using PB or AC and supplemented with 200 μM of Thioflavin-T (ThT; Sigma Aldrich #T3516) from 10 mM ThT stock solution (in MilliQ water).

Fresh solutions of 344 μM of EGCG (Sigma Aldrich #989-51-5) were prepared by dissolving EGCG in 100 mM sodium phosphate buffer pH 2.4, supplemented with 100 mM NaCl or in 20% acetic acid, supplemented with 100 mM NaCl, just before the experiment.

$EGCG_{ox}$ was prepared by dissolving 10 mM of EGCG in 10 mM phosphate buffer solution, pH 7.4 and incubating for 8 hours at 60 °C in a thermomixer (Ditabis). EGCG oxidation was followed by UV-Vis spectroscopy (Supplementary Fig. A.1). Subsequently, it was diluted to a final concentration of 344 μM using PB or AC.

Measurements of Aggregation Kinetics

For the inhibition experiments, 344 μM solutions of EGCG or $EGCG_{ox}$ were mixed with 344 μM insulin solutions in a 1:1 ratio. 3 replicates of each solution were then pipetted into a nonbinding surface plate (NBS; Corning #3881). Low binding plates are recommended [240] and extensively used for amyloid formation kinetic studies [241–244]. The plate was sealed using sealing tape (Nunc #232701). Kinetics of insulin aggregation was monitored at 60 °C without and with continuous shaking (960 rpm) by measuring ThT fluorescence emission intensity (excitation - 440 nm, emission - 480 nm) through the bottom of the plate using Synergy H4 Hybrid Multi-Mode (Biotek)

microplate reader for 15 hours (readouts were taken every 5 min under quiescent conditions and every 2 min under agitated conditions). 3 independent measurements were performed for each sample.

The highest ThT fluorescence emission value within each curve was assumed as I_{max}. Half-times (t_{50}) of aggregation process were obtained as described by Nielsen *et al.* [74]. Briefly, experimental data was fitted using Equation 2.1.

Evaluation of EGCG and EGCG$_{ox}$ effects on insulin aggregation process

The effects of EGCG and EGCG$_{ox}$ on insulin aggregation process were determined by comparing experimental values of t_{50} or I_{max} of control samples with the ones determined in the presence of EGCG or EGCG$_{ox}$ using one-way ANOVA. $P < 0.01$ was accepted as statistically significant.

Atomic Force Microscopy

Right after kinetic measurements the samples were collected and 20 μL of each sample, was deposited on freshly cleaved mica and incubated for 1 min. Subsequently, samples were rinsed with 1 ml of MilliQ water and dried under gentle airflow. Three-dimensional AFM maps were acquired using a Dimension Icon (Bruker) atomic force microscope operating in tapping mode and equipped with a silicon cantilever Tap300AI-G (40 N m^{-1}, Budget Sensors) with a typical tip radius of curvature of 8 nm. High-resolution (1024 $\times$ 1024 pixels) images were acquired. The scan rate was 0.5 Hz. AFM images were flattened using SPIP (Image Metrology) or NanoScope Analysis (Bruker) software.

Fourier-Transform Infrared Spectroscopy

Insulin fibrils were separated from buffer solution by centrifugation at 10000 $\times$ g for 30 min and subsequently resuspended in 1 ml of D_2O, the procedure was repeated three times. Finally, fibrils were resuspended in 0.3 ml of D_2O and sonicated for 1 min using Sonopuls 3100 (Bandelin) ultrasonic homogeniser equipped with MS73 tip (using 50% of the power, total energy applied to the sample - 1.12 kJ). Samples were

deposited between two CaF_2 transmission windows separated by 0.05 mm teflon spacers. The FTIR spectra were recorded using Vertex 80v (Bruker) IR spectrometer equipped with a mercury cadmium telluride detector, at room temperature under vacuum (≈2 mBar) conditions. 256 interferograms of 2 cm^{-1} resolution were averaged for each spectrum. Spectrum of D_2O was subtracted from the spectrum of each sample. All spectra were normalised to the same area of amide I/I' band (1700-1595 cm^{-1}). All data processing was performed using GRAMS software.

Materials and methods of section 4.2.1

Materials

Protein grade guanidine hydrochloride (GuHCl) was purchased from Carl Roth GmbH, guanidine thiocyanate (GuSCN) and other chemicals were purchased from Fisher Scientific UK.

Protein purification

The expression vector (plasmid pRSETB) harbouring nucleic acid sequence encoding N-terminally truncated mouse prion protein (rMoPrP89-230) fused to an N-terminal linker containing 6×His tail and a thrombin cleavage site, was a generous gift of Prof. Witold K. Surewicz.

The expression vector for rMoPrP89-230 was transformed into Ca^{2+}-competent *E. coli* BL-21 Star^{TM} (DE3) (Invitrogen) cells by heat shock, spread on LB agar plates containing ampicillin (100 μg/ml), and incubated for 16 h at 37 °C. 100 ml of LB medium supplemented with ampicillin (100 μg/ml) was inoculated with a single colony and grown overnight at 37 °C and 220 RPM shaking. Subsequently, 200 ml of LB medium containing ampicillin (100 μg/ml) was inoculated with 5 ml of overnight culture and incubated at 37 °C and 220 RPM shaking until an OD_{600} of 0.5-0.6 was reached. Protein expression was then induced by adding IPTG to a final concentration of 1 mM, and the incubation was continued for additional 18 h. The cell suspension was centrifuged at 15000 × g at 4 °C for 15 min. The cell pellet was resuspended in 100 ml

of buffer A (6 M GuHCl, 10 mM Tris, 100 mM potassium phosphate, 10 mM reduced glutathione, pH 8.0), homogenised with Potter–Elvehjem homogeniser and sonicated for 20 min on ice using Sonopuls 3100 (Bandelin) ultrasonic homogeniser equipped with VS70T tip (60s/60s horn, 70% duty cycle). The cell pellet was centrifuged at 20000 $\times$ g at 4 °C for 30 min. After centrifugation, the soluble protein fraction was added to 30 ml of Ni Sepharose^{TM} 6 (GE Healthcare) resin and stirred (80 RPM) for 30 min at 4 °C. The resin was poured into a XK26/20 (GE Healthcare) column and washed with 100 ml of buffer A at 3 ml/min flow rate. Subsequently, refolding of rMoPrP89-230 protein was performed by applying a 200 ml (1 ml/min) gradient of buffer A to buffer B (10 mM Tris, 100 mM potassium phosphate, pH 8.0). Protein impurities devoid of histidine tails were removed from the sepharose resin with 75 ml (3 ml/min) of 50 mM imidazole in buffer B. The rMoPrP89-230 was eluted with buffer C (10 mM Tris, 100 mM potassium phosphate, 500 mM imidazole, pH 6.4) at 3 ml/min flow rate. His tail-fused rMoPrP89-230 was dialysed 3 times against 4 l of buffer D (10 mM potassium phosphate, pH 6.4) at 4 °C. The His tail was cleaved with 5 units thrombin/mg protein. The cleaving reaction was carried out in buffer D at 4 °C overnight. A GSDP fusion at the N-terminus remained after thrombin cleavage of the linker. Subsequently, ion exchange chromatography was performed on a CM Sepharose Fast Flow column (20 ml) (GE Healthcare) using a linear 0-500 mM (3 ml/min) gradient of NaCl in buffer D. Then rMoPrP89-230 was dialysed 3 times against 4 l of buffer E (10 mM acetate, pH 4) at 4 °C, concentrated to the final concentration of $\approx$ 3 mg/ml and frozen at - 80 °C. Protein concentration was determined using the molar extinction coefficient $\epsilon = 27515 M^{-1} cm^{-1}$. The purity of the final product was determined by SDS-polyacrylamide gel electrophoresis. The identity of the protein was further confirmed by mass spectrometry (performed Dr. Vytautas Smirnovas). Formation of the disulfide bond was verified by the lack of free thiol groups in the folded protein.

De novo formation of distinct prion strains

To prepare different fibril strains, monomeric protein from a stock

solution was diluted to a concentration of 0.5 mg/ml in 50 mM phosphate buffer (pH 6) containing 2 M or 4 M GuHCl, and incubated for one week at 37 °C with 220 RPM shaking (in shaker incubator IKA KS 4000i).

Seeding experiments

For seeding experiments rPrP-A^{4M} fibrils were treated for 10 min using Bandelin Sonopuls 3100 ultrasonic homogeniser equipped with MS72 tip (using 20% power, cycles of 30 s/30 s sonication/rest, total energy applied to the sample per cycle — 0.36 kJ). The sample was kept on ice during the sonication. Right after the treatment, fibrils were mixed with 0.5 mg/ml of mouse prion solution in 2 M GuHCl in 50 mM phosphate buffer, pH 6, containing 50 μM ThT. Elongation kinetics at 60 °C temperature was monitored by ThT fluorescence assay (excitation at 470 nm, emission at 510 nm) using Qiagen Rotor-Gene Q real-time analyser [245]. ThT fluorescence curves were normalised by dividing each point by the maximum intensity of the curve.

Depolymerisation assay

For depolymerisation assays, amyloid fibrils were resuspended to a final concentration of 25 μM in 50 mM phosphate buffer, pH 6, containing 0.5 M GuSCN and homogenised by sonication (same way as in preparation of seeds). These solutions were diluted 1:4 in a buffer containing varying concentrations of GuSCN, and incubated for 60 min at 25 °C in Maximum RecoveryTM microtubes (Axygen Scientific, Inc., Union City, California, USA). 150 μl of samples were mixed with 850 μl of 100 mM phosphate buffer, pH 7, containing ThT (final concentration after dilution was 50 μM), then each mixture was sonicated for 15 s (same conditions as described above). Fluorescence was measured at 480 nm using the excitation wavelength of 440 nm. Depolymerisation curves were normalised by dividing each point by the average intensity of the points in the plateau region. Fractional loss of signal at increasing denaturant concentrations corresponds to the fraction of rMoPrP dissociated from amyloid fibrils.

Atomic force microscopy

For AFM experiments, 30 μL of the sample were deposited on freshly cleaved mica and left to adsorb for 1 min, the sample was rinsed with several ml of water and dried gently using airflow. AFM images were recorded in the Tapping-in-Air mode at a drive frequency of approximately 300 kHz, using a Dimension Icon (Bruker, Santa Barbara, California, USA) scanning probe microscope system. Aluminium-coated silicon tips (RTESPA-300) from Bruker were used as a probe. AFM images were flattened using SPIP (Image Metrology).

Fourier-Transform Infrared Spectroscopy

To prepare samples for the FTIR measurements, rMoPrP aggregates were separated from the buffer by centrifugation (30 min, 15.000 g), and resuspended in D_2O, sedimentation and resuspension was repeated three times to minimise the amount of GuHCl and H_2O. After resuspension samples were homogenized by 1 min sonication (same conditions as described above). The FTIR spectra were recorded using Bruker Alpha spectrometer equipped with deuterium triglycine sulfate (DTGS) detector. For all measurements, CaF_2 transmission windows and 0.1 mm Teflon spacers were used. Spectra were recorded at room temperature. For each spectrum, 256 interferograms of 2 cm^{-1} resolution were co-added. A corresponding buffer spectrum was subtracted from each sample spectrum. All the spectra were normalised to the same area of amide I/I' band. All data processing was performed using GRAMS software.

Materials and methods of section 4.2.2

Protein grade GuHCl was purchased from Carl Roth GmbH, GuSCN and other chemicals were purchased from Fisher Scientific UK.

rMoPrP89-230 purification was performed as described in previous section "Materials and methods of section 4.2.1".

Kinetics of spontaneous rMoPrP aggregation

Monomeric rMoPrP89-230 from a stock solution was diluted to a

concentration of 0.5 mg/ml in 50 mM phosphate buffer (pH 6.0) containing 2 M or 4 M GuHCl, and incubated at 37 °C with 220 RPM shaking (in shaker incubator IKA KS 4000i), or with 10 RPM rotation (in Fisherbrand Mini Tube Rotator). Formation of amyloid fibrils was monitored by periodically collecting 10 μl of sample, mixing it with 90 μl of 50 mM phosphate buffer (pH 6.0) containing 2 M or 4 M GuHCl, and 55.55 μM of ThT, and measuring ThT fluorescence emission (ex. 440 nm, em. 480 nm) intensity using Cary Eclipse (Varian) fluorimeter.

Kinetics of seed-induced aggregation reaction

For seeding experiments rMoPrP fibrils were treated for 10 min using Bandelin Sonopuls 3100 ultrasonic homogeniser equipped with MS72 tip (using 20% power, cycles of 30 s/30 s sonication/rest, total energy applied to the sample per cycle — 0.36 kJ). The sample was kept on ice during the sonication. Right after the treatment, fibrils were mixed with 0.5 mg/ml of mouse prion solution containing varying concentrations of GuHCl in 50 mM phosphate buffer, pH 6, supplemented with 50 μM ThT.

Elongation kinetics at 40-65 °C temperature range were monitored by ThT fluorescence assay using Qiagen Rotor-Gene Q real-time analyser (excitation at 470 nm, emission at 510 nm) [245] or Cary Eclipse fluorimeter (excitation at 440 nm, emission at 480 nm), or by measuring light scattering (600 nm) via Cary Eclipse fluorimeter. For light scattering measurements samples were prepared as described previously, but without ThT. ThT fluorescence and light scattering curves were normalised by dividing each point by the maximum intensity of the curve.

Atomic Force Microscopy

For AFM measurements, 20 μL of each sample, was deposited on freshly cleaved mica and incubated for 1 min. Subsequently, samples were rinsed with 1 ml of MilliQ water and dried under gentle airflow. Three-dimensional AFM maps were acquired using a Dimension Icon (Bruker) atomic force microscope operating in tapping mode and equipped with a silicon cantilever Tap300AI-G (40 N m^{-1}, Budget Sensors) with a typical tip radius of curvature of 8 nm. High-resolution

(1024 $\times$ 1024 pixels) images were acquired. The scan rate was 0.5 Hz. AFM images were flattened using SPIP (Image Metrology) software.

Fourier-Transform Infrared Spectroscopy

To prepare samples for the FTIR measurements, rMoPrP aggregates were separated from the buffer by centrifugation (30 min, 15000 g), and resuspended in 1 ml D_2O, sedimentation and resuspension was repeated four times to minimise the amount of GuHCl and H_2O (last resuspension was performed in 0.2 ml). After resuspension samples were homogenized by 1 min sonication (same conditions as described above). The FTIR spectra were recorded using Vertex 80v (Bruker) IR spectrometer equipped with a mercury cadmium telluride detector, at room temperature under vacuum ($\approx$2 mBar) conditions. 256 interferograms of 2 cm^{-1} resolution were averaged for each spectrum. Spectrum of D_2O was subtracted from the spectrum of each sample. All spectra were normalised to the same area of amide I/I' band (1700-1595 cm^{-1}). All data processing was performed using GRAMS software.

Depolymerisation assay

For depolymerisation assays, amyloid fibrils were resuspended to a final concentration of 25 μM in 50 mM phosphate buffer, pH 6, containing 0.5 M GuSCN and homogenised by sonication (same way as in preparation of seeds). These solutions were diluted 1:4 in a buffer containing varying concentrations of GuSCN, and incubated for 60 min at 25 °C in Maximum RecoveryTM microtubes (Axygen Scientific, Inc., Union City, California, USA). 150 μl of samples were mixed with 850 μl of 100 mM phosphate buffer, pH 7, containing ThT (final concentration after dilution was 50 μM), then each mixture was sonicated for 15 s (same conditions as described above). Fluorescence was measured at 480 nm using the excitation wavelength of 440 nm. Depolymerisation curves were normalised by dividing each point by the average intensity of the points in the plateau region. Fractional loss of signal at increasing denaturant concentrations corresponds to the fraction of rMoPrP dissociated from amyloid fibrils.

Materials and methods of section 4.3

Preparation of monomeric Aβ42 solution

The recombinant Aβ42 peptide was synthesised in Escherichia coli BL21 Gold (DE3) strain (Stratagene, CA, USA) and purified as described previously [246]. Briefly, cells were resuspended and sonicated in 8 M urea. Then ion exchange chromatography in batch mode was performed on a diethylaminoethyl (DEAE) cellulose resin, fractions containing Aβ42 peptide were collected and lyophilized. The lyophilized fractions were then purified using a Superdex 75 26/60 column (GE Healthcare, IL, USA), fractions containing recombinant Aβ42 were collected and lyophilized.

Solutions of monomeric Aβ42 peptide were prepared by dissolving lyophilised peptide in 6 M guanidinium hydrochloride (GuHCl). Monomeric Aβ42 peptide was purified from the presence of potential oligomeric species and GuHCl by gelfiltration in 20 mM sodium phosphate buffer, pH 8.0 containing 200 μM EDTA and 0.02 % NaN_3 using a Superdex 75 10/300 GL column (GE Healthcare) at a flow rate of 0.5 ml/min.

Aggregation of Aβ42

Solution of monomeric Aβ42 was diluted to the final concentration of 5 μM in 20 mM sodium phosphate buffer, pH 8.0, 200 μM EDTA and 0.02% NaN_3 in low-bind Eppendorf tubes. Two solutions: the first one containing monomeric Aβ42 with addition of 20 μM ThT as fluorescent tracer to monitor the kinetics of peptide aggregation over time, and the second, without ThT to follow the process of peptide aggregation via AFM, were prepared. 80 μL of each sample were pipetted into multiple wells of 96-well, half-area plate of black polystyrene with clear bottom and nonbinding surface (Corning 3881). The plate was sealed with a sealing tape to minimise the evaporation of the sample over the course of aggregation. Aggregation experiments were performed at 37 °C under quiescent conditions, ThT fluorescence was monitored using bottom optics in a Fluostar Omega (Fluostar Optima from BMG Labtech,

Aylesbury, UK) plate reader with 440 nm excitation and 480 nm emission filters. Samples without ThT were collected into low-bind Eppendorf tubes on ice after 0, 15, 30, 60 and 120 min and were deposited on bare mica using microfluidic spray deposition technique [217].

Microfluidic sample deposition

Samples collected after 0, 15, 30, 60 and 120 mins were deposited on atomically flat mica surface using microfluidic spray deposition technique [217]. Briefly, the samples taken at a different time points were subjected to the microfluidic spray device at a flowrate of 100 μL/h using syringe pump and sprayed for 30 s using a nitrogen gas pressure of 3.0 bar. The spray distance from the surface was 4 cm. Samples taken at 0, 15 and 30 min were diluted 5 times in 20 mM sodium phosphate buffer, pH 8.0, 200 μM EDTA and 0.02% NaN_3 before the spray. Samples taken at 60 and 120 min were sprayed without dilution.

AFM measurements

Atomic force microscopy was performed on atomically flat mica. Three-dimensional AFM maps were acquired using NX10 (Park systems) atomic force microscope operating in non-contact mode and equipped with a silicon cantilevers PPP-NCHR (42 N/m) or SSS-NCHR (42 N/m) (Park Systems, South Korea) with a typical tip radius of curvature of < 10 nm and 2 nm respectively. PPP-NCHR cantilevers were used for large area (10 $\times$ 10 to 25 $\times$ 25 μm; 2000 $\times$ 2000 to 3000 $\times$ 3000 pixels) imaging, while SSS-NCHR were used for a high-resolution imaging (1 $\times$ 1 to 3 $\times$ 3 μm; 1000 $\times$ 1000 to 2000 $\times$ 2000 pixels), with the scan rates $<$ 0.5 Hz.

In order to compare consistently the morphology of individual samples and avoid large imaging forces, which might induce uncertainties in measurements of sample dimensions, standardised experimental conditions were maintained by keeping a constant regime of phase change not exceeding $\Delta 20^\circ$ [247]. The change in oscillation amplitude is related to the sample morphology, while the change in phase reflects the dissipated energy during the tip-sample interaction, thus constant tip-sample interaction force can be maintained by keeping constant phase

change [247].

Image flattening and single molecule statistical analysis were performed using SPIP (Image Metrology, Hørsholm, Denmark) software. In order to keep consistency processing of all images was performed using the same parameters. Aggregates were masked from the flattening procedure in order to avoid artefacts of analysis. First, images were flattened by 0 order plane fit. Subsequently, images were flattened by plane and then line by line 1^{st} regression order fit. The latter step was repeated until the flat baseline in line profile of the image was reached. 2^{nd} regression order fit was applied in case of very crowded images or images with exceptionally high surface features. Height and width of each individual aggregate were measured by determining the cross-sectional diameter perpendicular to the aggregate axis. Length (or diameter in case of spheroidal particles) was determined by tracing along the median axis of each aggregate.

Chapter 4

Results and Discussions

4.1 Studies of insulin aggregation

4.1.1 pH-driven polymorphism of insulin fibrils

The results discussed in this section were published in PlosOne [14] together with following authors: Domantas Darguzis, Akvile Botyriute, Martynas Grigaliunas, Roland Winter and Vytautas Smirnovas.

I have performed part of FTIR measurements, performed AFM imaging and measurements of seeded aggregation kinetics, and analysed the data.

Studies that explore effects of various organic molecules on amyloid aggregation often use dimethyl sulfoxide (DMSO) to dissolve these compounds [244, 248–253]. Typically, the effects of residual DMSO concentration on aggregation kinetics are considered. However, it is known that alterations in the environmental conditions can modulate protein aggregation pathways, and result in formation of structurally distinct amyloid aggregates. Recently, our laboratory has performed a large screening of potential inhibitors of insulin aggregation at pH 2 in the presence of 5% residual DMSO [252]. Therefore, we decided to examine in detail whether a small amount of DMSO affects insulin aggregation process.

In order to determine the effects of DMSO on insulin aggregation process, the FTIR spectra of fibrils spontaneously formed in D_2O in the presence and absence of 5% DMSO, were compared (Fig. 4.1). To reveal possible changes induced by the use of D_2O instead of H_2O, which was required to avoid overlapping of infrared modes of H_2O with the amide

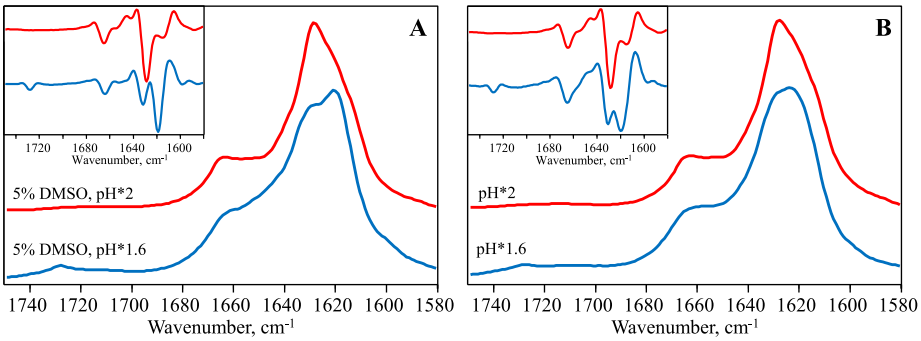

FIGURE 4.1: Absorption and second derivative (inset) FTIR spectra of fibrils grown in the presence (A) and absence of 5% (B) DMSO. Adapted from [14].

I mode of proteins, and to determine whether subtle alterations in pH may affect the fibrilization propensity of insulin, fibrils were prepared in heavy water samples at pH* 1.6 and pH* 2 (where pH* is the pH-meter readout uncorrected for isotopic effects [206]). pH* 1.6 was chosen in order to mimic similar concentrations of H^+ and D^+ [205], whereas pH* 2 was chosen to reach the same ionisation state of the protein in the two solvents (*i.e.* H_2O and D_2O) [206]. The FTIR spectra of insulin fibrils formed in the presence and absence of DMSO look similar (Fig. 4.1A, B). Interestingly, a rather small difference in pH* resulted in formation of fibrils with distinct amide I' band contours (Fig. 4.1A, B). The second derivative FTIR spectra of insulin fibrils formed at pH* 2 exhibit a major minimum at 1628 cm^{-1} and a minor one at 1615 cm^{-1}, whereas spectra of fibrils formed at pH* 1.6 exhibit a major minimum at 1619 cm^{-1} and a weaker one at 1631 cm^{-1} (Fig. 4.1A, B (insets)), suggesting predominantly β-sheet structures, however, with a significantly distinct hydrogen-bonding patterns. Insulin fibrils formed at pH* 1.6 exhibit an additional band outside the amide I' region at 1728 cm^{-1}, which was assigned to the stretching vibrations of a deuterated carboxyl group (-COOD) according to Surmacz-Chwedoruk *et al.* [84]. Similar spectral characteristics were recently described as a hallmark of distinct insulin fibril strains [84, 86].

Fibrils formed at pH* 1.6 in the presence of DMSO exhibit both straight and curved morphology (Fig. 4.2A), whereas fibrils formed in

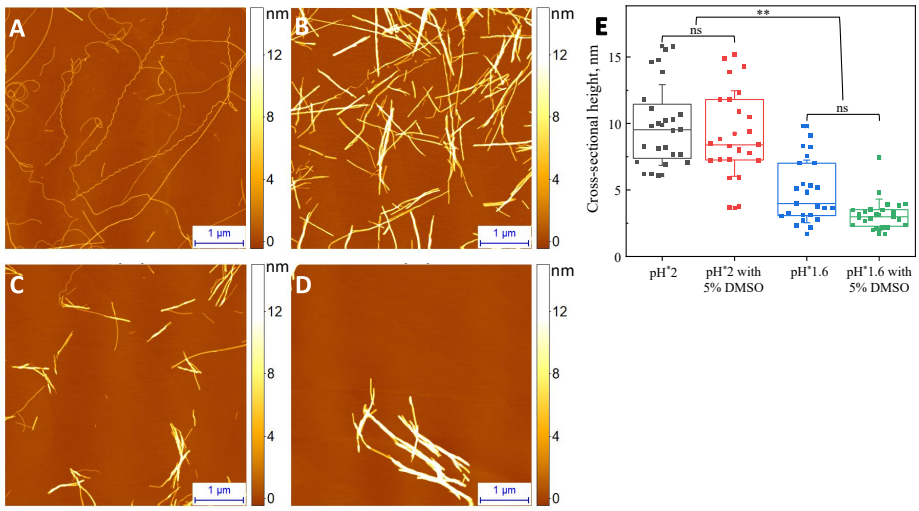

FIGURE 4.2: AFM images of insulin fibrils formed in the presence of DMSO at pH* 1.6 (A), and pH* 2 (B), or in the absence of DMSO at pH* 1.6 (C), and pH* 2 (D). (E) cross-sectional height of single fibrils. ** - significantly different at P < 0.05. ns - no significant difference at P < 0.05. Adapted from [14].

the absence of DMSO at pH* 1.6 (Fig. 4.2C), or at pH* 2 in presence (Fig. 4.2B) or absence (Fig. 4.2D) of DMSO, are typically straight. Analysis of fibril cross-sectional height revealed no significant differences between fibrils formed in the presence or absence of DMSO (Fig. 4.2E). The cross-sectional height of fibrils formed in the presence of DMSO was 9.2 $\pm$ 3.2 nm or 3.1 $\pm$ 1.2 nm at pH* 2 and pH* 1.6, respectively, whereas height of fibrils formed in the absence of DMSO was 9.9 $\pm$ 3.0 nm or 4.9 $\pm$ 2.4 nm at pH* 2 and pH* 1.6, respectively. The cross-sectional height of fibrils formed at pH* 1.6 is significantly lower than the height of fibrils formed at pH* 2 (Fig. 4.2E), suggesting formation of distinct fibril strains.

Insulin fibrils formed at pH* 1.6 or pH* 2 can self-propagate under both pH* conditions at 37 °C (Fig. 4.3). Fibrils formed at pH* 1.6 proliferate at a similar rate (the half-times (t_{50}) of seeded insulin aggregation are 47 $\pm$ 2 min and 48 $\pm$ 2 min at pH* 1.6 or pH* 2, respectively) under both pH* conditions, whereas fibrils formed at pH* 2 self-replicate faster under original environmental conditions (t_{50} are 197 $\pm$ 4 min and 112 $\pm$ 3 min at pH* 1.6 or pH* 2, respectively). In general fibrils formed

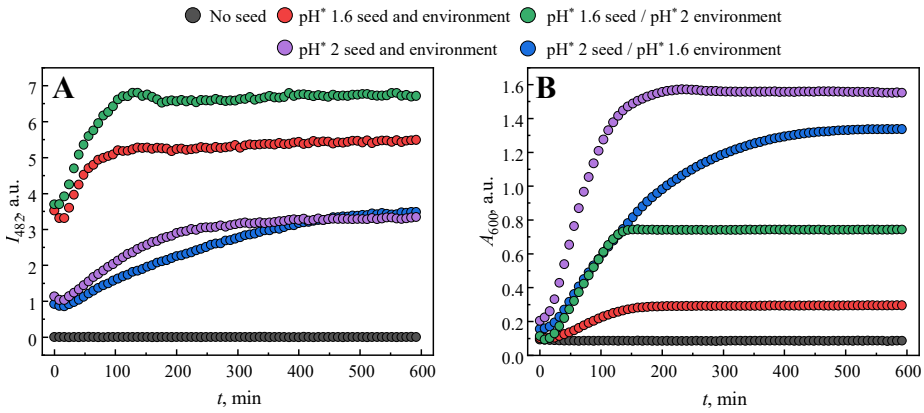

FIGURE 4.3: Kinetics of seed-induced insulin aggregation monitored by measuring ThT fluorescence intensity (A) or light absorbance at 600 nm (B). Adapted from [14].

at pH* 1.6 proliferate faster than the ones formed at pH* 2. It is evident that ThT fluorescence intensity, which marks formation of fibrillar aggregates, is seed-dependent: when compared to pH*2-seed-induced aggregates, pH* 1.6-seed-induced aggregates result in an about two times higher maximum ThT intensity. Interestingly, the opposite effect is evident when the formation of insulin aggregates is monitored by measuring absorbance at 600 nm, which changes together with the increasing size of aggregates due to light scattering. The pH* 2-type fibrils induce formation of insulin aggregates that strongly absorb visible light (600 nm), the absorbance being ≈25% lower in the case of seeding in the pH* 1.6 environment. The pH* 1.6-type fibrils induce formation of aggregates, which absorb visible light about 5 times weaker than the pH* 2-type fibrils, however, the absorbance is strongly increased at pH* 2 environment.

The FTIR spectra of pH*2-seed-induced insulin aggregates formed at pH*2 and pH*1.6 are almost identical (Fig. 4.4A). In case of pH* 1.6-seed-induced aggregates, the spectra of fibrils formed at pH* 1.6 and pH* 2 are similar, however, in pH* 2 the intensity of the band at 1631 cm^{-1} is slightly higher. These results confirm the ability of both types of insulin fibrils to self-propagate their conformation under environment distinct from the original one that governed the spontaneous formation

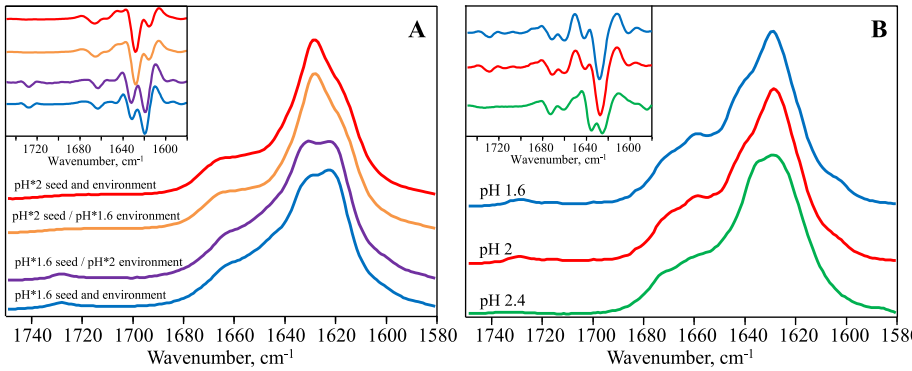

FIGURE 4.4: Absorption and second derivative (inset) FTIR spectra of seed-induced insulin aggregates (A) and insulin aggregates formed in H_2O environment at distinct pH (B). Adapted from [14].

of these structures, and suggest the existence of two distinct insulin fibril strains.

Surprisingly, the FTIR spectra of insulin fibrils spontaneously formed in H_2O at pH 1.6 and pH 2 look nearly identical (Fig. 4.4B). Second derivative spectra of fibrils formed at either pH* exhibit a major minimum at 1628 cm^{-1} and a minor one at 1641 cm^{-1}, and an additional band outside of the amide I/I' region at ≈1730 cm^{-1} (Fig. 4.4B (inset)). The FTIR spectrum of fibrils spontaneously formed in H_2O at pH 2.4 is slightly different from the previous two, the second derivative spectra has two similarly expressed minima at 1625 cm^{-1} and 1636 cm^{-1}, and also does not have an additional band at 1730 cm^{-1} (Fig. 4.4B). The secondary structure elements constituting amyloid fibrils are highly protected from hydrogen/deuterium exchange, and hence the most of the amide group hydrogen molecules stay unchanged despite resuspension of the aggregates in D_2O. This reflects in the blue-shift of the FTIR spectra, when compared to the spectra of insulin fibrils formed in D_2O.

The formation of distinct types of insulin fibrils was first described by David F. Waugh *et al.* [254] more than 60 years ago, however no structural or cross-seeding data were presented. More recently, formation of structurally different insulin fibril strains were reported in the

presence and absence of 20% ethanol (at pH* 1.5-1.9) [81–83], and using slightly different insulin forms (bovine insulin (*BI*) and recombinant Lys^{B31}-Arg^{B32} human insulin analogue (*KR*) (at pH* 1.9) [84, 86]. The spectral characteristics of latter insulin fibril strains are very similar to the ones observed in this study. The FTIR spectrum of insulin fibrils formed at pH* 2 is similar to the spectrum of *BI* strain, whereas spectrum of fibrils formed at pH* 1.6 looks very much alike the spectrum of *KR* strain. Thus the effect of two additional positively charged residues on the conformation of fibrillar structure is similar to the effect of ΔpH by -0.4 units. Such alterations in pH has a minor effect on the net charge of protein molecule, also, taking into account that in H_2O environment at pH 1.6 or pH 2 insulin forms same type fibrils, which display almost identical spectral characteristics, we may conclude ionisation state is not the factor governing formation of different strains. This rises the question: what could be this factor?

A possible answer to this question can be found by analysing results of recent studies [255–257], which at first glance seem to contradict our findings. In these studies, no differences in the FTIR spectra of insulin fibrils formed at different pH, ranging from 1.3 to 3.1, were observed, however, a noticeable change of the vibrational circural dichroism (VCD) spectra was seen between pH 2.1 and 2.4. This change in VCD spectra was explained by a different supramolecular chirality of the fibrillar structure [255, 256]. Moreover, it was demonstrated that small changes in pH can induce spontaneous inter-conversion of preformed fibril chirality, thus excluding the possibility of strains [257]. Even though the reported FTIR spectra lack a detailed description, the shape of the amide I band is very similar to the amide I' band observed in case of pH* 2 fibrils [255–257]. The concentration of insulin used in aforementioned studies was 60 mg/ml (10 times higher than used in this study), which means that the equilibrium was strongly shifted towards a higher oligomeric state of insulin in solution, as insulin tends to oligomerise even at much lower concentrations [258–260]. Therefore, the main factor that governs the formation of distinct insulin fibril strains could be the monomer-oligomer equilibrium.

The spectral features of the insulin fibrils formed in the presence of

20% ethanol [81–83] are similar to the ones observed in fibrils formed at pH* 1.6 or *KR* strain [84, 86]. In all three cases the second derivative FTIR spectra of insulin fibrils exhibit two minima, a major one at 1619-1620 cm^{-1} and a minor one at 1630-1631 cm^{-1}, in the amide I' region and an additional band outside outside of amide I' region at 1728-1730 cm^{-1}. Therefore it can be concluded that in all three cases formation of the same insulin fibril strain was observed. It is known that the presence of 20% ethanol induce the dissociation of native insulin dimers, resulting in predominantly monomeric insulin form at moderate concentrations [83, 87, 261]. The C-terminal part of the insulin B-chain is not amyloidogenic itself, however, it is involved in the formation on intramolecular β-sheet, which binds together native insulin dimers [86]. Thus it is possible that two additional charged amino acid residues could result in dissociation of dimers in case of KR insulin.

Taken all together the results obtained in this and all previously discussed studies suggest that formation of distinct insulin fibril strains could be governed by a shift of equilibrium between monomers and dimers (or higher oligomers). In particular, if the equilibrium is shifted towards oligomeric species, the insulin aggregation would result in the formation of pH* 2-like strain, whereas if the equilibrium is shifted towards monomers, aggregation reaction would result in the formation of pH* 1.6-like strain.

Several additional experiments were carried out to test this hypothesis. First, we checked if the equilibrium shift towards oligomeric species due to an increased insulin concentration could explain the differences observed between the pH* 1.6 and pH* 2 fibril strains. The FTIR spectra of 10 mM insulin fibrils, prepared at pH* 1.6 environment, is slightly different form the other spectra. In particular, the blue shift of the amide I' maximum is evident, when compared to the spectra of pH* 1.6 fibril strain (Fig. 4.5A). Moreover, an additional band at 1728 cm^{-1} is absent. The results suggest that the increased insulin concentration leads to the formation of distinct fibril strains. However, the spectrum is also different from the pH* 2 fibril strain (Fig. 4.5A). Thus these results do not add much to strengthen our hypothesis. It is worth noticing that unlike at lower concentrations, at high concentrations, insulin assembles into

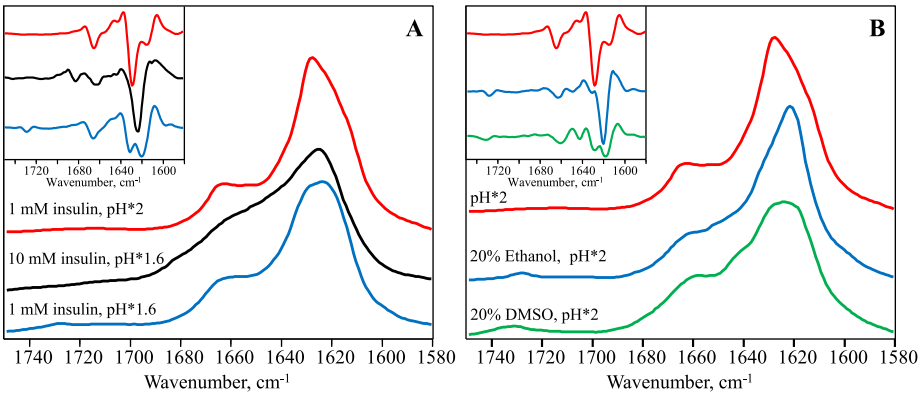

FIGURE 4.5: Absorption and second derivative (inset) FTIR spectra of insulin aggregates formed in high insulin concentration (A) or in the presence of organic cosolvents (B). Adapted from [14].

aggregates that form a gel-like substance, which suggests a different aggregation mechanism, and hence could explain the difference in FTIR spectra.

Second, we have repeated previously described experiments of insulin aggregation in the presence of 20% ethanol, and also examined the effect of higher DMSO concentrations (Fig. 4.5B). The presence of 20% of either organic cosolvent during insulin aggregation in the pH* 2 environment resulted in the formation of aggregates exhibiting spectral characteristics similar to the ones of pH* 1.6 fibril strain (Fig. 4.5B). These results confirms that ethanol and, to a lower extent, DMSO shifts the equilibrium towards the formation of pH* 1.6-like fibril strains.

Finally, we have determined the size distribution of insulin under various solution conditions using dynamic light scattering (DLS) (Fig. 4.6). The average size of insulin, dissolved in pH* 1.6 is lower than that of in pH* 2. The measured diameter of insulin in pH* 1.6 is 3.4 ± 0.7 nm, which is larger than that of insulin monomer, but smaller than that of a dimer [262]. At pH* 2, the diameter of insulin is 4.0 ± 0.6 nm, which is slightly larger than diameter of insulin dimer. Since DLS enables to determine only average properties of polydisperse sample, it does not allow the exact estimation of monomer oligomer content. However, the shift of the equilibrium towards dimeric/oligomeric

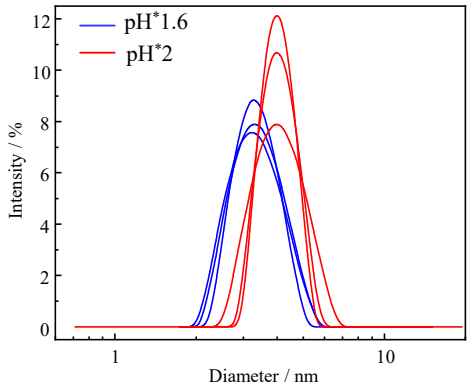

FIGURE 4.6: Size distribution of insulin in pH* 1.6 and pH* 2 solutions. Adapted from [14].

species at higher pH* is evident, and hence supports our hypothesis.

In general, the data presented in this study shows that distinct factors can induce polymorphism of insulin fibrils, and suggest that the monomer-dimer (oligomer) equilibrium might be the key factor governing the formation of distinct insulin strains. Moreover, it seems that all presented cases can be reduced to the formation of two insulin fibril strains: pH* 1.6-like and pH* 2-like.

4.1.2 Self-inhibition of insulin amyloid-like aggregation

The results discussed in this section were published in PCCP [15] together with following authors: Mantas Žiaunys and Vytautas Smirnovas.

I have conceived and designed the experiments and experimental models used for global fitting of data, performed AFM and FTIR measurements, performed part of DLS measurements, analysed the data, prepared figures, wrote the first version of the manuscript and reviewed its drafts.

The following text was reproduced by permission of the PCCP Owner Societies.

It is known that the alterations in environmental conditions can modulate protein aggregation pathways and result in formation of structurally distinct amyloid aggregates. Several sets of conditions, including presence of ethanol [81–83], different pH [14, 74], and using slightly different insulin forms (bovine insulin (*BI*) or recombinant Lys^{B31}-Arg^{B32} human insulin analogue (*KR*)) [84, 86], result in formation of distinct insulin fibril strains. The results discussed in a previous section suggest that all three cases lead to the formation of the same pair of insulin fibril strains. However, for a profound understanding of insulin fibril polymorphism, mechanistic studies of insulin aggregation at different environmental conditions are necessary. Recent collection of studies demonstrated the power of global fitting of kinetic models to elucidate molecular mechanisms of amyloid aggregation [12, 61–63, 88, 196, 263]. For instance, global fitting of insulin aggregation kinetics at pH 1.6 suggested a "classic" amyloid aggregation mechanism with a saturated elongation step [88]. Therefore, in order to reveal possible mechanistic differences leading towards the pH-induced polymorphism of insulin fibrils, we performed global fitting of kinetic models on the data of insulin aggregation at pH 2.4.

It is known that the presence of NaCl can affect aggregation kinetics, induce structural changes of proteins, or even modulate their aggregation pathways, resulting in the formation of distinct strains. Therefore, we monitored insulin aggregation process under several concentrations of NaCl.

Characterisation of initial and aggregated forms of insulin

The FTIR spectra of 5.0 mg/ml insulin dissolved in D_2O at pD 2.4 (pH-meter read out +0.4) [14, 205, 264], in the range from 0 to 100 mM NaCl, has one maxima in the amide I′ region at 1653 cm^{-1} and corresponding minima of the second derivative at 1656 cm^{-1} (Fig. 4.7A), which can be interpreted as a predominantly α-helical structure that is typical for native insulin [265]. Nearly identical spectral features in the presence and absence of NaCl suggest that the secondary structure is not affected by the salt in the examined range. Similarly, no obvious differences were observed in the circular dichroism (CD) spectra of insulin with and without salt (Fig. 4.7B).

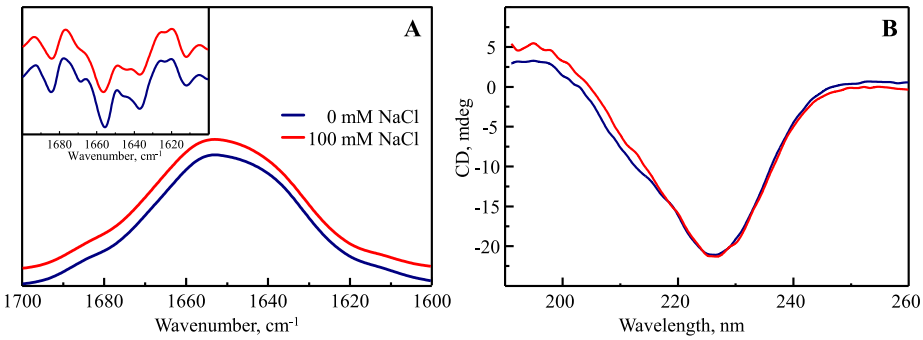

FIGURE 4.7: Absorption and second derivative FTIR spectra (A) and CD spectra (B) of insulin initial solutions in the presence and absence of NaCl. Adapted from [15].

Recently, it was demonstrated that elevated NaCl and protein, in particular amyloid-β and hen egg-white lysozyme, concentrations may induce formation of metastable oligomers [266, 267]. Analysis of insulin solutions using dynamic light scattering (DLS) revealed that the concentration of salt affects the average size of insulin particles (Fig. 4.8A). The maximum scattering intensity of the insulin sample in the absence of NaCl is at 3.7 $\pm$ 0.1 nm, which is slightly lower than the diameter of insulin dimer ($\approx$3.9 nm [262]). This value increases with rising salt concentration up to 3.9 $\pm$ 0.3 nm at 50 mM NaCl and finally reaches 4.3 $\pm$

0.1 nm at 100 mM NaCl, which is slightly lower than the diameter of insulin tetramer (≈5 nm [262]). Such gradual increase in particle size suggests formation of larger oligomers as the ionic strength of the solution increase. In addition, no scattering signal of particles above 5 nm was observed at NaCl concentrations lower than 75 mM (Fig. 4.8A). Given the exponential signal-to-size dependence in DLS, it is most likely that the majority of insulin would be distributed within monomers-dimers-tetramers in all three cases. Thus, the exact estimation of monomer oligomer content is difficult, however, the shift of the equilibrium towards dimeric/oligomeric species at higher salt concentrations is evident. This can be explained by electrostatic interactions. In particular, low pH values in solution result in strong electrostatic repulsive forces between protein molecules, which hinder the assembly of oligomeric forms. The addition of NaCl mitigates such effects by shielding electrostatic repulsion between positively charged insulin molecules by chloride ions, which facilitates the formation of larger oligomers [268]. According to Nielsen *et al.* [74], over the pH 2-8 range, the predominant form of zinc-free insulin should be dimeric at insulin concentration $<$ 1.5 mg/ml, and trameric at protein concentrations above 1.5 mg/ml, whereas the data obtained in this study suggest that in the absence of NaCl dimers are the predominant form even at 5.0 mg/ml concentration. It seems that the assumptions of Nielsen *et al.* [74] are based on small-angle X-ray scattering (SAXS) measurements [74], which were performed in the presence of 100 mM NaCl, and on the data obtained from analytical ultracentrifugation experiments [258], which were performed at pH 3.7 and pH 8. According to DLS results obtained in this and our previous study, both the addition of NaCl and increase in pH [14] result in the shift of equilibrium towards tetramers.

Since the monomer-oligomer equilibrium depends on the protein concentration, the measured particle size distribution is also concentration dependent. In the absence of NaCl, a minor increase in the hydrodynamic radius of insulin was observed as the protein concentration was risen from 0.5 to 5 mg/ml (Fig. 4.8B). A more obvious increase in particle radius is evident in the presence of NaCl, resulting in a greater divergence from particle sizes in the absence of salt at higher

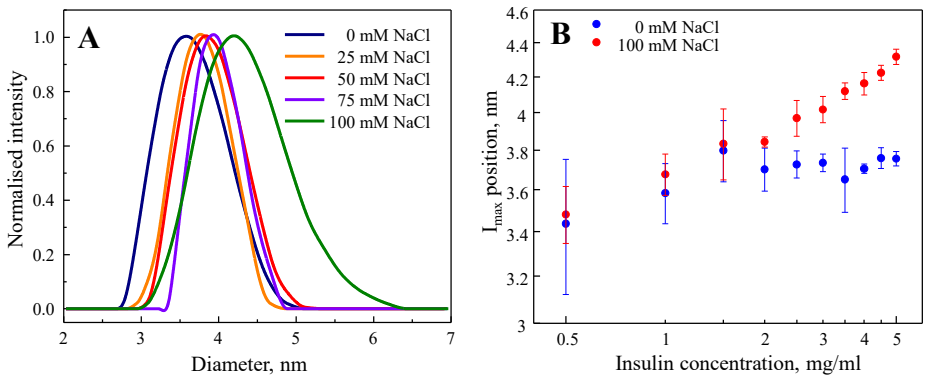

FIGURE 4.8: Size distribution of insulin in initial solutions. Scattering intensity distribution of insulin in initial solutions (A). Dependence of the maximum scattering intensity position on protein concentration (B). Error bars are standard deviations estimated from three repeats. Adapted from [15].

insulin concentrations. The results suggest a monomer-dimer equilibrium (with a possible small fraction of tetramers) throughout the entire range of insulin concentrations in the absence, and at insulin concentrations up to 2 mg/ml in the presence, of NaCl. A further increase in insulin concentration in the presence of NaCl shifts the equilibrium towards tetramers.

The FTIR spectra of insulin fibrils, prepared at pH 2.4, in the presence or absence of NaCl are almost identical (Fig. 4.9A). The second derivative FTIR spectra of fibrils formed under either conditions, exhibit two minima at 1636 cm^{-1} and 1627 cm^{-1} typical for β-sheets.

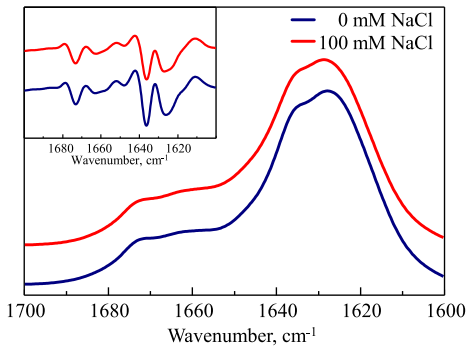

FIGURE 4.9: Absorption and second derivative (inset) FTIR spectra of insulin fibrils formed in the absence and presence of NaCl. Adapted from [15].

Analysis of the insulin aggregate morphology via AFM revealed no major differences between fibrils formed in absence or presence of NaCl (Fig. 4.10). The fibrils were straight, 0.5-3 μm in length, and typically 4-14 nm in cross-sectional height.

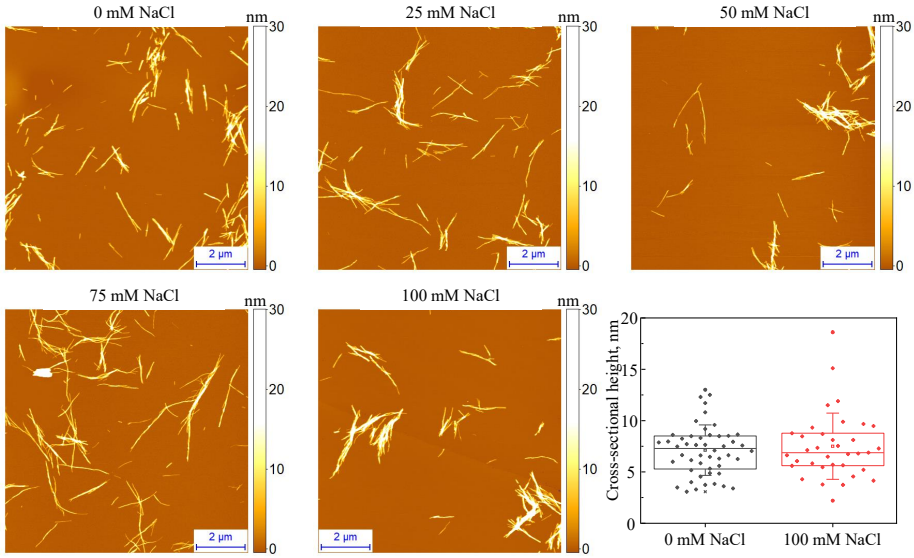

FIGURE 4.10: AFM images of insulin aggregates formed under different concentrations of NaCl in solutions. Error bars are standard deviations estimated from 35-50 measurements. Adapted from [15].

Kinetics of insulin aggregation

The kinetics of insulin (concentration range 0.5-5mg/ml) aggregation at pH 2.4 under five different NaCl concentrations ranging from 0 to 100 mM, were monitored using ThT assay. The first step in the kinetic analysis of fibril mass formation usually involves the selection of a set of suitable models [13], which might be difficult due to complex nature of the aggregation process. However, according to Meisl *et al.* [12], the number of model choices can be narrowed down by applying constrains on possible models. In particular, the curvature of double logarithmic plots of the aggregation half-time (t_{50}) *versus* initial monomer concentration can help to determine whether the aggregation reaction is monomer dependent or not, whereas the slope of this plot enables to

determine the reaction order. Therefore, aggregation reaction half-time plots are a good starting point in the selection of the models suitable for fitting.

In the absence of NaCl, a discontinuity in the half-time plots of insulin aggregation was observed (Fig. 4.11A), which suggest the presence of a saturation effect, whereas a low value of the scaling exponent (*i.e.* slope), which becomes $\approx$0 at insulin concentrations $>$ 3.0, point towards saturated elongation and fragmentation.

A rather unusual dependence of t_{50} on the initial insulin concentration was observed in the presence of NaCl (Fig. 4.11B-E). After the point of discontinuity there is a progressive increase of t_{50} values. This phenomena could not be related to the presence of a saturation effect, as the t_{50} values starts to increase at a different concentrations of insulin, depending on the concentration of NaCl in the sample. The point of discontinuity, after which the values of t_{50} starts to rise, shifts from 3.0 mg/ml in the absence of NaCl to 1.5 mg/ml in the presence of 100 mM NaCl. The positive slope of t_{50} plot is evident even at the lowest salt concentration. The scaling exponent, after the point of discontinuity, increased from $\approx$0 in absence of NaCl to $\approx$0.3-0.4 at higher NaCl concentrations. To our knowledge the positive value of scaling exponent cannot be associated with any known model or mechanism. The unusual increase in t_{50} values appear to be the result of competition between the aggregation-promoting effects of NaCl, which facilitate interactions between insulin molecules due to positive charge shielding, and the formation of off-pathway oligomers that may affect certain steps of the aggregation reaction.

Selection of models for global fitting

The four major events, including primary and secondary nucleation, elongation and fragmentation, constitute the basis of almost any model used to describe amyloid aggregation process. The model, containing all four events, became the "classic" model (Fig. 4.12), however in some cases the modifications of existent, or introduction of additional, microscopic events are necessary for a model to fit experimental data [12, 13, 61, 88, 196, 243]. None of the current modifications of the

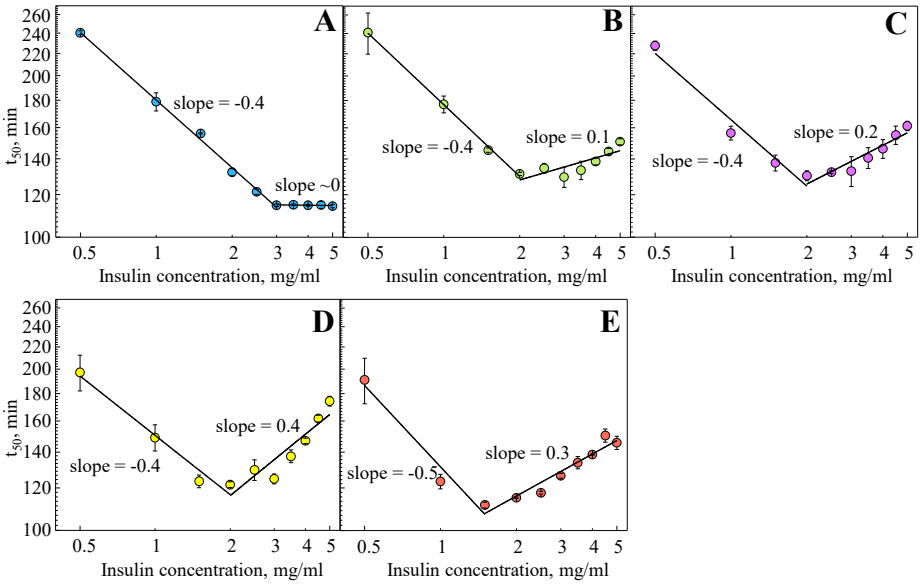

FIGURE 4.11: Dependence of aggregation reaction half-time on the initial concentration of insulin under conditions with 0 mM (A), 25 mM (B), 50 mM (C), 75 mM (D), 100 mM (E) NaCl. Error bars are standard deviations estimated from three repeats. Adapted from [15].

"classic" model consider the possible existence of oligomeric species that might be present in the initial sample, but would not directly participate in the aggregation reaction (Fig. 4.12). The formation of off-pathway oligomers alone would only result in proportional decrease of the initial monomer concentration, which can not explain an increase of t_{50} with rising concentration of monomers. However, an oligomer-induced inhibition could explain this phenomena, as we see a divergence in the hydrodynamic radius of insulin for samples over 1.5 mg/ml in the absence and presence of 100 mM NaCl (Fig. 4.8B), which matches with the discontinuity point in the half-time plots of insulin aggregation (Fig. 4.11). Moreover, inhibition of fibril formation by metastable off-pathway species was recently suggested for aggregation of lysozyme and amyloid-β at elevated NaCl concentrations [266]. However, unlike in our case, the formation of lysozyme and amyloid-β oligomers was detectable by evident changes in FTIR and CD spectra, as well as an increase in ThT fluorescence intensity.

According to Arosio *et al.* [196, 243] inhibition of primary nucleation would affect mainly the lag phase, inhibition of secondary nucleation would mostly affect the apparent growth rate, whereas inhibition of elongation would affect both the lag phase and the apparent growth rate. In our case, the lag time follows a similar tendency as t_{50} values (Supplementary Fig. A.2). At low protein concentrations, the higher NaCl concentration results in increase in apparent growth rates, whereas at high protein concentration the effect of salt is opposite (Supplementary Fig. A.2). Therefore, we hypothesise that the unusual dependence of t_{50} on initial insulin concentration may be caused by the formation of off-pathway oligomeric species, presumably tetramers, that bind to nuclei/fibrils ends ("capping" them).

	1° Nucleation	Elongation	Saturated elongation	2° Nucleation	Fragmentation	Monomer-Tetramer Equilibrium	"Capping"
	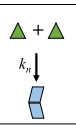	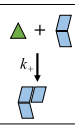	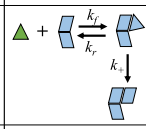	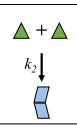	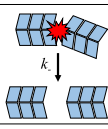	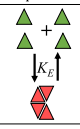	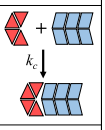
"Classic" model	+	+		+	+		
"Saturated elongation"	+		+	+	+		
"Classic + Tetramers"	+	+		+	+	+	
"Classic + Capping"	+	+		+	+	+	+

FIGURE 4.12: A schematic representation of microscopic events involved amyloid fibril formation process described by four different models. The rate constants are k_n (primary nucleation), k_+ (elongation), k_2 (secondary nucleation), k_- (fragmentation), and k_f and k_r (intermediate association and dissociation) as well as two additional steps, which include K_E (monomer–tetramer equilibrium) and k_c (aggregation center "capping"). Adapted from [15].

Global fitting of the experimental data

The four previously discussed aggregation models were used to fit experimental data acquired at five different ionic strength conditions. The "classic" model was the only model not sufficient to fit the experimental data sets obtained in the absence of NaCl (Fig. 4.13A), suggesting a need for either saturation effect (Fig. 4.13B) or formation of off-pathway intermediate species (Fig. 4.13C, D). Despite saturated elongation model fits the data set quite well, more than a half of t_{50} values calculated from the fit curves do not overlap with the experimental ones,

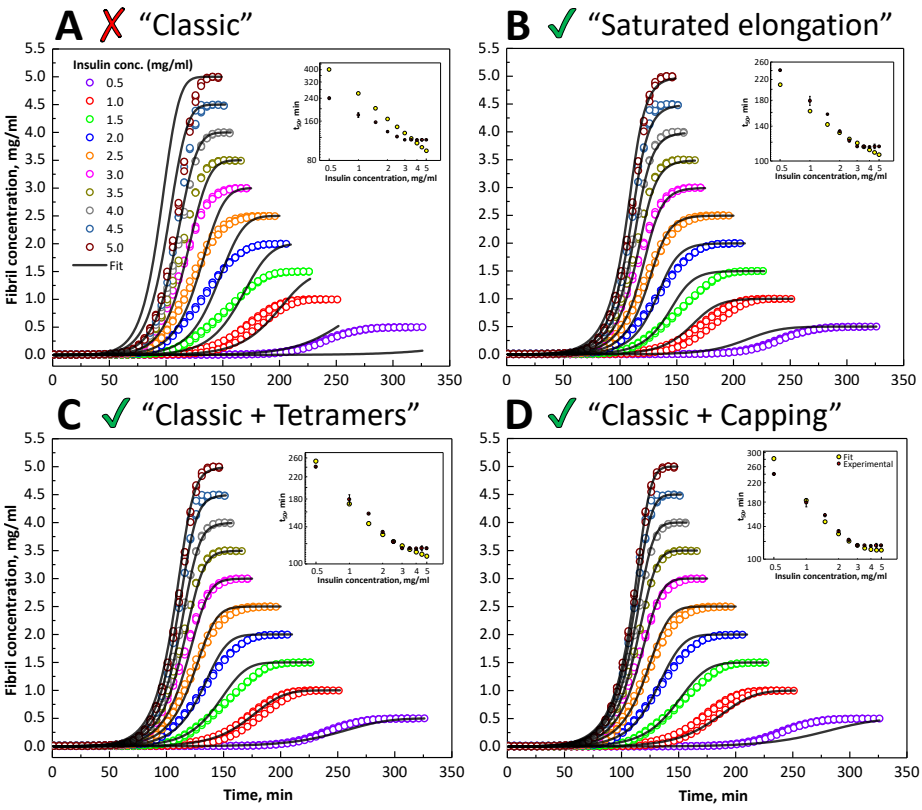

FIGURE 4.13: Global fit of the "Classic" (A), "Saturated elongation" (B), "Classic + Tetramers" (C), and "Classic + Capping" (D) model to the data sets with comparison of experimental and fit t_{50} values (inserts). In each case the primary and secondary nucleus size was set to 2. Open circles represent normalised experimental data (3 repeats for each protein concentration). Reprinted from [15].

whereas the values calculated from the fit curves of either model that accounts for a loss of viable monomers due to off-pathway oligomer formation, overlaps better. The "capping" step does not add much (and it should not, if insulin is predominantly monomeric or dimeric) apart from the better fit at the highest insulin concentrations, which can be explained by the presence of small amounts of tetramers.

In the presence of NaCl, models that do not include an inhibitory step were unable to account for the increase in t_{50} upon an increase of initial insulin concentration (Fig. 4.14A-C and Supplementary Figs.

A.3, A.4, A.5). As expected, the only model which was suitable to accurately fit experimental data was the one that includes an inhibition step (Fig. 4.14 D). The DLS results suggest that in the presence of 100 mM NaCl the equilibrium may be shifted towards tetramers at higher initial concentrations of insulin, whereas in the absence of salt, only a small number of tetramers may be present. These results explain both a good fit of the data set in the absence of NaCl by models involving monomer-oligomer equilibrium step, and only the "capping" model being able to fit the experimental data in the presence of salt. If it is assumed that the addition of NaCl does not alter the mechanism of insulin, but instead just affect the rates of microscopic events involved in the aggregation reaction, then it can be concluded that the tetramer-inhibition model is the one explaining the mechanism of insulin aggregation at pH 2.4.

The comparison of microscopic event rate constants (Table 4.1), acquired from global fitting of all data sets, revealed that all association events are accelerated by NaCl. This can be explained by the the salt-induced reduction of electrostatic repulsion between positively charged protein molecules. In addition, the presence of NaCl affects not only oligomerisation and aggregation rates, but also leads to a more efficient inhibition as a result of an increased "capping" rate. In contrast, the fibril fragmentation rate decreases upon increasing NaCl concentration, which is not surprising, as higher ionic strength may induce formation of fibril clusters, which should be harder to break [265]. Interestingly, the rate of secondary nucleation is affected by NaCl more than any other microscopic event involved in the aggregation process.

It is known that depending on environmental conditions insulin can exist in multiple forms, including monomeric, dimeric, tetrameric, and hexameric (only in the presence of Zn ions) [74]. Typically, oligomeric forms are seen just as off-pathway storage of insulin monomers, which are the key players in the aggregation reaction [74, 87, 265]. Aggregation of insulin was often studied at pH < 2 or in the presence of 20% acetic, the environmental conditions that favour the monomeric form [74, 88, 269], which is probably one of the main reasons why there was no clear evidence of the possible direct role of oligomeric forms of insulin in the

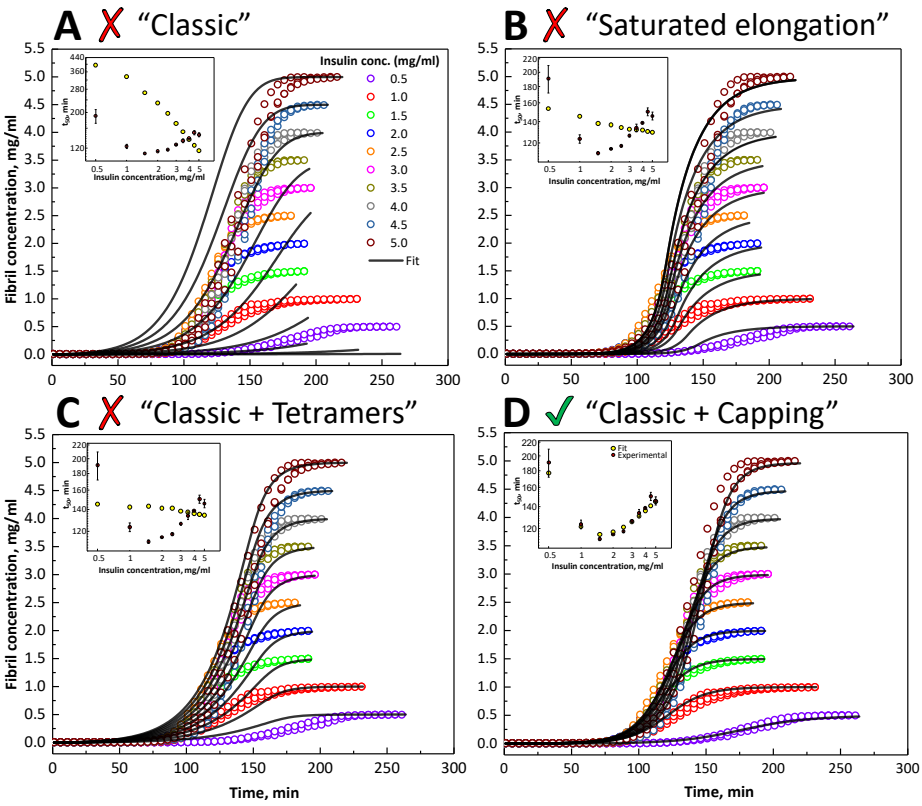

FIGURE 4.14: Global fit of the "Classic" (A), "Saturated elongation" (B), "Classic + Tetramers" (C), and "Classic + Capping" (D) model to the data sets with comparison of experimental and fit t_{50} values (inserts). In each case the primary and secondary nucleus size was set to 2. Open circles represent normalised experimental data (3 repeats for each protein concentration). Reprinted from [15].

amyloid aggregation reaction. The findings reported in this work supports the role of tetramers and adds one more piece to the global picture of the insulin aggregation mechanism. It is worth to notice that insulin fibrils formed at pH 2.4 are structurally distinct from the ones formed in pH < 2 [14], which suggest that oligomeric forms of insulin may play an important role in the polymorphism of amyloid fibrils.

TABLE 4.1: Reaction rate constants obtained from global fitting of all data sets, where $k_n k_+$ is the multiplicative rate constant of primary nucleation and elogation, $k_+ k_2$ - elongation and secondary nucleation, and $k_+ k_-$ - elongation and fragmentation. K_E is the monomer-tertramer equilibrium constant and k_c is the "capping" rate constant. The errors are the standard deviations estimated by fitting three different subsets of the replicates at each NaCl concentration. Reprinted from [15].

Conditions	**0 mM NaCl**	**25 mM NaCl**	**50 mM NaCl**	**75 mM NaCl**	**100 mM NaCl**
$k_n k_+$	$(8.6 \pm 0.5) \times 10^{-7}$	$(4.1 \pm 0.7) \times 10^{-7}$	$(4.1 \pm 0.8) \times 10^{-7}$	$(4.1 \pm 1.8) \times 10^{-6}$	$(1.4 \pm 0.2) \times 10^{-5}$
$k_+ k_2$	$(1.1 \pm 0.5) \times 10^{-6}$	$(3.1 \pm 0.4) \times 10^{-6}$	$(1.5 \pm 1.4) \times 10^{-4}$	$(4.0 \pm 1.5) \times 10^{-3}$	$(2.2 \pm 0.2) \times 10^{-2}$
$k_+ k_-$	$(2.2 \pm 0.1) \times 10^{-3}$	$(2.8 \pm 0.1) \times 10^{-3}$	$(3.9 \pm 0.3) \times 10^{-3}$	$(9.8 \pm 8.4) \times 10^{-4}$	$(3.6 \pm 1.6) \times 10^{-5}$
K_E	$(7.8 \pm 0.5) \times 10^{-3}$	$(6.8 \pm 0.6) \times 10^{-3}$	$(2.2 \pm 1.2) \times 10^{-2}$	$(2.7 \pm 2.1) \times 10^{-2}$	$(3.2 \pm 0.2) \times 10^{-1}$
k_c	$(5.3 \pm 0.3) \times 10^{-2}$	$(2.1 \pm 0.1) \times 10^{-1}$	$(2.4 \pm 0.5) \times 10^{-1}$	$(1.9 \pm 1.1) \times 10^{-0}$	$(8.7 \pm 0.3) \times 10^{-1}$

4.1.3 Environment is a key factor in determining the efficacy of anti-amyloid compounds – a case study with EGCG

The results discussed in this section were published in Biomolecules [270] together with the following authors: Andrius Sakalauskas, Rebecca Sternke-Hoffmann, Alessia Peduzzo, Mantas Ziaunys, Alexander K. Buell, and Vytautas Smirnovas.

I have conceived and designed the experiments, performed AFM and FTIR measurements, performed part of aggregation kinetics measurements, analysed the data, prepared figures, wrote the first version of the manuscript and reviewed its drafts.

The following text was reproduced under the terms and conditions of the Creative Commons Attribution (CC BY) license.

Numerous small molecular weight compounds, short peptides, and antibodies have been proposed as potential inhibitors of toxic oligomeric and fibrillar species assembly [271–276]. Despite significant and continuous efforts, however, there are still no effective disease modifying drugs or treatment modalities available for the majority of amyloid-related disorders (overall success rate of clinical trials is $<$ 0.5%) [277–282].

The formation of amyloid fibrils is a complex process, which involves several microscopic events [5, 11]. The alterations in environmental conditions can modulate these events resulting in the emergence of different pathways of amyloid fibril formation, leading to the formation of structurally distinct amyloid aggregates [5, 11, 14–16]. Such conformational variability is thought to be the generic property of amyloid proteins [11, 28, 29]. Moreover, the effects of compounds can vary depending on the conditions in which they are assayed (*i.e.* pH, temperature, buffer, interfaces, agitation and others) [276], possibly due to condition-induced chemical modifications of the compound [283–285]. Since the environmental conditions, under which aggregation of amyloid proteins is performed, can vary between different studies, the search and assessment of potential anti-amyloid compounds becomes extremely challenging as the results may lead to diverse conclusions.

Epigallocatechin-3-gallate (EGCG), the main and most significantly bioactive polyphenol found in green tea, has been reported to effectively inhibit the aggregation of a number of amyloidogenic peptides and proteins, including Aβ (related to AD) [235, 286], α-syn (related to PD) [235, 287–289], hIAPP (related to type-II diabetes) [290, 291], Htt exon 1 (related to Huntington's disease) [292], tau (related to AD and tauopathies) [293], SOD1 (related to amyotrophic lateral sclerosis)[294], PrP (related to prion diseases) [295] and others. Moreover, it was demonstrated that EGCG can induce remodeling and/or dissociation of pre-existing aggregate species [235, 287, 289, 296, 297]. Generally, EGCG could be considered as a "universal" inhibitor of amyloid aggregation, which could be used as a therapeutic agent for prevention and treatment of amyloid-related disorders. However, EGCG is unstable at neutral or alkaline pH [298–301] where it is susceptible to auto-oxidation, resulting in the formation of multiple EGCG products [283], which may differently effect amyloid aggregation [284, 285, 302].

Herein it is shown that the environment plays an important role in identification of anti-amyloid compounds. In particular, it is demonstrated that under certain circumstances the same molecule can be identified as a hit or as a failure, meaning that systematic exploration of the interplay of experimental conditions, compound stability and efficacy is crucial.

Kinetics of insulin aggregation in absence and presence of EGCG and EGCG$_{ox}$

First, the effects of EGCG and its auto-oxidation products (EGCG$_{ox}$) on insulin aggregation kinetics and maximum Thioflavin-T (ThT) fluorescence intensity were assessed (Fig. 4.15 and Supplementary Fig. A.6). When insulin aggregation reaction is performed in 100 mM phosphate buffer, pH 2.4 (PB), under quiescent conditions, the presence of EGCG results in almost 2 times longer half-time of insulin aggregation (t_{50}) and almost 2 times lower maximum ThT fluorescence intensity (I_{max}), when compared to the control sample. The effect of EGCG$_{ox}$ on insulin aggregation process is stronger and it results in almost 4 times longer t_{50} and almost 4 times higher I_{max}. Under agitated conditions in PB, EGCG has

no effect, while EGCG$_{ox}$ has a minor effect on the insulin aggregation process.

The presence of EGCG has no effect on both t_{50} and I_{max}, when the aggregation reaction is performed in 20% acetic acid (AC) under either quiescent or agitated conditions. Under quiescent conditions in AC, the presence of EGCG$_{ox}$ results in 2 times longer t_{50} and 20 times higher I_{max}, when compared to control sample. Under agitated conditions in AC, the presence of EGCG$_{ox}$ results in 3 times higher I_{max} and has a minor effect on t_{50}.

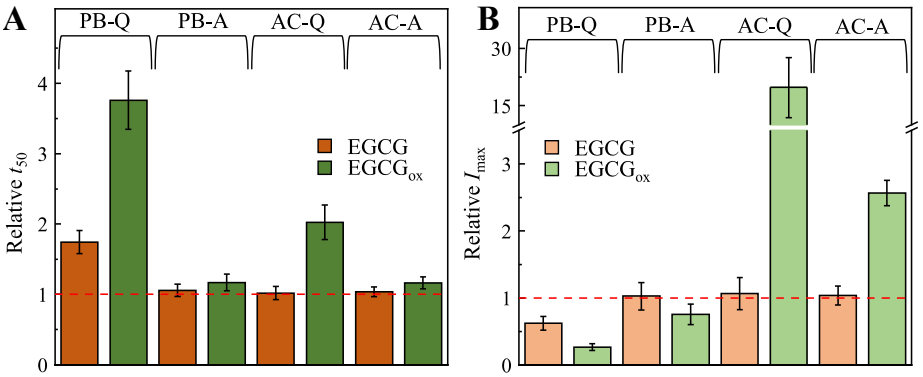

FIGURE 4.15: Effects of EGCG and EGCG$_{ox}$ on insulin aggregation kinetics (A) and maximum ThT fluorescence intensity (B). Abbreviations PB and AC represent environmental conditions (100 mM phosphate buffer and 20 % acetic acid, respectively), while Q and A denote agitation conditions (quiescent and agitated, respectively), under which insulin aggregation process was performed. Error bars are standard deviations. Reproduced from [270].

AFM analysis of insulin fibrils formed in absence and in presence of EGCG or EGCG$_{ox}$

Sample analysis via atomic force microscopy (AFM) confirmed formation of insulin fibrils within 15 hours in the absence and presence of EGCG or EGCG$_{ox}$ under all tested environmental conditions (Fig. 4.16 and Supplementary Figs. A.7, A.8, A.9, A.10). Typically, single fibrils are several hundred nanometres to a few micrometres in length and 3-10 nanometres in height. In PB fibrils tend to clump, larger bundles are evident under agitated conditions. In the presence of EGCG$_{ox}$ fibrils

seem to be more disperse. In AC more fibrils can be seen in the presence of $EGCG_{ox}$, when compared to the control sample. Fibrils formed in the presence of EGCG under all environmental conditions are similar to their respective control samples.

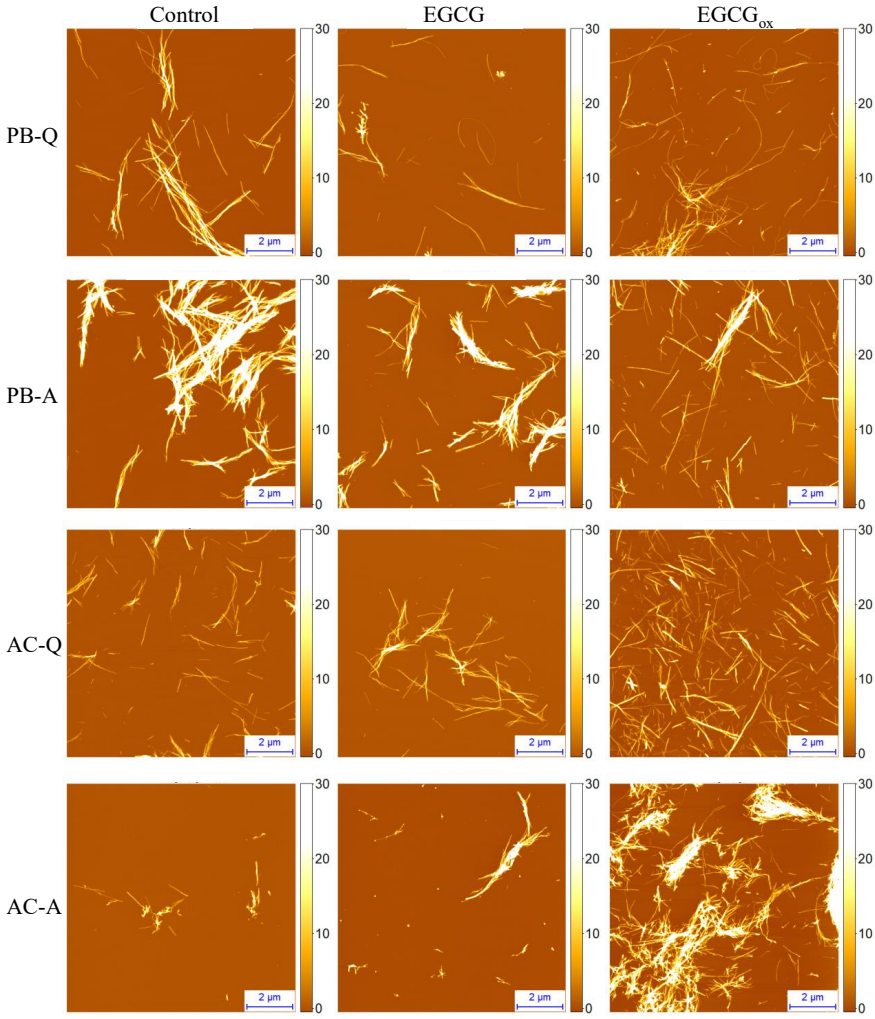

FIGURE 4.16: AFM images of insulin fibrils formed in PB or AC in the absence and presence of EGCG or $EGCG_{ox}$. Abbreviations Q and A denote agitation conditions (quiescent and agitated, respectively), under which insulin aggregation process was performed. Reproduced from [270].

Characterisation of secondary structure of insulin fibrils formed under distinct environmental conditions

Secondary structure of insulin amyloid fibrils was determined using Fourier-transform infrared (FTIR) spectroscopy. FTIR spectra of fibrils formed in AC under quiescent and agitated conditions are very similar (Fig. 4.17). Second derivative FTIR spectra of fibrils formed in AC under either agitation conditions exhibit a major minimum at 1627 cm^{-1} and a minor one at 1641 cm^{-1} in amide I/I' region, attributed to β-sheet structure and an additional band at 1729 cm^{-1} (Fig. 4.17 inset), which was assigned to the stretching vibrations of a deuterated carboxyl group (-COOD) according to Surmacz-Chwedoruk *et al.* [84]. Similarly, a major minimum at 1627 cm^{-1} in the Amide I/I' region, is present in case of fibrils formed in PB under agitated conditions, however, the other two minima observed in fibrils formed in AC are missing. Second derivative FTIR spectrum of insulin amyloid fibrils formed in PB under quiescent conditions exhibit two minima at 1625 cm^{-1} and 1637 cm^{-1} in the Amide I/I' region. The results confirms that fibrils formed without agitation in PB are structurally distinct from fibrils formed in AC, while the fibrils formed in PB with agitation seems to have a secondary structure profile, which looks like an intermediate between fibrils formed in PB under quiescent conditions and fibrils formed in AC under quiescent or agitated conditions.

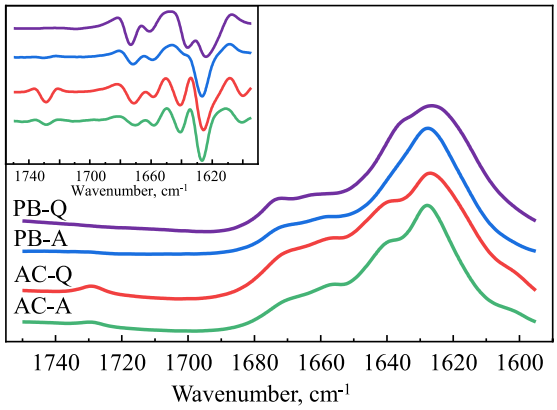

FIGURE 4.17: Absorption and second derivative (inset) FTIR spectra of insulin amyloid-like aggregates formed in PB and AC under quiescent and agitated conditions. Abbreviations PB and AC represent environmental conditions (100 mM phosphate buffer and 20% acetic acid, respectively), while Q and A denote agitation conditions (quiescent and agitated, respectively), under which insulin aggregation process was performed. Adapted from [270].

Assessment of effects of compounds on amyloid aggregation process

Effects of compounds on the process of amyloid fibril formation is often determined by comparing aggregation kinetics [235, 243, 244, 252, 263, 284–286, 303, 304] or/and maximum ThT fluorescence intensity [235, 244, 252, 284–286, 303, 305–307] in the absence and presence of the compound. The effects of EGCG and $EGCG_{ox}$ on insulin aggregation process performed under distinct environmental conditions were assessed using both aforementioned approaches (Fig. 4.15 and Supplementary Fig. A.11), the summary of effects is presented in (Table 4.2). If t_{50} and/or I_{max} would be chosen as the main criteria, EGCG would be indicated as an inhibitor only if the screening was performed in PB under quiescent conditions. In case of $EGCG_{ox}$ the picture is more complicated. $EGCG_{ox}$ would be indicated as an inhibitor independently of used criteria if the screening was performed in PB, while in AC, t_{50} would point towards an inhibitory effect, whereas I_{max} would suggest an aggregation-promoting effect. The results suggest, that depending on aggregation conditions and the screening criteria, the same compound can be indicated as a hit or a failure. This raises the question: what could be the reasons for such diverse results?

The changes in environmental conditions can modulate protein aggregation pathways resulting in the formation of structurally different amyloid aggregates (Fig. 4.18A) [14–16, 28, 29]. Therefore, it is plausible that species targeted by the compound might exist only under specific environmental conditions. Indeed, EGCG inhibits insulin aggregation reaction only when it is performed in PB under quiescent conditions (Fig. 4.15). AFM analysis did not reveal any major differences between insulin fibrils formed in the absence or presence of EGCG (Fig. 4.16). However, differences in second derivative FTIR spectra profiles (Fig. 4.17), suggest the possibility of different pathways and intermediates involved in the process of insulin fibril formation in PB under quiescent or agitated conditions, or in AC under both agitation conditions. Thus, it is possible that the species, targeted by EGCG, are only present under specific environmental conditions. A similar explanation can be valid for different relative t_{50} values observed in PB and AC in the

TABLE 4.2: Evaluation of EGCG and $EGCG_{ox}$ effects on insulin aggregation process. Reproduced from [270].

Assessed by change in t_{50}		
Conditions	EGCG	$EGCG_{ox}$
PB-Q	Inhibitory[1]	Inhibitory
PB-A	No Effect	Inhibitory
AC-Q	No Effect	Inhibitory
AC-A	No Effect	Inhibitory
Assessed by change in I_{max}		
	EGCG	$EGCG_{ox}$
PB-Q	Inhibitory	Inhibitory
PB-A	No Effect	Inhibitory
AC-Q	No Effect	Enhancing
AC-A	No Effect	Enhancing

[1]Established by comparing experimental values of t_{50} or I_{max} of control samples with the ones determined in the presence of EGCG or $EGCG_{ox}$ using one-way ANOVA. $P < 0.01$ was accepted as statistically significant.

presence of $EGCG_{ox}$ (Fig. 4.15A), however, a large increase in ThT fluorescence intensity in the presence of $EGCG_{ox}$ in AC (Fig. 4.15B) is harder to explain. Under agitated conditions, the effect of $EGCG_{ox}$ on insulin aggregation is weaker when compared to the one under quiescent conditions. Agitation in general accelerates amyloid aggregation process, mostly by inducing fibril fragmentation, as well as the detachment of aggregating species from the air-water or solid-water interface, where proteins have a strong tendency to accumulate and where in many cases the formation of aggregation-prone nuclei is likely to occur. Due to selectively enhanced individual aggregation steps, such as fragmentation or nucleation, the concentration of species that can be targeted by EGCG may be decreased and hence its inhibitory effect diminished.

An increase in ThT fluorescence intensity observed in the presence

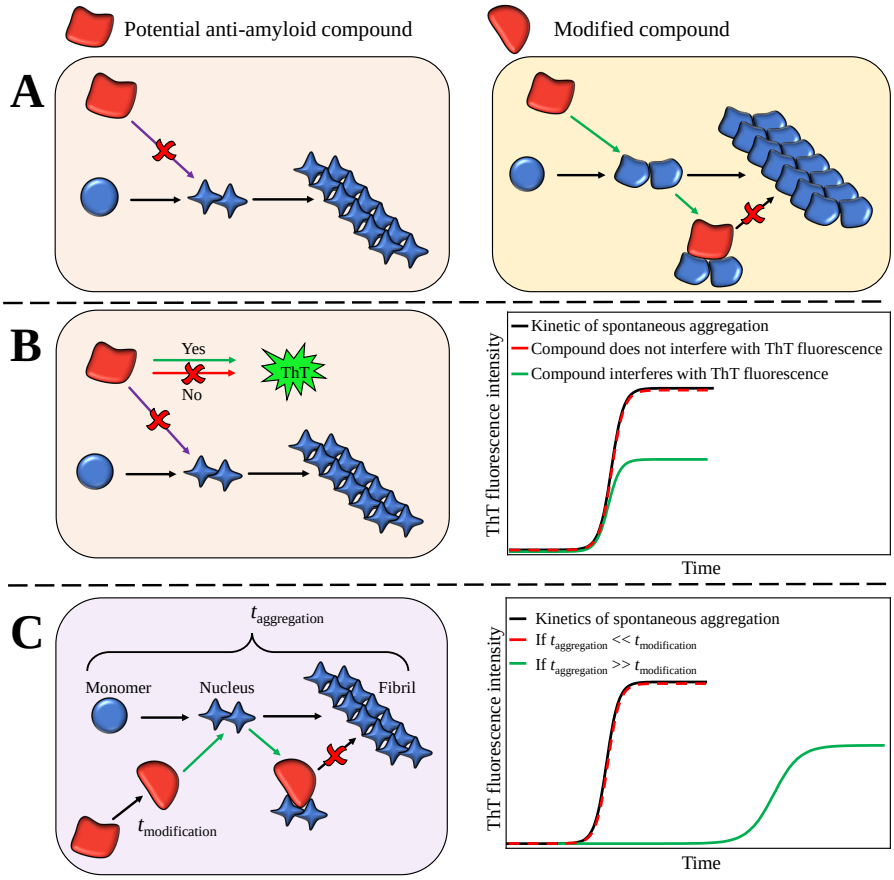

FIGURE 4.18: Schematic representation of possible effects of potential anti-amyloid compounds on the amyloid aggregation reaction performed under distinct environmental conditions. Alterations in environmental conditions can lead to the formation of distinct aggregate species of which only some are targeted by potential anti-amyloid compound (A), as in case of insulin aggregation in PB-Q and AC-Q. Some compounds can also interfere with ThT fluorescence intensity (B), suggesting inhibition, which is not confirmed by other experiments, such as AFM or the quantification of soluble protein at the final plateau of ThT intensity. Furthermore, specific environmental conditions induce modifications of the compound, which results in generation of products that target aggregation prone species (C). The compound modification can only manifest itself if it occurs with kinetics comparable to, or faster than the kinetics of aggregation. Distinct background colours represent different environmental conditions. Different shapes of aggregates represent distinct pathways reflecting the observed polymorphism of amyloid fibrils. Reproduced from [270].

of $EGCG_{ox}$ in AC can be interpreted as an increase in the fibril concentration. Indeed, relative abundance of insulin fibrils in AFM images seems to be higher in the presence of $EGCG_{ox}$ (Fig. 4.16) However, a simple increase in the quantity of formed fibrils alone is not sufficient to explain observed multi-fold increase in I_{max}. It was demonstrated that amyloid fibrils formed under distinct environmental conditions may possess different ThT binding sites [193, 308]. Therefore, since secondary structure of insulin fibrils formed in PB and AC is different (Fig. 4.17), it is possible that $EGCG_{ox}$ induces slight conformational changes of amyloid fibrils formed in AC, which results in the appearance of additional ThT binding sites, and hence in increased ThT fluorescence intensity. However, no obvious differences in morphology (Fig. 4.16 and Supplementary Figs. A.9, A.10) or secondary structure (Supplementary Fig. A.12) of insulin fibrils formed in AC in absence or presence of $EGCG_{ox}$ were observed. It is also possible that the change in ThT intensity arise from a direct interaction between fibril-bound ThT and $EGCG_{ox}$. It was previously reported that extrinsic compounds can dramatically change ThT fluorescence quantum yield, which has sometimes led to false interpretation of a compound under investigation as an inhibitor (Figure 4.18B) [309]. Therefore, absolute fluorescence intensity is often not a reliable criterion by which effects of compound under investigation could be assessed. It was shown that surfaces can also have a large impact on the protein aggregation process [240–242, 310, 311]. In particular, depending on both the surface chemistry and the physicochemical properties of the protein, foreign surfaces (*e.g.* cuvette, test tube or plate well walls, air-water-interface) can have different effects on the protein aggregation process [240–242, 310, 311]. Indeed, additional experiments showed that the large increase of I_{max} in the presence of $EGCG_{ox}$ depends on the surface of the microplate used (Fig. A.13). If insulin aggregation reaction in AC is performed in low-binding-plates, which are recommended [240] and are extensively used for amyloid aggregation kinetic studies [241–244], a multifold increase of I_{max} in the presence of $EGCG_{ox}$ is evident, whereas if the aggregation reaction is performed in untreated-plates, there is no obvious change in I_{max}. It is worth to notice that the effect of $EGCG_{ox}$ on t_{50} was also

weaker in untreated-plates (Supplementary Fig. A.13).

Specific environmental conditions may induce modifications of compounds resulting in generation of products that may have distinct effects [283–285, 312] (Fig. 4.18 A). For instance, at neutral or alkaline pH EGCG is not stable and oxidises within several hours. In general, the effect of $EGCG_{ox}$ on insulin aggregation process is stronger when compared to its non-oxidised form.

In conclusions, herein we demonstrate that the environmental conditions, under which amyloid aggregation reaction is performed, as well as the methods used for assessment of effects of compounds, play an essential role in identification of anti-amyloid compounds. Under certain circumstances, due to the different experimental design, distinct studies may identify the same compound as a hit or as a failure. Therefore, assessing effects as well as the intrinsic stability of the compounds of interest under several environmental conditions *in vitro* is essential for further development of the lead compound resulting in increased success rates in *in vivo* studies and clinical trials.

4.2 Studies of prion protein fibril self-replication

4.2.1 Polymorphism of amyloid fibrils can be defined by the concentration of seeds

The results discussed in this section were published in PeerJ [16] together with following authors: Katažyna Milto and Vytautas Smirnovas.

I have conceived and designed the experiments, performed AFM and FTIR measurements, performed aggregate stability assays, performed part of aggregation kinetics measurements, analysed the data, prepared figures, and reviewed drafts of the paper.

One of the most fascinating properties common among amyloidogenic proteins is the ability to form structurally diverse fibrils, termed "strains", the best-studied example being prions [8, 10, 20, 28, 29, 53]. *De novo* amyloid strains can be produced *in vitro* by altering environmental conditions, such as temperature [313], pH [14], agitation [314], concentration of denaturants [21], or co-solvents [82], typically, mildly denaturing conditions are necessary. Once formed, such strains are able to carry strain-specific properties even in unfavourable environmental conditions [14, 21, 82, 84, 127, 314]. This indicates that environment defines different strains during primary nucleation, but affects only kinetics, not the structure, of fibrils formed via elongation. However, formation of new distinct strains upon transmission of prions into a different environment has also been observed [9, 53, 117, 118]. This phenomena is sometimes referred to as a "strain mutation" or "conformational switching". Although the origin of this phenomena is not clear it is thought that alterations in the environment can result in generation of new PrP^{Sc} variants and hence strains, which are the best fit for self-propagation in the new environment. In the case of secondary nucleation, formation of new nuclei is induced by existing fibrils, however, it is not clear whether the structure of these nuclei is determined by the environment, or by structure of the fibrils. This raises the question: can secondary nucleation be a key player in conformational switching in amyloid-like fibril

strains?

De novo generation of prion strains

Artificial recombinant mouse prion protein (rMoPrP89-230) fibril strains were generated similarly as described by Cobb *et al.* [21]. Briefly, monomeric rMoPrP89-230 was incubated in 2 or 4 M of guanidine hydrochloride (GuHCl), the resulting fibrils were termed rPrP-A^{2M} and rPrP-A^{4M}, respectively. The conformational stability of aggregates, which is defined as resistance to chemically-induced fibril depolymerisation, has been used as one of the main parameters to characterise distinct fibril strains [21, 24]. rPrP-A^{2M} and rPrP-A^{4M} exhibit different conformational stability (Fig. 4.19). The midpoint of rPrP-A^{2M} fibril depolymerisation curve is at ≈1.8 M GuSCN, whereas the one of rPrP-A^{4M} is at ≈3.0 M GuSCN. This served as a hallmark of distinct strains in further experiments.

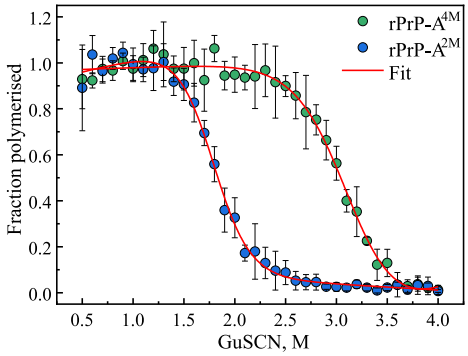

FIGURE 4.19: Profiles of GuSCN-induced depolymerisation of rPrP-A^{2M} and rPrP-A^{4M} fibrils. Error bars are standard deviations estimated from six repeats. Adapted from [16].

Kinetics of cross-seeded aggregation

It was previously demonstrated that rPrP-A^{2M} can not self-propagate in GuHCl concentrations above 2.5 M [245], therefore only one way cross-seeding is possible for rPrP-A^{2M} and rPrP-A^{4M} strains. Cross-seeding kinetics using different concentrations of rPrP-A^{4M} seeds were monitored via ThT assay (Fig. 4.20A, B, C). Addition of

TABLE 4.3: Reaction rate constants obtained from global fitting of all data sets. k_+, k_- and k_2 are the elongation, fragmentation and secondary nucleation rate constants, respectively. Adapted from [16].

Seed concentration	**5%**	**1%**	**0.2%**
k_+	1×10^{2}	1×10^{1}	4×10^{-1}
k_-	$< 1\times10^{-10}$	3×10^{-6}	5×10^{-4}
k_2	$< 1\times10^{-10}$	5×10^{-6}	5×10^{-4}

large amounts (5% from total protein concentration) of preformed rPrP-A^{4M} fibrils into rMoPrP89-230 monomer solution, results in rapid growth of amyloid fibrils from the very beginning, suggesting fast fibril elongation (Fig. 4.20A). Addition of intermediate amounts (1% from total protein concentration) of seed results in slow elongation at the beginning, however, after some time the rate of aggregation rapidly increases (Fig. 4.20B). Addition of low concentration (0.2% from total protein concentration) of seed results in very slow elongation, and the kinetics can be described by sigmoidal curve (Fig. 4.20C), which is typical in case of spontaneous aggregation, however, in the absence of seed no formation of fibrils was detected within the experimental time frame.

The model containing four major events, including primary and secondary nucleation, elongation and fragmentation, was used to fit experimental data sets (Fig. 4.20A, B, C). Comparison of rate constants of these events (Table 4.3), obtained from the global fitting of experimental data, revealed that upon decrease in seed concentration the elongation rate constant decrease, while the fragmentation and secondary nucleation rate constants increase. This suggest that aggregation reaction changes from elongation-driven process at high seed concentrations towards secondary nucleation/fragmentation-driven process at low seed concentrations.

Conformational stability of aggregates

The fibril depolymerisation assay revealed that conformational stability of fibrils formed in the presence of 5% of rPrP-A^{4M} seed is

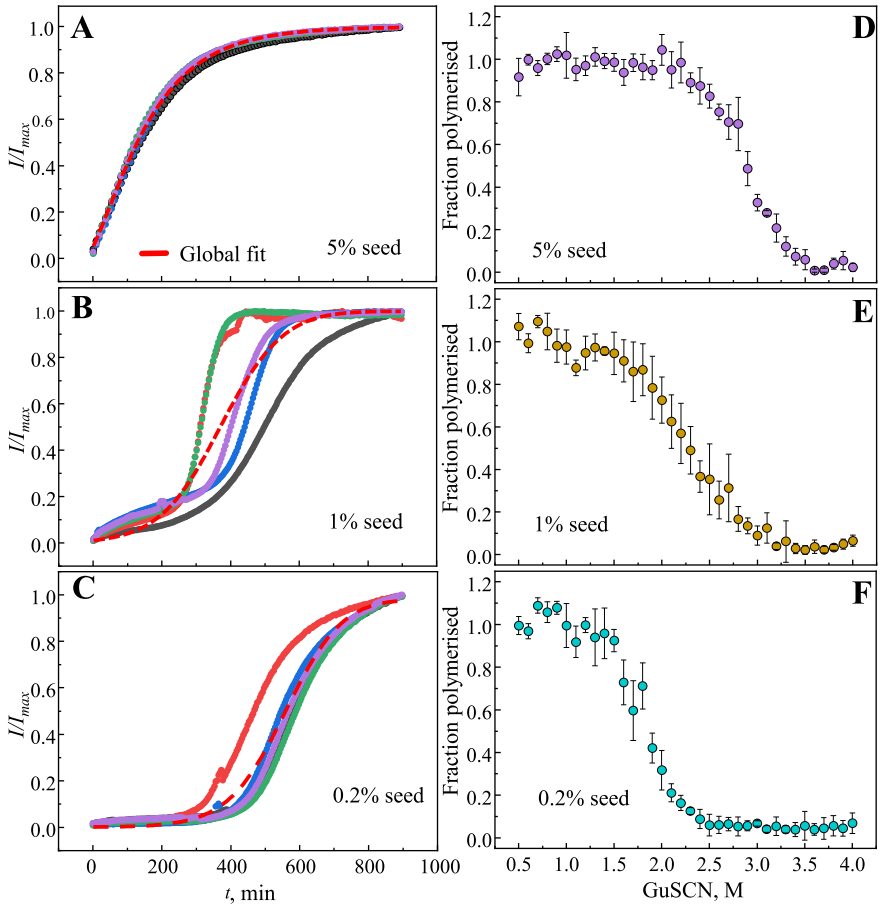

FIGURE 4.20: Seeded aggregation kinetics (A-C) and depolymerisation profiles of resulting fibrils (D-F). Solid lines of different colour are different repeats. Dashed line is the global fit. Error bars are standard deviations estimated from six repeats. Adapted from [16].

very similar to rPrP-A^{4M} fibril strain, the midpoint of depolymerisation curve is at ≈2.9 M GuSCN (Fig. 4.20D). The conformational stability of fibrils formed in the presence of 1% of rPrP-A^{4M} seed is lower than that of rPrP-A^{4M} strain, however, higher than that of rPrP-A^{2M} strain, the midpoint of depolymerisation curve is at ≈2.2 M GuSCN (Fig. 4.20E). Fibrils formed in the presence of 0.2% of rPrP-A^{4M} seed exhibit conformational stability similar to that of rPrP-A^{2M} strain, the midpoint of depolymerisation curve is at ≈1.8 M GuSCN (Fig. 4.20F).

The results allows to hypothesise that fibrils initiated by secondary nucleation do not follow the seeding template, despite using template as fibrils as nucleation sites.

Characterisation of fibril morphology via AFM

Sample analysis via AFM confirmed amyloid fibril formation under all experimental conditions (Fig. 4.21A, B, C, D). The length of single fibrils was typically between several hundred of nanometres to few micrometers. Analysis of fibril cross-sectional height revealed that average height of rPrP-A^{2M} strain fibrils is slightly higher than that of rPrP-A^{4M} strain fibrils (6.9 $\pm$ 2.6 nm and 5.4 $\pm$ 1.7 nm, respectively) (Fig. 4.21E). The cross-sectional height of fibrils formed in the presence of 0.2% of rPrP-A^{4M} seed is similar to the height of rPrP-A^{2M} strain, whereas the height of fibrils formed in the presence of 5% of seed is similar to the one of rPrP-A^{4M} strain.

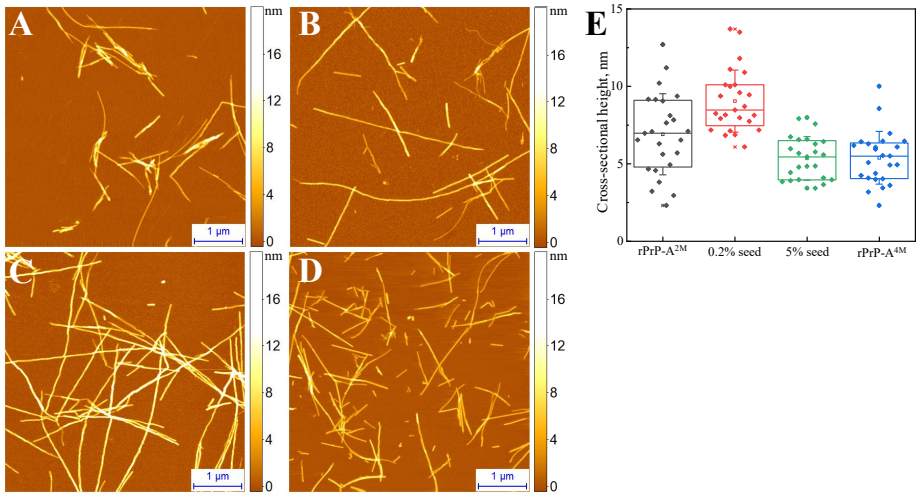

FIGURE 4.21: AFM images of rPrP-A^{4M} (A) and rPrP-A^{2M} (B) strains, and fibrils formed during cross-seeding in the presence of 5% (C) and 0.2% (D) of seeds. (E) cross-sectional height of single fibrils. Error bars are standard deviations estimated from 25 measurements. Adapted from [16].

Characterisation of secondary structure of fibrils via FTIR

Analysis of secondary structure profiles of aggregates using FTIR

revealed subtle differences between rPrP-A^{4M} and rPrP-A^{2M} strains (Fig. 4.22). The absorption FTIR spectrum of rPrP-A^{4M} strain exhibit one major maximum at 1620 cm^{-1} in amide I/I′ region, while the spectrum of rPrP-A^{2M} strain exhibit maximum at 1624 cm^{-1} (Fig. 4.22). The spectrum of fibrils formed in the presence of 5% of seed is almost identical to the spectrum of rPrP-A^{4M}, whereas the spectrum of fibrils formed in the presence of 0.2% of seed is similar to the spectrum of rPrP-A^{2M}. The results suggest that propagation of strain-specific structure depends on the amount of seeds and possibly on the mechanism of aggregation.

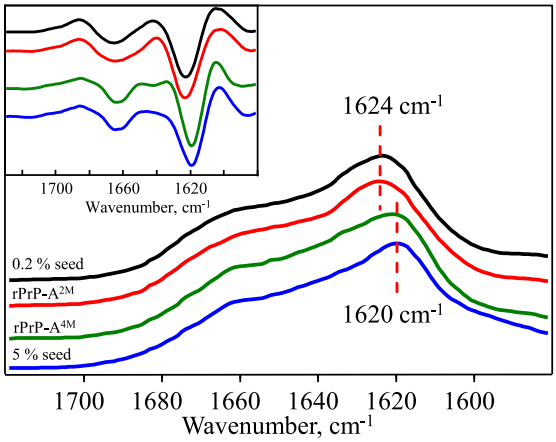

FIGURE 4.22: Absorption and second derivative (inset) FTIR spectra of rPrP fibrils. Adapted from [16].

Effect of seed sonication time on the aggregation kinetics and the conformational stability of formed aggregates

It was demonstrated that sonication can affect the elongation rate of fibrils [245]. As it is evident from the AFM images of fibrils before (Fig. 4.21A) and after sonication (Fig. 4.23), the sonication induces fragmentation of fibrils into shorter pieces, thus increasing the number of fibrils ends.

Addition of large amounts (5% from total protein concentration) of 30s sonicated rPrP-A^{4M} seeds results in aggregation kinetics similar to

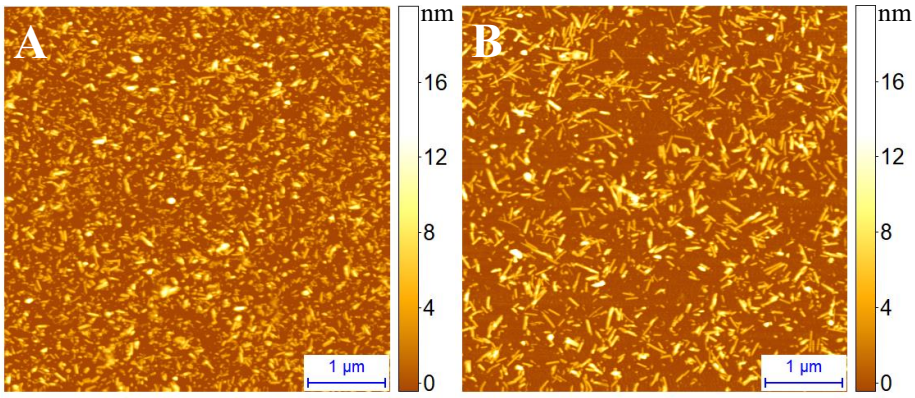

FIGURE 4.23: AFM images of rPrP-A^{4M} fibrils sonicated for 300s (A) or 30s (B). Adapted from [16].

the ones observed in case of 1% of 300s sonicated seed, whereas addition of 5% of unsonicated seeds results in aggregation kinetics similar to the ones observed in case of 0.2% of 300s sonicated seed (Fig. 4.24A, B). The conformational stability of fibrils formed in the presence of 30s sonicated seeds is higher than that of fibrils formed in the presence of unsonicated seeds (Fig. 4.24C, D). The midpoints of depolymerisation curves are at ≈2.8 M and 2.3 M GuSCN, respectively.

Generally, it is evident that the conformational stability of fibrils correlate with the aggregation kinetics. It is likely that PrP-A^{4M} and rPrP-A^{2M} fibril populations coexist in all samples, and different proportions of the two strains determine their depolymerisation profiles. The results suggest that secondary nucleation may play the key role in the "strain switching" phenomena. Moreover, secondary nucleation could explain "strain switching" in the absence of a species barrier, which was observed in cell cultures [19] and during protein misfolding cyclic amplification (PMCA) of recombinant PrP [22]. In summary, we hypothesise that self-propagation and "conformational switching" between amyloid strains is determined by the dominant microscopic events involved in the amyloid aggregation and self-propagation process. For instance, in cases when species barrier or environmental barrier interferes with fibril elongation, the secondary nucleation becomes the dominant event, which can induce formation of distinct strains. Furthermore, as we

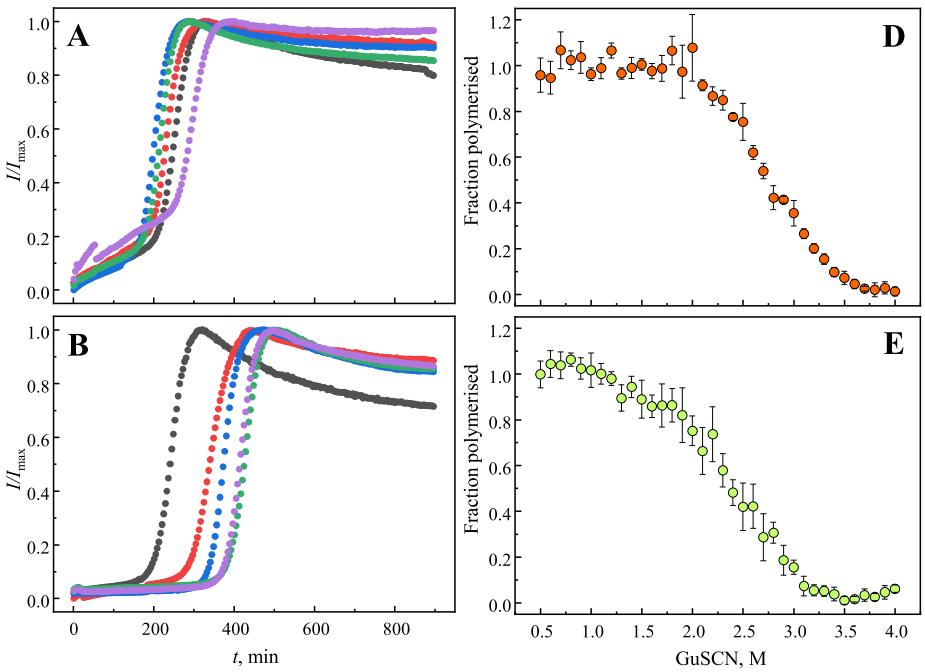

FIGURE 4.24: Effect of seed sonication on the aggregation kinetics (A-B) and the conformational stability of formed aggregates (C-D). Solid lines of different colour are different repeats. Error bars are standard deviations estimated from six repeats. Adapted from [16].

demonstrate in this study, the mechanism of self-replication is dependent on the concentration of preformed fibrils, which introduce a new dimension in cross-species and cross-environment seeding infection experiments.

4.2.2 Properties of prion fibril self-replication

The results presented in this section contain unpublished data.

I have conceived, designed and performed all experiments, and analysed the data.

Despite continuous efforts, there are no effective anti-prion treatment modalities to date. It seems that the key reason for this may be a poor understanding of prion fibril polymorphism phenomenon, and the mechanism of self-replication [9, 17, 126]. It is generally agreed that the alterations in environment is one of the main reasons leading to the emergence of distinct prion fibril strain *in vitro*, and in some cases *in vivo* [9, 17–27]. However, the mechanisms of self-propagation of distinct fibril strains is still not completely clear [9, 18, 19, 119]. Thus, studies of prion fibril-self replication are highly important not only for the mechanistic understanding of this process, but also for the development of effective anti-prion treatment modalities.

In order to obtain new insights about the self-replication process, we have generated distinct prion fibril strains and compared their properties of self-propagation. The results suggest, that under certain circumstances distinct fibril strains have almost identical probability to self-propagate, meaning that change in the dominant population may be mostly dependent on the overall initial concentration of the fibril strain. Moreover, a new phenomenon, which emerges during self-propagation reaction of distinct prion strains under different environmental conditions is described.

Formation of *de novo* prion strains

De novo prion strains were generated similarly as described by Cobb *et al.* [21] and Makarava *et al.* [314]. Briefly, mouse recombinant prion protein (rMoPrP) was incubated in solutions containing 2 M or 4 M GuHCl under different agitation conditions at 37 °C. Kinetics of spontaneous aggregation were followed via ThT assay (Fig. 4.25). The aggregation process of rMoPrP under vigorous shaking (220 RPM) conditions is faster than under gentle rotation (10 RPM) conditions (Fig. 4.25) (Table 4.5). Lower GuHCl concentrations also result in faster aggregation.

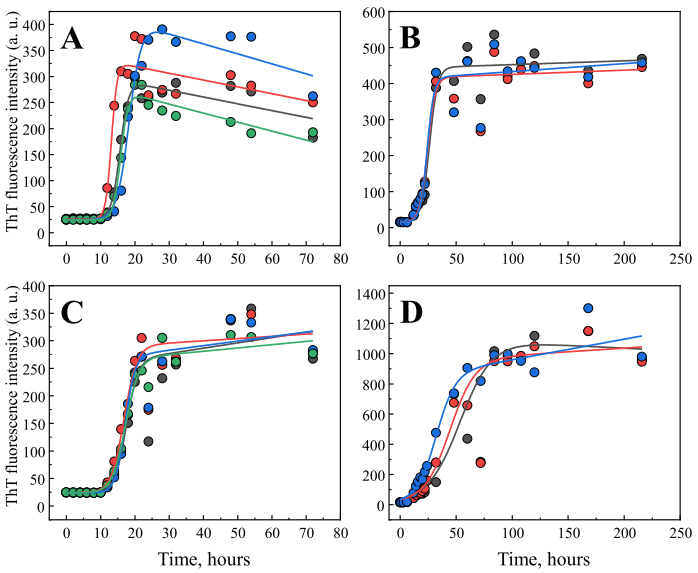

FIGURE 4.25: Kinetics of spontaneous rMoPrP aggregation. Kinetics of rMoPrP aggregation under shaking (A, B) or rotation (C, D) conditions in 2 M (A, C) or 4 M (B, D) GuHCl.

Interestingly, the difference between t_{lag} values under shaking and rotation conditions is smaller than the difference between t_{50} values. This also reflects in the values of apparent rate constants (k_{app}). The results suggest that even though the time required for the formation of detectable amounts of aggregates (*i.e.* the t_{lag}) is similar under both agitation conditions, the proliferation rate (k_{app}), is much faster under shaking conditions.

TABLE 4.4: The kinetic parameters of spontaneous rMoPrP aggregation reaction. Errors are standard deviations (n $\geq$ 3).

GuHCl conc.	**2 M**	**2 M**	**4 M**	**4 M**
Agitation:	**220 RPM**	**10 RPM**	**220 RPM**	**10 RPM**
t_{50}	15.8 $\pm$ 2.1 h	17.2 $\pm$ 0.3 h	24.9 $\pm$ 1.1 h	43.2 $\pm$ 11.1 h
t_{lag}	13.3 $\pm$ 1.4 h	13.7 $\pm$ 0.6 h	18.1 $\pm$ 0.7 h	20.5 $\pm$ 5.6 h
k_{app}	0.87 $\pm$ 0.25 h^{-1}	0.58 $\pm$ 0.09 h^{-1}	0.30 $\pm$ 0.03 h^{-1}	0.09 $\pm$ 0.02 h^{-1}

Aggregates formed in 2 M or 4 M GuHCl under vigorous shaking conditions hereafter will be referred to as S220_2M and S220_4M, respectively, whereas aggregates formed under gentle rotation conditions hereafter will be called R10_2M and R10_4 M, respectively.

Characterisation of *de novo* prion strains

Sample morphology analysis via AFM revealed clear differences between aggregates formed under distinct agitation conditions (Fig. 4.26). Aggregates formed under shaking conditions are typically spherical or short elongated structures (Fig. 4.26 A, B), from tens to few hundred nm in length (or diameter in case of spherical particles), whereas aggregates formed under rotation conditions exhibit typical fibrillar structure (Fig. 4.26 C, D) and are from several hundred nm to few μm in length. The cross-sectional height of aggregates formed under shaking conditions is larger than that of the aggregates formed under rotation conditions (Fig. 4.26 E). The cross-sectional height of aggregates formed under shaking conditions in 2 M or 4 M GuHCl is 15 ± 3 nm and 11.3 ± 3.3 nm, respectively, while the cross-sectional height of aggregates formed under rotation conditions is 5.9 ± 1.7 nm and 4.3 ± 1.5 nm, respectively. Generally, aggregates formed under higher concentration of GuHCl exhibit lower cross-sectional height. The results suggest the existence of distinct prion aggregate strains.

Analysis of secondary structure of aggregates formed under distinct environmental conditions via FTIR spectroscopy revealed structural differences (Fig. 4.27). FTIR spectrum of fibrils formed in 2 M GuHCl under shaking conditions exhibit maximum in amide I/I' region at $\approx$1625 cm^{-1} and corresponding major minimum of the second derivative at $\approx$1622 cm^{-1}, which can be interpreted as a predominantly β-sheet structure. The spectrum of fibrils formed in 4 M GuHCl under shaking conditions exhibit maximum at $\approx$1623 cm^{-1} and two corresponding minima of the second derivative at $\approx$1618 cm^{-1} and $\approx$1663 cm^{-1}, the latter one can be interpreted as β-turn. Similarly, the spectra of fibrils formed in 2 M GuHCl under rotation conditions exhibit maximum at $\approx$1626 cm^{-1} and two corresponding minima of the second derivative at $\approx$1623 cm^{-1} and $\approx$1662 cm^{-1}. The FTIR spectrum of fibrils formed in 4 M

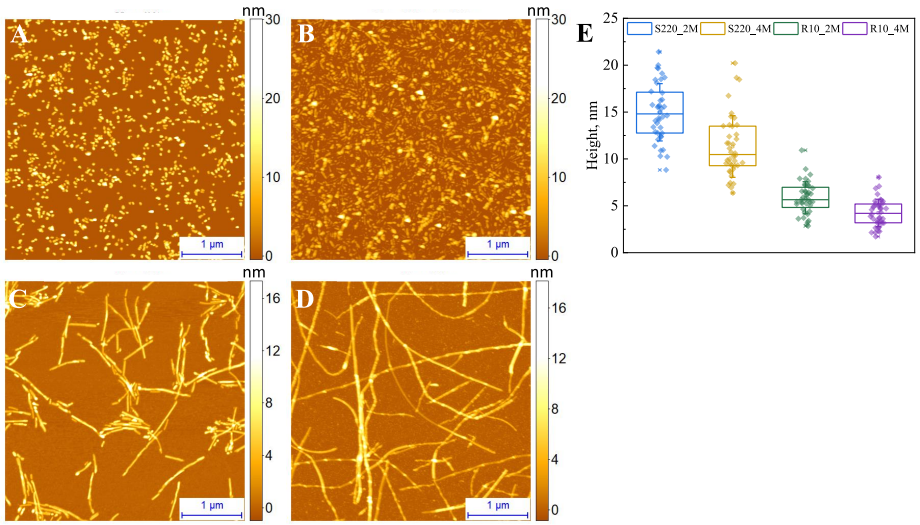

FIGURE 4.26: AFM images of rMoPrP aggregates formed under shaking (A, B) or rotation (C, D) conditions in 2 M (A, C) or 4 M (B, D) GuHCl. (E) cross-sectional height of formed aggregates. Error bars are standard deviations estimated from 50 measurements.

GuHCl under rotation conditions exhibit maximum at ≈1628 cm^{-1} and two corresponding minima of the second derivative at ≈1617 cm^{-1} and ≈1626 cm^{-1}. Differences between spectral profiles of fibrils suggest the existence of four distinct prion amyloid aggregate strains.

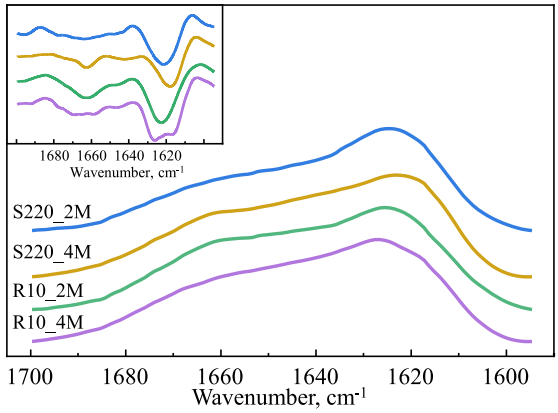

FIGURE 4.27: Absorption and second derivative (inset) FTIR spectra of rMoPrP aggregates.

The fibril depolymerisation assay revealed that aggregates, formed in 4 M GuHCl under shaking conditions, possess the highest conformational stability (the midpoints of depolymerisation curve is at ≈3 M GuSCN), whereas the aggregates formed in 2 M GuHCl exhibit the lowest conformational stability (the midpoints of depolymerisation curve is at ≈1.8 M GuSCN) (Fig. 4.28). rMoPrP aggregates formed under rotation conditions in 2 M or 4 M GuHCl exhibit similar conformational stability, the midpoints of depolymerisation curve are at ≈2.6 and ≈2.5 M GuSCN. Again, the results suggest the existence of distinct prion fibril strains.

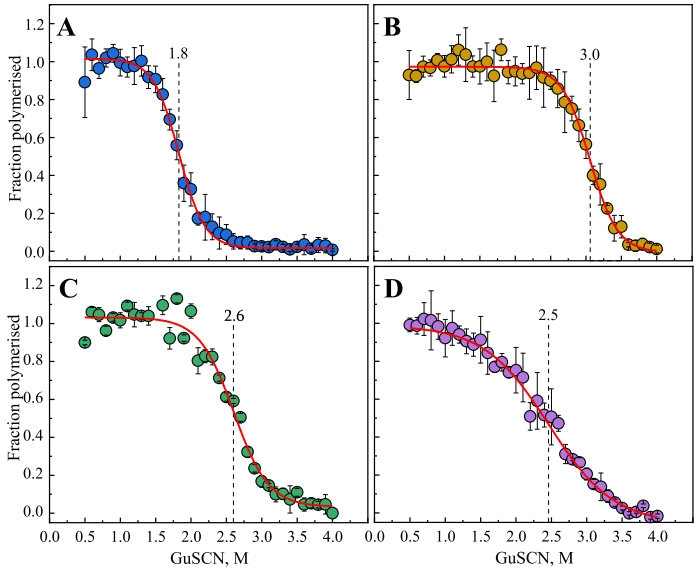

FIGURE 4.28: Conformatonal stability of rMoPrP aggregates. Depolymerisation curves of rMoPrP aggregates formed under shaking (A, B) or rotation (C, D) conditions in 2 M (A, C) or 4 M GuHCl (B, D). Error bars are standard deviations (n = 3-6).

Properties of prion fibril strain self-replication

All four prion strains are capable to self-propagate under environmental conditions close to the original ones (Fig. 4.29). In particular, seeded aggregation reaction was performed by adding 10% (from total protein concentration) of preformed aggregates into monomeric protein

TABLE 4.5: The proliferation rates of distinct prion strains. Error bars are standard deviations (n = 4).

Strain	S220_2M	R10_2M	S220_4M	R10_4M
t_{50}	22 ± 3 min	76 ± 26 min	338 ± 9 min	485 ± 55 min

solution containing 2 M (in case of S220_2M and R10_2M strain seeds) or 4 M (in case of S220_4M and R10_4M strain seeds) of GuHCl and incubating at 40 °C. It is worth to note that such high concentration of seed was used in order to reduce the probability of generation of distinct fibril strains via secondary nucleation dominated process [16]. Similarly to the aggregation kinetics observed during spontaneous formation of prion fibrils, the proliferation rate of prion strains formed in 2 M GuHCl (S220_2M and R10_2M) is faster than the rate of fibrils formed in 4 M GuHCl (S220_4M and R10_4M) (Table 4.5). In general, it is evident that distinct fibril strains form and proliferate at diverse rates, which is consistent with previously reported observations [4, 9, 20, 28, 53].

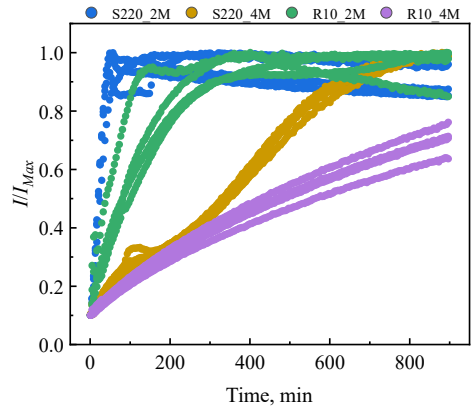

FIGURE 4.29: Kinetics of seed induced aggregation reaction.

Sample morphology analysis via AFM revealed that amyloid aggregates, formed in the presence of 10% of either prion strain aggregates, exhibit typical fibrillar structure, and are typically one to few μm in length, and are of similar cross-sectional height (Fig. 4.30). Interestingly, while the average height of fibrils formed in the presence of R10_2M or

R10_4M aggregates (7 ± 3 nm and 5.4 ± 2.3 nm, respectively) is similar to that of spontaneously formed aggregates (5.9 ± 1.7 nm and 4.3 ± 1.5 nm, respectively), the height of fibrils formed in the presence of S220_2M or S220_4M aggregates (5.5 ± 1.6 nm and 5.0 ± 1.8 nm, respectively) is lower than that of aggregates formed spontaneously (15 ± 3 nm and 11.3 ± 3.3 nm, respectively).

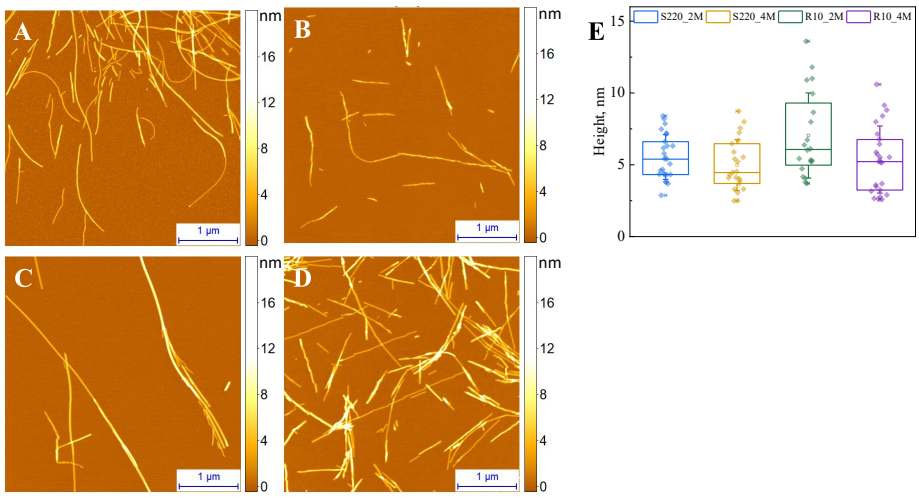

FIGURE 4.30: AFM images of rMoPrP aggregates formed in the presence of 10% of preformed S220_2M (A), S220_4M (B), R10_2M (C), or R10_4M fibrils (D). (E) Cross-sectional height of fibrils formed during seeded aggregation reaction. Error bars are standard deviations estimated from 25 measurements.

Analysis of secondary structure of seed-induced aggregates revealed that the structural profiles of seed-induced fibrils are similar to the profiles of the seeds (Fig. 4.31). The results suggest that all four strains are capable to proliferate by imprinting their structural template.

Since all four prion strains are capable to self-propagate under environmental conditions close to the original ones, it is interesting to see how alteration in environmental conditions (GuHCl concentration and temperature) may affect the self-replication properties of these strains. Moreover, performing seeded-aggregation reaction at different temperatures enables to map the energy landscape of fibril elongation [245,

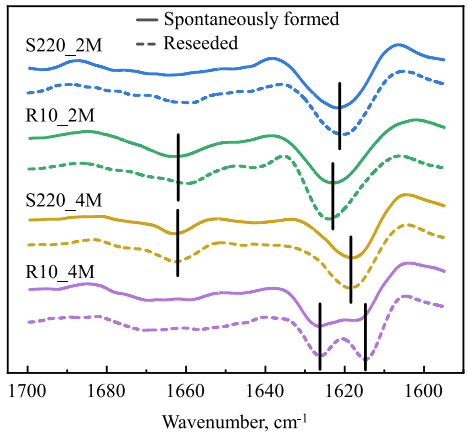

FIGURE 4.31: Second derivative FTIR spectra of spontaneously formed (solid lines) fibrils and aggregates formed during seed-induced aggregation reaction (dashed lines).

315–317]. In particular, it enables to determine enthalpy ($\Delta H^{\ddagger}$) of activation, which can be extracted directly from linear fits of kinetic data plotted in Arrhenius plot ($\Delta H^{\ddagger}$ = -R $\times$ $\Delta(\log k)/\Delta(1/T)$). Determining and comparing energy landscapes of distinct fibril strain elongation may bring new insights and a better understanding of fibril self-propagation process and polymorphism phenomena.

First, the effects of GuHCl concentration on rMoPrP fibril strain proliferation kinetics at 40 °C were assessed (Fig. 4.32). The S220_2M fibril strain is capable to efficiently proliferate in the solutions containing from 0.5 M to 3.0 M of GuHCl, at concentrations <1.0 M or >3.0 M, delay of self-replication process is evident (Fig. 4.32 A). Similarly, the R10_2M strain is capable to efficiently proliferate in the solutions containing from 1.0 M to 3.5 M of GuHCl (Fig. 4.32 B), while self propagation rates are very slow at 4-4.5 M of GuHCl. Both R10_4M and S220_4M fibril strains can efficiently self-propagate in the solutions containing from $\geq$1.5 M to 4.0 M and 4.5 M of GuHCl, respectively. (Fig. 4.32 C, D). In general, a correlation between conformational stability of fibril strain and the range under which strain is capable to proliferate is evident. Interestingly, both R10_2M and R10_4M fibril strains have similar conformational stability, however, the fibrils formed at 4 M of GuHCl

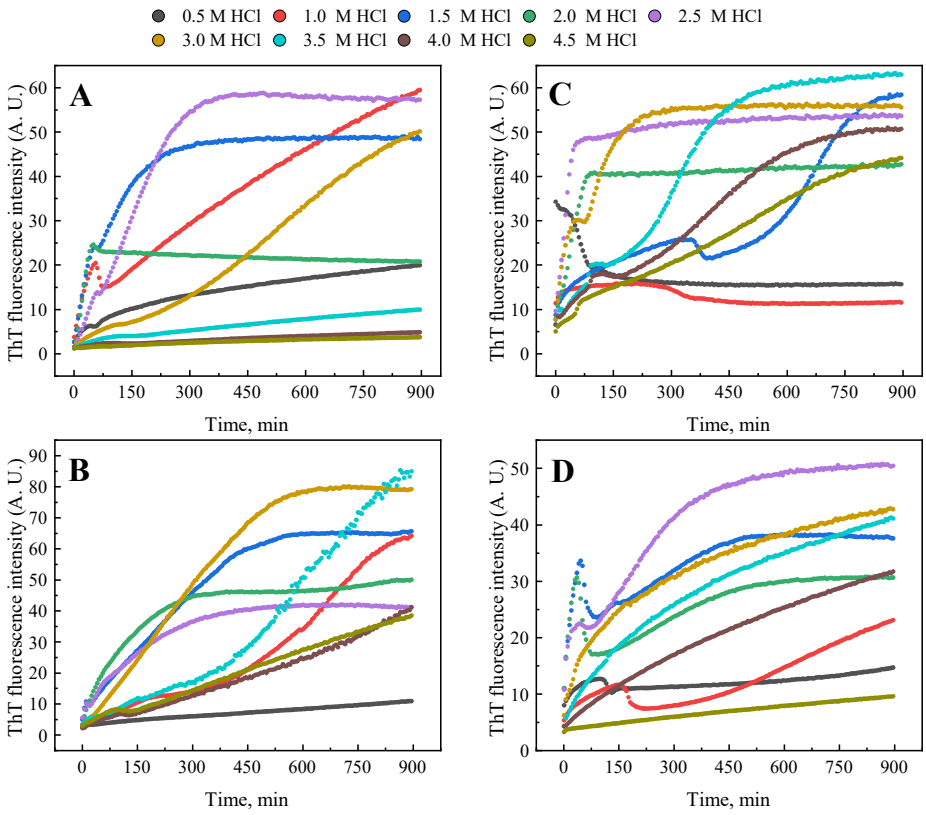

FIGURE 4.32: Kinetics of distinct rMoPrP fibril strains under several concentrations of GuHCl. A-D) Representative curves of S220_2M (A), R10_2M (B), S220_4M (C), or R10_4M (D) seed-induced aggregation reaction under several concentrations of GuHCl.

(R10_4M) self-propagate more efficiently under higher concentrations of GuHCl, than the fibrils formed at 2 M of GuHCl (R10_2M). This suggests that the range of GuHCl concentrations under which fibrils can self-replicate depends on their conformational stability, while the rate of self-propagation may be mostly dependent on the environment, which favours the formation of one or another fibril strain.

Rather strange kinetics were observed in certain cases, one of the best examples being kinetics observed during R10_4M fibril strain self-replication reaction in 1-2.5 M of GuHCl (Fig. 4.32C, D). A rapid increase

in ThT fluorescence intensity at the beginning of the seeded aggregation reaction is followed by a fast decline and a subsequent increase of ThT signal. This phenomena will be referred to as " the jump in ThT signal" in the following text. It is evident that the width (time of existence) and the height (change in ThT signal) of the jump in ThT signal is changing with the increasing GuHCl concentration. At first it is wide, upon increase in GuHCl concentration it becomes narrower until finally disappearing at highest GuHCl concentrations. The bi-phasic kinetics may suggest the existence of detectable intermediate species [266] or a possible remodeling of existing fibrils, however, analysis of secondary structure of aggregates via FTIR revealed no differences between aggregates during seeded aggregation reaction under distinct concentrations of GuHCl (Fig. 4.33). R10_4M fibril strain is capable of imprinting its structural conformation even under distinct environmental conditions.

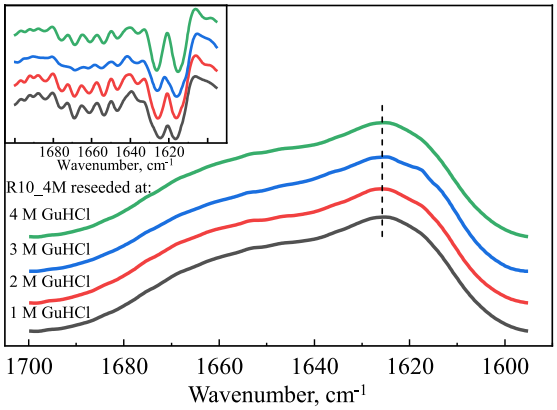

FIGURE 4.33: Absorption and second derivative (inset) FTIR spectra of fibrils formed during R10_4M seed-induce aggregation reaction at different concentrations of GuHCl.

Since it is evident that altering GuHCl concentration modulate the kinetics of fibril self-propagation, and in some cases even result in the emergence of quite strange kinetics, it is interesting to see how alterations in temperature may affect this process. Therefore, kinetics of seed-induced aggregation reactions were followed at a 40-65 °C temperature range under different concentrations of GuHCl.

First, we will discuss the kinetics of S220_2M (Supplementary Fig. A.14) and R10_2M (Supplementary Fig. A.15) fibril strain proliferation at different temperatures and GuHCl concentrations. It is evident that the increase in temperature facilitates the self-propagation reaction and extends the limits of conditions under which strains can efficiently self-replicate (Supplementary Figs. A.14. A.15). The drastic increase in self-replication rate at low (0.5-1.0 M) GuHCl concentrations (Supplementary Figs. A.14A, B and A.15A, B) upon increase in temperature can be explained by the thermal unfolding of rMoPrP. The protein is still folded at 0.5 M GuHCl over the temperature range 40-60 °C, at 1.0 M over the range of 40–55 °C, and at 1.5 M over the range of 40–50 °C. At higher concentrations of GuHCl the rMoPrP is mostly unfolded over the range of 40–65 °C [245]. Since fibril formation and elongation reaction requires complete rearrangement of native rMoPrP secondary structure [318–321], the thermal unfolding caused by the increase in temperature may significantly lower energetic barriers, and hence facilitate the reaction. The ThT signal jumps evident at low temperatures in the presence of 1-1.5 M, in case of S220_2M strain (Supplementary Fig. A.14B, C), or in the presence of 1-2.5 M of GuHCl, in case of R10_2M strain (Supplementary Fig. A.15B-E), disappear upon increase in temperature. At first glance one could assume that the jump in ThT signal might be related to the unfolding of native rMoPrP, however, the jumps are also evident in the presence of high concentrations of GuHCl, under which protein is unfolded. Interestingly, in case of S220_2M strain, the jump in ThT signal appears, or gets larger upon increase in temperature, at intermediate GuHCl concentrations (Supplementary Fig. A.14E, F, G). At high GuHCl concentrations, the S220_2M fibril strain self-replication is still delayed even at high temperatures (Supplementary Fig. A.14H, I), whereas R10_2M fibril strain proliferation is facilitated (Supplementary Fig. A.15H-I).

In case of S220_4M (Supplementary Fig. A.16) and R10_4M (Supplementary Fig. A.17) fibril strains, the effect of temperature on the kinetics of seed-induced aggregation reaction is similar to the one described previously. Upon increase in temperature seeded-aggregation rates become faster, as well as the range of GuHCl concentrations under which

strains can efficiently self-replicate becomes broader. In general, the jumps in ThT signal become less evident upon increase in temperature, the best examples being kinetics of S220_4M seed-induced aggregation reaction at 1.5 M of GuHCl (Supplementary Fig. A.16C), and kinetics of R10_4M seed-induced aggregation reaction at 1.5-2.5 M of GuHCl (Supplementary Fig. A.17C-E).

Similarities between self-propagation rates of distinct fibril strains at high temperature in the presence of 1.5-2.5 M of GuHCl (Fig. 4.34) suggest a common mechanisms of fibril self-replication. This means that under certain circumstances, distinct fibril strains have almost identical probability to dominate and self-propagate, meaning that change in the dominant population may be mostly dependent on the overall initial concentration of the fibril strain. This is also supported by our previous findings [16], however, experiments with multiple seeds in one solution are necessary and will be done in the future to prove this hypothesis.

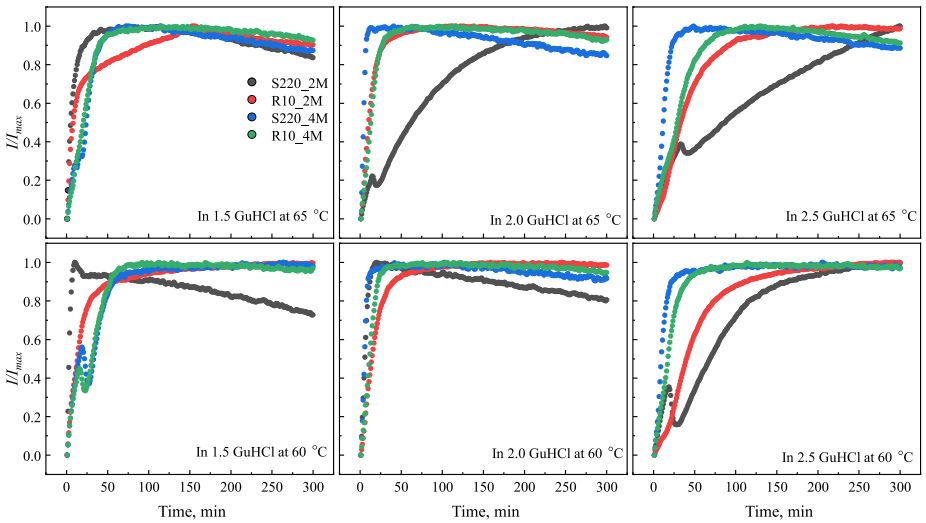

FIGURE 4.34: Comparison of kinetics of distinct prion strain self-replication.

Abnormalities in the kinetics of seed-induced aggregation reaction

One could assume the abnormalities in ThT signal may be related to

the equipment used (in this case RotorGeneQ real-time analyser), however, similar change in ThT signal was observed when seeded aggregation reaction was monitored using two distinct devices (RotorGeneQ real-time analyser and Cary Eclipse fluorimeter) (Fig. 4.35). Furthermore, one could think that the jump in ThT signal might be related to ThT itself, however, we observed similar changes in light scattering (LS) (Fig. 4.35) and deep-blue autofluorescence signals as well [322]. Thus, the abnormalities in the kinetics of seed-induced aggregation reaction are most likely related to the processes occurring during the fibril self-replication reaction.

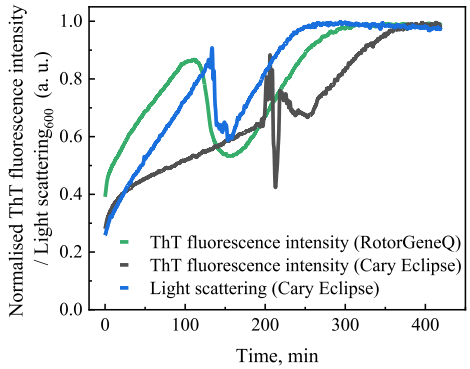

FIGURE 4.35: Kinetic of S220_4M seed-induce aggregation reaction in 1.5 M GuHCl at 50 °C monitored using distinct equipment and by different feedback signal.

Sample analysis via AFM revealed quite remarkable and unexpected results (Fig. 4.36). At the maximum of the first ThT signal peak, the fibrils are densely packed (Fig. 4.36A). At the minimum of the subsequent ThT signal decline, fibrils are less densely packed, however, small clumps of fibrils are evident (Fig. 4.36B). At the plateau of ThT signal, mostly separated fibrils are visible (Fig. 4.36C). One could expect the opposite change of fibril packing along the time-course of seeded aggregation reaction. The results are quite difficult to explain and interpret.

By taking into consideration all our observations, we propose the following hypothesis, which could explain the appearance of a jump in ThT and light scattering signal, and the AFM results.

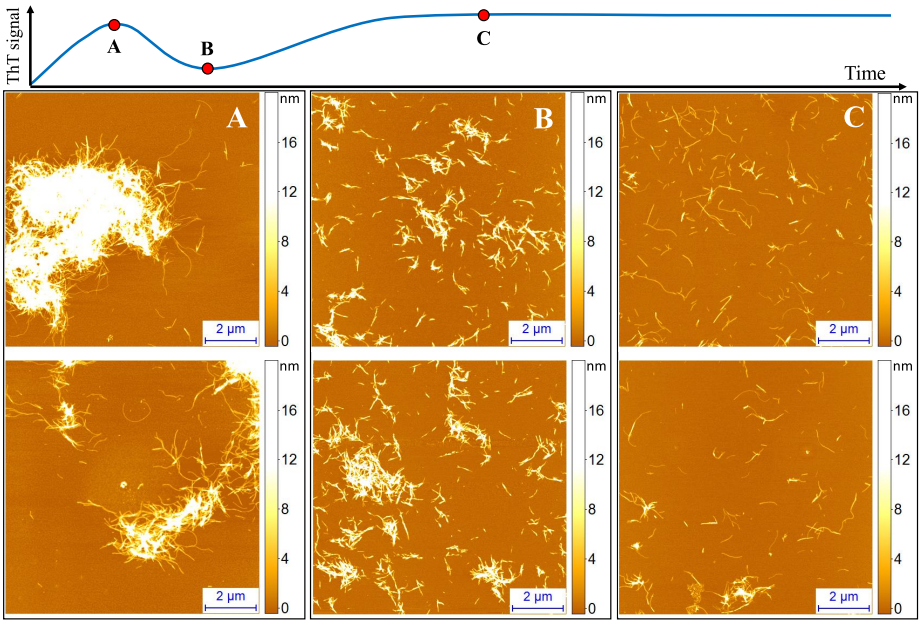

FIGURE 4.36: AFM images of samples collected at distinct time points of R10_4M seed-induced aggregation reaction performed in the presence of 1.5 M of GuHCl. Schematic representation of seed-induced aggregation reaction time-course, and sample collection points (Top panel). A) AFM images of aggregates present at the maximum of the first ThT signal peak. B) AFM images of aggregates present at the minimum of the subsequent ThT signal decline. C) AFM images of aggregates present at the plateau of ThT signal.

At the beginning of seed-induced aggregation reaction, free ThT molecules bind to the surface of fibrils, which results in an increase in ThT fluorescence intensity (Fig. 4.37 1.) [323–325]. Moreover, the protein monomers can condense on the fibril surface (secondary nucleation) [326, 327], which results in shielding of ThT molecules, bound to the fibril surface, from interactions with solvent, that leads to a reduction in fluorescence quenching effects [323–325]. Upon fibril elongation, more surface, where ThT molecules can bind, and monomers can condense on, is created, and hence, a gradual increase in ThT signal is evident. Secondary nucleation is a multi-step process, which involves several microscopic events including association of monomers with aggregates, nucleation on the surface and detachment [327]. At low monomer concentration the secondary nucleation is unsaturated

(*i.e.* dependent on monomer concentration), while at high protein concentration, the process is saturated [327]. Moreover, the alterations in environmental conditions may change not only the properties of protein interacting in solution, but also the strength of the adsorption (F_{AS}) of proteins onto the surface of the fibrils [326]. At low F_{AS}, proteins cover only a small fraction of the fibrils surface, and the protein adsorption and oligomer formation on the surface is the rate limiting step. At high F_{AS}, the fibril surface is substantially covered by proteins, however, the oligomer detachment becomes unfavourable. Nuclei will form only after the oligomers has reached a certain size, when inter-protein interactions, after the conformational, change overcomes the loss in the protein-fibril adsorption energy. Thus, stronger binding to the surface requires formation of larger oligomers in order to overcome the loss in favourable adsorption energy [326]. Moreover, in the regime of high F_{AS}, proteins are likely to distribute evenly on the fibril surface in order to increase their contact area with the surface, and also could form multiple layers [326]. Now we assume that ThT molecules that are shielded from the solvent contribute a sizeable portion of the overall ThT fluorescence emission intensity due to reduced quenching effects. Also, we assume that in our case secondary nucleation is saturated, and that F_{AS} is high. At a certain time point, the nuclei, capable of elongating, form from monomers on the surface of the fibril (Fig. 4.37 1.). When the nuclei become large enough, they detach from the surface of the fibril and expose fibril-bound ThT molecules to the solvent (Fig. 4.37 2.). If / when the rate of nuclei detaching k_{off} from the fibril surface becomes faster than the rate of monomer binding k_{on} to the fibril surface, the decrease in ThT fluorescence intensity signal is evident due to a large decline in ThT fluorescence quantum yield. The decrease in ThT signal, however, is temporary, as after some time the system reaches equilibrium, and the rate of nuclei detaching k_{off}, and monomers binding k_{on} to the fibril surface becomes similar (Fig. 4.37 3.). At this time point, change in ThT fluorescence intensity becomes mostly dependent on fibril and nuclei elongation, which generates new surface for ThT molecules to bind, and monomers to condense on. Therefore, gradual increase in ThT fluorescence intensity, mostly originating from increase in surface accessible

for ThT molecules to bind, is evident at later stages of seed-induced aggregation reaction.

Just before the drastic drop in ThT signal, large clumps of aggregates are present (Fig. 4.36A). It is possible that these clumps originate due to high F_{AS}, which makes oligomer/nuclei detachment from the fibril surface unfavourable, and therefore, results in formation of elongated aggregates on the surface of existing fibrils. However, once these aggregates reach critical size they detach from the fibrils. The relative abundance of fibril clumps at the time point just before the drop in ThT signal is higher than at the points where the decrease in ThT signal discontinues (Fig. 4.36B), or reaches a plateau (Fig. 4.36C). This could be due to a lower concentration of free monomers at these time points, which would result in formation of less secondary nuclei or elongated aggregates on the surface of existing fibrils, and therefore fibril clumps would be not as evident.

At the beginning of the reaction, the LS signal increases, which suggests an increase in particle size. For instance, binding of monomers to, and/or formation of nuclei on the surface of fibrils would result in an increase in size. Subsequently, LS signal drops, indicating decrease in particle size. For example, separation of nuclei from the surface of fibrils could cause this. Later, the light scattering signal increase again suggesting increase in average size of aggregate.

In general, it is evident that the drop in ThT signal is not an experimental error but rather a phenomenon related to the artefacts/abnormalities of secondary nucleation process, and deserves more attention as to our knowledge such an event previously has never been reported. In order to obtain a profound understanding of this phenomenon, in the future, seeded aggregation reaction will be performed using varying concentrations of seed and monomer, also mathematical modeling will be employed to obtain mechanistic insights, and a more detailed analysis of seed-induced aggregation reaction time-course via AFM will be performed.

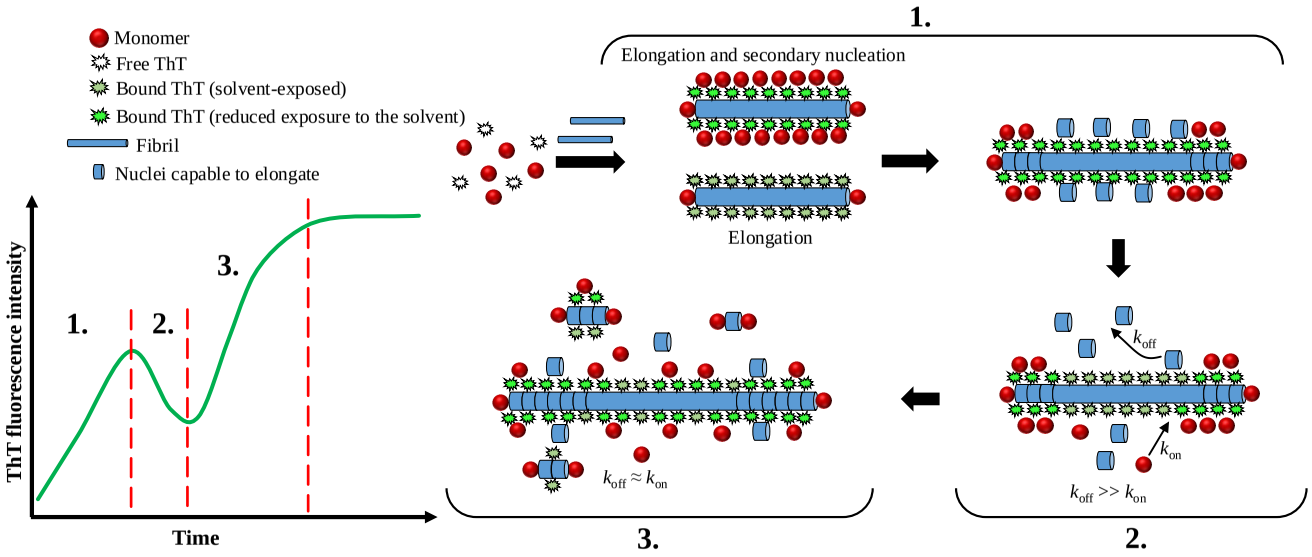

FIGURE 4.37: Schematic illustration of microscopic events that may cause abnormalities in kinetics of seed-induced aggregation reaction.

4.3 Resolving the heterogeneity and relative abundance of Aβ42 aggregates during amyloid formation

The results presented in this section contain unpublished data acquired during my internship in Michele Vendruscolo's lab at Cambridge University. Publication, based on the results acquired during this internship, will be prepared.

All experiments were performed under supervision of Dr. Francesco Simone Ruggeri, who conceived and designed the experiments. Purification and aggregation experiments of Aβ42 were performed by Dr. Sean Chia. Sample deposition using microfluidic device was performed by Tuuli Hakala. I have performed sample imaging via AFM, data processing and analysis, and prepared the figures.

Atomic force microscopy is one of the most powerful and versatile single-molecule analysis techniques used for imaging and characterisation of biomolecules [7, 42, 208, 209]. AFM is frequently employed to study the amyloid aggregation process [7, 42, 44, 214–217]. In particular, AFM enables to visualise and statistically characterise morphological properties (*e.g.* height, width and length) of polymorphic and heterogeneous species, including monomers, oligomers, protofibrillar structures and mature amyloid fibrils, present during the process of amyloid aggregation [7, 44, 214–223]. Such measurements, however, require deposition of sample onto solid substrates like atomically flat mica. In case of AFM measurements in air, a typical sample deposition procedure consists of three general steps: deposition of the sample on the solid atomically flat surface; rinsing with buffer or water to remove weakly bound molecules; and drying the sample using gentle airflow. The sample deposition time is extremely important, as the quantity of biomolecules bound to the substrate surface is proportional to the incubation time. However, during the time of physisorption the molecules can self-organise and self-assemble into artificial structures along crystalline order of the surface [328–330]. Moreover, due to differential adsorption, part of molecular species present in solution can be removed

during the rinsing and drying procedure, which results in a partial representation of the actual sample composition. All this makes control of the quantity of biomolecules deposited on the surface very challenging, also it is almost impossible to determine relative abundance of distinct species since there is no confined area. Therefore, generally AFM provides qualitative rather than quantitative information about amyloid aggregation process. Deposition artefacts are the main cause of misinterpretation of the content and biophysical properties of amyloidogenic proteins. These limitations, however, can be overcome by employing a recently developed advanced single-step microfluidic spray deposition platform [328].

The microfluidic spray device (Fig. 4.38) is able to transfer protein droplets of subpicoliter volumes onto the surface. The droplets dry in milliseconds, a timescale that is much shorter than the theoretically and experimentally predicted time of the lateral diffusion of a monomeric protein or aggregate on a liquid–solid interface [328, 329, 331–333]. This makes it impossible for proteins to move freely, and therefore they can not self-organise and self-assemble on the surface.

Spraying the sample on the substrate at a distance of h = 4 cm away from the surface generates spherical droplets, which after landing on the surface are of radius R_{range} = 2.9 - 7.2 μm (interquartile range) and which takes about t_{range} = 0.7 - 4.3 ms (interquartile range) to evaporate [328]. The diameter of the surface-dried droplet is 5.8 - 14.2 μm, therefore the whole droplet with all its constituents (in case of amyloidogenic proteins: monomers, oligomeric species, protofilaments and mature fibrils) can be imaged via AFM at high resolution (Fig. 4.38). The complete elucidation of amyloid fibril formation process is possible only if all conformational states, oligomeric and fibrillar structures adopted by the polypeptide chain during the process, as well as the thermodynamics and kinetics of all conformational changes are known [10]. Using a microfluidic device for sample deposition provides a unique possibility to perform profound qualitative and quantitative study of amyloid aggregation process via high-resolution AFM. Herein we exploited this unique possibility to study time-course of amyloid beta 42 (Aβ42) aggregation.

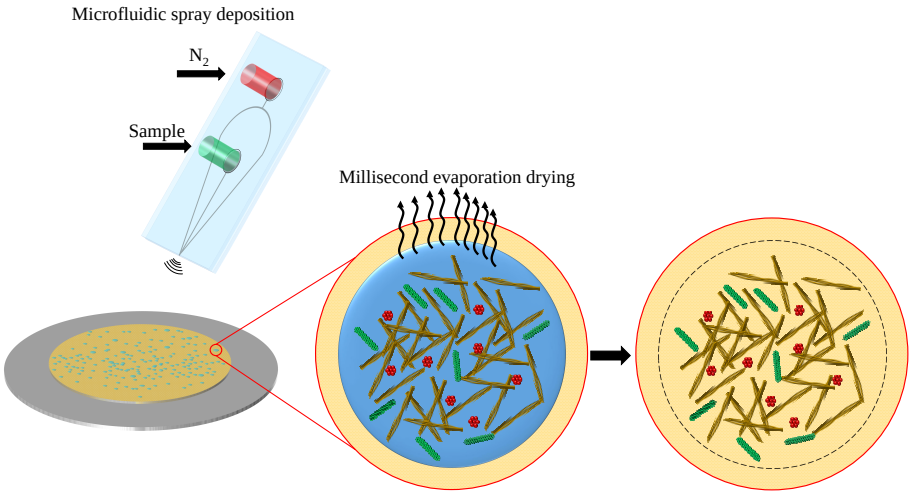

FIGURE 4.38: Schematic depiction of sample deposition using microfluidic spray device.

Amyloid aggregation: From monomeric Aβ42 to mature amyloid fibrils

In order to obtain new insights about amyloid protein aggregation process, we employed high-resolution AFM in combination with microfluidic spray deposition technique, to follow the aggregation time course of Aβ42, and to characterise the morphology, structural properties and the heterogeneity of the species present at distinct time points of aggregation reaction.

The kinetics of spontaneous Aβ42 aggregation reaction were monitored using ThT assay (Fig. 4.39A). Samples for deposition using the microfluidic device, and subsequent analysis via high-resolution AFM were collected at the very beginning of the aggregation reaction (t_0), at the middle (t_1) and end (t_2) of lag phase, at the middle of growth phase (t_3), and at the plateau phase (t_4).

Sample analysis via high-resolution AFM confirmed the possibility to image constituents of surface dried droplets (Fig. 4.39B-F). It is evident from the large area AFM images that constituents of droplets are scattered around the whole area of the surface-dried droplet, whereas almost no molecular species are present outside the periphery.

This means that there is a confined area within which all molecular species, present in the aggregation reaction solution, are present. These results serve as a proof of concept. Multiple images at each time point were taken to make sure that the results are consistent (Supplementary Fig. A.18).

Analysis of sample morphology revealed that at the early stages of Aβ42 aggregation (t_0 - t_1) mostly small spherical particles with a height of 0.5-3 nm, resembling monomeric and early oligomeric species, are present, and no fibrils are visible (Fig. 4.40 and Supplementary Fig. A.19). At the late lag phase (t_2) larger oligomers and short curvy protofibrils with a height of 3-4 nm were detected. In the middle of the growth phase (t_3) most of the oligomeric species had disappeared and were replace by short protofibrils and fibrils with a height of 3-4 nm and 5-7 nm, respectively. Elongated mature fibrils with a height of 5-7 nm are visible at the plateau phase (t_4). The results are consistent with previous observations [131, 216, 234].

Single-molecule statistical analysis and comparison of morphological properties (height, width and length (diameter for spherical particles)) of molecular species present during Aβ42 aggregation reaction revealed a progressive change in the dominant population of these species along the time-course of aggregation reaction (Fig. 4.41). At the initial stages of aggregation reaction (t_0) the majority of the population of molecular species have a height of $\approx$0.5-1 nm (Fig. 4.41 A, F) and a diameter of $\approx$4 nm (Fig. 4.41G). The dimensions of this major population corresponds to the one of Aβ42 monomers on a solid surface [216]. A relatively low dispersion of the data suggests that Aβ42 monomers are the predominant species at this time point. In the middle of the lag phase (t_1), a broader distribution of height ($\approx$0.5-3 nm) (Fig. 4.41B, F) and increase in average width ($\approx$6 nm) (Fig. 4.41G) of the molecular species is evident. This suggests appearance of early oligomeric species (dimers, trimers), and that monomers and early oligomers constitute the majority of population at this point of Aβ42 aggregation time course. At the late lag phase / early growth phase (t_2), the average height ($\approx$4 nm) (Fig. 4.41C, F) and width ($\approx$12 nm) (Fig. 4.41G) of molecular species is substantially larger than that determined for monomers

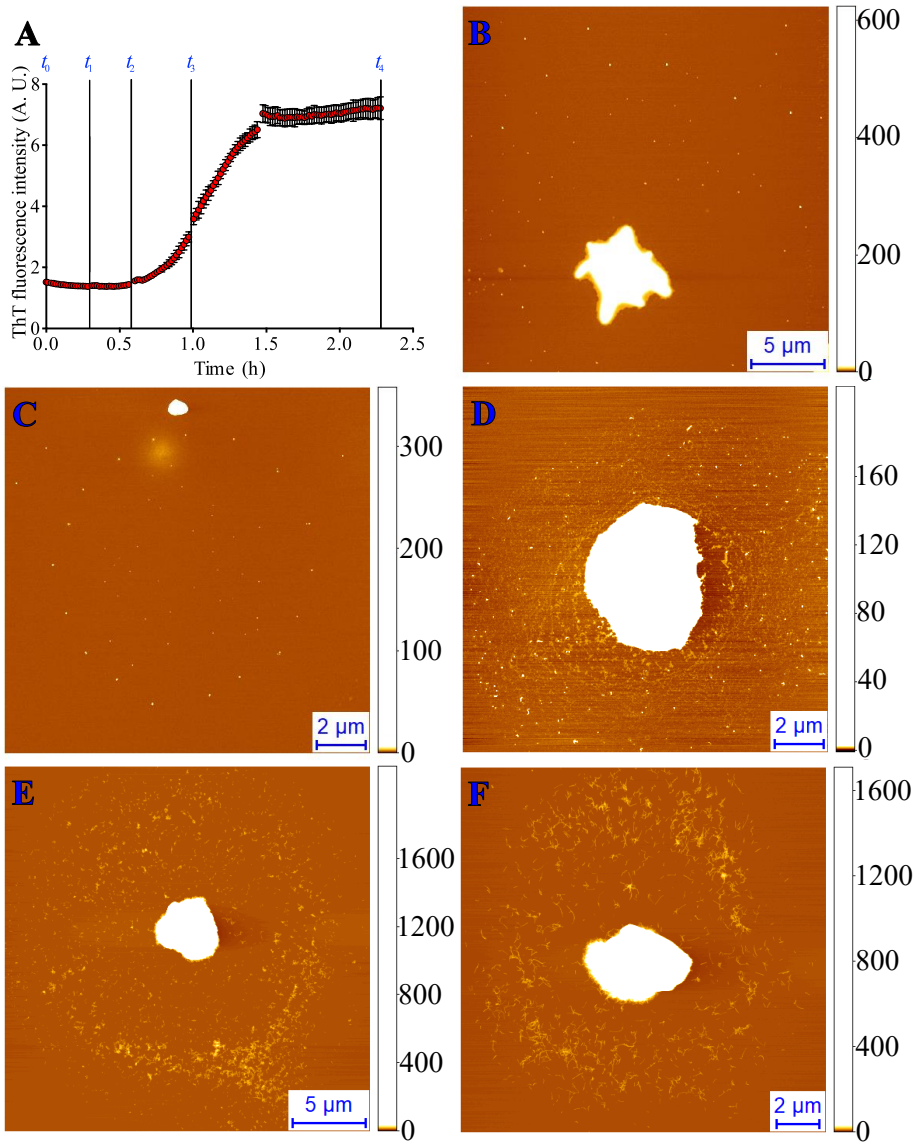

FIGURE 4.39: Monitoring of Aβ42 aggregation time course via ThT assay (A) and high-resolution AFM (B-F). B-F AFM images of samples collected at t_0 - t_4, respectively.

and early oligomers, implying that larger species such as late oligomers with a height of 3-4 nm, and protofibrils with a height of ≈3-4 nm constitute the majority of the population. However, since the average length

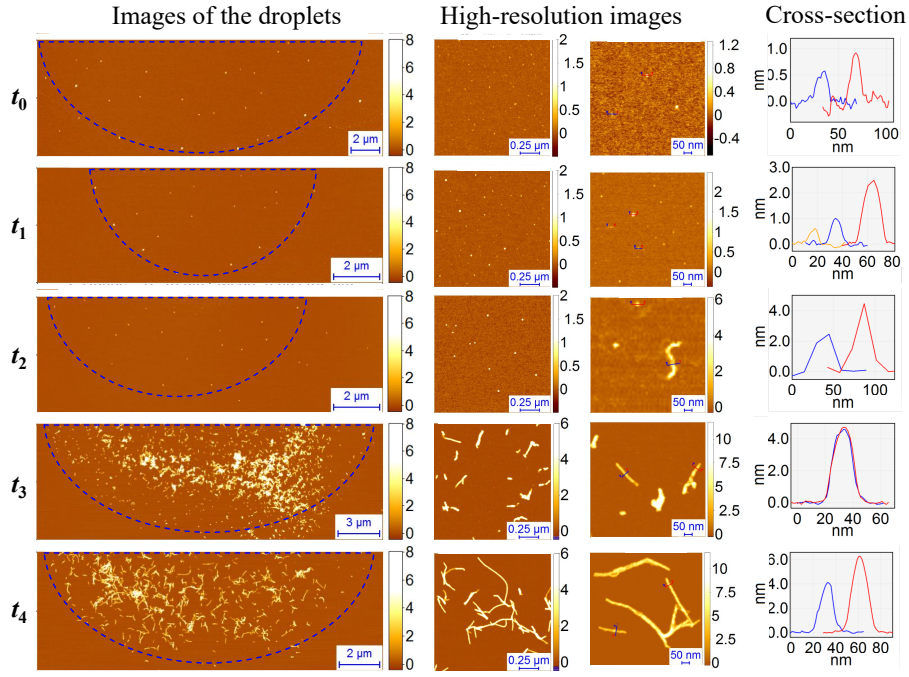

FIGURE 4.40: Analysis of morphology of species present during different stages of Aβ42 aggregation reaction.

(Fig. 4.41H) of the population at this time point is relatively low, it can be assumed that large oligomers constitute the major fraction, while protofibrils comprise smaller part of the population. Two major populations are evident in the histogram of distributions of height of molecular species present in the middle of the growth phase (t_3) and the plateau phase (t_4) (Fig. 4.41D, E). The first one has average height of ≈4 nm corresponding to the height of protofibrils [131, 216], whereas the second one has average height of ≈6 nm corresponding to height of mature fibrils [131, 216]. The only clear difference between species present at the middle of the growth phase and plateau phase is their length (Fig. 4.41 H), which is substantially larger at latter phase.

In general, it is evident from histograms of distribution of height, and distributions of average height, width, and length that the population of molecular species is more or less homogeneous only at the very beginning of aggregation reaction, while several co-existing species

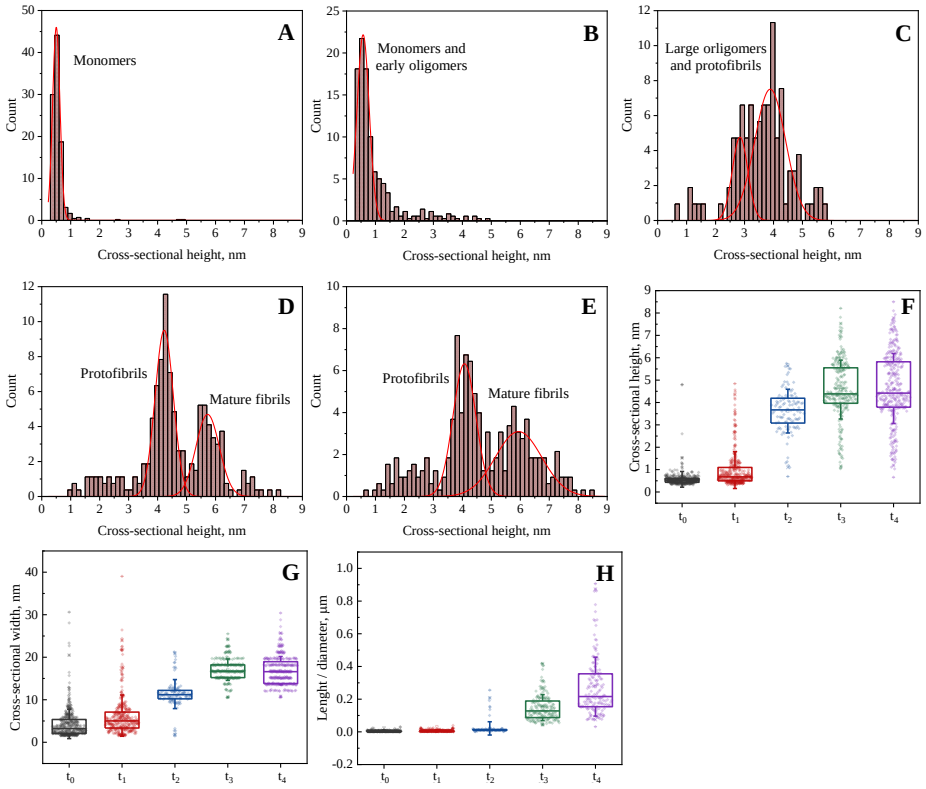

FIGURE 4.41: Single-molecule statistical analysis. A-E) histograms of height distribution of samples collected at t_0-t_4, respectively. Distribution of average cross-sectional height (F), width (G), and length (H) of samples collected at t_0-t_4, respectively. Error bars are standard deviations (n $\geq$ 100).

emerge at later stages of amyloid aggregation reaction.

A profound analysis of relative abundance of all molecular species at each time point of Aβ42 aggregation time course is ongoing and will be shown in a future publication.

In conclusion, we demonstrated that high-resolution atomic force microscopy in combination with microfluidic sample deposition platform enables the possibility to image all molecular species present during the Aβ42 aggregation time-course, and allows to acquire single-molecule quantitative data that is fundamental for complete elucidation of amyloid aggregation mechanisms.

Chapter 5

Conclusions

The development of effective prevention and treatment approaches of amyloid-related disorders requires a profound knowledge of complex processes of amyloid fibril formation and self-replication [5, 8]. Absence of effective disease modifying drugs or treatment modalities available for these diseases suggest that in general the process of amyloid fibril formation is still relatively poorly understood. The complete elucidation of this complex process is possible only when all species, present during the time-course of amyloid fibril formation, as well as the thermodynamics and kinetics of all conformational changes are known [5, 8]. Thus, the collaboration across various disciplines is necessary to provide deeper insight into the process of amyloid aggregation. Moreover, the alterations in environmental conditions can affect microsopic events, involved in the amyloid aggregation process, resulting in the emergence of distinct pathways of amyloid aggregation, leading to the formation of structurally distinct amyloid fibril strains [5, 9, 11, 14–27]. Although fascinating, conformational variability is still a poorly understood phenomena, and is another major reason of failure of anti-amyloid treatment modalities [9]. Since compounds that are effective against one fibril strain, may be ineffective against others [9]. Furthermore, the molecular and mechanistic links between protein aggregation and toxicity remain challenging to characterise [8]. Taken together, it is evident that mechanistic and structural studies of amyloid fibril formation, self-replication, and conformational variability are fundamental for profound understanding of amyloid aggregation process and subsequent development of effective therapeutic strategies

In this thesis, the aggregation process of human recombinant insulin, mouse recombinant prion protein fragment, and recombinant amyloid beta was studied using multiple biophysical techniques.

These studies brought new insights into the processes of amyloid fibril formation and self-replication, polymorphism phenomena, the process of anti-amyloid compound screening, and the studies of heterogeneous amyloid samples, and led to the following conclusions:

- **Monomer-oligomer equilibrium is the one of the main factors governing the formation of distinct insulin strains.**
- **Insulin amyloid aggregation may be inhibited by insulin oligomers.**
- **Environment is the key factor in determining the anti-amyloid efficacy of EGCG.**
- **Self-replication of amyloid fibril conformational template can proceed only via fibril elongation.**
- **Polymorphism of amyloid fibrils can be defined by the concentration of seeds.**
- **The abnormalities in ThT signal during seed-induced aggregation reaction may be related to the molecular events occurring during secondary nucleation process.**
- **Atomic force microscopy in combination with microfluidic sample deposition platform enables the possibility to image all molecular species present during amyloid aggregation time-course, and allows to acquire single-molecule quantitative data.**

References

1. Selkoe, D. J. & Hardy, J. The amyloid hypothesis of Alzheimer's disease at 25 years. *EMBO Molecular Medicine* **8,** 595–608. ISSN: 1757-4676 (2016).
2. Poewe, W. *et al.* Parkinson disease. *Nature Reviews Disease Primers* **3,** 1–21. ISSN: 2056676X (2017).
3. Mukherjee, A., Morales-Scheihing, D., Butler, P. C. & Soto, C. Type 2 diabetes as a protein misfolding disease. *Trends in Molecular Medicine* **21,** 439 –449. ISSN: 1471-4914 (2015).
4. Aguzzi, A., Nuvolone, M. & Zhu, C. The immunobiology of prion diseases. *Nature Reviews Immunology* **13,** 888–902. ISSN: 14741733 (2013).
5. Knowles, T. P. J., Vendruscolo, M. & Dobson, C. M. The amyloid state and its association with protein misfolding diseases. *Nature reviews. Molecular cell biology* **15,** 384–96. ISSN: 1471-0080 (2014).
6. Wisniewski, T. & Goñi, F. Immunotherapeutic Approaches for Alzheimer's Disease. *Neuron* **85,** 1162–1176. ISSN: 10974199 (2015).
7. Ruggeri, F. S., Šneideris, T., Vendruscolo, M. & Knowles, T. P. Atomic force microscopy for single molecule characterisation of protein aggregation. *Archives of Biochemistry and Biophysics* **664,** 134–148. ISSN: 00039861 (2019).
8. Chiti, F. & Dobson, C. M. Protein Misfolding, Amyloid Formation, and Human Disease: A Summary of Progress Over the Last Decade. en. *Annual Review of Biochemistry* **86,** 27–68. ISSN: 0066-4154, 1545-4509 (2017).

9. Marín-Moreno, A., Fernández-Borges, N., Espinosa, J. C., Andréoletti, O. & Torres, J. M. Transmission and Replication of Prions. *Progress in Molecular Biology and Translational Science* **150,** 181–201. ISSN: 18780814 (2017).

10. Chiti, F. & Dobson, C. M. Protein misfolding, functional amyloid, and human disease. *Annual review of biochemistry* **75,** 333–66. ISSN: 0066-4154 (2006).

11. Chiti, F. & Dobson, C. M. Protein misfolding, amyloid formation, and human disease: A summary of progress over the last decade. *Annual Review of Biochemistry* **86,** 27–68. ISSN: 0066-4154 (2017).

12. Meisl, G. *et al.* Molecular mechanisms of protein aggregation from global fitting of kinetic models. *Nature Protocols* **11,** 252–272. ISSN: 1754-2189 (2016).

13. Michaels, T. C. T. *et al.* Chemical Kinetics for Bridging Molecular Mechanisms and Macroscopic Measurements of Amyloid Fibril Formation. *Annual Review of Physical Chemistry* **69,** annurev–physchem–050317–021322. ISSN: 0066-426X (2018).

14. Sneideris, T. *et al.* pH-driven polymorphism of insulin amyloid-like fibrils. *PloS one* **10,** e0136602. ISSN: 1932-6203 (2015).

15. Ziaunys, M., Sneideris, T. & Smirnovas, V. Self-inhibition of insulin amyloid-like aggregation. *Physical Chemistry Chemical Physics* **20,** 27638–27645. ISSN: 1463-9076 (2018).

16. Sneideris, T., Milto, K. & Smirnovas, V. Polymorphism of amyloid-like fibrils can be defined by the concentration of seeds. *PeerJ* **3,** e1207. ISSN: 2167-8359 (2015).

17. Legname, G. & Moda, F. in *Prion Protein* (eds Legname, G. & Vanni, S.) 147 –156 (Academic Press, 2017).

18. Makarava, N. & Baskakov, I. V. The Evolution of Transmissible Prions: The Role of Deformed Templating. *PLoS Pathogens* **9** (ed True, H. L.) e1003759. ISSN: 1553-7374 (2013).

19. Li, J., Browning, S., Mahal, S. P., Oelschlegel, A. M. & Weissmann, C. Darwinian evolution of prions in cell culture. *Science* **327,** 869–872. ISSN: 00368075 (2010).

20. Colby, D. W. & Prusiner, S. B. Prions. *Cold Spring Harbor perspectives in biology* **3,** a006833. ISSN: 1943-0264 (2011).

21. Cobb, N. J., Apostol, M. I., Chen, S., Smirnovas, V. & Surewicz, W. K. Conformational Stability of Mammalian Prion Protein Amyloid Fibrils Is Dictated by a Packing Polymorphism within the Core Region. *Journal of Biological Chemistry* **289,** 2643–2650. ISSN: 0021-9258, 1083-351X (2014).

22. Smirnovas, V. *et al.* Distinct structures of scrapie prion protein (PrPSc)-seeded versus spontaneous recombinant prion protein fibrils revealed by hydrogen/deuterium exchange. *The Journal of biological chemistry* **284,** 24233–41. ISSN: 0021-9258 (2009).

23. Kim, C. *et al.* Artificial strain of human prions created in vitro. *Nature Communications* **9,** 1–11. ISSN: 20411723 (2018).

24. Wang, F. *et al.* Self-propagating, protease-resistant, recombinant prion protein conformers with or without in vivo pathogenicity. *PLoS Pathogens* **13,** 1–23. ISSN: 15537374 (2017).

25. Legname, G. *et al.* Synthetic Mammalian Prions. *Science* **305,** 673–676. ISSN: 0036-8075 (2004).

26. Colby, D. W. & Prusiner, S. B. De novo generation of prion strains. *Nature Reviews Microbiology* **9,** 771–777. ISSN: 1740-1526 (2011).

27. Moda, F. *et al.* Synthetic prions with novel strain-specified properties. *PLoS Pathogens* **11,** 1–28. ISSN: 15537374 (2015).

28. Guo, J. L. & Lee, V. M. Y. Cell-to-cell transmission of pathogenic proteins in neurodegenerative diseases. *Nature Medicine* **20,** 130–138. ISSN: 1546-170X (2014).

29. Adamcik, J. & Mezzenga, R. Amyloid polymorphism in the protein folding and aggregation energy landscape. *Angewandte Chemie - International Edition* **57,** 8370–8382. ISSN: 15213773 (2018).

30. Sipe, J. D. & Cohen, A. S. Review: history of the amyloid fibril. *Journal of structural biology* **130,** 88–98. ISSN: 1047-8477 (2000).

31. Iadanza, M. G., Jackson, M. P., Hewitt, E. W., Ranson, N. A. & Radford, S. E. A new era for understanding amyloid structures and disease. *Nature Reviews Molecular Cell Biology* **19,** 755–773. ISSN: 14710080 (2018).

32. Yakupova, E. I., Bobyleva, L. G., Vikhlyantsev, I. M. & Bobylev, A. G. Congo Red and amyloids: history and relationship. *Bioscience Reports* **39,** BSR20181415. ISSN: 0144-8463 (2019).

33. Elghetany, M. T., Saleem, A. & Barr, K. The Congo red stain revisited. *Annals of Clinical and Laboratory Science* **19,** 190–195. ISSN: 00917370 (1989).

34. Cohen, A. S. & Calkins, E. Electron Microscopic Observations on a Fibrous Component in Amyloid of Diverse Origins. *Nature* **183,** 1202–1203. ISSN: 0028-0836 (1959).

35. Benditt, E., Eriksen, N., Hermodson, M. & Ericsson, L. The major proteins of human and monkey amyloid substance: Common properties including unusual N-terminal amino acid sequences. *FEBS Letters* **19,** 169–173 (1971).

36. Glenner, G. G. *et al.* Creation of "Amyloid" Fibrils from Bence Jones Proteins in vitro. *Science* **174,** 712–714. ISSN: 0036-8075 (1971).

37. Costa, P. P., Figueira, A. S. & Bravo, F. R. Amyloid fibril protein related to prealbumin in familial amyloidotic polyneuropathy. *Proceedings of the National Academy of Sciences* **75,** 4499–4503. ISSN: 0027-8424 (1978).

38. Skinner, M. & Cohen, A. S. The prealbumin nature of the amyloid protein in familial amyloid polyneuropathy (FAP)-Swedish variety. *Biochemical and Biophysical Research Communications* **99,** 1326 – 1332. ISSN: 0006-291X (1981).

39. Selkoe, D. J. & Podlisny, M. B. Deciphering the genetic basis of Alzheimer's disease. *Annual review of genomics and human genetics* **3,** 67–99. ISSN: 1527-8204 (2002).

40. Morris, K. L. & Serpell, L. C. in *Amyloid Proteins: Methods and Protocols* (eds Sigurdsson, E. M., Calero, M. & Gasset, M.) 121–135 (Humana Press, Totowa, NJ, 2012). ISBN: 978-1-61779-551-0.

41. Fitzpatrick, A. W. P. *et al.* Atomic structure and hierarchical assembly of a cross- amyloid fibril. *Proceedings of the National Academy of Sciences* **110,** 5468–5473. ISSN: 0027-8424 (2013).

42. Ruggeri, F. S., Habchi, J., Cerreta, A. & Dietler, G. AFM-based single molecule techniques: Unraveling the amyloid pathogenic species. *Current pharmaceutical design* **22,** 3950–70. ISSN: 1873-4286 (2016).

43. Knowles, T. P. J. *et al.* Twisting transition between crystalline and fibrillar phases of aggregated peptides. *Physical Review Letters* **109,** 158101. ISSN: 0031-9007 (2012).

44. Adamcik, J. & Mezzenga, R. Study of amyloid fibrils via atomic force microscopy. *Current Opinion in Colloid and Interface Science* **17,** 369–376. ISSN: 13590294 (2012).

45. Hauser, C. A., Maurer-Stroh, S. & Martins, I. C. Amyloid-based nanosensors and nanodevices. *Chemical Society Reviews* **43,** 5326–5345. ISSN: 14604744 (2014).

46. Cherny, I. & Gazit, E. Amyloids: Not only pathological agents but also ordered nanomaterials. *Angewandte Chemie - International Edition* **47,** 4062–4069. ISSN: 14337851 (2008).

47. Knowles, T. P., Oppenheim, T. W., Buell, A. K., Chirgadze, D. Y. & Welland, M. E. Nanostructured films from hierarchical self-assembly of amyloidogenic proteins. *Nature Nanotechnology* **5,** 204–207. ISSN: 17483395 (2010).

48. Li, C. & Mezzenga, R. The interplay between carbon nanomaterials and amyloid fibrils in bio-nanotechnology. *Nanoscale* **5,** 6207–6218. ISSN: 20403364 (2013).

49. Chapman, M. R. Role of Escherichia coli curli operons in directing amyloid fiber formation. *Science* **295,** 851–855. ISSN: 00368075 (2002).

50. Fowler, D. M., Koulov, A. V., Balch, W. E. & Kelly, J. W. Functional amyloid - from bacteria to humans. *Trends in Biochemical Sciences* **32,** 217–224. ISSN: 09680004 (2007).

51. Shewmaker, F., McGlinchey, R. P. & Wickner, R. B. Structural insights into functional and pathological amyloid. *Journal of Biological Chemistry* **286,** 16533–16540. ISSN: 00219258 (2011).

52. Knowles, T. P. & Mezzenga, R. Amyloid fibrils as building blocks for natural and artificial functional materials. *Advanced Materials,* 6546–6561. ISSN: 15214095 (2016).

53. Aguzzi, A. & Calella, A. M. Prions: protein aggregation and infectious diseases. *Physiological reviews* **89,** 1105–52. ISSN: 0031-9333 (2009).

54. Hirschfield, G. & Hawkins, P. Amyloidosis: new strategies for treatment. *The International Journal of Biochemistry Cell Biology* **35,** 1608 –1613. ISSN: 1357-2725 (2003).

55. Alexandrescu, A. T. Amyloid accomplices and enforcers. *Protein Science* **14,** 1–12 (2005).

56. Kayed, R. & Lasagna-Reeves, C. a. Molecular mechanisms of amyloid oligomers toxicity. *Advances in Alzheimer's Disease* **3,** 67–78. ISSN: 22105727 (2012).

57. Hayden, E. Y. & Teplow, D. B. Biophysical Characterization of Amyloid beta Assembly. *Alzheimer's Disease: Insights into Low Molecular Weight and Cytotoxic Aggregates from In Vitro and Computer Experiments* **7** (ed Derreumaux, P.) 83–125 (2013).

58. Bhaskar, K. & Lamb, B. Non-fibrillar Amyloidogenic Protein Assemblies - Common Cytotoxins Underlying Degenerative Diseases. *Non-fibrillar Amyloidoigenic Protein Assemblies-Common Cytotoxins Underlying Degenerative Diseases* (eds Rahimi, F. & Bitan, G.) 289–317 (2012).

59. Balchin, D., Hayer-Hartl, M. & Hartl, F. U. In vivo aspects of protein folding and quality control. *Science* **353,** aac4354. ISSN: 0036-8075 (2016).

60. Labbadia, J. & Morimoto, R. I. The Biology of Proteostasis in Aging and Disease. *Annual Review of Biochemistry* **84,** 435–464. ISSN: 0066-4154 (2015).

61. Knowles, T. P. J. *et al.* An analytical solution to the kinetics of breakable filament assembly. *Science (New York, N.Y.)* **326,** 1533–7. ISSN: 1095-9203 (2009).

62. Meisl, G. *et al.* Differences in nucleation behavior underlie the contrasting aggregation kinetics of the Aβ40 and Aβ42 peptides. *Proceedings of the National Academy of Sciences of the United States of America* **111,** 9384–9. ISSN: 1091-6490 (2014).

63. Cohen, S. I. A. *et al.* Proliferation of amyloid-β42 aggregates occurs through a secondary nucleation mechanism. *Proceedings of the National Academy of Sciences of the United States of America* **110,** 9758–63. ISSN: 1091-6490 (2013).

64. Hamley, I. W. *The amyloid beta peptide: A chemist's perspective. role in Alzheimer's and fibrillization* **10,** 5147–5192 (2012).

65. Cárdenas-Aguayo, M. C., Silva-Lucero, M. C. & García, U. Physiological Role of Amyloid Beta in Neural Cells: The Cellular Trophic Activity. *Neurochemistry,* 1–26 (2014).

66. Prusiner, S. B. Novel proteinaceous infectious particles cause scrapie. *Science (New York, N.Y.)* **216,** 136–144. ISSN: 0036-8075 (1982).

67. Smirnovas, V. *et al.* Structural organization of brain-derived mammalian prions examined by hydrogen-deuterium exchange. *Nature structural & molecular biology* **18,** 504–506. ISSN: 1545-9993 (2011).

68. Wulf, M. A., Senatore, A. & Aguzzi, A. The biological function of the cellular prion protein: An update. *BMC Biology* **15,** 1–13. ISSN: 17417007 (2017).

69. Foderà, V., Librizzi, F., Groenning, M., van de Weert, M. & Leone, M. Secondary nucleation and accessible surface in insulin amyloid fibril formation. *The journal of physical chemistry. B* **112,** 3853–8. ISSN: 1520-6106 (2008).

70. Tornheim, K. & Ruderman, N. B. in *Metabolic Basis of Obesity* (ed Rexford, A.) 25–51 (Springer New York, New York, NY, 2011). ISBN: 9781441916068.

71. Haas, J. *et al.* Primary steps of pH-dependent insulin aggregation kinetics are governed by conformational flexibility. *ChemBioChem* **10,** 1816–1822. ISSN: 14394227 (2009).

72. Noormägi, A., Gavrilova, J., Smirnova, J., Tõugu, V. & Palumaa, P. Zn(II) ions co-secreted with insulin suppress inherent amyloidogenic properties of monomeric insulin. *The Biochemical journal* **430,** 511–8. ISSN: 1470-8728 (2010).

73. Brange, J. & Langkjœr, L. in *Stability and Characterization of Protein and Peptide Drugs: Case Histories* (eds Wang, Y. J. & Pearlman, R.) 315–350 (Springer US, Boston, MA, 1993). ISBN: 978-1-4899-1236-7.

74. Nielsen, L. *et al.* Effect of Environmental Factors on the Kinetics of Insulin Fibril Formation: Elucidation of the Molecular Mechanism †. *Biochemistry* **40,** 6036–6046. ISSN: 0006-2960 (2001).

75. Whittingham, J. L. *et al.* Insulin at pH 2: structural analysis of the conditions promoting insulin fibre formation. *Journal of molecular biology* **318,** 479–90. ISSN: 0022-2836 (2002).

76. Librizzi, F. & Rischel, C. The kinetic behavior of insulin fibrillation is determined by heterogeneous nucleation pathways. *Protein science : a publication of the Protein Society* **14,** 3129–34. ISSN: 0961-8368 (2005).

77. Nayak, A., Sorci, M., Krueger, S. & Belfort, G. A universal pathway for amyloid nucleus and precursor formation for insulin. *Proteins: Structure, Function and Bioinformatics* **74,** 556–565. ISSN: 08873585 (2009).

78. Li, Z. *et al.* Solution fibre spinning technique for the fabrication of tuneable decellularised matrix-laden fibres and fibrous micromembranes. *Acta Biomaterialia* **78,** 111–122. ISSN: 18787568 (2018).

79. Noormägi, A., Valmsen, K., Tõugu, V. & Palumaa, P. Insulin Fibrillization at Acidic and Physiological pH Values is Controlled by Different Molecular Mechanisms. *The protein journal* **34,** 398–403. ISSN: 1875-8355 (2015).

80. Saha, S. & Deep, S. Glycerol inhibits the primary pathways and transforms the secondary pathway of insulin aggregation. *Phys. Chem. Chem. Phys.* **18,** 18934–18948. ISSN: 1463-9076 (2016).

81. Dzwolak, W. *et al.* Ethanol-perturbed amyloidogenic self-assembly of insulin: Looking for origins of amyloid strains. *Biochemistry* **44,** 8948–8958. ISSN: 00062960 (2005).

82. Dzwolak, W., Smirnovas, V., Jansen, R. & Winter, R. Insulin forms amyloid in a strain-dependent manner: an FT-IR spectroscopic study. *Protein science : a publication of the Protein Society* **13,** 1927–1932. ISSN: 0961-8368 (2004).

83. Dzwolak, W. *et al.* Template-controlled conformational patterns of insulin fibrillar self-assembly reflect history of solvation of the amyloid nuclei. *Physical chemistry chemical physics : PCCP* **7,** 1349–51. ISSN: 1463-9076 (2005).

84. Surmacz-Chwedoruk, W., Babenko, V. & Dzwolak, W. Master and slave relationship between two types of self-propagating insulin amyloid fibrils. *The journal of physical chemistry. B* **118,** 13582–9. ISSN: 1520-5207 (2014).

85. Surmacz-Chwedoruk, W., Babenko, V., Dec, R., Szymczak, P. & Dzwolak, W. The emergence of superstructural order in insulin amyloid fibrils upon multiple rounds of self-seeding. *Scientific Reports* **6,** 1–12. ISSN: 20452322 (2016).

86. Surmacz-Chwedoruk, W., Nieznańska, H., Wójcik, S. & Dzwolak, W. Cross-seeding of fibrils from two types of insulin induces new amyloid strains. *Biochemistry* **51,** 9460–9469. ISSN: 00062960 (2012).

87. Grudzielanek, S., Smirnovas, V. & Winter, R. Solvation-assisted pressure tuning of insulin fibrillation: from novel aggregation pathways to biotechnological applications. *Journal of molecular biology* **356,** 497–509. ISSN: 0022-2836 (2006).

88. Meisl, G. *et al.* Scaling behaviour and rate-determining steps in filamentous self-assembly. *Chemical science* **8,** 7087–7097. ISSN: 2041-6520 (2017).

89. Foderà, V., van de Weert, M. & Vestergaard, B. Large-scale polymorphism and auto-catalytic effect in insulin fibrillogenesis. *Soft Matter* **6,** 4413. ISSN: 1744-683X (2010).

90. Dische, F. E. *et al.* Insulin as an amyloid-fibril protein at sites of repeated insulin injections in a diabetic patient. *Diabetologia* **31,** 158–61. ISSN: 0012-186X (1988).

91. Uversky, V. N. Unusual biophysics of intrinsically disordered proteins. *Biochimica et Biophysica Acta (BBA) - Proteins and Proteomics* **1834.** The emerging dynamic view of proteins:Protein plasticity in allostery,evolution and self-assembly, 932 –951. ISSN: 1570-9639 (2013).

92. Uversky, V. N. A Protein-Chameleon: Conformational Plasticity of -Synuclein, a Disordered Protein Involved in Neurodegenerative Disorders. *Journal of Biomolecular Structure and Dynamics* **21.** PMID: 12956606, 211–234 (2003).

93. Cremades, N. *et al.* Direct observation of the interconversion of normal and toxic forms of α-synuclein. *Cell* **149,** 1048–1059. ISSN: 00928674 (2012).

94. Lee, J., Culyba, E. K., Powers, E. T. & Kelly, J. W. Amyloid-β forms fibrils by nucleated conformational conversion of oligomers. *Nature Chemical Biology* **7,** 602–609. ISSN: 15524469 (2011).

95. Eakin, C. M., Berman, A. J. & Miranker, A. D. A native to amyloidogenic transition regulated by a backbone trigger. *Nature Structural and Molecular Biology* **13,** 202–208. ISSN: 15459993 (2006).

96. Sekijima, Y. *et al.* The biological and chemical basis for tissue-selective amyloid disease. *Cell* **121,** 73–85. ISSN: 00928674 (2005).

97. Uversky, V. N., Li, J. & Fink, A. L. Evidence for a Partially Folded Intermediate in α-Synuclein Fibril Formation. *Journal of Biological Chemistry* **276,** 10737–10744. ISSN: 00219258 (2001).

98. Pease, L. F. I. *et al.* Probing the nucleus model for oligomer formation during insulin amyloid fibrillogenesis. *Biophysical journal* **99 12,** 3979–85 (2010).

99. Thakur, A. K. *et al.* Polyglutamine disruption of the huntingtin exon 1 N terminus triggers a complex aggregation mechanism. *Nature Structural and Molecular Biology* **16,** 380–389. ISSN: 15459993 (2009).

100. Morris, A. M., Watzky, M. A. & Finke, R. G. Protein aggregation kinetics, mechanism, and curve-fitting: A review of the literature. *Biochimica et Biophysica Acta (BBA) - Proteins and Proteomics* **1794,** 375 –397. ISSN: 1570-9639 (2009).

101. Jarrett, J. T. & Lansburry, P. T. Seeding "one dimensional cristallization" of amyloid: a pathogenic mechanism in Alzheimer's disease and scrapie? *Cell* **73,** 1055–1058. ISSN: 00928674 (1993).

102. Masel, J., Jansen, V. A. & Nowak, M. A. Quantifying the kinetic parameters of prion replication. *Biophysical Chemistry* **77,** 139 –152. ISSN: 0301-4622 (1999).

103. Serio, T. R. *et al.* Nucleated Conformational Conversion and the Replication of Conformational Information by a Prion Determinant. *Science* **289,** 1317–1321. ISSN: 0036-8075 (2000).

104. Chiti, F. & Dobson, C. M. Amyloid formation by globular proteins under native conditions. *Nature Chemical Biology* **5,** 15–22. ISSN: 15524469 (2009).

105. Michaels, T. C. T., Garcia, G. A. & Knowles, T. P. J. Asymptotic solutions of the Oosawa model for the length distribution of biofilaments. *The Journal of Chemical Physics* **140,** 194906 (2014).

106. Sunde, M. *et al.* Common core structure of amyloid fibrils by synchrotron X-ray diffraction. *Journal of Molecular Biology* **273,** 729–739. ISSN: 00222836 (1997).

107. Sunde, M. & Blake, C. in *Protein Misassembly* (eds Richards, F. M., Eisenberg, D. S. & Kim, P. S.) 123 –159 (Academic Press, 1997).

108. Maji, S. K., Wang, L., Greenwald, J. & Riek, R. Structure-activity relationship of amyloid fibrils. *FEBS letters* **583 16,** 2610–7 (2009).

109. Knowles, T. P. *et al.* Role of intermolecular forces in defining material properties of protein nanofibrils. *Science* **318,** 1900–1903. ISSN: 00368075 (2007).

110. Reynolds, N. P. *et al.* Competition between crystal and fibril formation in molecular mutations of amyloidogenic peptides. *Nature Communications* **8.** ISSN: 20411723 (2017).

111. Adamcik, J., Castelletto, V., Bolisetty, S., Hamley, I. W. & Mezzenga, R. Direct observation of time-resolved polymorphic states in the self-assembly of end-capped heptapeptides. *Angewandte Chemie - International Edition* **50,** 5495–5498. ISSN: 14337851 (2011).

112. Petkova, A. T., Yau, W. M. & Tycko, R. Experimental constraints on quaternary structure in Alzheimer's β-amyloid fibrils. *Biochemistry* **45,** 498–512. ISSN: 00062960 (2006).

113. Paravastu, A. K., Leapman, R. D., Yau, W.-M. & Tycko, R. Molecular structural basis for polymorphism in Alzheimer's beta-amyloid fibrils. *Proceedings of the National Academy of Sciences of the United States of America* **105,** 18349–54. ISSN: 1091-6490 (2008).

114. Wasmer, C. *et al.* Amyloid fibrils of the HET-s(218-289) prion form a beta solenoid with a triangular hydrophobic core. *Science (New York, N.Y.)* **319,** 1523–6. ISSN: 1095-9203 (2008).

115. Van Melckebeke, H. *et al.* Atomic-resolution three-dimensional structure of HET-s(218-289) amyloid fibrils by solid-state NMR spectroscopy. *Journal of the American Chemical Society* **132,** 13765–75. ISSN: 1520-5126 (2010).

116. Cobb, N. J. & Surewicz, W. K. Prion strains under the magnifying glass. *Nature structural & molecular biology* **14,** 882–884. ISSN: 1545-9993 (2007).

117. Bruce, M. E. Scrapie strain variation and mutation. *British medical bulletin* **49,** 822–38. ISSN: 0007-1420 (1993).

118. J.D.F., W. *et al.* Human prion protein with valine 129 prevents expression of variant CJD phenotype. *Science* **306,** 1793–1796. ISSN: 0036-8075 (2004).

119. Collinge, J. Prion strain mutation and selection. *Science* **328,** 1111–1112. ISSN: 00368075 (2010).

120. Pattison, I. & Millson, G. Scrapie Produced Experimentally in Goats With Special Reference To the Clinical Syndrome. *Journal of Comparative Pathology and Therapeutics* **71,** 101 –IN10. ISSN: 0368-1742 (1961).

121. Bessen, R. A. & Marsh, R. F. Biochemical and physical properties of the prion protein from two strains of the transmissible mink encephalopathy agent. *Journal of Virology* **66,** 2096–2101. ISSN: 0022-538X (1992).

122. Ghaemmaghami, S. *et al.* Conformational Transformation and Selection of Synthetic Prion Strains. *Journal of Molecular Biology* **413,** 527 –542. ISSN: 0022-2836 (2011).

123. Angers, R. C. *et al.* Prion strain mutation determined by prion protein conformational compatibility and primary structure. *Science* **328,** 1154–1158. ISSN: 00368075 (2010).

124. Colby, D. W. *et al.* Design and construction of diverse mammalian prion strains. *Proceedings of the National Academy of Sciences* **106,** 20417–20422. ISSN: 0027-8424 (2009).

125. Ayers, J. I. *et al.* The Strain-Encoded Relationship between PrPSc Replication, Stability and Processing in Neurons is Predictive of the Incubation Period of Disease. *PLOS Pathogens* **7,** 1–13 (Mar. 2011).

126. Giles K, Olson SH & Prusiner SB. Developing Therapeutics for PrP Prion Diseases. *Cold Spring Harbor perspectives in medicine* **7,** 4 (2017).

127. Petkova, A. T. Self-Propagating, Molecular-Level Polymorphism in Alzheimer's -Amyloid Fibrils. *Science* **307,** 262–265. ISSN: 0036-8075 (2005).

128. Qiang, W., Kelley, K. & Tycko, R. Polymorph-specific kinetics and thermodynamics of β-amyloid fibril growth. *Journal of the American Chemical Society* **135,** 6860–6871. ISSN: 00027863 (2013).

129. Lu, J. X. *et al.* Molecular structure of β-amyloid fibrils in alzheimer's disease brain tissue. *Cell* **154,** 1257. ISSN: 10974172 (2013).

130. Kodali, R., Williams, A. D., Chemuru, S. & Wetzel, R. A(1–40) Forms Five Distinct Amyloid Structures whose -Sheet Contents and Fibril Stabilities Are Correlated. *Journal of Molecular Biology* **401,** 503 –517. ISSN: 0022-2836 (2010).

131. Jeong, J. S., Ansaloni, A., Mezzenga, R., Lashuel, H. A. & Dietler, G. Novel mechanistic insight into the molecular basis of amyloid polymorphism and secondary nucleation during amyloid formation. *Journal of Molecular Biology* **425,** 1765–1781. ISSN: 00222836 (2013).

132. Cohen, M. L. *et al.* Rapidly progressive Alzheimer's disease features distinct structures of amyloid-β. *Brain* **138,** 1009–1022. ISSN: 14602156 (2015).

133. Cohen, M., Appleby, B. & Safar, J. G. Distinct prion-like strains of amyloid beta implicated in phenotypic diversity of Alzheimer's disease. *Prion* **10,** 9–17. ISSN: 1933690X (2016).

134. Bousset, L. *et al.* Structural and functional characterization of two alpha-synuclein strains. *Nature Communications* **4.** ISSN: 20411723 (2013).

135. Peelaerts, W. *et al.* α-Synuclein strains cause distinct synucleinopathies after local and systemic administration. *Nature* **522,** 340–344. ISSN: 14764687 (2015).

136. Gath, J. *et al.* Unlike twins: An NMR comparison of two α-synuclein polymorphs featuring different toxicity. *PLoS ONE* **9,** 1–11. ISSN: 19326203 (2014).

137. Gath, J. *et al.* Yet another polymorph of α-synuclein: solid-state sequential assignments. *Biomolecular NMR Assignments* **8,** 395–404. ISSN: 1874270X (2014).

138. Tuttle, M. D. *et al.* Solid-state NMR structure of a pathogenic fibril of full-length human α-synuclein. *Nature Structural & Molecular Biology* **23,** 409–415. ISSN: 1545-9993 (2016).

139. Kaufman, S. K. *et al.* Tau Prion Strains Dictate Patterns of Cell Pathology, Progression Rate, and Regional Vulnerability In Vivo. *Neuron* **92,** 796–812. ISSN: 10974199 (2016).

140. Narasimhan, S. *et al.* Pathological Tau Strains from Human Brains Recapitulate the Diversity of Tauopathies in Nontransgenic Mouse Brain. *The Journal of Neuroscience* **37,** 11406–11423. ISSN: 0270-6474 (2017).

141. Guo, J. L. *et al.* Unique pathological tau conformers from Alzheimer's brains transmit tau pathology in nontransgenic mice. *The Journal of Experimental Medicine* **213,** 2635–2654. ISSN: 0022-1007 (2016).

142. Nielsen, L., Frokjaer, S., Carpenter, J. F. & Brange, J. Studies of the structure of insulin fibrils by Fourier transform infrared (FTIR) spectroscopy and electron microscopy. *Journal of Pharmaceutical Sciences* **90,** 29–37. ISSN: 00223549 (2001).

143. Bidhendi, E. E. *et al.* Two superoxide dismutase prion strains transmit amyotrophic lateral sclerosis–like disease. *Journal of Clinical Investigation* **126,** 2249–2253. ISSN: 0021-9738 (2016).

144. Bergh, J. *et al.* Structural and kinetic analysis of protein-aggregate strains in vivo using binary epitope mapping. *Proceedings of the National Academy of Sciences* **112,** 4489–4494. ISSN: 0027-8424 (2015).

145. Dill, K. A. & Chan, H. S. From Levinthal to pathways to funnels. *Nature Structural & Molecular Biology* **4,** 10–19. ISSN: 1545-9993 (1997).

146. Gsponer, J. & Vendruscolo, M. Theoretical Approaches to Protein Aggregation. *Protein & Peptide Letters* **13,** 287–293. ISSN: 09298665 (2006).

147. Hartl, F. U. & Hayer-Hartl, M. Converging concepts of protein folding in vitro and in vivo. *Nature Structural and Molecular Biology* **16,** 574–581. ISSN: 15459993 (2009).

148. Balchin, D., Hayer-Hartl, M. & Hartl, F. U. In vivo aspects of protein folding and quality control. *Science* **353.** ISSN: 0036-8075 (2016).

149. Baldwin, A. J. *et al.* Metastability of Native Proteins and the Phenomenon of Amyloid Formation. *Journal of the American Chemical Society* **133,** 14160–14163. ISSN: 0002-7863 (2011).

150. Eichner, T., Kalverda, A. P., Thompson, G. S., Homans, S. W. & Radford, S. E. Conformational Conversion during Amyloid Formation at Atomic Resolution. *Molecular Cell* **41,** 161–172. ISSN: 10972765 (2011).

151. Jaunmuktane, Z. & Brandner, S. Transmissible human proteopathies: an expanding field. *Diagnostic Histopathology* **25,** 16–22. ISSN: 18767621 (2019).

152. Brandner, S. & Jaunmuktane, Z. Prion disease: experimental models and reality. *Acta Neuropathologica* **133,** 197–222. ISSN: 14320533 (2017).

153. Caughey, B. & Baron, G. S. Prions and their partners in crime. *Nature* **443,** 803–810. ISSN: 0028-0836 (2006).

154. Gajdusek, D. Unconventional viruses and the origin and disappearance of kuru. *Science* **197,** 943–960. ISSN: 0036-8075 (1977).

155. Glasse, R. Cannibalism in the Kuru region of New Guinea. *Transactions of the New York Academy of Sciences* **29,** 748–54 (May 1967).

156. Koch, T. K., Berg, B. O., De Armond, S. J. & Gravina, R. F. Creutzfeldt–Jakob Disease in a Young Adult with Idiopathic Hypopituitarism. *New England Journal of Medicine* **313.** PMID: 3897861, 731–733 (1985).

157. Frontzek, K. *et al.* Iatrogenic and sporadic Creutzfeldt-Jakob disease in two sisters without mutation in the prion protein gene. *Prion* **6896,** 00–00. ISSN: 1933-6896 (2015).

158. Spencer, M. D., Knight, R. S. G. & Will, R. G. First hundred cases of variant Creutzfeldt-Jakob disease: retrospective case note review of early psychiatric and neurological features. *BMJ* **324,** 1479–1482. ISSN: 0959-8138 (2002).

159. Will, R. *et al.* A new variant of Creutzfeldt-Jakob disease in the UK. *The Lancet* **347,** 921 –925. ISSN: 0140-6736 (1996).

160. Chazot, G. *et al.* New variant of Creutzfeldt-Jakob disease in a 26-year-old French man. *The Lancet* **347,** 1181. ISSN: 0140-6736 (1996).

161. Surewicz, W. K. & Apostol, M. I. in *Prion Proteins* (ed Tatzelt, J.) 135–167 (Springer Berlin Heidelberg, Berlin, Heidelberg, 2011). ISBN: 978-3-642-24067-6.

162. Tanaka, M., Collins, S. R., Toyama, B. H. & Weissman, J. S. The physical basis of how prion conformations determine strain phenotypes. *Nature* **442,** 585–589. ISSN: 14764687 (2006).

163. Osherovich, L. Z. & Weissman, J. S. The Utility of Prions. *Developmental Cell* **2,** 143 –151. ISSN: 1534-5807 (2002).

164. Uptain, S. M. & Lindquist, S. Prions as Protein-Based Genetic Elements. *Annual Review of Microbiology* **56.** PMID: 12142498, 703–741 (2002).

165. Padrick, S. B. & Miranker, A. D. Islet Amyloid: Phase Partitioning and Secondary Nucleation Are Central to the Mechanism of Fibrillogenesis. *Biochemistry* **41.** PMID: 11926832, 4694–4703 (2002).

166. Ramachandran, G. & Udgaonkar, J. B. Evidence for the Existence of a Secondary Pathway for Fibril Growth during the Aggregation of Tau. *Journal of Molecular Biology* **421.** Amyloid Structure, Function, and Molecular Mechanisms (Part I), 296 –314. ISSN: 0022-2836 (2012).

167. Buell, A. K. *et al.* Solution conditions determine the relative importance of nucleation and growth processes in -synuclein aggregation. *Proceedings of the National Academy of Sciences* **111,** 7671–7676. ISSN: 0027-8424 (2014).

168. Hu, M. & Robertson, N. P. Transmissible amyloid protein: evidence from iatrogenic CJD. *Journal of Neurology* **265,** 1726–1729. ISSN: 0340-5354 (2018).

169. Saelices, L. *et al.* Amyloid seeding of transthyretin by ex vivo cardiac fibrils and its inhibition. *Proceedings of the National Academy of Sciences* **115,** E6741–E6750. ISSN: 0027-8424 (2018).

170. Olsson, T. T., Klementieva, O. & Gouras, G. K. Prion-like seeding and nucleation of intracellular amyloid-β. *Neurobiology of Disease* **113,** 1–10. ISSN: 1095953X (2018).

171. Mathias Jucker & Lary C. Walker. Self-propagation of pathogenic protein aggregates in neurodegenerative diseases. *Nature* **501,** 45–51 (2013).

172. Frontzek, K, Lutz, M., Aguzzi, A, Kovacs, G. & Budka, H. Amyloid-β pathology and cerebral amyloid angiopathy are frequent in iatrogenic Creutzfeldt-Jakob disease after dural grafting. *Swiss Medical Weekly,* 1–5. ISSN: 1424-7860 (2016).

173. Smethurst, P. *et al.* In vitro prion-like behaviour of TDP-43 in ALS. *Neurobiology of Disease* **96,** 236 –247. ISSN: 0969-9961 (2016).

174. Li, J. Y. *et al.* Lewy bodies in grafted neurons in subjects with Parkinson's disease suggest host-to-graft disease propagation. *Nature Medicine* **14,** 501–503. ISSN: 10788956 (2008).

175. Kordower, J. H., Chu, Y., Hauser, R. A., Olanow, C. & Freeman, T. B. Transplanted dopaminergic neurons develop PD pathologic changes: A second case report. *Movement Disorders* **23,** 2303–2306.

176. Jaunmuktane, Z. *et al.* Evidence for human transmission of amyloid-β pathology and cerebral amyloid angiopathy. *Nature* **525,** 247–50. ISSN: 1476-4687 (2015).

177. Holmes, B. B. *et al.* Heparan sulfate proteoglycans mediate internalization and propagation of specific proteopathic seeds. *Proceedings of the National Academy of Sciences* **110,** E3138–E3147. ISSN: 0027-8424 (2013).

178. Sanders, D. W. *et al.* Distinct Tau Prion Strains Propagate in Cells and Mice and Define Different Tauopathies. *Neuron* **82,** 1271 – 1288. ISSN: 0896-6273 (2014).

179. Lee, H.-J., Patel, S. & Lee, S.-J. Intravesicular Localization and Exocytosis of -Synuclein and its Aggregates. *Journal of Neuroscience* **25,** 6016–6024. ISSN: 0270-6474 (2005).

180. Kfoury, N., Holmes, B. B., Jiang, H., Holtzman, D. M. & Diamond, M. I. Trans-cellular propagation of Tau aggregation by fibrillar species. *Journal of Biological Chemistry* **287,** 19440–19451. ISSN: 00219258 (2012).

181. Porto-Carreiro, I., Février, B., Paquet, S., Vilette, D. & Raposo, G. Prions and exosomes: From PrPc trafficking to PrPsc propagation. *Blood Cells, Molecules, and Diseases* **35.** Including Workshop on Exosomes: Part III, 143 –148. ISSN: 1079-9796 (2005).

182. Vella, L. J., Sharples, R. A., Nisbet, R. M., Cappai, R. & Hill, A. F. The role of exosomes in the processing of proteins associated with neurodegenerative diseases. *European Biophysics Journal* **37,** 323–332. ISSN: 1432-1017 (2008).

183. Ren, P. H. *et al.* Cytoplasmic penetration and persistent infection of mammalian cells by polyglutamine aggregates. *Nature Cell Biology* **11,** 219–225. ISSN: 14657392 (2009).

184. Münch, C., O'Brien, J. & Bertolotti, A. Prion-like propagation of mutant superoxide dismutase-1 misfolding in neuronal cells. *Proceedings of the National Academy of Sciences* **108,** 3548–3553. ISSN: 0027-8424 (2011).

185. Domert, J. *et al.* Spreading of amyloid- peptides via neuritic cell-to-cell transfer is dependent on insufficient cellular clearance. *Neurobiology of Disease* **65,** 82 –92. ISSN: 0969-9961 (2014).

186. Frost, B., Jacks, R. L. & Diamond, M. I. Propagation of Tau misfolding from the outside to the inside of a cell. *Journal of Biological Chemistry* **284,** 12845–12852. ISSN: 00219258 (2009).

187. Hansen, C. *et al.* -Synuclein propagates from mouse brain to grafted dopaminergic neurons and seeds aggregation in cultured human cells. *The Journal of Clinical Investigation* **121,** 715–725 (Feb. 2011).

188. Desplats, P. *et al.* Inclusion formation and neuronal cell death through neuron-to-neuron transmission of alpha-synuclein. *Proceedings of the National Academy of Sciences of the United States of America* **106,** 13010–5. ISSN: 1091-6490 (2009).

189. Sardar Sinha, M. *et al.* Alzheimer's disease pathology propagation by exosomes containing toxic amyloid-beta oligomers. *Acta Neuropathologica* **136,** 41–56. ISSN: 1432-0533 (2018).

190. Gustafsson, G. *et al.* Secretion and Uptake of α-Synuclein Via Extracellular Vesicles in Cultured Cells. *Cellular and Molecular Neurobiology* **38,** 1539–1550. ISSN: 1573-6830 (2018).

191. Gousset, K. & Zurzolo, C. Tunnelling nanotubes. *Prion* **3,** 94–98. ISSN: 1933-6896 (2009).

192. Abounit, S., Wu, J. W., Duff, K., Victoria, G. S. & Zurzolo, C. Tunneling nanotubes: A possible highway in the spreading of tau and other prion-like proteins in neurodegenerative diseases. *Prion* **10.** PMID: 27715442, 344–351 (2016).

193. Biancalana, M. & Koide, S. Molecular mechanism of Thioflavin-T binding to amyloid fibrils. *Biochimica et biophysica acta* **1804,** 1405–12. ISSN: 0006-3002 (2010).

194. Amdursky, N., Erez, Y. & Huppert, D. Molecular rotors: what lies behind the high sensitivity of the thioflavin-T fluorescent marker. *Accounts of chemical research* **45,** 1548–57. ISSN: 1520-4898 (2012).

195. Cohen, S. I. A., Vendruscolo, M., Dobson, C. M. & Knowles, T. P. J. From macroscopic measurements to microscopic mechanisms of protein aggregation. *Journal of Molecular Biology* **421,** 160–171. ISSN: 00222836 (2012).

196. Arosio, P., Cukalevski, R., Frohm, B., Knowles, T. P. J. & Linse, S. Quantification of the concentration of Aβ42 propagons during the lag phase by an amyloid chain reaction assay. *Journal of the American Chemical Society* **136,** 219–25. ISSN: 1520-5126 (2014).

197. Aprile, F. A. *et al.* Inhibition of α-Synuclein Fibril Elongation by Hsp70 Is Governed by a Kinetic Binding Competition between α-Synuclein Species. *Biochemistry* **56,** 1177–1180. ISSN: 15204995 (2017).

198. Aprile, F. A. *et al.* Selective targeting of primary and secondary nucleation pathways in Aβ42 aggregation using a rational antibody scanning method. *Science Advances* **3,** e1700488. ISSN: 2375-2548 (2017).

199. Habchi, J. *et al.* Cholesterol catalyses Aβ42 aggregation through a heterogeneous nucleation pathway in the presence of lipid membranes. *Nature Chemistry* **10,** 673–683. ISSN: 17554349 (2018).

200. Stuart, B. H. *Infrared Spectroscopy: Fundamentals and Applications* 1–224. ISBN: 9780470011140 (2005).

201. Kong, J. & Yu, S. Fourier transform infrared spectroscopic analysis of protein secondary structures. *Acta Biochimica et Biophysica Sinica* **39,** 549–559. ISSN: 16729145 (2007).

202. Sarroukh, R., Goormaghtigh, E., Ruysschaert, J. M. & Raussens, V. ATR-FTIR: A "rejuvenated" tool to investigate amyloid proteins. *Biochimica et Biophysica Acta - Biomembranes* **1828,** 2328–2338. ISSN: 00052736 (2013).

203. Barth, A. Infrared spectroscopy of proteins. **1767,** 1073–1101 (2007).

204. Moran, S. D. & Zanni, M. T. How to get insight into amyloid structure and formation from infrared spectroscopy. *Journal of Physical Chemistry Letters* **5,** 1984–1993. ISSN: 19487185 (2014).

205. Glasoe, P. K. & Long, F. A. Use of glass electrodes to measure acidities in deuterium oxide 1,2. *The Journal of Physical Chemistry* **64,** 188–190. ISSN: 0022-3654 (1960).

206. Bundi, A. & Wüthrich, K. 1H-nmr parameters of the common amino acid residues measured in aqueous solutions of the linear tetrapeptides H-Gly-Gly-X-L-Ala-OH. *Biopolymers* **18,** 285–297. ISSN: 10970282 (1979).

207. Sarroukh, R. *et al.* Transformation of amyloid β(1-40) oligomers into fibrils is characterized by a major change in secondary structure. *Cellular and molecular life sciences : CMLS* **68,** 1429–38. ISSN: 1420-9071 (2011).

208. Hölscher, H., Falter, J. & Schirmeisen, A. in *Characterization of Materials* 9, 2191–2197 (John Wiley & Sons, Inc., Hoboken, NJ, USA, 2012).

209. Dufrêne, Y. F. *et al.* Imaging modes of atomic force microscopy for application in molecular and cell biology. *Nature Nanotechnology* **12,** 295–307. ISSN: 1748-3387 (2017).

210. Yacoot, A. & Koenders, L. Aspects of scanning force microscope probes and their effects on dimensional measurement. *Journal of Physics D: Applied Physics* **41.** ISSN: 00223727 (2008).

211. Zhong, Q., Inniss, D., Kjoller, K. & Elings, V. Fractured polymer/silica fiber surface studied by tapping mode atomic force microscopy. *Surface Science* **290,** L688 –L692. ISSN: 0039-6028 (1993).

212. Chang, K. C., Chiang, Y. W., Yang, C. H. & Liou, J. W. Atomic force microscopy in biology and biomedicine. *Tzu Chi Medical Journal* **24,** 162–169. ISSN: 10163190 (2012).

213. Goldsbury, C. S., Scheuring, S. & Kreplak, L. in *Current Protocols in Protein Science* November, 17.7.1–17.7.19 (John Wiley & Sons, Inc., Hoboken, NJ, USA, 2009). ISBN: 0471140864.

214. Drolle, E., Hane, F., Lee, B. & Leonenko, Z. Atomic force microscopy to study molecular mechanisms of amyloid fibril formation and toxicity in Alzheimer's disease. *Drug Metabolism Reviews* **46,** 207–223. ISSN: 10979883 (2014).

215. Qamar, S. *et al.* FUS phase peparation is modulated by a molecular chaperone and methylation of arginine cation-π interactions. *Cell* **173,** 720–734.e15. ISSN: 00928674 (2018).

216. Ruggeri, F. S. *et al.* Influence of the β-sheet content on the mechanical properties of aggregates during amyloid fibrillization. *Angewandte Chemie - International Edition* **54,** 2462–2466. ISSN: 15213773 (2015).

217. Ruggeri, F. S. *et al.* Identification and nanomechanical characterization of the fundamental single-strand protofilaments of amyloid α-synuclein fibrils. *Proceedings of the National Academy of Sciences,* 201721220. ISSN: 0027-8424 (2018).

218. Sokolov, D. V. in *Methods in molecular biology (Clifton, N.J.)* 323–367 (2013). ISBN: 978-1-62703-353-4.

219. Sweers, K. K., Stöckl, M., Bennink, M. L. & Subramaniam, V. in *Bio-nanoimaging* 309–322 (Elsevier, 2014). ISBN: 9780123944313.

220. Khalaf, O. *et al.* The H50Q mutation enhances α-synuclein aggregation, secretion, and toxicity. *Journal of Biological Chemistry* **289,** 21856–21876. ISSN: 1083351X (2014).

221. Ansaloni, A. *et al.* One-pot semisynthesis of exon 1 of the huntingtin protein: New tools for elucidating the role of posttranslational modifications in the pathogenesis of Huntington's disease. *Angewandte Chemie - International Edition* **53,** 1928–1933. ISSN: 14337851 (2014).

222. Hong, D. P., Han, S., Fink, A. L. & Uversky, V. N. Characterization of the non-fibrillar α-synuclein oligomers. *Protein and Peptide Letters* **18,** 230–240 (2011).

223. Hoyer, W., Cherny, D., Subramaniam, V. & Jovin, T. M. Rapid self-assembly of α-synuclein observed by in situ atomic force microscopy. *Journal of Molecular Biology* **340,** 127–139. ISSN: 00222836 (2004).

224. Adamcik, J. *et al.* Understanding amyloid aggregation by statistical analysis of atomic force microscopy images. *Nature Nanotechnology* **5,** 423–428. ISSN: 1748-3387 (2010).

225. Fändrich, M. On the structural definition of amyloid fibrils and other polypeptide aggregates. *Cellular and Molecular Life Sciences* **64,** 2066–2078. ISSN: 1420682X (2007).

226. Kad, N. M. *et al.* Hierarchical assembly of beta2-microglobulin amyloid in vitro revealed by atomic force microscopy. *Journal of molecular biology* **330,** 785–797. ISSN: 00222836 (2003).

227. Khurana, R *et al.* A general model for amyloid fibril assembly based on morphological studies using atomic force microscopy. *Biophys.J.* **85,** 1135–1144. ISSN: 00063495 (2003).

228. Knowles, T. P., Smith, J. F., Craig, A., Dobson, C. M. & Welland, M. E. Spatial persistence of angular correlations in amyloid fibrils. *Physical Review Letters* **96,** 1–4. ISSN: 00319007 (2006).

229. Watanabe-Nakayama, T. *et al.* High-speed atomic force microscopy reveals structural dynamics of amyloid β _{1–42} aggregates. *Proceedings of the National Academy of Sciences* **113,** 5835–5840. ISSN: 0027-8424 (2016).

230. Blackley, H. K. *et al.* In-situ atomic force microscopy study of β-amyloid fibrillization. *Journal of Molecular Biology* **298,** 833–840. ISSN: 00222836 (2000).

231. Goldsbury, C., Frey, P., Olivieri, V., Aebi, U. & Müller, S. A. Multiple assembly pathways underlie amyloid-beta fibril polymorphisms. *Journal of molecular biology* **352,** 282–98. ISSN: 0022-2836 (2005).

232. Hasecke, F. *et al.* Origin of metastable oligomers and their effects on amyloid fibril self-assembly. *Chemical Science* **9,** 5937–5948. ISSN: 2041-6520 (2018).

233. Lin, Y. C., Li, C. & Fakhraai, Z. Kinetics of surface-mediated fibrillization of amyloid-β (12-28) peptides. *Langmuir* **34,** 4665–4672. ISSN: 15205827 (2018).

234. Mastrangelo, I. A. *et al.* High-resolution atomic force microscopy of soluble Aβ42 oligomers. *Journal of Molecular Biology* **358,** 106–119. ISSN: 00222836 (2006).

235. Bieschke, J. *et al.* EGCG remodels mature α-synuclein and amyloid-β fibrils and reduces cellular toxicity. *Proceedings of the National Academy of Sciences* **107,** 7710–7715. ISSN: 0027-8424 (2010).

236. Iljina, M. *et al.* Nanobodies raised against monomeric α-synuclein inhibit fibril formation and destabilize toxic oligomeric species. *BMC Biology* **15,** 1–14. ISSN: 17417007 (2017).

237. Kakinen, A. *et al.* Nanoscale inhibition of polymorphic and ambidextrous IAPP amyloid aggregation with small molecules. *Nano Research* **11,** 3636–3647. ISSN: 19980000 (2018).

238. Orsini, F., Ami, D., Lascialfari, A. & Natalello, A. Inhibition of lysozyme fibrillogenesis by hydroxytyrosol and dopamine: An Atomic Force Microscopy study. *International Journal of Biological Macromolecules* **111,** 1100–1105. ISSN: 18790003 (2018).

239. Ryu, J., Kanapathipillai, M., Lentzen, G. & Park, C. B. Inhibition of β-amyloid peptide aggregation and neurotoxicity by α-d-mannosylglycerate, a natural extremolyte. *Peptides* **29,** 578–584. ISSN: 01969781 (2008).

240. Murray, A. N., Palhano, F. L., Bieschke, J. & Kelly, J. W. Surface adsorption considerations when working with amyloid fibrils in multiwell plates and Eppendorf tubes. *Protein Science* **22,** 1531–1541. ISSN: 09618368 (2013).

241. Risor, M. W. *et al.* Critical Influence of cosolutes and surfaces on the assembly of serpin-derived amyloid fibrils. *Biophysical Journal* **113,** 580 –596. ISSN: 0006-3495 (2017).

242. Vácha, R., Linse, S. & Lund, M. Surface effects on aggregation kinetics of amyloidogenic peptides. *Journal of the American Chemical Society* **136,** 11776–11782. ISSN: 15205126 (2014).

243. Arosio, P. *et al.* Kinetic analysis reveals the diversity of microscopic mechanisms through which molecular chaperones suppress amyloid formation. *Nature Communications* **7,** 10948. ISSN: 2041-1723 (2016).

244. Šneideris, T. *et al.* Looking for a generic inhibitor of amyloid-like fibril formation among flavone derivatives. *PeerJ* **3,** e1271. ISSN: 2167-8359 (2015).

245. Milto, K., Michailova, K. & Smirnovas, V. Elongation of mouse prion protein amyloid-like fibrils: Effect of temperature and denaturant concentration. *PLoS ONE* **9,** 1–5. ISSN: 19326203 (2014).

246. Hellstrand, E., Boland, B., Walsh, D. M. & Linse, S. Amyloid β-protein aggregation produces highly reproducible kinetic data and occurs by a two-phase process. *ACS chemical neuroscience* **1,** 13–8. ISSN: 1948-7193 (2010).

247. Ruggeri, F. S. *et al.* Nanoscale studies link amyloid maturity with polyglutamine diseases onset. *Scientific Reports* **6,** 1–11. ISSN: 20452322 (2016).

248. McKoy, A. F., Chen, J., Schupbach, T. & Hecht, M. H. A novel inhibitor of amyloid β (Aβ) peptide aggregation: from high throughput screening to efficacy in an animal model of Alzheimer disease. *The Journal of biological chemistry* **287,** 38992–9000. ISSN: 1083-351X (2012).

249. Noor, H., Cao, P. & Raleigh, D. P. Morin hydrate inhibits amyloid formation by islet amyloid polypeptide and disaggregates amyloid fibers. *Protein Science* **21,** 373–382. ISSN: 09618368 (2012).

250. Habchi, J. *et al.* Systematic development of small molecules to inhibit specific microscopic steps of Aβ42 aggregation in Alzheimer's disease. *Proceedings of the National Academy of Sciences* **114,** E200–E208. ISSN: 0027-8424 (2017).

251. Mahdavimehr, M. *et al.* Inhibition of HEWL fibril formation by taxifolin: Mechanism of action. *PLoS ONE* **12,** 9–11. ISSN: 19326203 (2017).

252. Malisauskas, R., Botyriute, A., Cannon, J. G. & Smirnovas, V. Flavone Derivatives as Inhibitors of Insulin Amyloid-Like Fibril Formation. *Plos One* **10,** 1–14. ISSN: 1932-6203 (2015).

253. Kurnik, M. *et al.* Potent α-Synuclein Aggregation Inhibitors, Identified by High-Throughput Screening, Mainly Target the Monomeric State. *Cell Chemical Biology* **25,** 1389–1402.e9. ISSN: 24519448 (2018).

254. Waugh, D. F., Wilhelmson, D. F., Commerford, S. L. & Sackler, M. L. Studies of the Nueleation and Growth Reactions of Selected Types of Insulin Fibrils. *Journal of the American Chemical Society* **75,** 2592–2600. ISSN: 15205126 (1953).

255. Kurouski, D., Dukor, R. K., Lu, X., Nafie, L. A. & Lednev, I. K. Normal and reversed supramolecular chirality of insulin fibrils probed by vibrational circular dichroism at the protofilament level of fibril structure. *Biophysical Journal* **103,** 522–531. ISSN: 00063495 (2012).

256. Kurouski, D., Lombardi, R. A., Dukor, R. K., Lednev, I. K. & Nafie, L. A. Direct observation and pH control of reversed supramolecular chirality in insulin fibrils by vibrational circular dichroism. *Chemical Communications* **46,** 7154–7156. ISSN: 13597345 (2010).

257. Kurouski, D., Dukor, R. K., Lu, X., Nafie, L. A. & Lednev, I. K. Spontaneous inter-conversion of insulin fibril chirality. *Chemical Communications* **48,** 2837–2839. ISSN: 1364548X (2012).

258. Bryant, C. *et al.* Acid stabilization of insulin. *Biochemistry* **32,** 8075–8082. ISSN: 0006-2960 (1993).

259. Nielsen, L., Frokjaer, S., Brange, J., Uversky, V. N. & Fink, A. L. Probing the mechanism of insulin fibril formation with insulin mutants. *Biochemistry* **40,** 8397–8409. ISSN: 00062960 (2001).

260. Nettleton, E. J. *et al.* Characterization of the Oligomeric States of Insulin in Self-Assembly and Amyloid Fibril Formation by Mass Spectrometry. *Biophysical Journal* **79,** 1053–1065. ISSN: 00063495 (2000).

261. Millican, R. L. & Brems, D. N. Equilibrium Intermediates in the Denaturation of Human Insulin and Two Monomeric Insulin Analogs. *Biochemistry* **33,** 1116–1124. ISSN: 0006-2960 (1994).

262. Banga, A. *Therapeutic Peptides and Proteins* 2nd ed. ISBN: 978-0-8493-1630-2 (CRC Press, 2005).

263. Arosio, P., Vendruscolo, M., Dobson, C. M. & Knowles, T. P. J. Chemical kinetics for drug discovery to combat protein aggregation diseases. *Trends in Pharmacological Sciences* **35,** 127–135. ISSN: 01656147 (2014).

264. Makhatadze, G. I., Clore, G. M. & Gronenborn, A. M. Solvent isotope effect and protein stability. *Nature structural biology* **2,** 852–5. ISSN: 1072-8368 (1995).

265. Smirnovas, V. & Winter, R. Revealing Different Aggregation Pathways of Amyloidogenic Proteins by Ultrasound Velocimetry. *Biophysical Journal* **94,** 3241–3246. ISSN: 00063495 (2008).

266. Hasecke, F. *et al.* Origin of metastable oligomers and their effects on amyloid fibril self-assembly. *Chemical Science* **9,** 5937–5948. ISSN: 20416539 (2018).

267. Miti, T., Mulaj, M., Schmit, J. D. & Muschol, M. Stable, metastable, and kinetically trapped amyloid aggregate phases. *Biomacromolecules* **16,** 326–35. ISSN: 1526-4602 (2015).

268. Babenko, V., Surmacz-Chwedoruk, W. & Dzwolak, W. On the function and fate of chloride ions in amyloidogenic self-assembly of insulin in an acidic environment: Salt-induced condensation of fibrils. *Langmuir* **31,** 2180–2186. ISSN: 15205827 (2015).

269. Selivanova, O. M. *et al.* How to determine the size of folding nuclei of protofibrils from the concentration dependence of the rate and lag-time of Aggregation. II. Experimental application for insulin and LysPro insulin: Aggregation morphology, kinetics, and sizes of nuclei. *Journal of Physical Chemistry B* **118,** 1198–1206. ISSN: 15206106 (2014).

270. Sneideris, T. *et al.* The Environment Is a Key Factor in Determining the Anti-Amyloid Efficacy of EGCG. *Biomolecules* **9,** 1–17. ISSN: 2218273X (2019).

271. Castellani, R. J., Plascencia-Villa, G. & Perry, G. The amyloid cascade and Alzheimer's disease therapeutics: theory versus observation. *Laboratory Investigation.* ISSN: 15300307 (2019).

272. Porat, Y., Abramowitz, A. & Gazit, E. Inhibition of amyloid fibril formation by polyphenols: Structural similarity and aromatic interactions as a common inhibition mechanism. *Chemical Biology and Drug Design* **67,** 27–37. ISSN: 17470277 (2006).

273. Mangialasche, F., Solomon, A., Winblad, B., Mecocci, P. & Kivipelto, M. Alzheimer's disease: clinical trials and drug development. *The Lancet Neurology* **9,** 702–716. ISSN: 14744422 (2010).

274. Molino, S. *et al.* Polyphenols in dementia: From molecular basis to clinical trials. *Life Sciences* **161,** 69–77. ISSN: 18790631 (2016).

275. Goyal, D., Shuaib, S., Mann, S. & Goyal, B. Rationally Designed Peptides and Peptidomimetics as Inhibitors of Amyloid-β (Aβ) Aggregation: Potential Therapeutics of Alzheimer's Disease. *ACS Combinatorial Science* **19,** 55–80. ISSN: 21568944 (2017).

276. Stefani, M. & Rigacci, S. Protein folding and aggregation into amyloid: The interference by natural phenolic compounds. *International Journal of Molecular Sciences* **14,** 12411–12457. ISSN: 14220067 (2013).

277. Mehta, D., Jackson, R., Paul, G., Shi, J. & Sabbagh, M. Why do trials for Alzheimer's disease drugs keep failing? A discontinued drug perspective for 2010-2015. *Expert Opinion on Investigational Drugs* **26,** 735–739. ISSN: 17447658 (2017).

278. Mathur, S., Dewitte, S., Robledo, I., Isaacs, T. & Stamford, J. Rising to the challenges of clinical trial improvement in Parkinson's disease. *Journal of Parkinson's Disease* **5,** 263–268. ISSN: 1877718X (2015).

279. Athauda, D. & Foltynie, T. Challenges in detecting disease modification in Parkinson's disease clinical trials. *Parkinsonism and Related Disorders* **32,** 1–11. ISSN: 18735126 (2016).

280. Al-Ansari, A. & Robertson, N. P. Creutzfeldt–Jacob disease: new directions in diagnosis and therapeutics. *Journal of Neurology* **264,** 1029–1031. ISSN: 0340-5354 (2017).

281. Yaari, R. & Hake, A. Alzheimer's disease clinical trials: past failures and future opportunities. *Clinical Investigation* **5,** 297–309. ISSN: 2041-6792 (2015).

282. Cummings, J. L., Morstorf, T. & Zhong, K. Alzheimer's disease drug-development pipeline: few candidates, frequent failures. en. *Alzheimer's research & therapy* **6,** 37. ISSN: 1758-9193 (2014).

283. Wei, Y. *et al.* Certain (-)-epigallocatechin-3-gallate (EGCG) auto-oxidation products (EAOPs) retain the cytotoxic activities of EGCG. *Food Chemistry* **204,** 218–226. ISSN: 18737072 (2016).

284. An, T. T., Feng, S. & Zeng, C. M. Oxidized epigallocatechin gallate inhibited lysozyme fibrillation more strongly than the native form. *Redox Biology* **11,** 315–321. ISSN: 22132317 (2017).

285. Palhano, F. L., Lee, J., Grimster, N. P. & Kelly, J. W. Toward the Molecular Mechanism(s) by Which EGCG Treatment Remodels Mature Amyloid Fibrils. *Journal of the American Chemical Society* **135,** 7503–7510. ISSN: 0002-7863 (2013).

286. Liu, Y. *et al.* Structural characteristics of (-)-epigallocatechin-3-gallate inhibiting amyloid Aβ42 aggregation and remodeling amyloid fibers. *RSC Advances* **5,** 62402–62413. ISSN: 20462069 (2015).

287. Zhao, J. *et al.* (-)-Epigallocatechin-3-gallate (EGCG) inhibits fibrillation, disaggregates amyloid fibrils of α-synuclein, and protects PC12 cells against α-synuclein-induced toxicity. *RSC Advances* **7,** 32508–32517. ISSN: 20462069 (2017).

288. Qing, H. *et al.* Epigallocatechin Gallate (EGCG) Inhibits Alpha-Synuclein Aggregation: A Potential Agent for Parkinson's Disease. *Neurochemical Research* **41,** 2788–2796. ISSN: 0364-3190 (2016).

289. Roy, S. & Bhat, R. Suppression, disaggregation, and modulation of γ-Synuclein fibrillation pathway by green tea polyphenol EGCG. *Protein Science* **28,** 382–402. ISSN: 1469896X (2019).

290. Lee, Y.-H. *et al.* Zinc boosts EGCG's hIAPP amyloid Inhibition both in solution and membrane. *Biochimica et biophysica acta. Proteins and proteomics.* ISSN: 1878-1454 (2018).

291. Xu, Z.-X. *et al.* Inhibitory Mechanism of Epigallocatechin Gallate on Fibrillation and Aggregation of Amidated Human Islet Amyloid Polypeptide. *ChemPhysChem* **18,** 1611–1619. ISSN: 14394235 (2017).

292. Ehrnhoefer, D. E. *et al.* Green tea (-)-epigallocatechin-gallate modulates early events in huntingtin misfolding and reduces toxicity in Huntington's disease models. *Human Molecular Genetics* **15,** 2743–2751. ISSN: 09646906 (2006).

293. Wobst, H. J., Sharma, A., Diamond, M. I., Wanker, E. E. & Bieschke, J. The green tea polyphenol (-)-epigallocatechin gallate prevents the aggregation of tau protein into toxic oligomers at substoichiometric ratios. *FEBS Letters* **589,** 77–83 (2015).

294. Srinivasan, E. & Rajasekaran, R. Probing the inhibitory activity of epigallocatechin-gallate on toxic aggregates of mutant (L84F) SOD1 protein through geometry based sampling and steered molecular dynamics. *Journal of Molecular Graphics and Modelling* **74,** 288–295. ISSN: 10933263 (2017).

295. Roberts, B. E. *et al.* A synergistic small-molecule combination directly eradicates diverse prion strain structures. *Nature Chemical Biology* **5,** 936–946. ISSN: 15524469 (2009).

296. Townsend, D. *et al.* Epigallocatechin-3-gallate remodels apolipoprotein A-I amyloid fibrils into soluble oligomers in the presence of heparin. *Journal of Biological Chemistry* **293,** 12877–12893. ISSN: 1083351X (2018).

297. Andrich, K. & Bieschke, J. Natural Compounds as Therapeutic Agents for Amyloidogenic Diseases. *Natural Compounds as Therapeutic Agents for Amyloidogenic Diseases* **863,** 139–161. ISSN: 22148019 (2015).

298. Zhu, Q. Y., Zhang, A., Tsang, D., Huang, Y. & Chen, Z. Y. Stability of green tea catechins. *Journal of Agricultural and Food Chemistry* **45,** 4624–4628. ISSN: 00218561 (1997).

299. Hatano, T., Ohyabu, T. & Yoshida, T. The structural variation in the incubation products of (-)-epigallocatechin gallate in neutral solution suggests its breakdown pathways. *Heterocycles* **65** (Feb. 2005).

300. Sang, S., Lee, M. J., Hou, Z., Ho, C. T. & Yang, C. S. Stability of tea polyphenol (-)-epigallocatechin-3-gallate and formation of dimers and epimers under common experimental conditions. *Journal of Agricultural and Food Chemistry* **53,** 9478–9484. ISSN: 00218561 (2005).

301. Zeng, L., Ma, M., Li, C. & Luo, L. Stability of tea polyphenols solution with different pH at different temperatures. *International Journal of Food Properties* **20,** 1–18. ISSN: 15322386 (2017).

302. Hirohata, M. *et al.* The anti-amyloidogenic effect is exerted against Alzheimer's β-amyloid fibrils in vitro by preferential and reversible binding of flavonoids to the amyloid fibril structure. *Biochemistry* **46,** 1888–1899. ISSN: 00062960 (2007).

303. Joshi, P. *et al.* A fragment-based method of creating small-molecule libraries to target the aggregation of intrinsically disordered proteins. *ACS Combinatorial Science* **18,** 144–153. ISSN: 21568944 (2016).

304. Andrich, K. *et al.* Aggregation of full-length immunoglobulin light chains from systemic light chain amyloidosis (AL) patients is remodeled by epigallocatechin-3-gallate. *Journal of Biological Chemistry* **292,** 2328–2344. ISSN: 1083351X (2017).

305. Aarabi, M.-H. The role of two natural flavonoids on human amylin aggregation. *African Journal of Pharmacy and Pharmacology* **6,** 2374–2379 (2012).

306. Chaudhury, S. *et al.* Probing the inhibitory potency of epigallocatechin gallate against human γB-crystallin aggregation: Spectroscopic, microscopic and simulation studies. *Spectrochimica Acta Part A: Molecular and Biomolecular Spectroscopy* **192,** 318 –327. ISSN: 1386-1425 (2018).

307. Jayamani, J. & Shanmugam, G. Gallic acid, one of the components in many plant tissues, is a potential inhibitor for insulin amyloid fibril formation. *European Journal of Medicinal Chemistry* **85,** 352–358. ISSN: 17683254 (2014).

308. Sulatskaya, A. I. *et al.* Stoichiometry and affinity of thioflavin T binding to Sup35p amyloid fibrils. *PLoS ONE* **11,** 1–14. ISSN: 19326203 (2016).

309. Buell, A. K., Dobson, C. M., Knowles, T. P. J. & Welland, M. E. Interactions between Amyloidophilic Dyes and Their Relevance to Studies of Amyloid Inhibitors. eng. *Biophys J* **99,** 3492–3497 (2010).

310. Campioni, S. *et al.* The presence of an air-water interface affects formation and elongation of α-synuclein fibrils. *Journal of the American Chemical Society* **136,** 2866–2875. ISSN: 00027863 (2014).

311. Linse, S. Mechanism of amyloid protein aggregation and the role of inhibitors. *Pure and Applied Chemistry* **91,** 211–229. ISSN: 13653075 (2019).

312. Zhu, M., Han, S. & Fink, A. Oxidized quercetin inhibits α-synuclein fibrillization. *Biochim. Biophys. Acta* **1830,** 2872–2881 (2013).

313. Tanaka, M., Chien, P., Yonekura, K. & Weissman, J. S. Mechanism of cross-species prion transmission: An infectious conformation compatible with two highly divergent yeast prion proteins. *Cell* **121,** 49–62. ISSN: 00928674 (2005).

314. Makarava, N., Ostapchenko, V. G., Savtchenko, R. & Baskakov, I. V. Conformational switching within individual amyloid fibrils. *Journal of Biological Chemistry* **284,** 14386–14395. ISSN: 00219258 (2009).

315. Cohen, S. I. *et al.* Distinct thermodynamic signatures of oligomer generation in the aggregation of the amyloid-β peptide. *Nature Chemistry* **10,** 523–531. ISSN: 17554349 (2018).

316. Knowles, T. P. *et al.* Kinetics and thermodynamics of amyloid formation from direct measurements of fluctuations in fibril mass. *Proceedings of the National Academy of Sciences of the United States of America* **104,** 10016–10021. ISSN: 00278424 (2007).

317. Buell, A. K. *et al.* Detailed Analysis of the Energy Barriers for Amyloid Fibril Growth. *Angewandte Chemie International Edition* **51,** 5247–5251 (2012).

318. Rodriguez, R. A., Chen, L. Y., Plascencia-Villa, G. & Perry, G. Thermodynamics of Amyloid-β Fibril Elongation: Atomistic Details of the Transition State. *ACS Chemical Neuroscience* **9,** 783–789. ISSN: 19487193 (2018).

319. Esler, W. P. *et al.* Alzheimer's disease amyloid propagation by a template-dependent dock- lock mechanism. *Biochemistry* **39,** 6288–6295. ISSN: 00062960 (2000).

320. Cannon, M. J., Williams, A. D., Wetzel, R. & Myszka, D. G. Kinetic analysis of beta-amyloid fibril elongation. *Analytical Biochemistry* **328,** 67–75. ISSN: 00032697 (2004).

321. Cobb, N. J., Apetri, A. C. & Surewicz, W. K. Prion protein amyloid formation under native-like conditions involves refolding of the C-terminal α-helical domain. *Journal of Biological Chemistry* **283,** 34704–34711. ISSN: 00219258 (2008).

322. Ziaunys, M., Sneideris, T. & Smirnovas, V. Exploring the potential of deep-blue autofluorescence for monitoring amyloid fibril formation and dissociation. *PeerJ* **7,** e7554. ISSN: 2167-8359 (2019).

323. Thompson, A. J. *et al.* Molecular Rotors Provide Insights into Microscopic Structural Changes during Protein Aggregation. *Journal of Physical Chemistry B* **119,** 10170–10179. ISSN: 15205207 (2015).

324. Voropai, E. S. *et al.* Spectral properties of thioflavin T and its complexes with amyloid fibrils. *Journal of Applied Spectroscopy* **70,** 868–874. ISSN: 00219037 (2003).

325. Freire, S., De Araujo, M. H., Al-Soufi, W. & Novo, M. Photophysical study of Thioflavin T as fluorescence marker of amyloid fibrils. *Dyes and Pigments* **110,** 97–105. ISSN: 01437208 (2014).

326. Šarić, A., Michaels, T. C. T., Zaccone, A., Knowles, T. P. J. & Frenkel, D. Kinetics of spontaneous filament nucleation via oligomers: Insights from theory and simulation. *The Journal of Chemical Physics* **145,** 211926. ISSN: 0021-9606 (2016).

327. Linse, S. Monomer-dependent secondary nucleation in amyloid formation. *Biophysical Reviews* **9,** 329–338. ISSN: 18672469 (2017).

328. Ruggeri, F. S. *et al.* Microfluidic deposition for resolving single-molecule protein architecture and heterogeneity. *Nature Communications* **9.** ISSN: 20411723 (2018).

329. Kastantin, M., Langdon, B. B. & Schwartz, D. K. A bottom-up approach to understanding protein layer formation at solid–liquid interfaces. *Advances in Colloid and Interface Science* **207.** Special Issue: Helmuth Möhwald Honorary Issue, 240 –252. ISSN: 0001-8686 (2014).

330. Losic, D., Martin, L. L., Aguilar, M.-I. & Small, D. H. -Amyloid fibril formation is promoted by step edges of highly oriented pyrolytic graphite. *Peptide Science* **84,** 519–526 (2006).

331. Zhao, D., Watson, J. B. & Xie, C.-W. Amyloid beta prevents activation of calcium/calmodulin-dependent protein kinase II and AMPA receptor phosphorylation during hippocampal long-term potentiation. *Journal of neurophysiology* **92,** 2853–2858. ISSN: 0022-3077 (2004).

332. Tilton, R., Gast, A. & Robertson, C. Surface diffusion of interacting proteins. Effect of concentration on the lateral mobility of adsorbed bovine serum albumin. *Biophysical Journal* **58,** 1321 –1326. ISSN: 0006-3495 (1990).

333. Ravichandran, S. & Talbot, J. Mobility of Adsorbed Proteins: A Brownian Dynamics Study. *Biophysical Journal* **78,** 110 –120. ISSN: 0006-3495 (2000).

Appendix A

Supplementary material

A.1 EGCG oxidation followed by UV-Vis spectroscopy

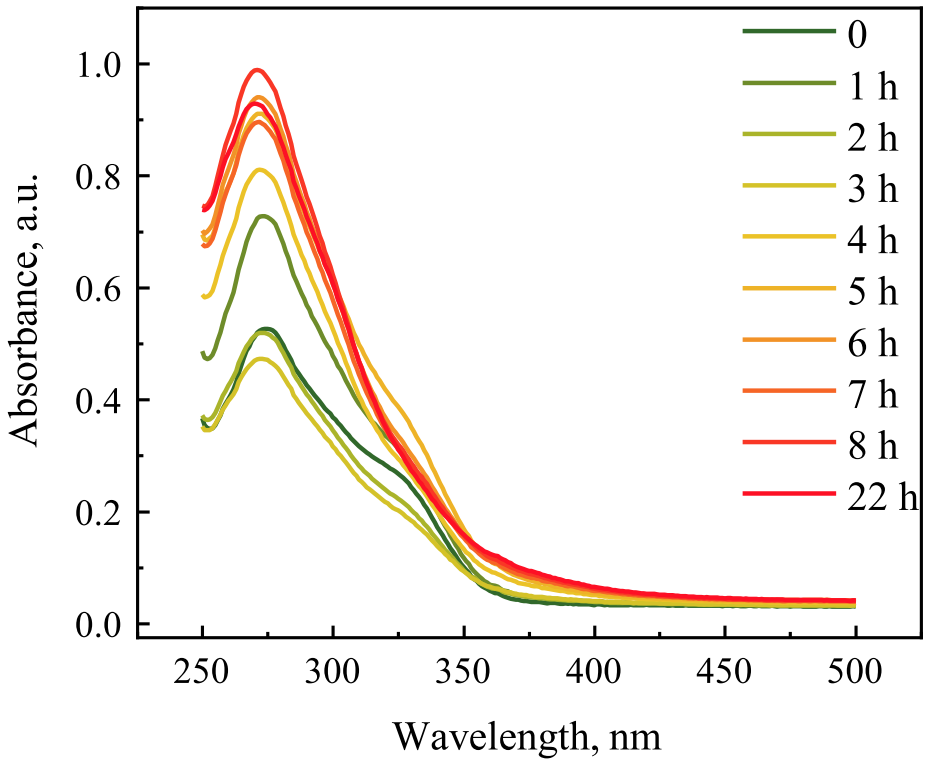

FIGURE A.1: UV-Vis spectra of 10 mM EGCG in 10 mM sodium phosphate buffer pH 7.4 at 60 °C, corresponding to the conditions where a stock solution of $EGCG_{Ox}$ for the insulin experiments was produced. Measurements were performed by Rebecca Sternke-Hoffmann at Institute of Physical Biology, Heinrich-Heine-University, Düsseldorf, Germany.

A.2 Self-inhibition of insulin amyloid-like aggregation

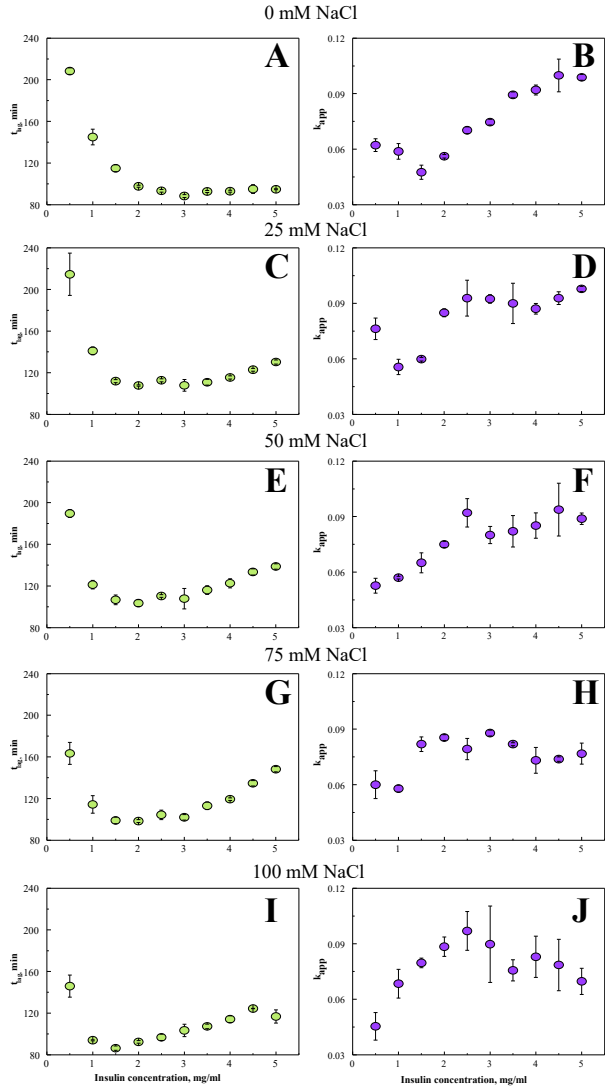

FIGURE A.2: Dependence of insulin aggregation lag time (t_{lag}) (A, C, E, F, I) and apparent growth rate constant (k_{app}) (B, D, F, H, J) on concentration under a range of NaCl concentrations from 0 to 100 mM. Error bars are standard deviations estimated from three repeats.

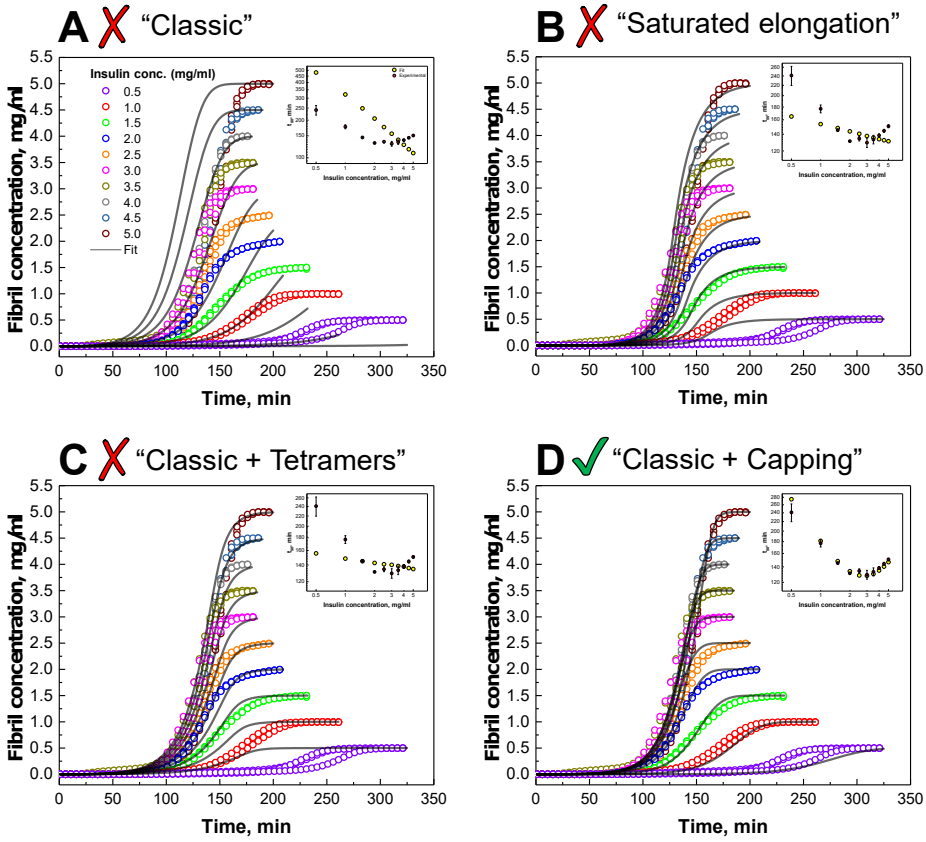

FIGURE A.3: Global fits of experimental data with 25 mM NaCl. The global fit of "Classic" (A), "Saturated elongation" (B), "Classic + Tetramers" (C) and "Classic + Capping" (D) model to the experimental data. In each case primary and secondary nucleus size was set to 2. Open circles represent normalised experimental data (3 repeats for each protein concentration).

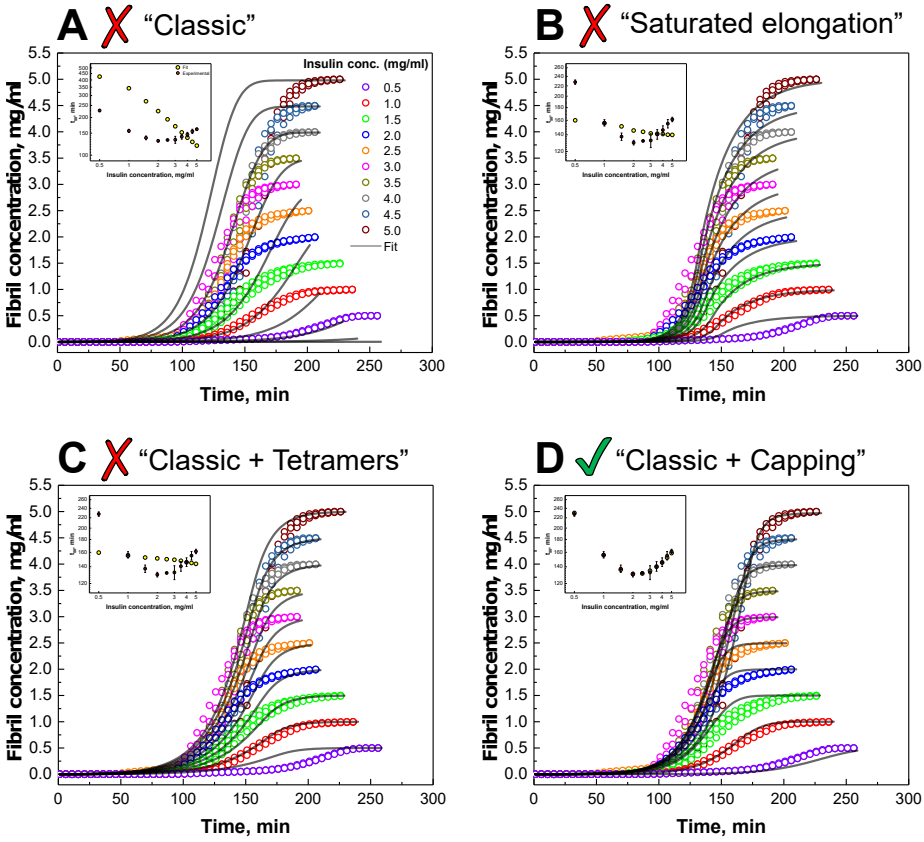

FIGURE A.4: Global fits of experimental data with 50 mM NaCl. The global fit of "Classic" (A), "Saturated elongation" (B), "Classic + Tetramers" (C) and "Classic + Capping" (D) model to the experimental data. In each case primary and secondary nucleus size was set to 2. Open circles represent normalised experimental data (3 repeats for each protein concentration).

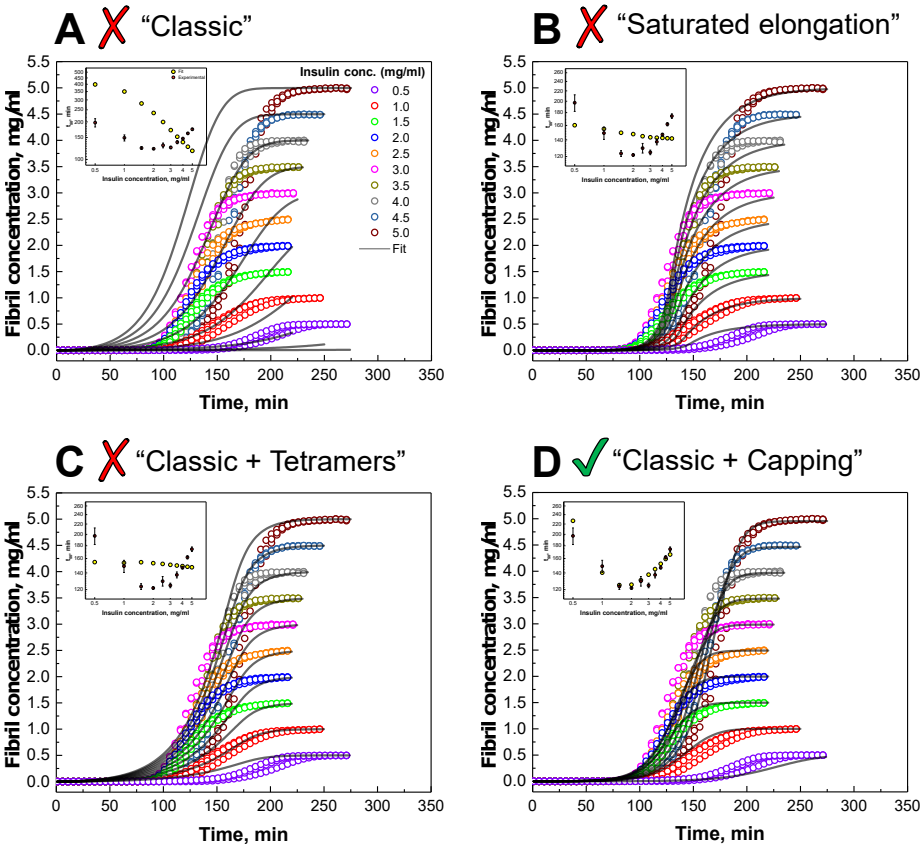

FIGURE A.5: Global fits of experimental data with 75 mM NaCl. The global fit of "Classic" (A), "Saturated elongation" (B), "Classic + Tetramers" (C) and "Classic + Capping" (D) model to the experimental data. In each case primary and secondary nucleus size was set to 2. Open circles represent normalised experimental data (3 repeats for each protein concentration).

A.3 Environment is a key factor in determining the efficacy of anti-amyloid compounds – a case study with EGCG

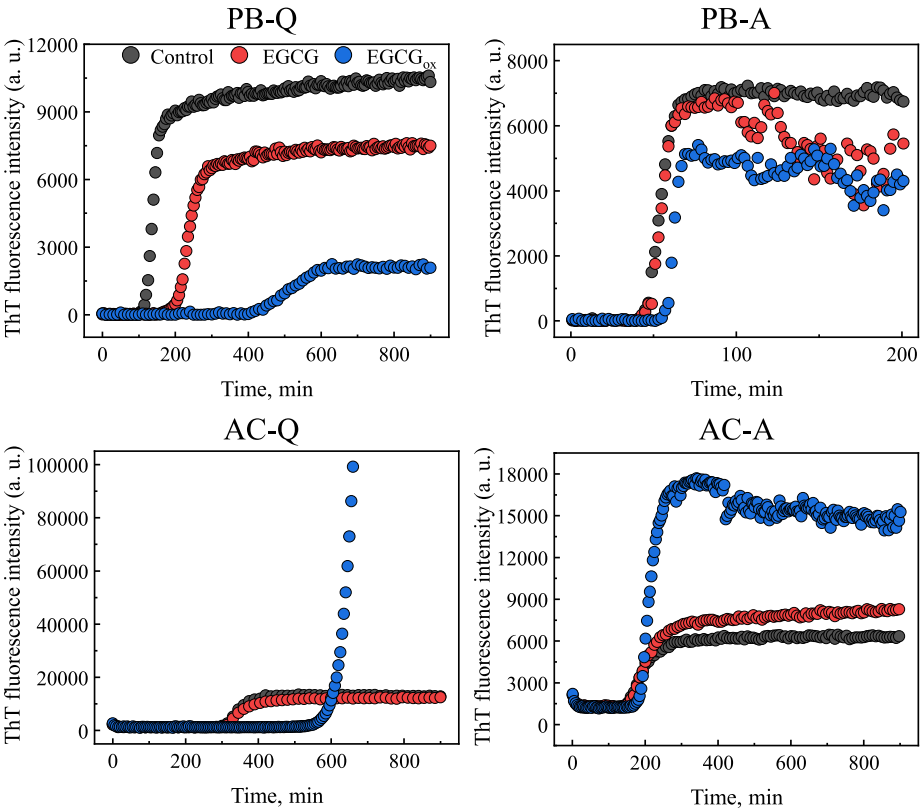

FIGURE A.6: Representative curves of insulin aggregation kinetics in the absence and presence of EGCG or EGCG$_{ox}$ under different environmental conditions. Abbreviations PB and AC represent environmental conditions (100 mM phosphate buffer and 20 % acetic acid, respectively), while Q and A denote agitation conditions (quiescent and agitated, respectively), under which the insulin aggregation reaction was performed.

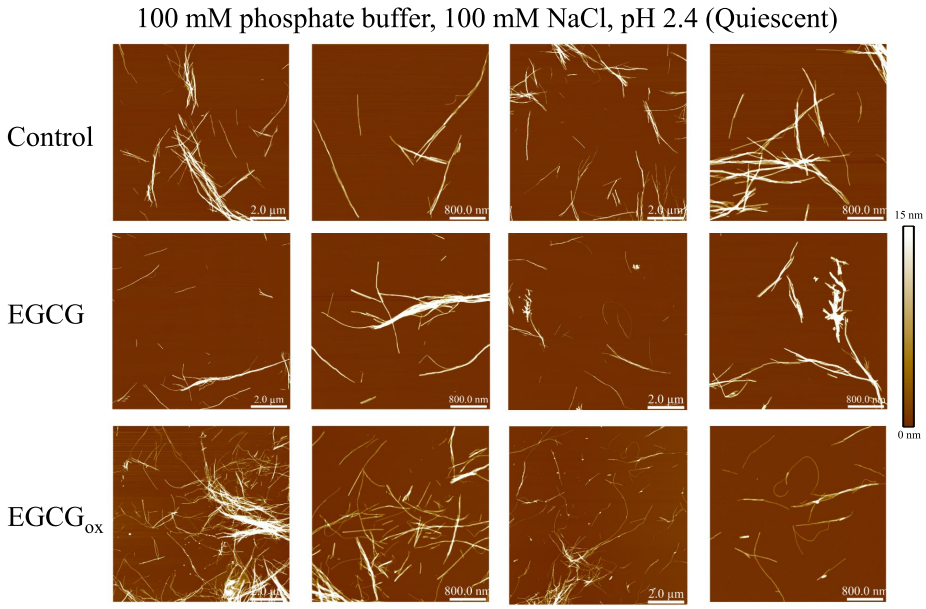

FIGURE A.7: AFM images of insulin fibrils formed in PB under quiescent conditions in the absence and presence of EGCG or EGCG$_{ox}$.

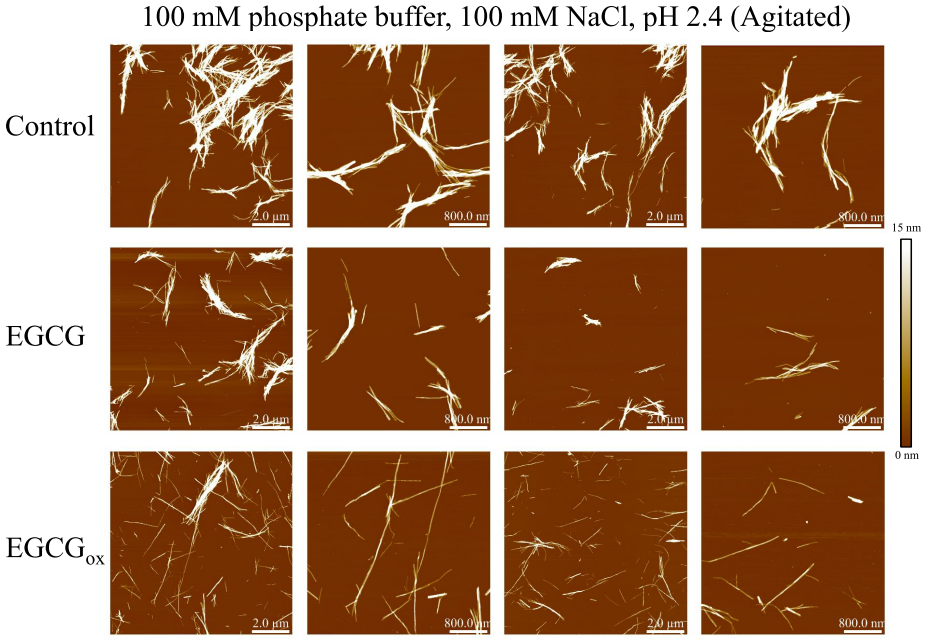

FIGURE A.8: AFM images of insulin fibrils formed in PB under agitated conditions in the absence and presence of EGCG or EGCG$_{ox}$.

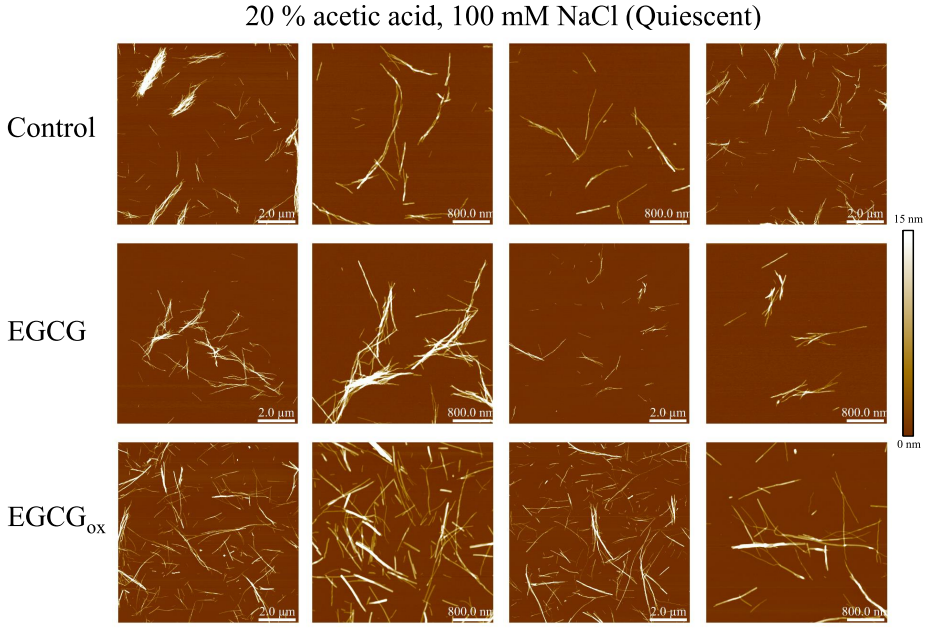

FIGURE A.9: AFM images of insulin fibrils formed in AC under quiescent conditions in the absence and presence of EGCG or EGCG$_{ox}$.

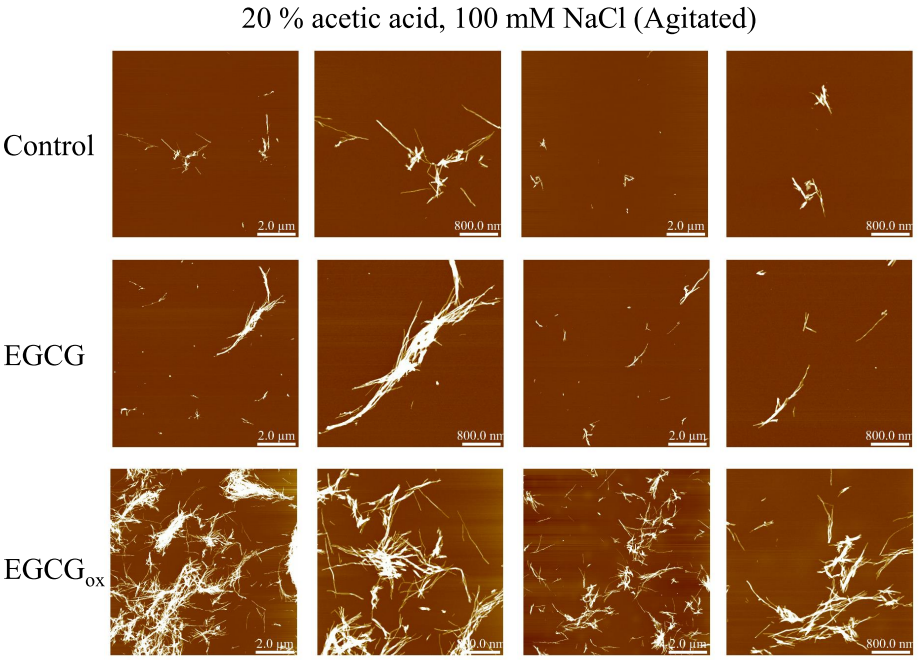

FIGURE A.10: AFM images of insulin fibrils formed in AC under agitated conditions in the absence and presence of EGCG or EGCG$_{ox}$.

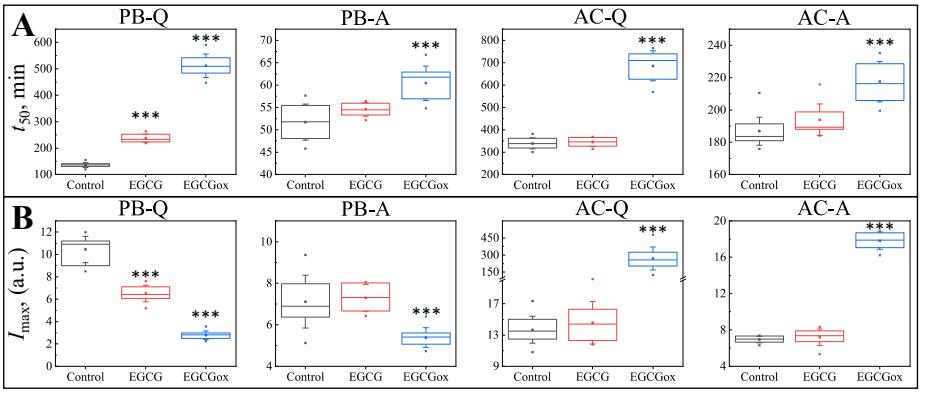

FIGURE A.11: Evaluation of EGCG and EGCG$_{ox}$ effects on t_{50} (A) and I_{max} (B) using one-way ANOVA. *** - Significantly different ($P < 0.01$).

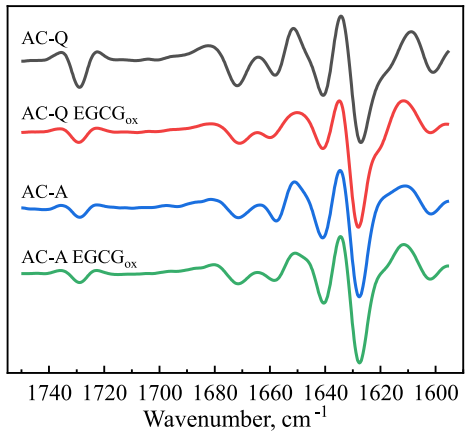

FIGURE A.12: Second derivative FTIR spectra of insulin amyloid-like aggregates formed in AC in the absence and presence of EGCG$_{ox}$. Abbreviation AC represent environmental conditions (20% acetic acid), while Q and A denote agitation conditions (quiescent and agitated, respectively), under which insulin aggregation process was performed.

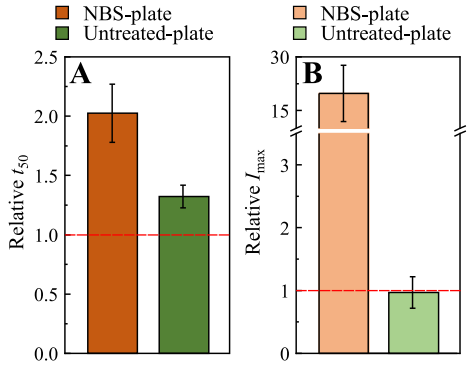

FIGURE A.13: Effect of EGCG$_{ox}$ on t_{50} (A) and I_{max} (B) in AC assessed in NBS-plates and untreated-plates. The error bars represent standard deviations.

A.4 Properties of prion fibril self-replication

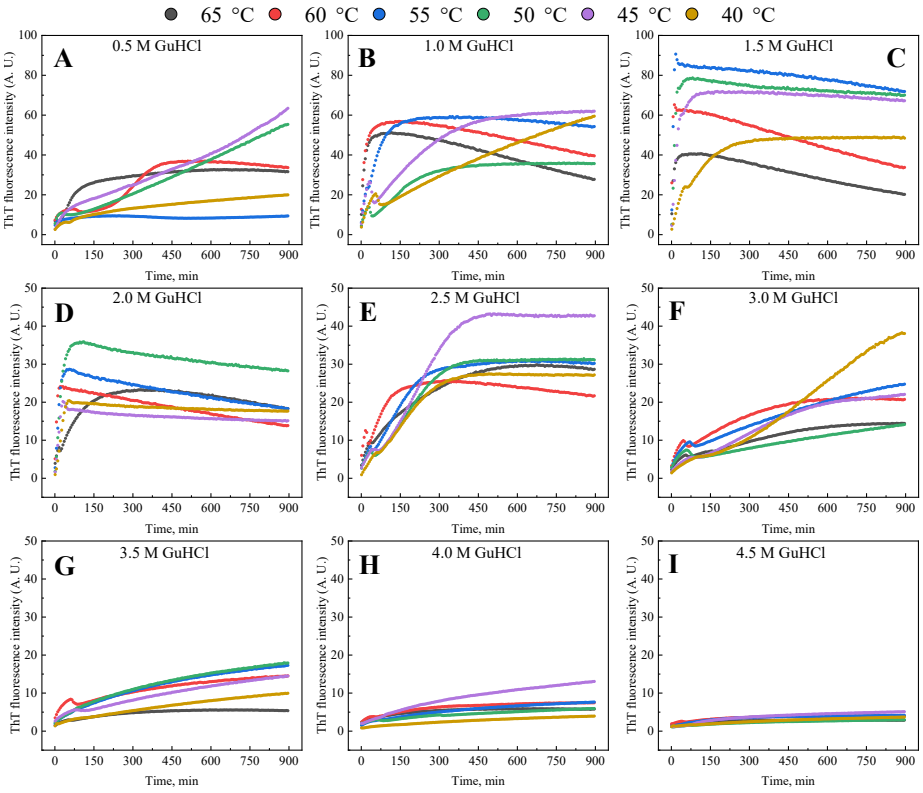

FIGURE A.14: Kinetics of S220_2M fibril strain self-propagation. A-I) kinetics of seed-induced aggregation reaction in the presence of 0.5-4.5 M of GuHCl, respectively.

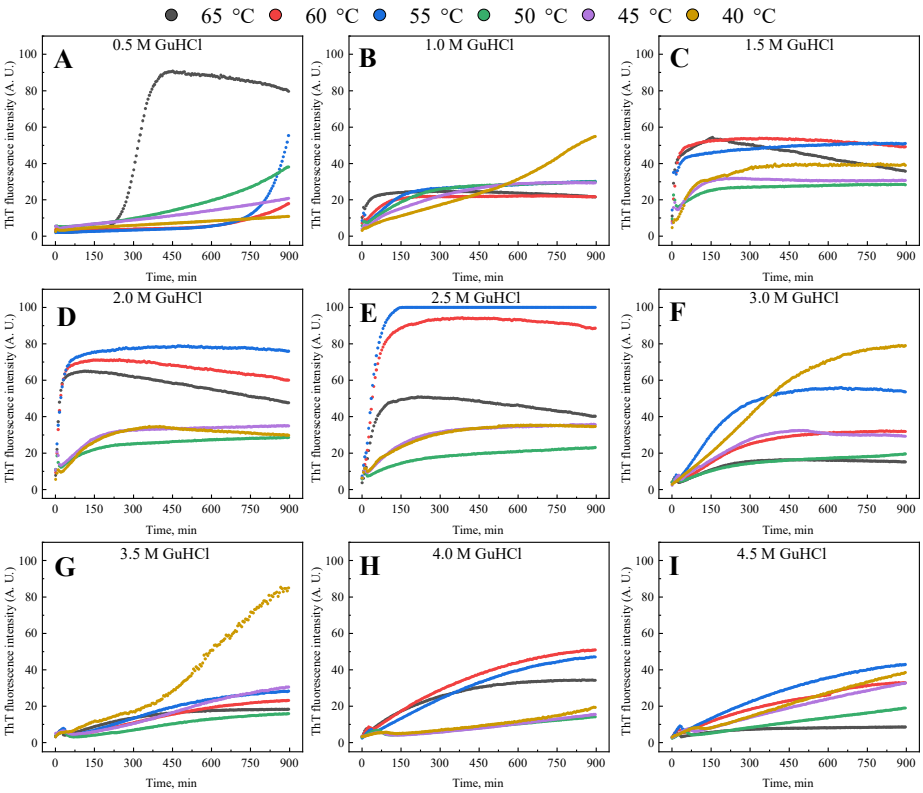

FIGURE A.15: Kinetics of R10_2M fibril strain self-propagation. A-I) kinetics of seed-induced aggregation reaction in the presence of 0.5-4.5 M of GuHCl, respectively.

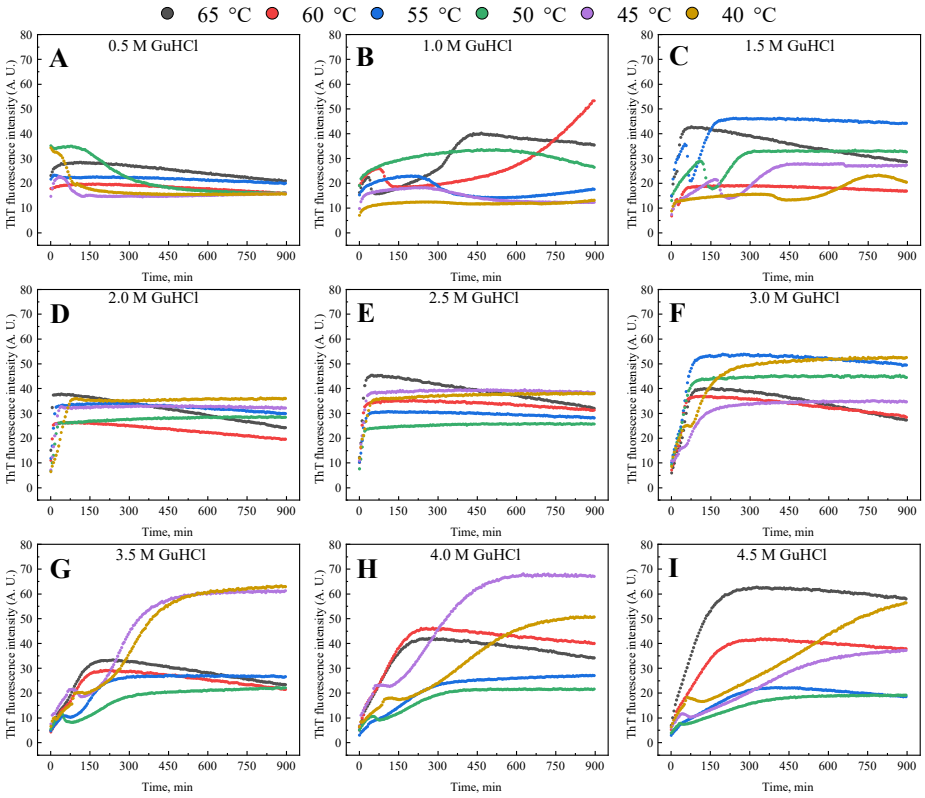

FIGURE A.16: Kinetics of S220_4M fibril strain self-propagation. A-I) kinetics of seed-induced aggregation reaction in the presence of 0.5-4.5 M of GuHCl, respectively.

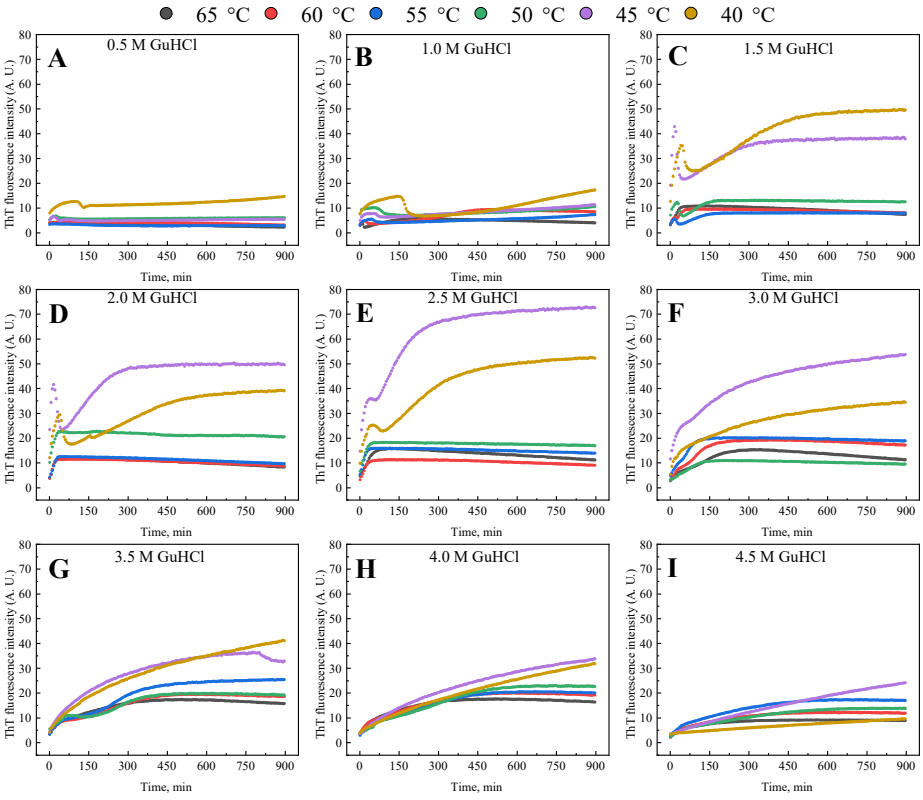

FIGURE A.17: Kinetics of R10_4M fibril strain self-propagation. A-I) kinetics of seed-induced aggregation reaction in the presence of 0.5-4.5 M of GuHCl, respectively.

A.5 Resolving the heterogeneity and relative abundance of Aβ42 aggregates during amyloid formation

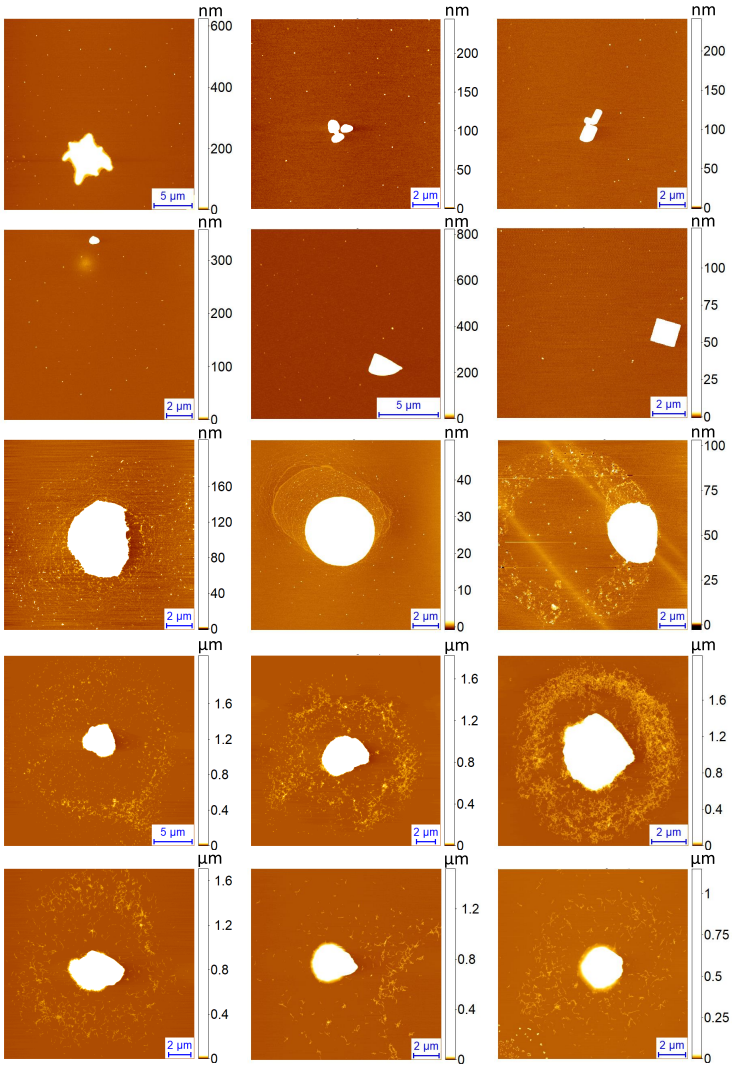

FIGURE A.18: Monitoring of Aβ42 aggregation time course via high-resolution AFM. Images of samples collected at t_0 - t_4, respectively.

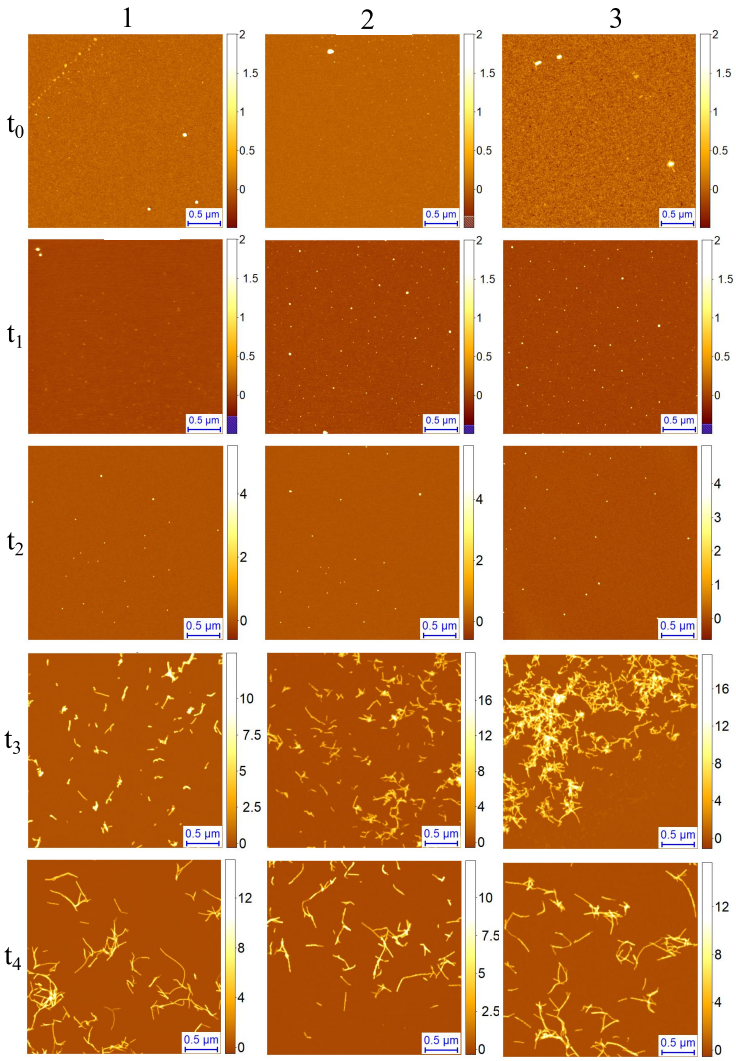

FIGURE A.19: Morphology of species present during different stages of Aβ42 aggregation reaction. The height scale is in nm.

Curriculum Vitae

Tomas Šneideris

Telephone: +370 652 31742
E-mail: Tomas.Sneideris@bti.vu.lt

Education

Degree: **PhD student in Biochemistry** (Since 2015).
Institution: Institute of Biotechnology, Life Sciences Center, Vilnius University, Vilnius, Lithuania.
Thesis title: Towards understanding amyloid fibril formation and self-replication.
Supervisor: Dr. Vytautas Smirnovas.

Degree: **MSc in Bioengineering** (2013-2015).
Institution: Vilnius Gediminas Technical University, Vilnius, Lithuania.
Thesis title: Production of recombinant amyloid beta peptide and evaluation of potential inhibitors of its aggregation.
Supervisor: Dr. Vytautas Smirnovas.

Degree: **BSc in Bioengineering** (2009-2013).
Institution: Vilnius Gediminas Technical University, Vilnius, Lithuania.
Thesis title: Production of recombinant mouse PrP23-230.
Supervisor: Dr. Vytautas Smirnovas.

Professional experience

2017 - to date: **Junior researcher** at Department of Biothermodynamics and Drug Design, Institute of Biotechnology, Life Sciences Center, Vilnius University, Vilnius, Lithuania.

2015 - 2018: **Researcher biologist** at Department of Biothermodynamics and Drug Design, Institute of Biotechnology, Vilnius University, Vilnius, Lithuania.

2013 - 2015: **Laboratory assistant** at Department of Biothermodynamics and Drug Design, Institute of Biotechnology, Vilnius University, Vilnius, Lithuania.

Internships

2018.06.2 – 2019.02.16: **Department of Chemistry, Cambridge University**, Cambridge, United Kingdom, group leader prof. Michele Vendruscolo, supervisor Dr. Francesco Simone Ruggeri.

2018.04.07 – 2018.04.15: **Institute of Biological Chemistry, Academia Sinica**, Taipei, Taiwan.

2015.04.23 – 2015.04.25: **Warsaw University**, Warsaw, Poland.

2015.02.18 – 2015.03.04: **Dortmund Technical University**, Dortmund, Germany.

International schools

2017: **2nd NGP-net Winter School on Experimental Methods to Characterize Non-Globular Proteins**, Marseille, France.

2016: **13th Greta Pifat Mrzljak International School of Biophysics**, Split, Croatia.

Academic achievements and awards

Scholarship for academic achievements
2019 • The Research Council of Lithuania
Scholarship to attend "8th Scandinavian Conference of Amyloid Diseases and Amyloid Mechanisms (ADAM8)"
2019 • The Research Council of Lithuania
Best poster award at the international conference "Vita Scientia 2018"
2018 • Vita Scientia
Scholarship to attend "62nd Annual Meeting of Biophysical Society"
2018 • COST action BM1405
Scholarship for academic achievements
2018 • The Research Council of Lithuania
Scholarship to attend "Prion 2018" conference
2018 • The Research Council of Lithuania
Scholarship for academic achievements
2017 • The Research Council of Lithuania
Scholarship to attend "2nd NGP-net Winter School on Experimental Methods to Characterize Non-Globular Proteins"
2017 • COST action BM1405
Scholarship to attend "13th Greta Pifat Mrzljak International School of Biophysics"
2016 • EBSA
Award for work cycle "Research of amyloid protein aggregation"
2016 • The Lithuanian Academy of Sciences

List of publications

Publications included in this thesis

- **Sneideris, T.**; Sakalauskas, A.; Sternke-Hoffmann, R.; Peduzzo, A.; Ziaunys, M.; Buell, A.; Smirnovas, V. *The environment is a key factor in determining the anti-amyloid efficacy of EGCG*, **Biomolecules** 2019, 9, 855.

- Ziaunys, M.; **Sneideris, T.**; Smirnovas, V. *Self-inhibition of insulin amyloid-like aggregation*. **PCCP**, 2018, vol. 20, p. 27638-27645.

- **Sneideris, T.**; Darguzis, D.; Botyriute, A.; Grigaliunas, M.; Winter, R.; Smirnovas, V. *pH-Driven Polymorphism of Insulin Amyloid-Like Fibrils*. **PlosOne**, 2015, vol. 10, p. e0136602.

- **Sneideris, T.**; Milto, K.; Smirnovas, V. *Polymorphism of amyloid-like fibrils can be defined by the concentration of seeds*. **PeerJ**, 2015, vol. 3, p. e1207.

Publications not included in this thesis

- Pampuscenko, K.; Morkuniene, R.; **Sneideris, T.**; Smirnovas, V.; Budvytyte, R.; Valincius, G.; Brown G.C.; Borutaite, V. *Extracellular tau induces microglial phagocytosis of living neurons in cell cultures* **Journal of Neurochemistry**, 2019, 13:e14940.

- Ziaunys, M; **Sneideris, T**; Smirnovas, V. *Exploring the potential of deep-blue autofluorescence for monitoring amyloid fibril formation and dissociation*. **PeerJ**, 2019 vol 7, e7554.

- Ruggeri, F. S.; **Šneideris, T.**; Chia S.; Vendruscolo, M.; Knowles, T. P. J. *Characterizing Individual Protein Aggregates by Infrared Nanospectroscopy and Atomic Force Microscopy*. **JoVE**, 2019, e60108.

- Schilling, C.; Mack, T.; Lickfett, S.; Sieste, S.; Ruggeri, F. S.; **Sneideris, T.**; Dutta, A.; Bereau, T.; Naraghi, R.; Sinske, D.; Knowles, T.P.J.; Synatschke, C.V.; Weil, T.; Knöll, B. *Sequence-Optimized Peptide Nanofibers as Growth Stimulators for Regeneration of Peripheral Neurons*. **Advanced Functional Materials**, 2019, vol 1809112, 1-15 p.

- Ruggeri, F. S.; **Šneideris, T.**; Vendruscolo, M.; Knowles T.P.J. *Atomic force microscopy for single molecule characterisation of protein aggregation*. **Archives of Biochemistry and Biophysics**, 2019, vol. 664, 134-148 p.

- **Sneideris, T.**; Baranauskiene, L.; Cannon, J. G.; Rutkiene, R., Meskys, R.; Smirnovas, V. *Looking for a generic inhibitor of amyloid-like fibril formation among flavone derivatives*. **PeerJ**, 2015, vol. 3, p. e1271.

List of conferences

- **Šneideris, T.**; Sakalauskas, A.; Žiaunys, M.; Smirnovas, V. *Environment is the key factor in detection of anti-amyloid compounds*, 8^{th} Scandinavian Conference of Amyloid Diseases and Amyloid Mechanisms (ADAM8), Lund, Sweden, 2019.
- **Šneideris, T.**; Kulicka, E.; Smirnovas, V., *Properties of prion self-replication*, 3^{rd} Ulm Meeting on Biophysics of Amyloid Formation, Ulm, Germany, 2019.
- **Šneideris, T.**; Smirnovas, V. *Effect of temperature and denaturant concentration on the elongation of distinct mouse prion protein fibril strains*, The Coins 2018, Vilnius, Lithuania, 2018.
- **Šneideris, T.**; Kulicka, E.; Smirnovas, V. *Properties of prion self-replication*, Prion 2018, Santiago de Compostela, Spain, 2018.
- **Šneideris, T.**; Smirnovas, V. *Effect of temperature and denaturant concentration on the elongation of distinct mouse prion protein fibril strains*, 61^{st} International Conference for Students of Physics and Natural Sciences Open readings 2018, Vilnius, Lithuania, 2018.
- **Šneideris, T.**; Kulicka, E.; Smirnovas, V. *Polymorphism of prion protein amyloid-like fibrils*, 62^{nd} Annual Meeting of Biophysical Society, San Francisco, USA, 2018.
- **Šneideris, T.**; Kulicka, E.; Stanilko, R.; Smirnovas, V. *Effect of the environment on amyloid aggregation*, International Conference Vita Scientia, Vilnius, Lithuania, 2018.
- **Šneideris, T.**; Baranauskienė, L.; Cannon, J. G.; Rutkienė, R.; Meškys, R.; Smirnovas, V. *Looking for a generic inhibitor of amyloid-like fibril formation among flavone derivatives*, Protein misfolding in disease - Toxic aggregation-prone proteins in ageing and

age-related diseases: from structure to pathology and spreading, Roscoff, France, 2016.

- **Šneideris, T**.; Baranauskienė, L.; Cannon, J. G.; Rutkienė, R.; Meškys, R.; Smirnovas, V. *Looking for a generic inhibitor of amyloid-like fibril formation among flavone derivatives*, XIV Conference of the Lithuanian Biochemical Society, Druskininkai, Lithuania, 2016.

- **Šneideris, T.**; Milto, K.; Smirnovas, V. *Polymorphism of amyloid-like fibrils can be defined by the concentration of seeds*, International Conference Vita Scientia, Vilnius, Lithuania, 2016.

- **Šneideris, T.**; Milto, K.; Smirnovas, V.,*Polymorphism of amyloid-like fibrils can be defined by the concentration of seeds*, First NGP-NET Symposium on Non-Globular Proteins, Porto, Portugal, 2015

Summary in Lithuanian
Daktaro disertacijos santrauka

Turinys

Įvadas

Daugiau nei penkiasdešimties žmogaus ligų, įskaitant Alzheimerio ligą (AL) [1], Parkinsono ligą (PL) [2], II tipo diabetą [3], bei prionų ligas [4], atsiradimas ir progresija yra siejama su specifinių peptidų ir baltymų nesugebėjimu įgauti natyvią konformaciją ar išlikti joje, bei toliau sekančia šių monomerinių peptidų ar baltymų konversija į netirpius fibrilinius agregatus, dar žinomus kaip amiloidai.

Pastaraisiais metais amiloidų susidarymo tyrimai tapo ypač aktualūs, kadangi buvo pripažinta, jog daugelis su amiloidais siejamų ligų nebėra retos ir yra vienos iš dažniausiai pasireiškiančių ligų senstančioje visuomenėje [5]. Milijonai žmonių visame pasaulyje kenčia nuo šių ligų, vien Alzheimerio ar Parkinsono ligomis sergančių žmonių yra daugiau nei 50 milijonų [1, 2, 6].

Nepaisant reikšmingų mokslininkų pastangų, molekuliniai ir mechanistiniai ryšiai tarp baltymų agregacijos ir agregatų toksiškumo išlieka neaiškūs ir sunkiai charakterizuojami. Taip pat šiai dienai, deja, nėra nei vieno veiksmingo vaistinio preparato ar gydymo metodo skirto ligų siejamų su amiloidais prevencijai ar gydymui [7, 8]. Vienos iš pagrindinių to priežasčių yra be galo sudėtingi amiloidinių agregatų susidarymo ir savireplikacijos mechanizmai, bei sąlyginiai skurdus šių mechanizmų supratimas [8, 9]. Sėkminga bet kokios ligos prevencija ar gydymas yra galimi tik tuomet jei dauguma procesų susijusių su ligos atsiradimu bei progresija yra žinomi ir yra pakankamai gerai suprasti [8]. Visiškas amiloidinių agregatų susidarymo proceso išaiškinimas yra galimas tik tuomet jei yra žinomos visos konformacinės būsenos ir oligomerinės struktūros kurias įgauna polipeptidinė grandinė šio proceso metu, bei yra žinomi visų konformacinių virsmų termodinaminiai ir kinetiniai parametrai [10].

Amiloidinių fibrilių susidarymas yra sudėtingas procesas, susidedantis iš keleto mikroskopinių įvykių, įskaitant pirminę ir antrinę nukleaciją, agregatų ilgėjimą (elongaciją), ir fibrilių lūžinėjimą (fragmentaciją) [5, 11–13]. Pokyčiai aplinkos sąlygose gali paveikti šiuos mikroskopinius įvykius ir nulemti alternatyvių agregacijos kelių atsiradimą, dėl ko gali susidaryti struktūriškai skirtingi amiloidiniai

ageregatai, dar kitaip vadinami fibrilių "kamienais" [5, 9, 11, 14–27]. Manoma, kad toks konformacinis kintamumas yra bendroji amiloidinių baltymų savybė [11, 28, 29]. Konformacinis amiloidinių fibrilių kintamumas yra dar viena priežastis dėl ko yra taip sunku sukurti veiksmingus vaistinius preparatus ar gydymo metodus, kadangi junginiai, kurie efektyviai stabdo vieno tipo (kamieno) amiloidinių fibrilių susidarymą, gali būti neveiksmingi prieš kito tipo fibrilių susidarymą [9].

Baltymų amiloidinių fibrilių susidarymo, savireplikacijos, bei konformacinio kintamumo tyrimai yra esminės svarbos, nes tik esant pakankamai giliam supratimui apie šiuos procesus bus įmanoma sukurti efektyvius amiloidinių ligų prevencijos ir gydymo metodus.

Tikslas

Tirti baltymų amiloidinių fibrilių susidarymo, savireplikacijos, bei konformacinio kintamumo procesus, ir gauti naujų žinių apie šiuos procesus.

Užduotys

- Ištirti įvairių faktorių poveikį insulino amiloidinių fibrilių formavimuisi.
- Tirti skirtingų prioninio baltymo fibrilių kamienų savireplikacijos savybes ir gauti naujų žinių apie šį procesą.
- Atlikti amiloido beta 42 agregacijos proceso tyrimus atominės jėgos mikroskopu mėginio užnešimui panaudojant mikroslašėlių išpurškimo įrenginį.

Mokslinis naujumas

Šiame darbe yra pateikiamos naujos mechanistinės įžvalgos apie skirtingų insulino fibrilių kamienų susidarymą. Atlikus įvairių faktorių poveikio insulino amiloidinių fibrilių susidarymui tyrimą buvo nustatyta, jog vienas iš pagrindinių faktorių, nulemiančių vieno ar kito insulino fibrilių kamieno susidarymą, yra pusiausvyra tarp monomerinės ir oligomerinės insulino formų.

Manoma, kad oligomerinės insulino formos tiesiogiai nedalyvauja insulino fibrilių susidaryme ir yra tik laikinos formos skirtos insulino monomerų saugojimui [30–32]. Šiame darbe pirmą kartą parodytas tiesioginis oligomerinių insulino formų vaidmuo amiloidinių fibrilių susidarymo procese. Pastarasis atradimas ženkliai prisidėjo prie gilesnio insulino agregacijos mechanizmo supratimo ir priartino mus vienu žingsniu arčiau prie visiško insulino agregacijos mechanizmo išaiškinimo.

Siekiant surasti efektyvius vaistus skirtus kovoti su amiloidinėmis ligomis atlikta galybė tyrimų, kurių metu tirtas daugybės junginių poveikis, tačiau šiai dienai nėra nei vieno efektyvaus vaistinio preparato skirto amiloidinėms ligoms gydyti. Šiame darbe yra pademonstruota jog aplinkos sąlygos, kuriomis yra atliekama amiloidų agregacijos reakcija ir tiriamas molekulės poveikis jai, bei kriterijai kuriais remiantis yra vertinamas poveikis, yra vieni iš pagrindinių faktorių kurie nulemia ar molekulė bus identifikuota kaip potencialus prieš amiloidinis vaistas ar ne.

Šiame darbe pateikiamos naujos mechanistinės įžvalgos apie prionų savireplikacijos procesą. Pirmą kartą yra pademonstruojama, kad konformacinis prioninio baltymo fibrilių kintamumas, jų savireplikacijos reakcijos metu, priklauso nuo susidariusių agregatų, kuriais inicijuojama reakcija, koncentracijos. Taip pat darbe yra aprašomas naujas fenomenas, kuris atsiranda esant tam tikroms aplinkos sąlygoms prioninio baltymo fibrilių savireplikacijos reakcijos metu. Taip pat yra iškeliama hipotezė galinti paaiškinti šio fenomeno kilmę.

Galiausiai darbe yra pademonstruojama jog atominės jėgos mikroskopija kartu su mikroskysčių išpurškimo platforma suteikia unikalią galimybę vizualizuoti visas agreguojančių baltymų formas (monomerai, oligomerai, protofibrilės ir fibrilės) egzistuojančias amiloidinės agregacijos metu. AFM ir mikrolašelių išpurškimo platformos kombinacija leido pirmą kartą gauti kiekybinę ir kokybinę informaciją apie šias formas vienos molekulės lygmenyje.

Ginamieji teiginiai

- Insulino monomerų-oligomerų pusiausvyra yra vienas iš

pagrindinių faktorių nulemiančių skirtingų insulino fibrilių kamienų susidarymą.

- Neamiloidogeninės oligomerinės insulino formos tiesiogiai dalyvauja insulino agregacijos procese ir jį slopina.
- Aplinkos sąlygos yra vienas iš pagrindinių faktorių nulemiančių epigalokatechino-3-galato (EGCG) prieš-amiloidinį poveikį.
- Amiloidinių fibrilių kamienui-specifiškos struktūros perdavimas ir dauginimas (savireplikacija) vyksta tik fibrilių ilgėjimo metu.
- Neįprastas ThT signalo pokytis fibrilių savireplikacijos reakcijos metu yra susijęs su mikroskopiniais įvykiais vykstančiais antrinės nukleacijos proceso metu.
- Atominės jėgos mikroskopija kartu su mikroskysčių išpurškimo platforma suteikia unikalią galimybę vizualizuoti visas agreguojančių baltymų formas (monomerai, oligomerai, protofibrilės ir fibrilės) egzistuojančias amiloidinės agregacijos metu, bei gauti kiekybinę ir kokybinę informaciją apie šias formas vienos molekulės lygmenyje.

Disertacijos struktūra

Disertaciją sudaro šešios dalys: įvadas, literatūros apžvalga, metodai, rezultatai ir jų aptarimas, išvados ir literatūros sąrašas. Čia pateikiama disertacijos santrauka.

Literatūros apžvalga

Baltymai - vienos svarbiausių biomolekulių, kurios dalyvauja beveik visuose biologiniuose procesuose. Tam, kad atliktų savo funkciją, šios biomolekulės turi įgauti natyvią funkcionalią konformaciją [8, 29]. Tam tikrais atvejais baltymai nesugeba įgauti ar likti natyvioje konformacijoje ir yra linkę agreguoti į netirpius fibrilinius agregatus, dar žinomus kaip amiloidai. Tokių amiloidinių agregatų susidarymas yra siejamas su daugiau nei penkiasdešimt žmogaus ligų, įskaitant Alzheimerio ligą. Nepaisant mokslininkų pastangų, šiai dienai nėra nei vieno efektyvaus vaistinio preparato skirto šioms ligoms gydyti. Viena iš pagrindinių to priežasčių yra santykinai skurdus amiloidinės agregacijos proceso supratimas [8, 9].

Daktaro disertacijos literatūros apžvalgoje trumai aprašyta amiloidinių baltymų atradimo istorija. Taip pat aprašytos su amiloidinais baltymais siejamos žmonių ligos. Paaiškinti amiloidinių fibrilių susidarymo, savireplikacijos ir plitimo žmogaus organizme ir tarp individų mechanizmai. Aprašyti biofizikiniai metodai naudojami amiloidinių agregatų tyrimuose.

Metodai

Insulino agregatų formavimas. 1 mM koncentracijos insulino, 100 mM natrio fosfatinis buferinis tirpalas (H_2O arba D_2O aplinkoje) esant skirtingai tirpalo pH (H_2O) arba pH* (D_2O) buvo inkubuojamas MHR 23 termomikseryje 24 valandas 60 °C temperatūroje esant 300 aps./min maišymui.

0,5-5 mg/ml insulino, 0-100 mM NaCl, 100 mM natrio fosfatinis buferinis tirpalas pH 2,4 buvo inkubuojamas MHR 23 termomikseryje 24 valandas 60 °C temperatūroje nesant maišymo. Insulino agregacijos kinetikos matavimams, į anksčiau minėtus insulino tirpalus buvo pridėta 100 μM ThT. Agregacijos kinetika sekta matuojant ThT fluorescencijos intensyvumo pokytį laike naudojant Qiagen Rotor-Gene Q realaus laiko analizatorių. Agregacijos reakcijos kinetikos parametrai nustatyti taip pat kaip aprašyta [30] literatūros šaltinyje.

172 μM insulino, 100 mM NaCl, 100 mM natrio fosfatinis buferinis tirpalas pH 2,4 arba 20% acto rūgšties, 100 mM NaCl tirpalas nesant ir esant 172 μM EGCG arba $EGCG_{ox}$ buvo inkubuojamas MHR 23 termomikseryje 24 valandas 60 °C temperatūroje nesant maišymo. Insulino agregacijos kinetikos matavimams, į anksčiau minėtus insulino tirpalus buvo pridėta 100 μM ThT. Agregacijos kinetika sekta matuojant ThT fluorescencijos intensyvumo pokytį laike naudojant Qiagen Rotor-Gene Q realaus laiko analizatorių. Agregacijos reakcijos kinetikos parametrai nustatyti taip pat kaip aprašyta [30] literatūros šaltinyje.

Insulino agregatų morfologijos nustatymas. 20-30 μl insulino agregatų tirpalo buvo užnešta ant žėručio paviršiaus. Po 1 min žėrutis buvo nuplautas 1 ml distiliuoto vandens ir nudžiovintas po švelnia oro srove. Insulino agregatų morfologija vizualizuota Bruker Dimension Icon atominės jėgos mikroskopu.

Insulino ir jo agregatų antrinės struktūros nustatymas. Insulino fibrilės, susidariusios H_2O aplinkoje, buvo nucentrifuguotos (10000-20000 $\times$ g, 30 min) ir resuspenduotos D_2O. Insulino fibrilės, susidariusios D_2O aplinkoje arba resuspenduotos D_2O, buvo 1 min ardytos ultragarsu. IR sugerties spektrai išmatuoti IR Nicolet 5700 arba Bruker Vertex 80v spektrometru.

Insulino mėginių šviesos sklaidos matavimas. Pradiniai insulino tirpalai nufiltruoti per 45 μm porų dydžio švirkštinį filtrą. Šviesos sklaidos matavimai atlikti Malvern Zetasizer μV aparatu.

Insulino agregacijos kinetikos duomenų aprašymas matematiniais modeliais. Insulino agregacijos kinetikos, nesant ir esant NaCl, duomenų aprašymas matematiniais modeliais buvo atliktas naudojantis rModeler programa. Buvo panaudoti 4 modeliai: "Klasikinis", "Įsotintos elongacijos", "Klasikinis + Tetramerai" ir "Klasikinis + Uždengimas".

EGCG ir EGCG$_{ox}$ poveikio insulino amiloidinei agregacijai įvertinimas. EGCG ir EGCG$_{ox}$ poveikis insulino amiloidinei agregacijai įvertintas atlikus t_{50} ir I_{max} verčių dispersinę analizę (ANOVA).

Pelės rekombinantinio prioninio baltymo fragmento (rMoPrP) gryninimas. Pelės rekombinantinio prioninio baltymo fragmento (rMoPrP) gryninimas buvo atliktas taip pat kaip nurodyta [33, 34] literatūros šaltiniuose.

rMoPrP fibrilių formavimas. rMoPrP amiloidinės fibrilės buvo suformuotos remiantis protokolais aprašytais [21, 35] literatūros šaltiniuose. 0,5 mg/ml rMoPrP89-230, 2 M arba 4 M guanidino hidrochlorido (GuHCl), 50 mM natrio fosfatinis buferinis tirpalas, pH 6 buvo inkubuojamas 72-216 h 37 °C temperatūroje esant energingam (220 aps./min (IKA KS 4000i purtyklėje)) arba švelniam (10 aps./min (Fisherbrand Mini Tube rotatoriuje)) maišymo tipui.

rMoPrP fibrilių savireplikacijos reakcijos kinetikos matavimai. Amiloidinės rMoPrP fibrilės buvo ledo vonelėje 10 min ardytos Bandelin Sonopuls 3100 ultragarsiniu homogenizatoriumi naudojant MS 72 antgalį (esant 20% amplitudei), kas 30 s darant 30 s pertrauką.

Į 0,5 mg/ml rMoPrP monomerų, 0,5-4,5 M GuHCl, 50 μM ThT, 50 mM natrio fosfato pH 6 buferinį tirpalą pridedama 0,2-10% rMoPrP ultragarsu suardytų agregatų. Savireplikacijos reakcijos kinetika stebima skirtingose temperatūrose (40-65 °C) matuojant ThT fluorescencijos intensyvumo pokytį laike naudojant Qiagen Rotor-Gene Q realaus laiko analizatorių arba Cary Eclipse fluorimetrą. Kuomet agregacijos reakcija buvo sekama matuojant šviesos sklaidą (600 nm) naudojant Cary

Eclipse fluorimetrą, viskas buvo daryta taip pat kaip ir prieš tai tik tirpale nesant ThT.

rMoPrP morfologijos nustatymas. 20-30 μl rMoPrP agregatų tirpalo buvo užnešta ant žėručio paviršiaus. Po 45s - 1 min žėrutis buvo nuplautas 1-2 ml distiliuoto vandens ir nudžiovintas po švelnia oro srove. rMoPrP agregatų morfologija vizualizuota Bruker Dimension Icon atominės jėgos mikroskopu.

rMoPrP fibrilių antrinės struktūros nustatymas. rMoPrP fibrilės buvo nucentrifuguotos (15000$\times$g, 30 min) ir resuspenduotos. Tuomet resuspendotos fibrilės buvo 1 min ledo vonelėje, ardytos Bandelin Sonopuls 3100 ultragarsiniu homogenizatoriumi naudojant MS 72 antgalį (esant 20% amplitudei). IR sugerties spektrai išmatuoti Bruker Alpha arba Bruker Vertex 80v IR spektrometru.

Aβ42 agregacijos kinetikos matavimas. Paruošiami du Aβ42 tirpalai: 5 μM Aβ42, 200 μM EDTA, 0,02% NaN_3, 20 mM fosfatinis buferinis tirpalas, pH 8 be ThT ir su 20 μM ThT. Tirpalai išpilstomi po kelis pakartojimus po 80 μM į 96 šulinėlių plokštelę. Plokštelės su mėginiais patalpinamos į Fluostar Omega mikroplokštelių skaitytuvą. Inkubuojama 37 °C temperatūroje nesant maišymo. Aβ42 agregacijos kinetika sekama matuojant mėginių, į kuriuos buvo įdėta ThT, ThT fluorescencijos intensyvumo pokytį laike. Mėginiai, į kuriuos nebuvo įdėta ThT, buvo surinkti iš plokštelės po 0, 15, 30, 60 ir 120 min inkubacijos ir iškart užnešti ant žėručio paviršiaus panaudojant mikrolašelių išpurškimo platformą [36].

Aβ42 agregatų užnešimas ant substrato panaudojant mikrolašėlių išpurškimo platformą. Mėginiai, paimti skirtingu Aβ42 agregacijos reakcijos laiko momentu, 100 μL/h greičiu suleidžiami į mikrolašelių išpurškimo platformą panaudojant švirkštinę pompą ir panaudojant suspausto azoto dujas (3 bar) išpurškiami ant žėručio paviršiaus. Mėginio išpurškimas vykdomas 30s, atstumas nuo mikrolašelių išpurškimo platformos iki žėručio paviršiaus buvo 4 cm.

Aβ42 agregatų morfologijos vizualizavimas. Aβ42 agregatų mėginių, užneštų ant žėručio paviršiaus, morfologija buvo vizualizuota PARK Systems NX10 atominės jėgos mikroskopu.

Rezultatai ir jų aptarimas

Konformacinis insulino fibrilių variabilumas

Siekiant nustatyti DMSO poveikį insulino agregacijos procesui, atlikti insulino fibrilių, spontaniškai susiformavusių D_2O aplinkoje nesant ir esant 5% DMSO, antrinės struktūros tyrimai infraraudonųjų (IR) spindulių spektroskopijos metodu (Pav. 1). Taip pat, siekiant išsiaiškinti galimus pokyčius paskatintus D_2O naudojimo vietoje H_2O, kas buvo būtina norint išvengti H_2O ir baltymų amido I IR spektro dedamųjų persiklojimo [37], bei siekiat nustatyti ar mažas pH pokytis turi įtakos insulino fibrilių susidarymui, insulino fibrilės buvo pagamintos D_2O esant pH^* 1,6 ir pH^* 2 (kur pH^* yra pH-metro rodmuo neatsižvelgus į izotopinį efektą [38]). pH^* 1,6 buvo pasirinktas siekiant imituoti aplinką, kurioje D^+ ir H^+ koncentracijos būtų panašios [39]. Tuo metu pH^* 2 buvo pasirinktas siekiant sukurti aplinką, kurioje baltymo molekulės šoninių funkcinių grupių jonizacijos laipsnis D_2O aplinkoje būtų panašus į jonizacijos laipsnį H_2O aplinkoje [38].

Insulino amiloidinių fibrilių antrinės struktūros tyrimas. Insulino amiloidinių fibrilių, susidariusių nesant ir esant DMSO, IR sugerties spektrai atrodo identiškai (Pav. 1), tačiau įdomu tai, jog mažas pH^* skirtumas nulėmė insulino fibrilių, su skirtingais amido I' profiliais, susidarymą (Pav. 1A). Insulino fibrilių, susiformavusių pH^* 2 aplinkoje, IR sugerties spektro antroji išvestinė turi du minimumus amido I' regione, vieną ties 1628 cm^{-1} bei kitą ties 1615 cm^{-1}. Tuo metu insulino fibrilių, susiformavusių pH^* 1,6 aplinkoje, FTIR spektro antroji išvestinė turi du minimumus ties 1619 cm^{-1} ir 1631 cm^{-1} (Pav. 1B). Insulino fibrilės, susiformavusios pH^* 1,6 aplinkoje, taip pat turi papildomą IR sugerties signalo dedamąją ne amido I' regione ties 1728 cm^{-1}. Panašios spektrinės charakteristikos nesenai buvo įvardintos kaip vienas iš pagrindinių skirtingų insulino fibrilių kamienų požymių [40, 41].

Įdomu tai, kad insulino fibrilių, susidariusių H_2O aplinkoje esant pH 1,6 arba pH 2, IR sugerties spektrai yra identiški (Pav. 1C). Tiek pH 1,6, tiek pH 2 aplinkoje susidariusių fibrilių IR sugerties spektro antroji

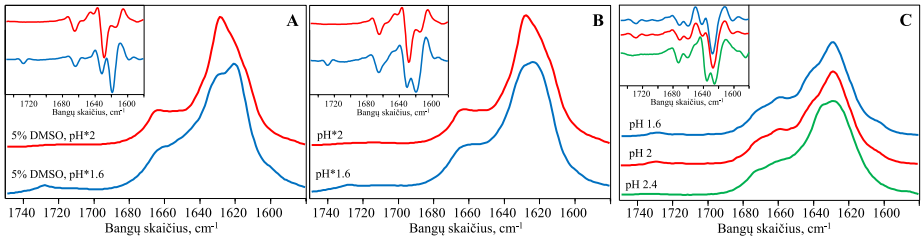

PAV. 1: Insulino fibrilių, susidariusių D_2O tirpale esant (A) ir nesant (B) 5% DMSO, arba H_2O tirpale esant skirtingam pH (C), IR sugerties spektrai ir jų antrinės išvestinės (įterptinis grafikas).

išvestinė turi du minimumas amido I/I' regione ties 1628 cm^{-1} ir 1641 cm^{-1}, bei vieną minimumą ties $\approx$1730 cm^{-1} ne amido I/I' regione. Tuo metu insulino fibrilių, susidariusių H_2O aplinkoje esant pH 2,4, IR sugerties spektras skiriasi nuo prieš tai aptartų, IR sugerties spektro antroji išvestinė turi du minimumas ties 1625 cm^{-1} ir 1636 cm^{-1} (Pav. 1C). Amiloidinių fibrilių antrinės struktūros elementai yra gerai apsaugoti nuo vandenilio/deuterio mainų, todėl daugumos amido grupių vandenilio molekulės yra nepakitusios nepaisant to, jog fibrilės buvo resuspenduotos D_2O. Tai atsispindi ir fibrilių resuspenduotų D_2O IR spektre, kuris lyginant su D_2O pagamintų fibrilių IR spektru yra pasistūmęs link didesnio bangų skaičiaus.

Nesenai literatūroje buvo aprašytas tyrimas, kurio rezultatai iš pirmo žvilgsnio prieštarauja šio darbo rezultatams [42–44]. Šių tyrimų metu nebuvo pastebėta jokių skirtumų tarp insulino fibrilių, susidariusių esant skirtingam aplinkos pH (pH 1,3-3,1), IR sugerties spektrų. Tačiau pastarųjų IR spektrų amido I regiono forma yra labai panaši į fibrilių susiformavusių pH^* 2 aplinkoje. Pastaruosiuose tyrimuose naudota insulino koncentracija buvo 60 mg/ml (10 kartų daugiau nei šio tyrimo metu), tai reiškia, kad monomerų-oligomerų pusiausvyra buvo stipriai pastumta link oligomerinių insulino formų, nes insulinas oligomerizuojasi net ir daug žemesnėse koncentracijose [45–47]. Todėl galime daryti prielaidą, kad monomerų-oligomerų pusiausvyra yra galimai pagrindinis faktorius nulemiantis skirtingų insulino fibrilių kamienų susidarymą.

Siekiant patikrinti šią hipotezę buvo atlikti keli papildomi tyrimai.

Visų pirma buvo patikrinta ar pusiausvyros poslinkis link oligomerinių insulino formų susidarymo gali paaiškinti skirtumus tarp pH* 1,6 tipo ir pH* 2 tipo fibrilių kamienų. 10 mM insulino fibrilių, susidariusių pH* 1,6 aplinkoje, IR sugerties spektras skiriasi nuo 1 mM insulino fibrilių, susidariusių pH* 1,6 aplinkoje, spektro (Pav. 2A). Tai leidžia daryti prielaidą, kad padidėjusi insulino koncentracija nulemia kito insulino fibrilių kamieno susidarymą. Tačiau pastarasis IR spektras taip pat skiriasi ir nuo 1 mM insulino fibrilių, susidariusių pH* 2 aplinkoje, spektro (Pav. 2A). Todėl šie rezultatai nepaaiškina iškeltos hipotezės. Toliau buvo pakartoti jau anksčiau literatūroje aprašyti insulino agregacijos eksperimentai esant 20% etanolio, bei atlikti agregacijos eksperimentai esant 20% DMSO (Pav. 2B). Insulino agregacijos pH* 2 tirpale esant 20% bet kurio iš šių dviejų organinių tirpiklių, susiformuoja insulino fibrilės, kurių IR sugerties spektras yra labai panašus į pH* 1,6 aplinkoje susidarančio insulino fibrilių kamieno spektrą. Šie rezultatai patvirtina, kad etanolis ir mažesniu mastu DMSO, pastumia pusiausvyrą link monomerinės insulino formos ir tuo pačiu link pH* 1,6 tipo fibrilių susidarymo

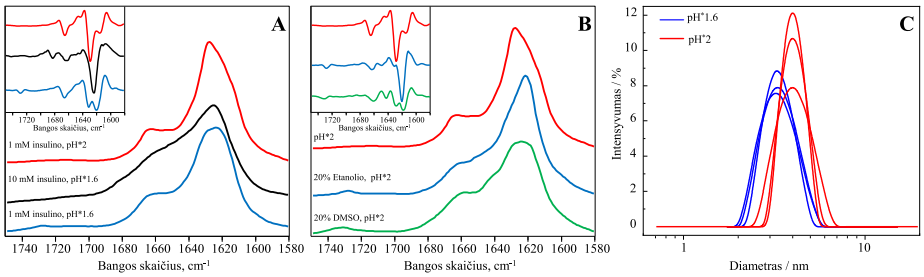

PAV. 2: Insulino fibrilių, susidariusių esant aukštai insulino koncentracijai (A) arba tirpale esant organinių tirpiklių (B), IR sugerties spektrai ir jų antrinės išvestinės (įterptinis grafikas). Insulino dalelių dydžio pasiskirstymas pH* 1.6 ir pH* 2 tirpale (C).

Galiausiai siekiant nustatyti insulino dalelių dydžio pasiskirstymą pH* 1,6 ir pH* 2 tirpaluose, atlikti šių mėginių dinaminės šviesos sklaidos (DLS) matavimai (Pav. 2C). Vidutinis insulino, ištirpinto pH* 1,6, dydis yra mažesnis nei insulino ištirpinto pH* 2. pH* 1,6 tirpale insulino diametras yra 3.4 $\pm$ 0.7 nm, tai yra šiek tiek daugiau nei insulino monomero diametras, tačiau mažiau nei insulino dimero

diametras [48]. Tuo metu pH* 2 tirpale insulino diametras yra 4.0 ± 0.6 nm, tai yra šiek tiek daugiau nei insulino dimero diametras. DLS matavimai leidžia nustatyti tik vidurkinį polidispersiško tirpalo dalelių dydį, todėl tikslaus monomerų-oligomerų pasiskirstymo neįmanoma nustatyti. Tačiau tai, kad aukštesnis pH* pastumia pusiausvyrą link insulino dimerinės/oligomerinės formos yra akivaizdu.

Remiantis visais gautais rezultatais ir pastebėjimais galime daryti išvadą, jog insulino monomerų-oligomerų pusiausvyra yra vienas pagrindinių faktorių nulemiančių skirtingos konformacijos insulino fibrilių susidarymą.

Neamiloidogeninės oligomerinės insulino formos tiesiogiai dalyvauja insulino agregacijos procese ir jį slopina

Siekiant detalaus insulino polimorfizmo supratimo yra būtina atlikti mechanistinius insulino agregacijos tyrimus. Globalus kinetinių kreivių aprašymas eksperimentiniais modeliais leidžia nustatyti galimus amiloidinės agregacijos mechanizmus [12, 49–54]. Pavyzdžiui, insulino agregacijos pH 1,6 aplinkoje kinetikos analizė leido nustatyti, kad šiomis sąlygomis insulino agregacija vyksta pagal "Klasikinį" amiloidų agregacijos mechanizmą su įsotintos elongacijos žingsniu [49]. Siekiant išsiaiškinti galimus mechanistinius skirtumus nulemiančius pH-sužadintą insulino fibrilių polimorfizmą, insulino agregacijos pH 2,4 aplinkoje kinetikos duomenis pabandėme aprašyti keletu eksperimentinių modelių. Yra žinoma, jog NaCl gali paveikti amiloidinės agregacijos kinetiką, taip pat gali paskatinti baltymo struktūros pokyčius, ar net daryti įtaką baltymo agregacijos mechanizmui, dėl ko gali susiformuoti skirtingi fibrilių kamienai. Dėl visų šių priežasčių mes stebėjome insulino agregacijos procesą esant kelioms skirtingoms NaCl koncentracijoms.

Pradinės ir agreguotos insulino formų charakterizavimas. Insulino tirpalų DLS matavimai atskleidė, jog vidutinis insulino dalelių dydis priklauso nuo NaCl koncentracijos (Pav. 3A). Maksimalus šviesos išsibarstymas nesant NaCl yra ties 3.7 ± 0.1 nm dalelių diametru, kas yra

šiek tiek mažiau nei insulino dimero diametras (≈3.9 nm [48]). Didinant NaCl koncentraciją tirpale vidutinis dalelių diametras padidėja iki 3.9 ± 0.3 nm esant 50 mM NaCl ir galiausiai pasiekia 4.3 ± 0.1 nm tirpale esant 100 mM NaCl. Pastarųjų dalelių diametras yra šiek tiek mažesnis nei insulino tetramero (≈5 nm [48]). Toks laipsniškas dalelių dydžio didėjimas leidžia daryti prilaidą jog kylanti tirpalo joninė jėga skatina didesnių oligomerų susidarymą. Kadangi monomerų-oligomerų pusiausvyra priklauso nuo baltymo koncentracijos, tai ir išmatuotas dalelių dydžio pasiskirstymas yra priklausomas nuo baltymo koncentracijos. Nesant NaCl, hidrodinaminis insulino spindulys padidėja nežymiai insulino koncentracijai augant nuo 0,5 iki 5 mg/mL (Pav. 3B). Tuo metu daug didesnis dalelių dydžio pokytis, kuris yra aiškiausiai matomas esant aukštai insulino koncentracijai, yra pastebimas insulino tirpale esant 100 mM NaCl. Šie rezultatai leidžia daryti prielaidą, jog visame insulino koncentracijų ruože nesant ir iki 2 mg/mL insulino esant NaCl egzistuoja monomerų-dimerų pusiausvyra. Tuo metu esant NaCl ir insulino koncentracijai $>$ 2 mg/mL pusiausvyra yra paslinkta link insulino tetramerų.

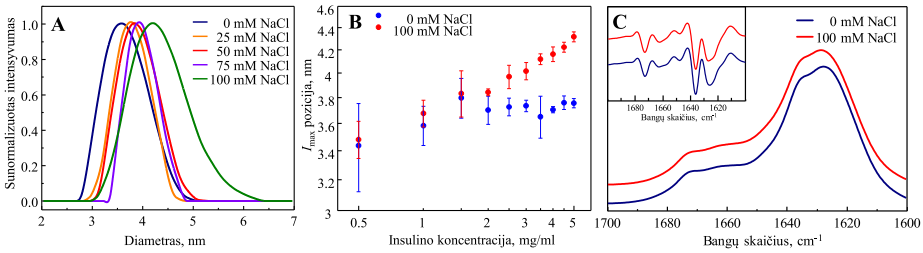

PAV. 3: Dalelių dydžio pasiskirstymas pradiniuose insulino tirpaluose ir insulino agregatų antrinės struktūros profiliai esant skirtingai NaCl koncentracijai. A - šviesos išsibarstymo intensyvumo pasiskirstymas. B - šviesos išsibarstymo smailės viršūnės pozicijos priklausomybė nuo insulino koncentracijos. C - Insulino fibrilių, susiformavusių tirpale, nesant ir esant NaCl, IR sugerties spektrai ir jų antrosios išvestinės (įterptinis grafikas).

Insulino fibrilių, susiformavusių pH 2,4 aplinkoje nesant ir esant NaCl, FTIR spektrai yra beveik identiški (Pav. 3C). Antroji FTIR spektrų išvestinė turi dvi dedamąsias amido I/I' regione ties 1636 cm^{-1} ir 1627 cm^{-1}, kurios yra tipiškos β-klostėms. Taigi, galime daryti išvadą, jog

tiek nesant, tiek esant iki 100 mM NaCl, susiformuoja tokio pačio tipo amiloidinės insulino fibrilės.

Insulino agregacijos kinetika. Iš insulino agregacijos puslaikio grafiko (Pav. 4A) matyti, kad tirpale nesant druskos t_{50} mažėja didėjant pradinei insulino koncentracijai, kol galiausiai pasiekia plato. Šie rezultatai leidžia daryti prielaidą, jog yra stebimas įsotinimo efektas [55]. Maža kreivės krypties koeficiento reikšmė, kuri galiausiai tampa lygi $\approx$0 aukštose insulino koncentracijose, leidžia daryti prielaidą, jog agregatų ilgėjimo ir lūžinėjimo procesai yra įsotinti [12], t. y. negali vykti greičiau toliau augant insulino koncentracijai.

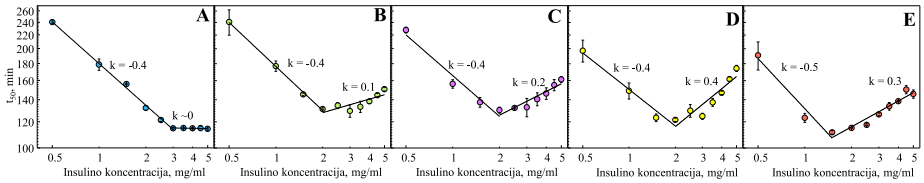

PAV. 4: Insulino agregacijos puslaikio priklausomybės nuo pradinės insulino koncentracijos esant 0 mM (A), 25 mM (B), 50 mM (C), 75 mM (D), 100 mM (E) NaCl koncentracijai.

Tirpale nesant druskos yra stebima neįprasta t_{50} priklausomybė nuo insulino koncentracijos (Pav. 4B-E). Iš pradžių t_{50} mažėja didėjant insulino koncentracijai, tačiau pasiekus tam tikrą koncentraciją ("lūžio" tašką) vėl ima augti. Šis fenomenas negali būti susijęs su įsotinimo efektu, nes po lūžio taško t_{50} nenusistovi, o ima didėti. Mūsų žiniomis, teigiama kreivės krypties koeficiento reikšmė nėra siejama nei su vienu žinomu eksperimentiniu modeliu ar agregacijos mechanizmu.

Eksperimentiniai modeliai. Keturi pagrindiniai įvykiai, apibūdinantys amiloidinės agregacijos procesą, yra priminė ir antrinė nukleacija, fibrilių ilgėjimas ir lūžinėjamas. Eksperimentinis modelis, į kurį yra įtraukti visi šie procesai, yra vadinamas "Klasikiniu" (Pav. 5). Tam tikrais atvejais šis modelis nesugeba aprašyti eksperimentinių duomenų ir dalinės modelio modifikacijos ar naujų mikroskopinių agregacijos žingsnių įtraukimas yra būtinas [12, 13, 49, 51, 53, 56]. Insulino koncentracijai esant didesnei nei 1,5 mg/ml, buvo matoma aiški insulino hidrodinaminio spindulio divergencija tirpale nesant ir

esant 100 NaCl (Pav. 3B), tai sutampa ir su lūžio tašku insulino agregacijos puslaikio grafikuose (Pav. 4). Taigi, yra matoma aiški koreliacija tarp insulino oligomerų susidarymo ir agregacijos laiko ilgėjimo (t_{50} didėjimo). Remiantis visais pastebėjimais mes iškėlėme hipotezę, jog neįprasta t_{50} priklausomybė nuo pradinės insulino koncentracijos galimai atsiranda dėl susidariusių insulino oligomeru (tetramerų), kurie nedalyvauja tiesiogiai agregacijos reakcijoje, tačiau gali "uždengti" agregacijos centro ar fibrilės galus (Pav. 5) ir taip slopinti jų ilgėjimą ir tuo pačiu agregacijos reakciją.

Modelis	Pirminė nukleacija	Elongacija	Įsotinta elongacija	Antrinė nukleacija	Lūžinėjimas	Monomerų-tetramerų pusiausvyra	„Uždengimas“
„Klasikinis”	+	+		+	+		
„Įsotintos elongacijos”	+		+	+	+		
„Klasikinis + Tetramerai”	+	+		+	+	+	
„Klasikinis + uždengimas”	+	+		+	+	+	+

PAV. 5: Keturi agregacijos modeliai ir juos sudarantys mikroskopiniai agregacijos įvykiai apibūdinantys amiloidinės agregacijos procesą. Greičio konstantos yra žymimos: k_n (pirminės nukleacijos), k_+ (elongacijos), k_2 (antrinės nukleacijos), k_- (lūžinėjimo), k_f ir k_r (tarpinių formų asociacijos ir disociacijos), K_E (monomerų-tetramerų pusiausvyros), ir k_c (agregacijos centrų "uždengimo").

Globalus eksperimentinių duomenų aprašymas. "Klasikinis", "Įsotintos elongacijos", "Klasikinis + Tetramerai" ir "Klasikinis + Uždengimas" agregacijos modeliai buvo panaudoti aprašyti eksperimentinius duomenis gautus insulino agregacijos metu esant penkios skirtingoms NaCl koncentracijoms. "Klasikinis" modelis buvo vienintelis modelis kuris nesugebėjo pakankamai gerai aprašyti insulino agregacijos kinetikos, nesant NaCl (duomenys darbo santraukoje nepateikti). Tai reiškia, kad papildomi žingsniai kaip įsisotinęs fibrilių ilgėjimo procesas ar oligomerų, kurie tiesiogiai nedalyvauja agregacijos reakcijoje, susidarymas, yra reikalingi norint aprašyti insulino agregacijos procesą pH 2,4 tirpale nesant NaCl.

Kaip ir buvo tikėtasi, modeliai, kuriuose nėra įtrauktas agregacijos slopinimo žingsnis, nesugebėjo tinkamai aprašyti insulino agregacijos,

esant 100 mM NaCl, kinetikos duomenų (Pav. 6A-C). Vienintelis modelis, kuris sugebėjo tinkamai aprašyti eksperimentinius duomenis buvo tas kuris numato galimą neamiloidogeninių oligomerų, kurie gali slopinti agregacijos reakciją, susidarymą (Pav. 6D). Iš DLS rezultatų (Pav. 3) galime spręsti, jog aukštos koncentracijos insulino tirpaluose esant 100 mM NaCl pusiausvyra yra stipriai pastumta link tetramerinės insulino formos, o tuo metu nesant NaCl tik labai maža dalis insulino bus tetramerinėje formoje. Šie rezultatai paaiškina tiek kodėl tik tie modeliai, kuriuose yra įtrauktas monomerų-oligomerų pusiausvyros žingsnis, sugeba gerai aprašyti eksperimentinius duomenis gautus nesant NaCl, tiek tai, kad modelis, numatantis agregacijos proceso slopinimo insulino tetramerais galimybę, yra vienintelis sugeba tinkamai aprašyti eksperimentinius duomenis gautus esant NaCl. Jei padarysime prielaidą, kad NaCl pridėjimas į insulino tirpalą nepakeičia insulino agregacijos mechanizmo, o tik paveikia mikroskopinių agregacijos žingsnių greičius, tuomet galime daryti išvadą, kad modelis numatantis agregacijos reakcijos slopinimą insulino tetramerais yra tas, kuris paaiškina insulino agregacijos pH 2,4 tirpale mechanizmą.

Paprastai oligomerinės insulino formos yra laikomos tarpinėmis, neamiloidogeninėmis formomis, kurios tik laikinai sumažina agreguoti galinčių insulino monomerų koncentraciją [30–32]. Šiame darbe pateikiame įrodymus apie galimą tiesioginį insulino oligomerinių formų vaidmenį amiloidinių fibrilių susidarymo procese. Šios mechanistinės įžvalgos ženkliai prisideda prie gilesnio insulino agregacijos mechanizmo supratimo.

Aplinkos sąlygos yra vienas iš pagrindinių faktorių nulemiančių potencialių prieš amiloidinių junginių identifikavimą

Galybė mažos molekulinės masės junginių, trumpų peptidų, ir antikūnų buvo pasiūlyti kaip potencialūs toksinių oligomerinių ir fibrilinių agregatų susidarymo slopikliai [57–62]. Deja, nepaisant reikšmingų mokslininkų pastangų, šiai dienai nėra nė vieno efektyvaus vaistinio preparato skirto su amiloidais siejamoms ligoms gydyti [63–68].

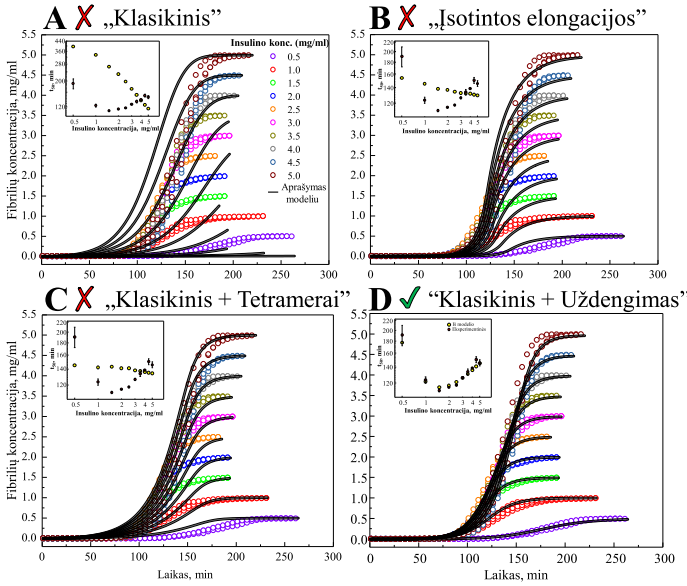

PAV. 6: Globalus insulino agregacijos kinetikos, esant 100 mM NaCl, aprašymas "Klasikiniu" (A), "įsotintos elongacijos" (B), "klasikinis + tetramerai" (C) ir "klasikinis + uždengimas" (D) modeliais. Įterptiniame grafike yra palygintos eksperimentiškai nustatytos ir iš modelio nustatytos t_{50} vertės.

Epigalokatechino-3-galatas (EGCG) yra vienas iš pagrindinių polifenolių randamų žaliojoje arbatoje. Literatūros šaltiniuose EGCG yra įvardinamas kaip efektyvus keleto amiloidinių baltymų agregacijos slopiklis [69–72]. Taip pat buvo pademonstruota, jog EGCG gali paskatinti susiformavusių fibrilių persitvarkymą / disociaciją [69, 70, 72–74]. Bendrai paėmus EGCG gali būti laikomas "universaliu" amiloidinės agregacijos slopikliu. Tačiau, EGCG yra nestabilus neutraliame ar šarminiame pH [75–78] kur jis auto-oksiduojasi. EGCG auto-oksidacijos metu susidaro keletas produktų iš kurių kiekvienas gali turėti skirtingą poveikį amiloidinei agregacijai [79–81].

Šiame darbe nusprendėme įvertinti EGCG poveikį insulino fibrilių susidarymui esant skirtingoms aplinkos sąlygoms.

Insulino agregacijos kinetikos nesant ir esant EGCG arba EGCG$_{ox}$ tyrimas. Visų pirma nustatėme EGCG ir jo auto-oksidacijos produktų (EGCG$_{ox}$) poveikį insulino agregacijos kinetikai ir maksimaliam ThT

fluorescencijos intensyvumui (I_{max}). Kuomet insulino agregacijos reakcija buvo vykdoma 100 mM fosfatiniame buferiniame tirpale, pH 2,4 (PB) be maišymo, pridėjus EGCG insulino agregacijos puslaikis (t_{50}) padidėjo, o I_{max} sumažėjo du kartus lyginant su kontrole (Pav. 7). EGCG$_{ox}$ efektas buvo daug stipresnis, t_{50} padidėjo, o I_{max} sumažėjo beveik 4 kartus. Esant maišymui PB, EGCG beveik neturėjo poveikio, o EGCG$_{ox}$ poveikis insulino amilodinei agregacijai buvo nežymus (Pav. 7).

EGCG nedaro jokio poveikio t_{50} ar I_{max} kuomet insulino agregacijos reakcija yra vykdoma 20% acto rūgštyje (AC) tiek nesant tiek esant maišymui (Pav. 7). Lyginant su kontrole, nesat maišymo AC pridėjus EGCG$_{ox}$ t_{50} padidėjo du kartus, o I_{max} padidėjo net 20 kartų (Pav. 7). Esant maišymui AC, pridėjus EGCG$_{ox}$ I_{max} padidėja 3 kartus, t_{50} nuo kontroles skiriasi nežymiai.

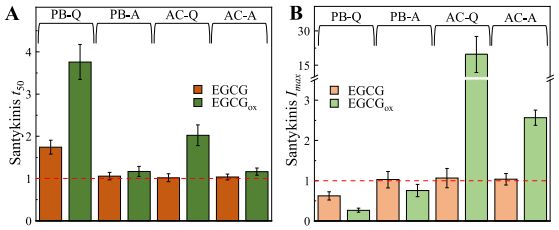

PAV. 7: EGCG ir EGCG$_{ox}$ poveikis insulino agregacijos kinetikai (A) ir maksimaliam ThT fluorescencijos intensyvumui (B). PB - 100 mM fosfatinis buferinis tirpalas. AC - 20% acto rūgšties tirpalas. Q - agregacijos reakcija vyksta nesant maišymo. A - agregacijos reakcija vyksta esant maišymui. Paklaidos yra standartiniai nuokrypiai.

Insulino agregatų susidariusių skirtingomis aplinkos sąlygomis nesant ir esant EGCG arba EGCG$_{ox}$ morfologijos tyrimas atominės jėgos mikroskopu. Mėginių analizė atominės jėgos mikroskopu patvirtino, kad visais atvejais praėjus 15 val nuo agregacijos reakcijos pradžios susiformuoja kelių mikrometrų ilgio ir 3-10 nm aukščio amiloidinės insulino fibrilės (Pav. 8). PB susiformavusios fibrilės yra linkusios sulipti į guzus, didesni guzai yra matomi kuomet agregacijos reakcija buvo vykdoma esant purtymui. Mėginyje esant EGCG$_{ox}$ fibrilės atrodo mažiau sulipusios. Lyginant su kontrole, AC susiformuoja daugiau fibrilių kuomet mėginyje yra EGCG$_{ox}$. Mėginyje esant EGCG, visomis tirtomis sąlygomis susidaro amiloidinės fibrilės panašios į tas

kurios susidarė atitinkamomis aplinkos sąlygomis be EGCG.

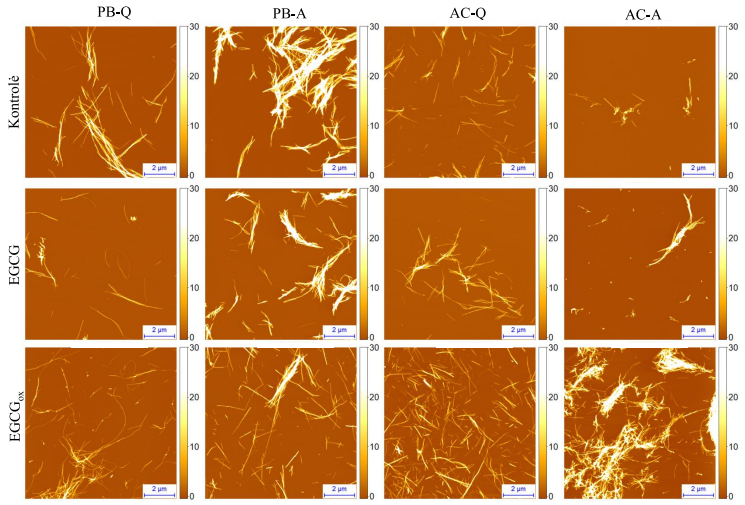

PAV. 8: Insulino agregatai susidarę skirtingomis aplinkos sąlygomis nesant ir esant EGCG arba EGCG$_{ox}$.

Insulino fibrilių antrinės struktūros charakterizavimas. Insulino fibrilių, susidariusių AC nesant ir esant maišymui, antrosios FTIR spektrų išvestinės yra beveik identiškos, abi turi du minimumus amido I/I' regione ties 1627 cm^{-1} ir 1641 cm^{-1}, bei papildomą minimumą ne amido I/I' regione ties 1729 cm^{-1} (Pav. 9). Insulino fibrilių, susiformavusių PB esant maišymui, antroji FTIR spektro išvestinė taip pat panaši į prieš tai aptartų fibrilių, tačiau matomas tik vienas minimumas amido I/I' regione ties 1627 cm^{-1}. Insulino fibrilių, susiformavusių PB nesant maišymui, FTIR spektro išvestinė turi du minimumus amido I/I' regione ties 1625 cm^{-1} ir 1637 cm^{-1}. Rezultatai leidžia teigti, jog fibrilės susidariusios PB nesant maišymo yra struktūriškai skirtingos nuo susidariusių AC. Tuo metu fibrilių, susidariusių PB esant maišymui, antrinės struktūros profilis atrodo kaip tarpinis tarp fibrilių susidariusių PB nesant purtymo ir fibrilių susidariusių AC tiek nesant tiek esant purtymui.

Junginių poveikio amiloidinės agregacijos procesui įvertinimas. Junginių poveikis amiloidinių fibrilių susidarymo procesui yra dažnai vertinamas lyginant agregacijos kinetiką [52, 56] ir/arba maksimalų

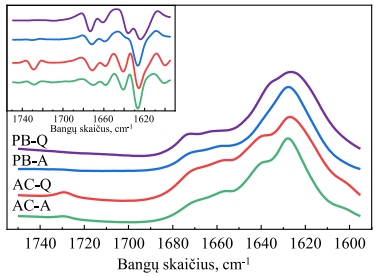

PAV. 9: Insulino fibrilių susiformavusių PB arba AC tirpale nesant ir esant maišymui IR sugerties spektrai ir jų antrosios išvestinės (įterptinis grafikas).

ThT fluorescencijos intensyvumą [82, 83] mėginyje esant ir nesant junginio. Šiame darbe EGCG ir $EGCG_{ox}$ poveikis insulino agregacijai, kuri vyko skirtingomis aplinkos sąlygomis buvo įvertinas naudojant abu ankščiau minėtus faktorius (Pav. 7) (Lentelė 1). Jei t_{50} ir/arba I_{max} pokytis būtų pasirinktas kaip pagrindinis vertinimo kriterijus, tuomet EGCG būtų indikuotas kaip potencialus amiloidinės agregacijos slopiklis tik jei agregacijos reakcija vyktų PB nesant purtymo. $EGCG_{ox}$ būtų indikuotas kaip potencialus agregacijos slopiklis nepaisant pasirinkto vertinimo kriterijaus jei agregacijos reakcija vyktų PB nesant arba esant purtymui. Tuo tarpu jei reakcija vyktų AC vertinant pagal t_{50} pokytį $EGCG_{ox}$ būtų indikuotas kaip agregacijos slopiklis, o jei pagal I_{max} - kaip agregaciją skatinanti molekulė. Remiantis rezultatais galime daryti prielaidą, jog priklausomai nuo to kokiomis sąlygomis yra vykdoma agregacijos reakcija, bei koks kriterijus yra pasirinktas nustatyti tiriamos molekulės poveikiui, tas pats junginys gali būti indikuotas kaip anti-amiloidinis ir ne.

Akivaizdu, jog aplinkos sąlygos, kuriomis yra atliekama amiloidų agregacijos reakcija ir tiriamas molekulės poveikis jai, bei kriterijai kuriais remiantis yra vertinamas poveikis, yra ypač svarbūs faktoriai kurie nulemia ar molekulė bus identifikuota kaip potencialus prieš amiloidinis vaistas ar ne. Todėl molekulių poveikis amiloidinės agregacijos procesui turėtų būti vertinamas agregacijos reakciją atliekant keliose skirtingose aplinkos sąlygose. Tai leistų padidinti sėkmę tolimesniuose prieš klinikiniuose ir klinikiniuose tyrimuose.

LENTELĖ 1: EGCG ir $EGCG_{ox}$ poveikio insulino agregacijos procesui vertinimas.

Vertinant pagal t_{50} pokytį		
Sąlygos	EGCG	$EGCG_{ox}$
PB-Q	Slopinantis[1]	Slopinantis
PB-A	Nėra poveikio	Slopinantis
AC-Q	Nėra poveikio	Slopinantis
AC-A	Nėra poveikio	Slopinantis
Vertinant pagal I_{max} pokytį		
Sąlygos	EGCG	$EGCG_{ox}$
PB-Q	Slopinantis	Slopinantis
PB-A	Nėra poveikio	Slopinantis
AC-Q	Nėra poveikio	Skatinantis
AC-A	Nėra poveikio	Skatinantis

[1]Nustatyta atlikus t_{50} arba I_{max} dispersinę analizę (ANOVA).

Konformacinis amiloidinių fibrilių variabilumas priklauso nuo pradinės agregatų, dalyvaujančių fibrilių savireplikacijos reakcijoje, koncentracijos

Viena iš įdomiausių amiloinių baltymų savybių yra tai, kad tas pats baltymas gali suformuoti struktūriškai skirtingas amiloidines fibriles, kitaip dar vadinamas "kamienais". Prioniniai baltymai yra vienas iš geriausių to pavyzdžių [20, 28, 84]. Buvo pastebėta, jog tam tikrais atvejais prioninio baltymo agregatus perkėlus į kitas aplinkos sąlygas gali susiformuoti ir kito kamieno fibrilės [9, 84–86]. Šis fenomenas dar vadinamas "kamienų mutacija" arba "konformaciniu pasikeitimu". Nors tiksli šio fenomeno kilmė nėra žinoma yra manoma, kad tam tikrais atvejais pokyčiai aplinkos sąlygose paskatina susidaryti to tipo agregatus, kurie yra labiausiai tinkami savireplikuotis esamoje aplinkoje. Antrinės nukleacijos metu naujų agregacijos branduolių susidarymas yra katalizuojamas jau susidariusių amiloidinių fibrilių paviršiaus. Tačiau nėra aišku ar taip susiformavusių agregacijos branduolių struktūra yra nulemta aplinkos sąlygų ar fibrilių struktūros. Taigi kyla klausimas: ar antrinė nukleacija gali būti atsakinga už amiloidinių fibrilių kamienų mutaciją?

Konformaciškai skirtingų fibrilių formavimas. Monomerinis rMoPrP89-230 buvo inkubuojamas 2 arba 4 M guanidino hidrochlorido (GuHCl) tirpale, susiformavę agregatai buvo atitinkamai pavadinti rPrP-A^{2M} ir rPrP-A^{4M}. Konformacinis agregatų stabilumas, kuris yra apibūdinamas kaip atsparumas chemikalais inicijuotai fibrilių depolimerizacijai, yra vienas iš pagrindinių kriterijų pagal kurį galima atskirti skirtingus fibrilių kamienus [21, 24]. rPrP-A^{2M} ir rPrP-A^{4M} fibrilių kamienų konformacinis stabilumas yra skirtingas (Pav. 10). rPrP-A^{2M} fibrilių depolimerizacijos kreivės vidurio taškas yra ties ≈1,8 M guanidino tiocianato (GuSCN), o rPrP-A^{4M} - ties ≈3,0 M GuSCN. Šie rezultatai leidžia daryti prielaidą, jog suformavome skirtingus rMoPrP89-230 fibrilių kamienus.

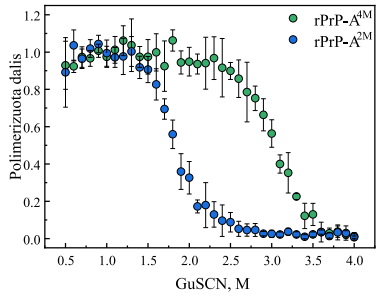

PAV. 10: rPrP-A^{2M} ir rPrP-A^{4M} fibrilių depolimerizacijos kreivės. Paklaidos yra standartiniai nuokrypiai.

Amiloidinių fibrilių savireplikacijos reakcijos kinetika. Jau anksčiau buvo pademonstruota, kad rPrP-A^{2M} kamienas negali savireplikuotis GuHCl koncentracijose aukštesnėse nei 2.5 M [33], todėl galime tirti tik rPrP-A^{4M} galimybę savireplikuotis 2 M GuHCl, bet ne rPrP-A^{2M} - 4 M GuHCl. rPrP-A^{4M} savireplikacijos kinetika 2 M GuHCl, esant kelioms rPrP-A^{4M} koncentracijoms, buvo stebima matuojant ThT fluorescencijos intensyvumą (Pav. 11A, B, C). Į rMoPrP89-230 monomerų tirpalą 2 M GuHCl pridėjus 5% (nuo bendros baltymo koncentracijos) rPrP-A^{4M} agregatų, stebimas labai staigus ThT fluorescencijos pokytis, todėl galime teigti jog fibrilių ilgėjimas yra labai greitas (Pav. 11A). Pridėjus 1% rPrP-A^{4M} agregatų, fibrilių ilgėjimas yra lėtas agregacijos reakcijos pradžioje, tačiau po kurio laiko labai staigiai pagreitėja (Pav. 11B).

Pridėjus 0,2% rPrP-A^{4M} agregatų, fibrilių ilgėjimas yra labai lėtas (Pav. 11C), agregacijos reakcijos kinetika yra sigmoidinės formos, kuri yra būdinga spontaninės agregacijos reakcijos kinetikai. Tačiau nesant sėklos, spontaninis agregatų susidarymas per eksperimentinį laiko tarpą nebuvo pastebėtas.

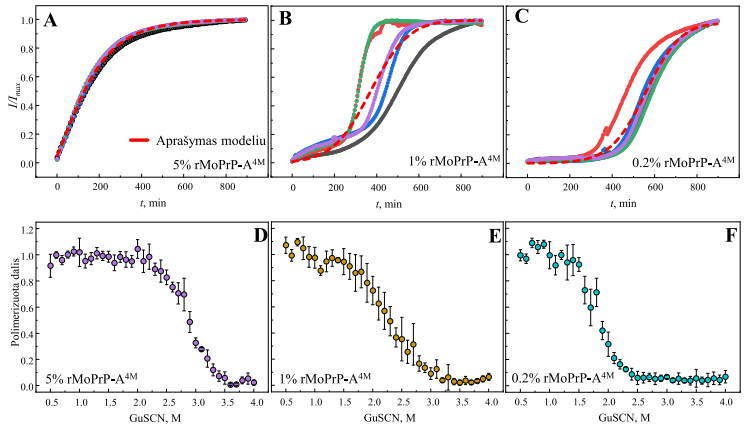

PAV. 11: rPrP-A^{4M} fibrilių savireplikacijos reakcijos kinetika esant skirtingai pradinei fibrilių koncentracijai (A-C). Savireplikacijos reakcijos metu susiformavusių fibrilių konformacinis stabilumas (D-F). Paklaidos yra standartiniai nuokrypiai.

Konformacinis agregatų stabilumas. Fibrilių konformacinio stabilumo tyrimas atskleidė, kad fibrilių, susiformavusių pridėjus 5% rPrP-A^{4M} agregatų, konformacinis stabilumas yra beveik toks pats kaip ir pačių rPrP-A^{4M} agregatų, depolimerizacijos kreivės vidurio taškas yra ties ≈2,9 M GuSCN (Pav. 11D). Fibrilių, susiformavusių pridėjus 1% rPrP-A^{4M} agregatų, konformacinis stabilumas yra mažesnis nei rPrP-A^{4M} agregatų, tačiau didesnis nei rPrP-A^{2M} agregatų, depolimerizacijos kreivės vidurio taškas yra ties ≈2,2 M GuSCN (Pav. 11E). Fibrilių, susiformavusių pridėjus 0,2% rPrP-A^{4M} agregatų, konformacinis stabilumas yra panašus į rPrP-A^{2M} fibrilių kamieno, depolimerizacijos kreivės vidurio taškas yra ties ≈1,8 M GuSCN. Rezultatai leidžia daryti prielaidą, jog fibrilės, kurių susidarymas buvo inicijuotas antrinės nukleacijos, neįgauna tokios pats struktūros kaip fibrilės, kurios buvo panaudotos kaip šablonas savireplikacijos reakcijos metu.

Fibrilių morfologijos analizė. Mėginių analizė atominės jėgos mikroskopu patvirtino, kad visomis eksperimentinėmis sąlygomis susidarė amiloidinės fibrilės (duomenys darbo santraukoje nepateikti). Pavienių fibrilių ilgis buvo tarp kelių šimtų nanometrų iki kelių mikrometrų. Fibrilių aukščio analizė atskleidė, jog vidutinis rPrP-A^{2M} fibrilių kamieno aukštis yra 6.9 $\pm$ 2.6 nm, o rPrP-A^{4M} fibrilių kamieno - 5.4 $\pm$ 1.7 nm. Fibrilių, susidariusių pridėjus 0.2% of rPrP-A^{4M} agregatų, aukštis yra panašus į rPrP-A^{2M} kamieno fibrilių, o fibrilių, susidariusių pridėjus 5% of rPrP-A^{4M} agregatų, - į rPrP-A^{4M} kamieno fibrilių.

Fibrilių antrinės struktūros charakterizavimas. Agregatų antrinės struktūros profilių analizė FTIR spektroskopijos metodu atskleidė subtilius skirtumus tarp rPrP-A^{2M} ir rPrP-A^{4M} fibrilių kamienų (Pav. 12). rPrP-A^{4M} fibrilių IR sugerties spektras turi vieną maksimumą amido I/I' regione ties 1620 cm^{-1}, o rPrP-A^{2M} - ties 1624 cm^{-1} (Pav. 12). Fibrilių, susidariusių pridėjus 5% rPrP-A^{4M}, IR sugerties spektras yra labai panašus į PrP-A^{4M} agregatų, o fibrilių, susidariusių pridėjus 0,2% rPrP-A^{4M}, - į rPrP-A^{2M} agregatų. Šie rezultatai leidžia daryti prielaidą, jog fibrilių kamienui-specifiškos struktūros perdavimas ir dauginimas (savireplikacija) priklauso nuo pradinės agregatų koncentracijos ir ar reakcija yra priklausoma nuo fibrilių ilgėjimo ar antrinės nukleacijos.

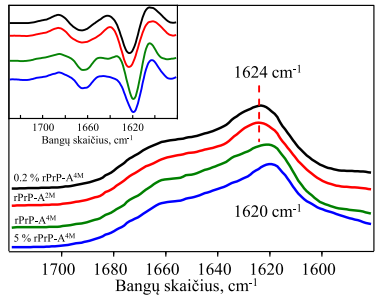

PAV. 12: rMoPrP fibrilių IR sugerties spektrai ir jų antrosios išvestinės (įterptinis grafikas).

Bendrai paėmus yra akivaizdu, jog konformacinis fibrilių stabilumas koreliuoja su agregacijos reakcijos kinetika. Tikėtina, kad PrP-A^{4M} ir rPrP-A^{2M} fibrilių kamienai koegzistuoja visuose tirtuose

mėginiuose. Skirtingas šių kamienų koncentracijos santykis galimai nulemia skirtumus matomus fibrilių depolimerizacijos kreivių profiliuose. Remiantis visais rezultatai galime daryti išvadą, kad antrinė nukleacija vaidina svarbų vaidmenį kamienų konformaciniame kintamume.

Prioninio baltymo fibrilių savirepikacijos savybių tyrimas

Nepaisant reikšmingų mokslininkų pastangų šiai dienai nėra nei vieno veiksmingo vaistinio preparato skirto ligų siejamų su amiloidais prevencijai ar gydymui [7, 8]. Vienos iš pagrindinių to priežasčių yra be galo sudėtingi amiloidinių fibilių susidarymo ir savireplikacijos procesai, bei sąlyginiai skurdus šių procesų supratimas. [8, 9, 17–19, 87, 88].

Siekiant gauti gilesnį supratimą apie fibrilių savireplikacijos procesą, šiame darbe buvo tirtas skirtingų pelės prioninio baltymo fibrilių savireplikacijos savybės.

Prioninio baltymo fibrilių formavimas. Monomerinis rMoPrP89-230 buvo inkubuojamas 2 M arba 4 M guanidino hidrochlorido tirpale (GuHCl) 37 °C temperatūroje esant energingam maišymui (220 aps./min (purtyklėje)) arba švelniam (10 aps./min (rotatoriuje)) maišymui.

Agregatai susidarę 2 M GuHCl arba 4 M GuHCl esant energingam maišymui toliau šiame darbe bus vadinami atitinkamai S220_2M ir S220_4M, o agregatai susidarę esant švelniam maišymui - R10_2M ir R10_4M.

Skirtingų rMoPrP89-230 fibrilių kamienų savireplikacijos savybės. Kadangi visi rMoPrP89-230 agregatų kamienai sugeba savireplikuotis esant aplinkos sąlygoms artimoms toms kuriomis šie kamienai spontaniškai susiformavo (duomenys darbo santraukoje nepateikti) yra įdomu ištirti kaip pokyčiai aplinkos sąlygose (GuHCl koncentracija ir temperatūra) paveiks šių kamienų savireplikacijos savybes.

Visų pirma ištirta GuHCl koncentracijos įtaka rMoPrP89-230 fibrilių kamienų savireplikacijos kinetikai 40 °C temperatūroje nesant maišymo (Pav. 13). S220_2M fibrilių kamienas sugeba efektyviai savireplikuotis

tirpaluose kuriuose yra nuo 1 M iki 3 M GuHCl (Pav. 13A). GuHCl koncentracijai esant <1.0 M arba >3.0 M, S220_2M savireplikacijos reakcija yra labai lėta, eksperimento laiko intervale ThT signalas praktiškai nekinta. R10_2M fibrilių kamienas sugeba efektyviai savireplikuotis tirpaluose kuriuose yra nuo 1 M iki 3,5 M GuHCl (Pav. 13C, D). GuHCl koncentracijai esant 4-4,5 M R10_2M savireplikacijos reakcija yra lėta, o esant 0,5 M GuHCl - ypač lėta (Pav. 13B). R10_4M ir S220_4M fibrilių kamienai sugeba efektyviai savireplikuotis tirpaluose kuriuose yra nuo 1,5 M iki 4 M (R10_4M) arba 4,5 M (S220_4M) GuHCl (Pav. 13C, D). Bendrai paėmus yra matoma koreliacija tarp fibrilių kamieno konformacinio stabilumo ir GuHCl koncentracijos ruožo kuriame kamienas sugeba efektyviai savireplikuotis. Įdomu tai, kad R10_2M ir R10_4M fibrilių kamienų konformacinis stabilumas yra panašus, tačiau fibrilių, spontaniškai susidariusių 4 M GuHCl tirpale (R10_4M), savireplikacijos greitis esant aukštai (4-4,5 M) GuHCl koncentracijai yra didesnis nei fibrilių kurios susiformavo 2 M GuHCl tirpale (R10_2M). Tai leidžia daryti prielaidą, kad GuHCl koncentracijos ruožas kuriame fibrilės gali efektyviai savireplikuotis priklauso nuo jų konformacinio stabilumo, o savireplikacjos greitis - nuo aplinkos sąlygų, kurios yra palankesnės spontaniniam vieno ar kito fibrilių kamieno susidarymui.

Tam tikrais atvejais buvo stebima gana keista savireplikacijos reakcijos kinetika. Pavyzdžiui, R10_4M fibrilių kamieno savireplikacijos reakcijos metu 1-2,5 M GuHCl tirpale (Pav. 13C, D) ThT fluorescencijos intensyvumas iš pradžių staigiai didėja, tačiau po kurio laiko ima staigiai kristi ir vėliau vėl augti. Šis fenomenas toliau šiame darbe bus vadinamas "ThT signalo šuoliu". Iš (Pav. 13 D) grafiko matyti, kad ThT signalo šuolio pozicija kinta kartu su didėjančia GuHCl koncentracija. Esant žemai GuHCl koncentracijai šuolis yra gana žemas ir platus, GuHCl koncentracijai kylant šuolis tampa siauresnis kol galiausiai visiškai išnyksta aukštose GuHCl koncentracijose. Dvi-fazė agregacijos reakcijos kinetika leidžia daryti prielaidą jog reakcijos metu galimai susidaro tarpinė agregatų rūšis [89], arba jog vyksta esamų fibrilinių agregatų persitvarkymas. Fibrilių, susidariusių tirpale esant 1-4 M GuHCl, antrinės struktūros analizė atskleidė, kad visų šių agregatų antrinė struktūra yra vienoda (duomenys darbo santraukoje

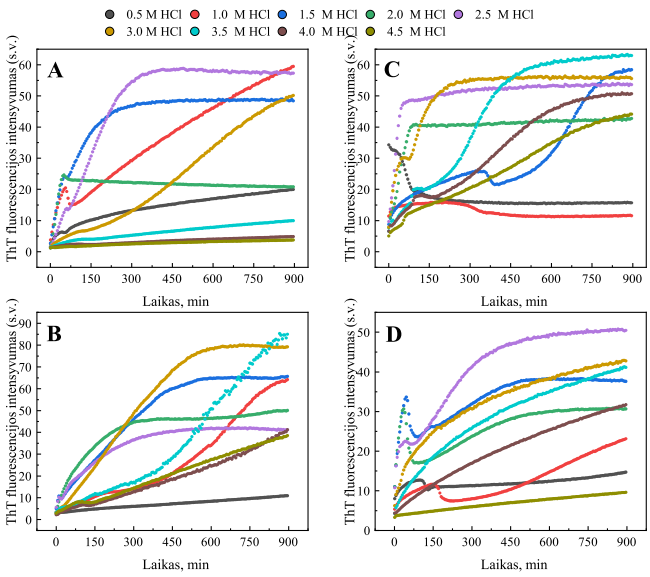

PAV. 13: S220_2M (A), R10_2M (B), S220_4M (C), ir R10_4M (D) fibrilių kamienų savireplikacijos reakcijos kinetika esant skirtingai GuHCl koncentracijai.

nepateikti). Tai reiškia, kad R10_4M fibrilių kamienas sugeba perduoti kamienui-būdingą struktūra net ir nepalankiomis aplinkos sąlygomis. Taigi kyla klausimas: kokia yra ThT signalo šuolio kilmė?

Kadangi buvo akivaizdu, jog kintanti GuHCl daro įtaką rMoPrP89-230 fibrilių kamienų savireplikacijos kinetikai, bei tam tikrais atvejais nulemia ThT signalo šuolio atsiradimą, yra įdomu išsiaiškinti kaip kintanti aplinkos temperatūra paveiks šį procesą. Todėl rMoPrP89-230 fibrilių kamienų savireplikacijos reakcijos kinetika 0,5-4,5 M GuHCl tirpaluose buvo stebėta esant skirtingai aplinkos temperatūrai (40-65 °C) (Duomenys darbo santraukoje nėra pateikti). Bendrai paėmus didinant aplinkos temperatūrą fibrilių savireplikacijos reakcija visais atvejais pagreitėjo. Taip pat kylant aplinkos temperatūrai ThT signalo šuolis tampa mažiau akivaizdus ar net visai išnyksta.

Savireplikacijos reakcijos kinetikos anomalijos. Galima manyti jog neįprastas ThT fluorescencijos pokytis galimai yra susijęs su prietaisu kuris yra naudojamas sekti savireplikacijos reakcijai (šiuo atveju RotorGeneQ realaus laiko analizatorius), tačiau panašūs pokyčiai ThT

fluorescencijos signale buvo matomi net ir tuomet kai savireplikacijos reakcija buvo sekama visiškai kitu prietaisu (Cary Eclipse fluorimetras) (Pav. 14). Tuomet galima manyti, jog ThT signalo šuolis galimai yra susijęs su pačiu ThT, tačiau panašus šuolis buvo matomas ir tuomet kai agregacijos savireplikacijos reakcija buvo sekama matuojant šviesos sklaidą (Pav. 14) arba deep-Blue autofluorescenciją [90]. Taigi panašu, kad neįprasta savireplikacijos reakcijos kinetika yra susijusi su tam tikrais molekuliniais procesais kurie vyksta šios reakcijos metu.

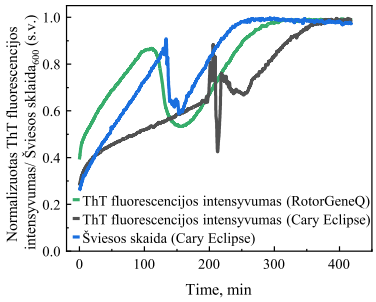

PAV. 14: S220_4M savireplikacijos reakcijos 1.5 M GuHCl tirpale, 50 °C temperatūroje, kinetika sekama skirtingais prietaisais matuojant ThT fluorescencijos intensyvumą arba šviesos sklaidą.

Atlikus mėginių analizę atominės jėgos mikroskopu buvo gauti gana netikėti rezultatai (Pav. 15). Pirmojo ThT signalo pakilimo viršūnėje paimto mėginio AFM nuotraukoje matyti, kad fibrilės yra tankiai sulipusios į didelius guzus (Pav. 15A). Po to sekančio ThT signalo kritimo minimume paimto mėginio AFM nuotraukoje matyti, jog fibrilės yra mažiau tankiai sulipusios, tačiau sulipusių fibrilių guzai yra vis vien matomi (Pav. 15B). Mėginio, paimto kuomet ThT signalas pasiekia plato, AFM nuotraukoje matyti daugiausia pavienės amiloidinės fibrilės (Pav. 15C). Paprastai būtų galima tikėtis jog savireplikacijos eigoje fibrilių susipakavimas turėtų būti priešingas, t. y. reakcijos pradžioje turėtume matyti pavienes fibriles, o pabaigoje fibriles sulipusias į didžiulius gabalus.

Remiantis visai anksčiau aptartais pastebėjimais buvo iškelta hipotezė, kuri gali paaiškinti neįprastą savireplikacijos reakcijos kinetiką.

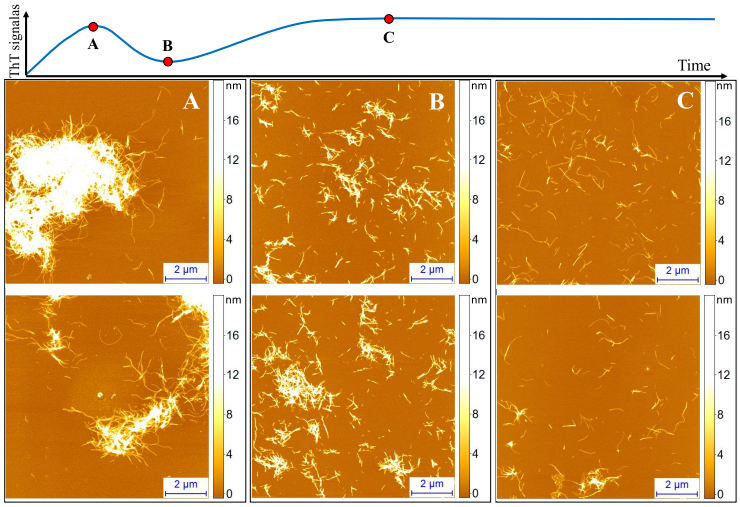

PAV. 15: Amiloidiniai agregatai egzistuojantys pirmojo ThT signalo pakilimo viršūnėje (A), sekančio ThT signalo kritimo minimume (B) ir kuomet ThT signalas pasiekia plato (C).

Savireplikacijos reakcijos pradžioje, ThT molekulės jungiasi prie fibrilių paviršiaus ir dėl to yra stebimas ThT fluorescencijos intensyvumas padidėjimas (Pav. 16 1.) [91–93]. Baltymo monomerai gali kondensuotis ant egzistuojančių fibrilių paviršiaus (antrinė nukleacija) [94, 95] ir taip dalinai uždengti prie fibrilių prisijungusias ThT molekules. Dėl to sumažėja ThT molekulių sąveika su tirpikliu ir tuo pačiu sumažėja fluorescencijos gesinimo efektai [91–93]. Fibrilėms ilgėjant susidaro daugiau paviršiaus prie kurio gali jungtis ThT molekulės ir ant kurio gali kondensuotis baltymo monomerai, dėl to yra stebimas laipsniškas ThT signalo augimas. Antrinė nukleacija yra daugiapakopis procesas, kurį sudaro keli mikroskopiniai įvykiai kaip monomerų asociacija su agregatais, nukleacija ant agregatų paviršiaus ir susidariusių agregacijos branduolių atsiskyrimas nuo paviršiaus [95]. Esant žemai monomerų koncentracijai, antrinė nukleacija yra neįsotinta (t. y. yra priklausoma nuo monomerų konc.), o tuo metu esant aukštai monomerų koncentracijai - įsotinta [95]. Pokyčiai aplinkos sąlygose gali nulemti ne tik tirpale sąveikaujančių baltymų savybes, bet ir baltymo molekulių adsorbcijos ant fibrilių paviršiaus jėgos (F_{AS}) stiprumą [94]. Esant silpnai F_{AS}, baltymo molekulės padengia tik mažą dalį fibrilių

paviršiaus, ir reakcijos greitis tampa priklausomas nuo monomerų adsorbcijos ir oligomerų susiformavimo ant fibrilių paviršiaus greičio. Esant stipriai F_{AS}, didžioji dalis fibrilių paviršiaus yra padengta baltymo monomerais, tačiau šiuo atveju oligomerų atsijungimas nuo fibrilių paviršiaus tampa energetiškai nepalankus. Agregacijos branduolys susiformuos tik tuomet kai oligomerai pasieks tam tikrą dydį kai tarpmolekulinės baltymo molekulių sąveikos jėga, po konformacinio virsmo, taps stipresnė nei baltymo-fibrilių adsorbcijos jėga. Kitaip tariant kuo stipresnė baltymo adsorbcijos prie fibrilių paviršiaus jėga tuo didesni oligomerai turi susidaryti, kad būtų galima įveikti teigiamą adsorbcijos energiją ir oligomerai galėtų atsiskirti nuo fibrilių paviršiaus [94]. Esant stipriai F_{AS}, taip pat tikėtina, jog monomerai tolygiai pasiskirstys ant fibrilių paviršiaus tam kad padidintų savo kontakto su paviršiumi plotą, bei suformuos kelis sluoksnius [94]. Dabar padarysime prielaidą, kad ThT molekulių uždengtų monomerais, fluorescencijos intensyvumas sudaro didžiąją dalį fiksuojamo fluorescencijos intensyvumo, ir kad mūsų atvejų antrinė nukleaciją yra įsotinta bei F_{AS} yra stipri. Tuomet tam tikru laiko momentu, agregacijos branduoliai, galintys ilgėti, susiformuoja iš monomerų ant fibrilės paviršiaus (Pav. 16 1.). Kai branduoliai tampa pakankamai dideli jie atsiskiria nuo fibrilių paviršiaus dėl ko palengvėja ThT molekulių, prisijungusių prie fibrilių, sąveika su tirpikliu ir tuo pačiu padidėja fluorescencijos gesinimas (Pav. 16 2.). Kai/ jei branduolių atsijungimo nuo fibrilių greitis (k_{off}) yra didesnis nei monomerų prisijungimo prie fibrilių paviršiaus (k_{on}), yra stebimas ThT fluorescencijos intensyvumo signalo mažėjimas dėl atsiradusio stipraus fluorescencijos gesinimo. ThT fluorescencijos signalo mažėjimas yra laikinas, nes po kurio laiko sistemoje nusistovi pusiausvyra ir k_{off} ir k_{on} tampa panašūs (Pav. 16 3.). Šiuo lako momentu, pokytis ThT fluorescencijos intensyvumo signale tampa labiausiai priklausomas nuo agregacijos branduolių ir fibrilių ilgėjimo, kurie sukuria naują paviršių prie kurio gali jungtis laisvos ThT molekulės bei kondensuotis baltymo monomerai. Taigi vėlesnėse savireplikacijos reakcijos stadijose, laipsniškas ThT fluorescencijos intensyvumo signalo didėjimas daugiausia atsiranda dėl didėjančio paviršiaus prie kurio gali jungti ThT.

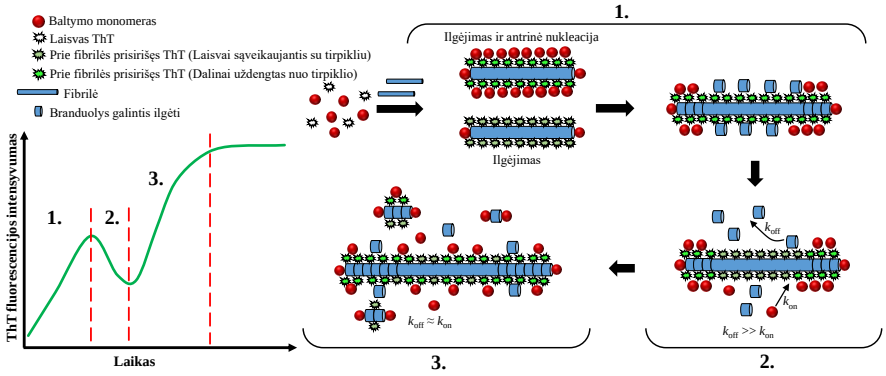

PAV. 16: Mikroskopiniai įvykiai kurie gali sukelti anomalijas savireplikacijos reakcijos kinetikoje.

Mėginiuose, paimtuose prieš drastišką ThT signalo kritimą, buvo matyti, kad fibrilės yra sulipusios į didelius guzus (Pav. 15A). Galima manyti, jog tokie fibrilių guzai susiformuoja dėl stiprios F_{AS}, dėl kurios oligomerų/agregacijos branduolių atsijungimas nuo fibrilių yra energetiškai apsunkintas. Kadangi agregacijos branduoliai negali atsijungti nuo fibrilių paviršiaus, jie ilgėja ant paviršiaus ir atsijungia nuo paviršiaus tik tuomet kai pasiekia kritinį dydį. Santykinė fibrilių guzų gausa yra didesnė prieš pat ThT signalo mažėjimą nei laiko momentu kai ThT signalas nustoja mažėti (Pav. 15B) ar pasiekia plato (Pav. 15C). Tai galima paaiškinti tuo jog laisvų baltymo monomerų koncentracija pastaraisiais laiko momentais yra mažesnė nei pradiniu laiko momentu. Dėl to antrinės nukleacijos metu susiformuoja mažiau branduolių kurie ilgėja ant egzistuojančių fibrilių paviršiaus, ir dėl to fibrilių guzai yra mažiau akivaizdūs.

Savireplikacijos reakcijos pradžioje, šviesos sklaidos signalas didėja (Pav. 14). Iš to galime spręsti, jog vidutinis dalelių dydis tirpale didėja. Pavyzdžiui dėl to, kad monomerai prisijungia ant egzistuojančių fibrilių paviršiaus, ant fibrilių paviršiaus susidaro agregacijos branduoliai, arba fibrilės ilgėja. Tam tikru laiko momentu, šviesos sklaidos signalas ima staigiai mažėti. Tai leidžia daryti išvadą, jog vidutinis dalelių dydis tirpale turėjo staigiai sumažėti. Pailgėjusių agregacijos branduolių atsiskyrimas nuo fibrilių paviršiaus (ir tuo pačiu fibrilių guzų iširimas)

galėtų tai paaiškinti.

Bendrai paėmus yra akivaizdu, kad neįprastas ThT fluorescencijos signalo pokytis nėra eksperimentinė klaida, o fenomenas susijęs su antrinės nukleacijos proceso anomalijomis. Šis fenomenas nusipelno didesnio mokslininkų dėmesio, nes mūsų žiniomis iki šiol toks fenomenas mokslinėje literatūroje nebuvo aprašytas.

Amiloido beta 42 agregatų heterogeniškumo ir santykinio paplitimo skirtingu agregacijos reakcijos laiko momentu tyrimas

Atominės jėgos mikroskopija (AFM) yra vienas iš galingiausių ir universaliausių vienos-molekulės analizės metodų skirtų biomolekulių vaizdinimui ir charakterizavimui [7, 96–98]. AFM yra dažnai naudojama tirti amiloidinių baltymų agregacijos procesą [7, 36, 96, 99–102]. Norit atlikti mėginių vaizdinimą atominės jėgos mikroskopu, mėginiai turi būti užnešti ant kieto substrato, pavyzdžiui atomiškai lygaus žėručio paviršiaus. Tipinė mėginių paruošimo AFM vaizdinimui procedūra susideda iš trijų žingsnių: mėginio užnešimo ant atomiškai lygaus paviršiaus; mėginio nuplovimo distiliuotu vandeniu ar buferiniu tirpalu; ir mėginio džiovinimo po švelniu oro srautu. Mėginio inkubacijos ant atomiškai lygaus paviršiaus laikas yra ypač svarbus. Biomolekulių, prisijungusių prie substrato, koncentracija yra proporcinga inkubacijos laikui, tačiau, per ilgas inkubacijos laikas gali paskatinti šių molekulių saviorganizaciją ant substrato paviršiaus į dirbtines struktūras [103–105]. Dėl diferencinės adsorbcijos, dalis molekulių, esančių mėginio tirpale, gali būti pašalintos nuo substrato paviršiaus, nuplovimo žingsnio metu, ir dėl to bus galima susidaryti tik dalinį vaizdą apie mėginyje esančias biomolekules. Dėl visų šių priežasčių kontroliuoti biomolekulių, užneštų ant substrato, kiekį yra didžiulis iššūkis. Visi šie apribojimai gali būti apeiti mėginio užnešimui panaudojant mikroskysčių išpurškimo platformą [103]. Mikroskysčių išpurškimo įrenginys gali išpurkšti subpikolitro mėginio lašelius ant substrato paviršiaus. Nusileidę ant substrato lašeliai išdžiūva per porą milisekundžių. Šis laiko tarpas yra trumpesnis nei teoretiškai

ir eksperimentiškai nustatytas monomerinių baltymų ar agregatų difuzijos greitis skysčio-kieto kūno fazių riboje [103, 104, 106–108]. Dėl to baltymo molekulės negali laisvai judėti ir saviorganizuotis ant substrato paviršiaus. Tai reiškia, kad mikroskysčių išpurškimo platformos panaudojimas mėginių užnešimui ant substrato paviršiaus, sukuria unikalią galimybę atlikti kokybinę ir kiekybinę amiloidų agregacijos proceso analizę atominės jėgos mikroskopu. Šiame darbe ši galimybė buvo panaudota siekiant ištirti amiloido beta 42 (Aβ42) agregacijos procesą.

Amiloidinė agregacija: nuo monomerinio Aβ42 iki amiloidinių fibrilių. Aβ42 agregacijos reakcija buvo stebima matuojant ThT fluorescencijos intensyvumą (Pav. 17A). Mėginiai analizei atominės jėgos mikroskopu buvo paimti pačios agregacijos reakcijos pradžioje (t_0), *lag* fazės viduryje (t_1) ir pabaigoje (t_2), viduryje augimo fazės (t_3), ir plato fazėje (t_4).

Mėginių analizė atominės jėgos mikroskopu patvirtino, jog galime atvaizduoti visą ant paviršiaus išdžiuvusio lašelio turinį (Pav. 17B-F). Iš AFM nuotraukų matyti, kad lašeliuose esančios biomolekulės yra daugiausia pasiskleidusios po visą išdžiuvusio lašelio plotą, o už lašelio periferijos jų praktiškai nėra. Tai reiškia, jog turime uždarą sistemą, ir galime nustatyti visas joje esančias biomolekules.

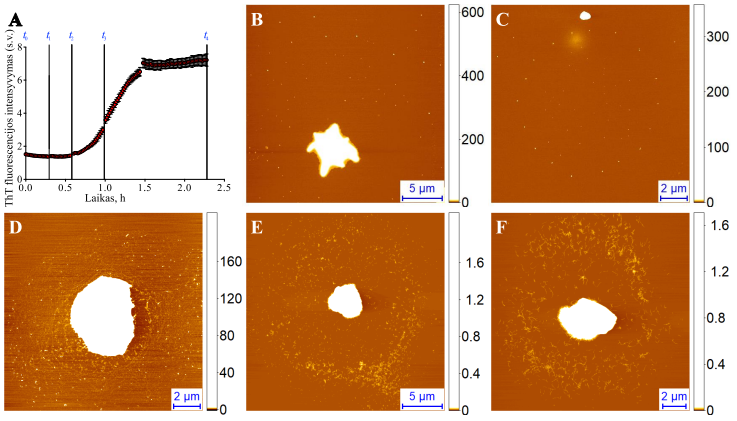

PAV. 17: Aβ42 agregacijos kinetika (A) ir mėginių, paimtų skirtingu agregacijos laiko momentu (t_0 - t_4, B-F atitinkamai), vizualizavimas AFM.

Ankstyvose Aβ42 agregacijos stadijose (t_0 - t_1), pagrinde yra matomos mažos 0.5-3 nm aukščio sferinės dalelės, galimai baltymo monomerai ar maži oligomerai (Pav. 18). *lag* fazės (t_2) gale yra matomi 3-4 nm aukščio sferinės formos oligomerai bei pailgos, vingiuotos protofibrilės. Viduryje augimo fazės (t_3), dauguma oligomerinių agregatų išnyksta ir yra pakeičiami trumpomis 3-4 nm aukščio protofibrilėmis ir 5-7 nm fibrilėmis. Plato fazėje yra pagrinde matomos ilgos 5-7 nm fibrilės (t_4). Rezultatai gerai sutampa su anksčiau literatūroje aprašytais pastebėjimais [101, 109, 110].

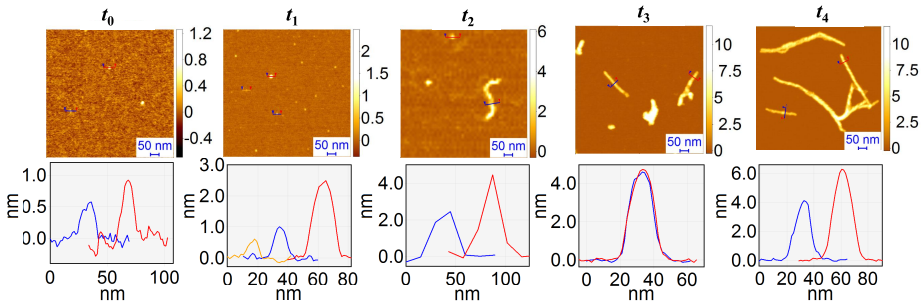

PAV. 18: Mėginių, paimtų skirtingu Aβ42 agregacijos reakcijos laiko momentu, morfologija.

Statistinis agregatų morfologijos savybių (aukščio, pločio ir ilgio (diametro sferinių dalelių atveju)) palyginimas atskleidė laipsnišką dominuojančios biomolekulių rūšies pokytį Aβ42 agregacijos proceso metu (Pav. 19). Pradinėse agregacijos proceso stadijose (t_0) didžiosios dalies biomolekulių aukštis yra $\approx$0.5-1 nm (Pav. 19A, F), o diametras $\approx$4 nm (Pav. 19 G). Šios dimensijos sutampa su Aβ42 monomerų [101]. Sąlyginiai mažas duomenų išsibarstymas leidžia daryti daryti išvadą jog agregacijos reakcijos pradžioje egzistuojančių biomolekulių pagrindą sudaro Aβ42 monomerai. *lag* fazės viduryje, yra matomas platesnis biomoleklių aukščio ($\approx$0.5-3 nm) (Pav. 19B, F) pasiskirstymas. Vidutinis biomolekulių diametras taip pat didesnis ($\approx$6 nm) (Pav. 19G). Tai leidžia daryti prielaidą, jog šiuo agregacijos reakcijos laiko momentu susidaro ankstyvieji oligomerai (dimerai, trimerai), ir kad Aβ42 monomerai ir oligomerai sudaro didžiąją dalį biomolekulių populiacijos. Vėlyvojoje *lag* fazėje / ankstyvojoje augimo fazėje (t_2),

vidutinis biomolekulių aukštis (≈4 nm) (Pav. 19C, F) ir plotis (≈12 nm) (Pav. 19G) yra reikšmingai didesnis nei Aβ42 monomerų ar ankstivųjų oligomerų, kas leidžia daryti prielaidą, kad 3-4 nm aukščio vėlyvieji oligomerai ir protofibrilės sudaro didžiąją dalį biomolekulių populiacijos šiuo laiko momentu. Kadangi vidutinis biomolekulių populiacijos ilgis (Pav. 19H) šiuo laiko momentu yra santykinai mažas, galime daryti prielaidą jog didesnę biomolekulių populiacijos dalį sudaro vėlyvieji oligomerai, o protofibrilės - mažesnę. Iš biomolekulių aukščio pasiskirstymo histogramos matyti, jog augimo fazės viduryje (t_3) ir plato fazėje (t_4) egzistuoja dvi biomolekulių populiacijos (Pav. 19D, E). Vidutinis pirmosios populiacijos aukštis yra ≈4 nm, kas atitinka Aβ42 protofibrilių aukštį [101, 109], o antrosios - ≈6 nm, kas atitinka amiloidinių fibrilių aukštį [101, 109]. Vienintelis aiškus skirtumas tarp biomolekulių populiacijų viduryje augimo fazės ir plato fazėje yra jų ilgis, kuris yra ženkliai didesnis vėlesnėje agregacijos fazėje (Pav. 19H).

Iš aukščio pasiskirstymo histogramos ir aukščio, pločio ir ilgio pasiskirstymo yra akivaizdu, kad homogeniška biomolekulių populiacija egzistuoja tik pačioje agregacijos reakcijos pradžioje, o visuose vėlesniuose fazėse, tuo pačiu metu egzistuoja bent kelios skirtingos biomolekulių populiacijos. Apibendrinant, yra akivaizdu, kad aukštos rezoliucijos atominės jėgos mikroskopija kartu su mikroskysčių išpurškimo platforma leidžia atvaizduoti visas biomolekules egzistuojančias Aβ42 agregacijos reakcijos metu, atlikti statistine šių biomolekulių morfologijos analizę bei nustatyti Aβ42 monomerų, oligomerų, protofibrilinių ir fibrilinių agregatų santykinį pasiskirstymą skirtingu agregacijos reakcijos laiko momentu.

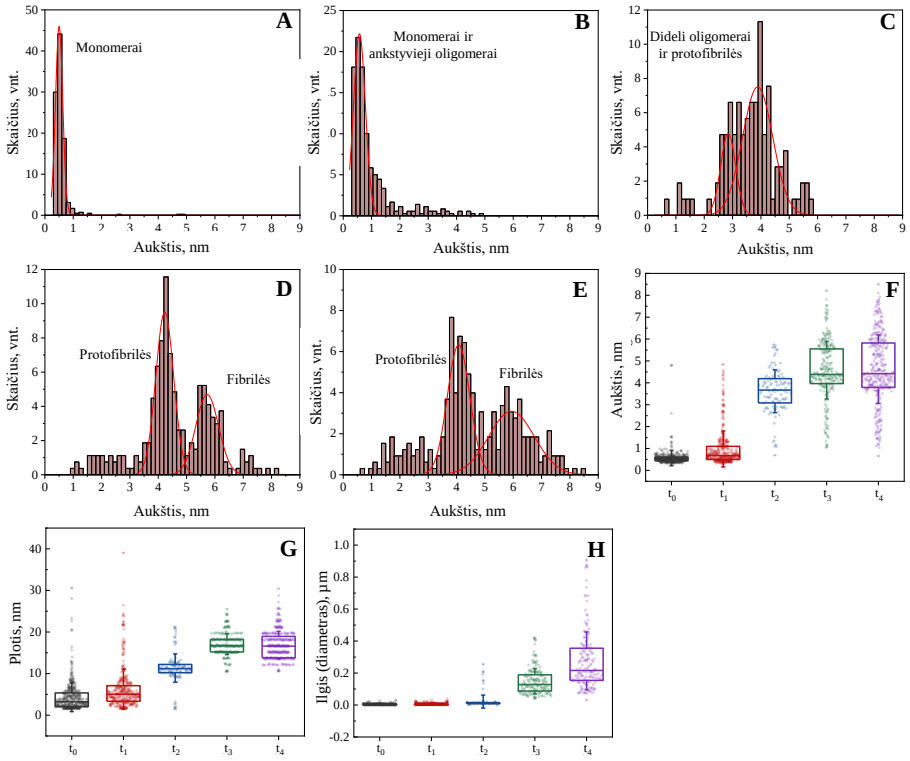

PAV. 19: Mėginių, paimtų skirtingu Aβ42 agregacijos reakcijos laiko momentu, aukščio pasiskirstymo histogramos (A-F, t_0 - t_4) ir aukščio (F), pločio (G) ir ilgio (H) pasiskirstymas.

Išvados

Šiame darbe buvo tirtas amiloidinių baltymų (insulino, pelės rekombinantinio prioninio baltymo fragmento bei rekombinantinio amiloido beta 42) agregacijos procesas. Darbo metu buvo gauti reikšmingi rezultatai kurie leido praplėsti esamą supratimą apie amiloidinių fibrilių, jų savireplikacijos bei konformacinio kintamumo procesus. Remiantis gautais rezultatais buvo padarytos sekančios išvados:

- Insulino monomerų-oligomerų pusiausvyra yra galimai vienas iš pagrindinių faktorių nulemiančių skirtingų insulino fibrilių kamienų susidarymą.
- Neamiloidogeninės oligomerinės insulino formos tiesiogiai dalyvauja insulino agregacijos procese ir jį slopina.
- Aplinkos sąlygos yra vienas iš pagrindinių faktorių nulemiančių EGCG prieš-amiloidinį poveikį.
- Amiloidinių fibrilių kamienui-specifiškos struktūros perdavimas ir dauginimas (savireplikacija) vyksta tik fibrilių ilgėjimo metu..
- Neįprastas ThT signalo pokytis fibrilių savireplikacijos reakcijos metu yra susijęs su mikroskopiniais įvykiais vykstančiais antrinės nukleacijos proceso metu.
- Atominės jėgos mikroskopija kartu su mikroskysčių išpurškimo platforma suteikia unikalią galimybę vizualizuoti visas agreguojančių baltymų formas (monomerai, oligomerai, protofibrilės ir fibrilės) egzistuojančias amiloidinės agregacijos metu, bei gauti kiekybinę ir kokybinę informaciją apie šias formas vienos molekulės lygmenyje.

Padėka

Nuoširdžiai dėkoju visiems, kurie man padėjo ir suteikė motyvacijos doktorantūros studijų metu.

Dėkoju darbo vadovui Dr. Vytautui Smirnovui už suteiktą nuostabią galimybę pradėti savo kelionę į amiloidų pasaulį, jo nuoširdumą, gaires, asmenini palaikymą ir už pasidalintą patirtį bei žinias. Visi šie metai praleisti Vytauto laboratorijoje labai stipriai prisidėjo prie mano profesinio ir asmeninio tobulėjimo.

Ačiū už naudingus patarimus ir asmeninį palaikymą visam amiloidų tyrimų grupės kolektyvui, ypač Mantui Žiauniui, Andriui Sakalauskui, Katažynai Milto ir Akvilei Botyriūtei už bendradarbiavimą, mokslines diskusijas, ir svarbiausia už draugystę ir kartu smagiai praleistą laiką. Taip pat norėčiau padėkoti Marynui Grigaliūnui, Domantui Dargužiui, Romuald Stanilko, Elžbietai Kulicka ir Karinai Sluckaitei už bendradarbiavimą ir smagų laiką laboratorijoje. Už draugišką atmosfera noriu padėkoti visam Biotermodinamikos ir vaistų tyrimų skyriaus kolektyvui.

Dėkoju Vilmai Michailovienei už suteiktus baltymų gryninimo įgūdžius, Dr. Marijai Jankunec už supažindinimą su atominės jėgos mikroskopija bei prieiga prie atominės jėgos mikroskopo, Prof. Gediminui Niaurai, Dr. Ilja Ignatjev ir Martynui Talaikiui už galimybę pasinaudoti IR spektrometru, Dr. Linai Baranauskienei už jos patarimus.

Už priėmimą ir galimybę tobulinti savo įgūdžius esu dėkingas Prof. Michele Vendruscolo, Dr. Francesco Simone Ruggeri ir Prof. Tuomas Knowles (Kembridžo universitetas, Jungtinė Karalystė). Ačiū šių grupių nariams už draugišką atmosferą, efektyvų darbą ir bendradarbiavimą, ypač Dr. Tadas Kartanas, Dr. Sean Chia, Dr. Ryan Limbocker, Tuuli Hakala, Rodrigo Cataldi, Tom Scheidt, Dr. Benedetta Mannini, Zenon Toprakcioglu, Magdalena Czekalska, Yufan Xu ir Ella Feng.

Esu dėkingas Lietuvos mokslo tarybai, Lietuvos mokslo akademijai ir Vilniaus Universitetui už finansinę paramą.

Didžiausia mano padėka tėvams, broliui, sesei ir Gretai už asmeninį palaikimą ir besąlygišką tikėjimą manimi.

CURRICULUM VITAE - Tomas Šneideris

Tel.: +370 652 31742 e-paštas: Tomas.Sneideris@bti.vu.lt

Išsilavinimas

Laipsnis: **Doktorantūros studijos, biochemija** (2015-2019).
Institucija: Biotechnologijos institutas, Gyvybės mokslų centras, Vilniaus universitetas, Vilnius, Lietuva.
Darbo tema: Baltymų amiloidinių fibrilių susidarymo ir savireplikacijos savybių tyrimas.
Darbo vadovas: Dr. Vytautas Smirnovas.

Laipsnis: **Bioinžinerijos magistras** (2013-2015).
Institucija: Vilniaus Gedimino technikos universitetas, Vilnius, Lietuva.
Darbo tema: Rekombinantinio amiloido beta gamyba ir potencialių jo agregacijos slopiklių įvertinimas.
Darbo vadovas: Dr. Vytautas Smirnovas.

Laipsnis: **Bioinžinerijos bakalauras** (2009-2013).
Institucija: Vilniaus Gedimino technikos universitetas, Vilnius, Lietuva.
Darbo tema: Rekombinantinio pelės PrP23-230 gamyba.
Darbo vadovas: Dr. Vytautas Smirnovas.

Profesinė patirtis

2017 - dabar: **Jaunesnysis mokslo darbuotojas** Biotechnologijos institutas, Gyvybės mokslų centras, Vilniaus universitetas, Vilnius, Lietuva.

2015 - 2018: **Tyrėjas biologas** Biotechnologijos institutas, Gyvybės mokslų centras, Vilniaus universitetas, Vilnius, Lietuva.

2013 - 2015: **Laborantas** Biotechnologijos institutas, Gyvybės mokslų centras, Vilniaus universitetas, Vilnius, Lietuva.

Stažuotės

2018.06.2 – 2019.02.16: **Chemijos departamentas, Kembridžo universitetas**, Kembridžas, Jungtinė Karalystė.

2018.04.07 – 2018.04.15: **Biologinės chemijos institutas, Academia Sinica**, Taipėjus, Taivanas.

2015.02.18 – 2015.03.04: **Dortmundo technikos universitetas**, Dortmundas, Vokietija.

Tarptautinės mokyklos

2017: **2nd NGP-net Winter School on Experimental Methods to Characterize Non-Globular Proteins**, Marselis, Prancūzija.

2016: **13th Greta Pifat Mrzljak International School of Biophysics**, Splitas, Kroatija.

Akademiniai pasiekimai ir apdovanojimai

Stipendija už akademinius pasiekimus
2019 • Lietuvos mokslo taryba
Stipendija dalyvauti tarptautinėje konferencijoje "8th Scandinavian Conference of Amyloid Diseases and Amyloid Mechanisms (ADAM8)"
2019 • Lietuvos mokslo taryba
Geriausias stendinis pranešimas "Vita Scientia 2018" konferencijoje
2018 • Vita Scientia
Stipendija dalyvauti tarptautinėje konferencijoje "62nd Annual Meeting of Biophysical Society"
2018 • COST action BM1405
Stipendija už akademinius pasiekimus
2018 • Lietuvos mokslo taryba
Stipendija dalyvauti tarptautinėje konferencijoje "Prion 2018"
2018 • Lietuvos mokslo taryba
Stipendija už akademinius pasiekimus

2017 • Lietuvos mokslo taryba

Stipendija dalyvauti tarptautinėje mokykloje "2nd NGP-net Winter School on Experimental Methods to Characterize Non-Globular Proteins"

2017 • COST veikla BM1405

Stipendija dalyvauti tarptautinėje mokykloje "13th Greta Pifat Mrzljak International School of Biophysics"

2016 • EBSA

Apdovanojimas už darbų ciklą “Amiloidinių baltymų agregacijos tyrimai“

2016 • Lietuvos mokslų akademija

Literatūros sąrašas

(1) Selkoe, D. J.; Hardy, J. *EMBO Molecular Medicine* **2016**, *8*, 595–608.

(2) Poewe, W.; Seppi, K.; Tanner, C. M.; Halliday, G. M.; Brundin, P.; Volkmann, J.; Schrag, A. E.; Lang, A. E. *Nature Reviews Disease Primers* **2017**, *3*, 1–21.

(3) Mukherjee, A.; Morales-Scheihing, D.; Butler, P. C.; Soto, C. *Trends in Molecular Medicine* **2015**, *21*, 439 –449.

(4) Aguzzi, A.; Nuvolone, M.; Zhu, C. *Nature Reviews Immunology* **2013**, *13*, 888–902.

(5) Knowles, T. P. J.; Vendruscolo, M.; Dobson, C. M. *Nature reviews. Molecular cell biology* **2014**, *15*, 384–96.

(6) Wisniewski, T.; Goñi, F. *Neuron* **2015**, *85*, 1162–1176.

(7) Ruggeri, F. S.; Šneideris, T.; Vendruscolo, M.; Knowles, T. P. *Archives of Biochemistry and Biophysics* **2019**, *664*, 134–148.

(8) Chiti, F.; Dobson, C. M. *Annual Review of Biochemistry* **2017**, *86*, 27–68.

(9) Marín-Moreno, A.; Fernández-Borges, N.; Espinosa, J. C.; Andréoletti, O.; Torres, J. M. *Progress in Molecular Biology and Translational Science* **2017**, *150*, 181–201.

(10) Chiti, F.; Dobson, C. M. *Annual review of biochemistry* **2006**, *75*, 333–66.

(11) Chiti, F.; Dobson, C. M. *Annual Review of Biochemistry* **2017**, *86*, 27–68.

(12) Meisl, G.; Kirkegaard, J. B.; Arosio, P.; Michaels, T. C. T.; Vendruscolo, M.; Dobson, C. M.; Linse, S.; Knowles, T. P. J. *Nature Protocols* **2016**, *11*, 252–272.

(13) Michaels, T. C. T.; Šarić, A.; Habchi, J.; Chia, S.; Meisl, G.; Vendruscolo, M.; Dobson, C. M.; Knowles, T. P. J. *Annual Review of Physical Chemistry* **2018**, *69*, annurev–physchem–050317–021322.

(14) Sneideris, T.; Darguzis, D.; Botyriute, A.; Grigaliunas, M.; Winter, R.; Smirnovas, V. *PloS one* **2015**, *10*, e0136602.

(15) Ziaunys, M.; Sneideris, T.; Smirnovas, V. *Physical Chemistry Chemical Physics* **2018**, *20*, 27638–27645.

(16) Sneideris, T.; Milto, K.; Smirnovas, V. *PeerJ* **2015**, *3*, e1207.

(17) Legname, G.; Moda, F. In *Prion Protein*, Legname, G., Vanni, S., Eds.; Progress in Molecular Biology and Translational Science, Vol. 150; Academic Press: 2017, pp 147 –156.

(18) Makarava, N.; Baskakov, I. V. *PLoS Pathogens* **2013**, *9*, ed. by True, H. L., e1003759.

(19) Li, J.; Browning, S.; Mahal, S. P.; Oelschlegel, A. M.; Weissmann, C. *Science* **2010**, *327*, 869–872.

(20) Colby, D. W.; Prusiner, S. B. *Cold Spring Harbor perspectives in biology* **2011**, *3*, a006833.

(21) Cobb, N. J.; Apostol, M. I.; Chen, S.; Smirnovas, V.; Surewicz, W. K. *Journal of Biological Chemistry* **2014**, *289*, 2643–2650.

(22) Smirnovas, V.; Kim, J.-I.; Lu, X.; Atarashi, R.; Caughey, B.; Surewicz, W. K. *The Journal of biological chemistry* **2009**, *284*, 24233–41.

(23) Kim, C.; Xiao, X.; Chen, S.; Haldiman, T.; Smirnovas, V.; Kofskey, D.; Warren, M.; Surewicz, K.; Maurer, N. R.; Kong, Q.; Surewicz, W.; Safar, J. G. *Nature Communications* **2018**, *9*, 1–11.

(24) Wang, F.; Wang, X.; Orrú, C. D.; Groveman, B. R.; Surewicz, K.; Abskharon, R.; Imamura, M.; Yokoyama, T.; Kim, Y. S.; Vander Stel, K. J.; Sinniah, K.; Priola, S. A.; Surewicz, W. K.; Caughey, B.; Ma, J. *PLoS Pathogens* **2017**, *13*, 1–23.

(25) Legname, G.; Baskakov, I. V.; Nguyen, H.-O. B.; Riesner, D.; Cohen, F. E.; DeArmond, S. J.; Prusiner, S. B. *Science* **2004**, *305*, 673–676.

(26) Colby, D. W.; Prusiner, S. B. *Nature Reviews Microbiology* **2011**, *9*, 771–777.

(27) Moda, F.; T. Le, T. N.; Aulić, S.; Bistaffa, E.; Campagnani, I.; Virgilio, T.; Indaco, A.; Palamara, L.; Andréoletti, O.; Tagliavini, F.; Legname, G. *PLoS Pathogens* **2015**, *11*, 1–28.

(28) Guo, J. L.; Lee, V. M. Y. *Nature Medicine* **2014**, *20*, 130–138.

(29) Adamcik, J.; Mezzenga, R. *Angewandte Chemie - International Edition* **2018**, *57*, 8370–8382.

(30) Nielsen, L.; Khurana, R.; Coats, A.; Frokjaer, S.; Brange, J.; Vyas, S.; Uversky, V. N.; Fink, A. L. *Biochemistry* **2001**, *40*, 6036–6046.

(31) Smirnovas, V.; Winter, R. *Biophysical Journal* **2008**, *94*, 3241–3246.

(32) Grudzielanek, S.; Smirnovas, V.; Winter, R. *Journal of molecular biology* **2006**, *356*, 497–509.

(33) Milto, K.; Michailova, K.; Smirnovas, V. *PLoS ONE* **2014**, *9*, 1–5.

(34) Swietnicki, W.; Morillas, M.; Chen, S. G.; Gambetti, P.; Surewicz, W. K. *Biochemistry* **2000**, *39*, PMID: 10631004, 424–431.

(35) Makarava, N.; Ostapchenko, V. G.; Savtchenko, R.; Baskakov, I. V. *Journal of Biological Chemistry* **2009**, *284*, 14386–14395.

(36) Ruggeri, F. S.; Benedetti, F.; Knowles, T. P. J.; Lashuel, H. A.; Sekatskii, S.; Dietler, G. *Proceedings of the National Academy of Sciences* **2018**, 201721220.

(37) Barth, A. **2007**, *1767*, 1073–1101.

(38) Bundi, A.; Wüthrich, K. *Biopolymers* **1979**, *18*, 285–297.

(39) Glasoe, P. K.; Long, F. A. *The Journal of Physical Chemistry* **1960**, *64*, 188–190.

(40) Surmacz-Chwedoruk, W.; Nieznańska, H.; Wójcik, S.; Dzwolak, W. *Biochemistry* **2012**, *51*, 9460–9469.

(41) Surmacz-Chwedoruk, W.; Babenko, V.; Dzwolak, W. *The journal of physical chemistry. B* **2014**, *118*, 13582–9.

(42) Kurouski, D.; Dukor, R. K.; Lu, X.; Nafie, L. A.; Lednev, I. K. *Biophysical Journal* **2012**, *103*, 522–531.

(43) Kurouski, D.; Lombardi, R. A.; Dukor, R. K.; Lednev, I. K.; Nafie, L. A. *Chemical Communications* **2010**, *46*, 7154–7156.

(44) Kurouski, D.; Dukor, R. K.; Lu, X.; Nafie, L. A.; Lednev, I. K. *Chemical Communications* **2012**, *48*, 2837–2839.

(45) Bryant, C.; Spencer, D. B.; Miller, A.; Bakaysa, D. L.; McCune, K. S.; Maple, S. R.; Pekar, A. H.; Brems, D. N. *Biochemistry* **1993**, *32*, 8075–8082.

(46) Nielsen, L.; Frokjaer, S.; Brange, J.; Uversky, V. N.; Fink, A. L. *Biochemistry* **2001**, *40*, 8397–8409.

(47) Nettleton, E. J.; Tito, P.; Sunde, M.; Bouchard, M.; Dobson, C. M.; Robinson, C. V. *Biophysical Journal* **2000**, *79*, 1053–1065.

(48) Banga, A., *Therapeutic Peptides and Proteins*, 2nd ed.; CRC Press: 2005.

(49) Meisl, G.; Rajah, L.; Cohen, S. A. I.; Pfammatter, M.; Šarić, A.; Hellstrand, E.; Buell, A. K.; Aguzzi, A.; Linse, S.; Vendruscolo, M.; Dobson, C. M.; Knowles, T. P. J. *Chemical science* **2017**, *8*, 7087–7097.

(50) Cohen, S. I. A.; Linse, S.; Luheshi, L. M.; Hellstrand, E.; White, D. A.; Rajah, L.; Otzen, D. E.; Vendruscolo, M.; Dobson, C. M.; Knowles, T. P. J. *Proceedings of the National Academy of Sciences of the United States of America* **2013**, *110*, 9758–63.

(51) Arosio, P.; Cukalevski, R.; Frohm, B.; Knowles, T. P. J.; Linse, S. *Journal of the American Chemical Society* **2014**, *136*, 219–25.

(52) Arosio, P.; Vendruscolo, M.; Dobson, C. M.; Knowles, T. P. J. *Trends in Pharmacological Sciences* **2014**, *35*, 127–135.

(53) Knowles, T. P. J.; Waudby, C. A.; Devlin, G. L.; Cohen, S. I. A.; Aguzzi, A.; Vendruscolo, M.; Terentjev, E. M.; Welland, M. E.; Dobson, C. M. *Science (New York, N.Y.)* **2009**, *326*, 1533–7.

(54) Meisl, G.; Yang, X.; Hellstrand, E.; Frohm, B.; Kirkegaard, J. B.; Cohen, S. I. a.; Dobson, C. M.; Linse, S.; Knowles, T. P. J. *Proceedings of the National Academy of Sciences of the United States of America* **2014**, *111*, 9384–9.

(55) Meisl, G.; Rajah, L.; Cohen, S. A. I.; Pfammatter, M.; Šarić, A.; Hellstrand, E.; Buell, A. K.; Aguzzi, A.; Linse, S.; Vendruscolo, M.; Dobson, C. M.; Knowles, T. P. J. *Chem. Sci.* **2017**.

(56) Arosio, P.; Michaels, T. C. T.; Linse, S.; Månsson, C.; Emanuelsson, C.; Presto, J.; Johansson, J.; Vendruscolo, M.; Dobson, C. M.; Knowles, T. P. J. *Nature Communications* **2016**, *7*, 10948.

(57) Castellani, R. J.; Plascencia-Villa, G.; Perry, G. *Laboratory Investigation* **2019**.

(58) Porat, Y.; Abramowitz, A.; Gazit, E. *Chemical Biology and Drug Design* **2006**, *67*, 27–37.

(59) Mangialasche, F.; Solomon, A.; Winblad, B.; Mecocci, P.; Kivipelto, M. *The Lancet Neurology* **2010**, *9*, 702–716.

(60) Molino, S.; Dossena, M.; Buonocore, D.; Ferrari, F.; Venturini, L.; Ricevuti, G.; Verri, M. *Life Sciences* **2016**, *161*, 69–77.

(61) Goyal, D.; Shuaib, S.; Mann, S.; Goyal, B. *ACS Combinatorial Science* **2017**, *19*, 55–80.

(62) Stefani, M.; Rigacci, S. *International Journal of Molecular Sciences* **2013**, *14*, 12411–12457.

(63) Mehta, D.; Jackson, R.; Paul, G.; Shi, J.; Sabbagh, M. *Expert Opinion on Investigational Drugs* **2017**, *26*, 735–739.

(64) Mathur, S.; Dewitte, S.; Robledo, I.; Isaacs, T.; Stamford, J. *Journal of Parkinson's Disease* **2015**, *5*, 263–268.

(65) Athauda, D.; Foltynie, T. *Parkinsonism and Related Disorders* **2016**, *32*, 1–11.

(66) Al-Ansari, A.; Robertson, N. P. *Journal of Neurology* **2017**, *264*, 1029–1031.

(67) Yaari, R.; Hake, A. *Clinical Investigation* **2015**, *5*, 297–309.

(68) Cummings, J. L.; Morstorf, T.; Zhong, K. *Alzheimer's research & therapy* **2014**, *6*, 37.

(69) Zhao, J.; Liang, Q.; Sun, Q.; Chen, C.; Xu, L.; Ding, Y.; Zhou, P. *RSC Advances* **2017**, *7*, 32508–32517.

(70) Bieschke, J.; Russ, J.; Friedrich, R. P.; Ehrnhoefer, D. E.; Wobst, H.; Neugebauer, K.; Wanker, E. E. *Proceedings of the National Academy of Sciences* **2010**, *107*, 7710–7715.

(71) Qing, H.; McGeer, P. L.; Zhang, Y.; Yang, Q.; Dai, R.; Zhang, R.; Guo, J.; Wong, W.; Xu, Y.; Quan, Z. *Neurochemical Research* **2016**, *41*, 2788–2796.

(72) Roy, S.; Bhat, R. *Protein Science* **2019**, *28*, 382–402.

(73) Townsend, D.; Hughes, E.; Akien, G.; Stewart, K. L.; Radford, S. E.; Rochester, D.; Middleton, D. A. *Journal of Biological Chemistry* **2018**, *293*, 12877–12893.

(74) Andrich, K.; Bieschke, J. *Natural Compounds as Therapeutic Agents for Amyloidogenic Diseases* **2015**, *863*, 139–161.

(75) Zhu, Q. Y.; Zhang, A.; Tsang, D.; Huang, Y.; Chen, Z. Y. *Journal of Agricultural and Food Chemistry* **1997**, *45*, 4624–4628.

(76) Hatano, T.; Ohyabu, T.; Yoshida, T. *Heterocycles* **2005**, *65*.

(77) Sang, S.; Lee, M. J.; Hou, Z.; Ho, C. T.; Yang, C. S. *Journal of Agricultural and Food Chemistry* **2005**, *53*, 9478–9484.

(78) Zeng, L.; Ma, M.; Li, C.; Luo, L. *International Journal of Food Properties* **2017**, *20*, 1–18.

(79) Palhano, F. L.; Lee, J.; Grimster, N. P.; Kelly, J. W. *Journal of the American Chemical Society* **2013**, *135*, 7503–7510.

(80) Hirohata, M.; Hasegawa, K.; Tsutsumi-Yasuhara, S.; Ohhashi, Y.; Ookoshi, T.; Ono, K.; Yamada, M.; Naiki, H. *Biochemistry* **2007**, *46*, 1888–1899.

(81) An, T. T.; Feng, S.; Zeng, C. M. *Redox Biology* **2017**, *11*, 315–321.

(82) Joshi, P.; Chia, S.; Habchi, J.; Knowles, T. P.; Dobson, C. M.; Vendruscolo, M. *ACS Combinatorial Science* **2016**, *18*, 144–153.

(83) Aarabi, M.-H. *African Journal of Pharmacy and Pharmacology* **2012**, *6*, 2374–2379.

(84) Aguzzi, A.; Calella, A. M. *Physiological reviews* **2009**, *89*, 1105–52.

(85) Bruce, M. E. *British medical bulletin* **1993**, *49*, 822–38.

(86) Wadsworth, J. D. F.; Asante, E. A.; Desbruslais, M.; Linehan, J. M.; Joiner, S.; Gowland, I.; Welch, J.; Stone, L.; Lloyd, S. E.; Hill, A. F.; Brandner, S.; Collinge, J. *Science* **2004**, *306*, 1793–1796.

(87) Giles K; Olson SH; Prusiner SB *Cold Spring Harbor perspectives in medicine* **2017**, *7*, 4.

(88) Collinge, J. *Science* **2010**, *328*, 1111–1112.

(89) Hasecke, F. et al. *Chemical Science* **2018**, *9*, 5937–5948.

(90) Ziaunys, M.; Sneideris, T.; Smirnovas, V. *PeerJ* **2019**, *7*, e7554.

(91) Thompson, A. J.; Herling, T. W.; Kubánková, M.; Vyšniauskas, A.; Knowles, T. P.; Kuimova, M. K. *Journal of Physical Chemistry B* **2015**, *119*, 10170–10179.

(92) Voropai, E. S.; Samtsov, M. P.; Kaplevskii, K. N.; Maskevich, A. A.; Stepuro, V. I.; Povarova, O. I.; Kuznetsova, I. M.; Turoverov, K. K.; Fink, A. L.; Uverskii, V. N. *Journal of Applied Spectroscopy* **2003**, *70*, 868–874.

(93) Freire, S.; De Araujo, M. H.; Al-Soufi, W.; Novo, M. *Dyes and Pigments* **2014**, *110*, 97–105.

(94) Šarić, A.; Michaels, T. C. T.; Zaccone, A.; Knowles, T. P. J.; Frenkel, D. *The Journal of Chemical Physics* **2016**, *145*, 211926.

(95) Linse, S. *Biophysical Reviews* **2017**, *9*, 329–338.

(96) Ruggeri, F. S.; Habchi, J.; Cerreta, A.; Dietler, G. *Current pharmaceutical design* **2016**, *22*, 3950–70.

(97) Hölscher, H.; Falter, J.; Schirmeisen, A. In *Characterization of Materials*; 9; John Wiley & Sons, Inc.: Hoboken, NJ, USA, 2012; Vol. 2, pp 2191–2197.

(98) Dufrêne, Y. F.; Ando, T.; Garcia, R.; Alsteens, D.; Martinez-Martin, D.; Engel, A.; Gerber, C.; Müller, D. J. *Nature Nanotechnology* **2017**, *12*, 295–307.

(99) Drolle, E.; Hane, F.; Lee, B.; Leonenko, Z. *Drug Metabolism Reviews* **2014**, *46*, 207–223.

(100) Qamar, S. et al. *Cell* **2018**, *173*, 720–734.e15.

(101) Ruggeri, F. S.; Adamcik, J.; Jeong, J. S.; Lashuel, H. A.; Mezzenga, R.; Dietler, G. *Angewandte Chemie - International Edition* **2015**, *54*, 2462–2466.

(102) Adamcik, J.; Mezzenga, R. *Current Opinion in Colloid and Interface Science* **2012**, *17*, 369–376.

(103) Ruggeri, F. S.; Charmet, J.; Kartanas, T.; Peter, Q.; Chia, S.; Habchi, J.; Dobson, C. M.; Vendruscolo, M.; Knowles, T. P. *Nature Communications* **2018**, *9*.

(104) Kastantin, M.; Langdon, B. B.; Schwartz, D. K. *Advances in Colloid and Interface Science* **2014**, *207*, Special Issue: Helmuth Möhwald Honorary Issue, 240 –252.

(105) Losic, D.; Martin, L. L.; Aguilar, M.-I.; Small, D. H. *Peptide Science* **2006**, *84*, 519–526.

(106) Zhao, D.; Watson, J. B.; Xie, C.-W. *Journal of neurophysiology* **2004**, *92*, 2853–2858.

(107) Tilton, R.; Gast, A.; Robertson, C. *Biophysical Journal* **1990**, *58*, 1321 –1326.

(108) Ravichandran, S.; Talbot, J. *Biophysical Journal* **2000**, *78*, 110 –120.

(109) Jeong, J. S.; Ansaloni, A.; Mezzenga, R.; Lashuel, H. A.; Dietler, G. *Journal of Molecular Biology* **2013**, *425*, 1765–1781.

(110) Mastrangelo, I. A.; Ahmed, M.; Sato, T.; Liu, W.; Wang, C.; Hough, P.; Smith, S. O. *Journal of Molecular Biology* **2006**, *358*, 106–119.

Copies of publications included in this thesis

PLOS | ONE

RESEARCH ARTICLE

pH-Driven Polymorphism of Insulin Amyloid-Like Fibrils

Tomas Sneideris[1], Domantas Darguzis[1], Akvile Botyriute[1], Martynas Grigaliunas[1], Roland Winter[2], Vytautas Smirnovas[1]*

1 Department of Biothermodynamics and Drug Design, Vilnius University Institute of Biotechnology, Vilnius, Lithuania, **2** Physical Chemistry I–Biophysical Chemistry, Faculty of Chemistry and Chemical Biology, TU Dortmund University, Dortmund, Germany

* vytautas.smirnovas@bti.vu.lt

Citation: Sneideris T, Darguzis D, Botyriute A, Grigaliunas M, Winter R, Smirnovas V (2015) pH-Driven Polymorphism of Insulin Amyloid-Like Fibrils. PLoS ONE 10(8): e0136602. doi:10.1371/journal.pone.0136602

Editor: Byron Caughey, Rocky Mountain Laboratories, NIAID, NIH, UNITED STATES

Received: April 28, 2015

Accepted: August 5, 2015

Published: August 27, 2015

Data Availability Statement: All relevant data are within the paper and its Supporting Information files.

Funding: This research was funded by the European Social Fund under the Global Grant Measure, project number VP1-3.1-ŠMM-07-K-02-020. The funders had no role in study design, data collection and analysis, decision to publish, or preparation of the manuscript.

Competing Interests: The authors have declared that no competing interests exist.

Abstract

Prions are infective proteins, which can self-assemble into different strain conformations, leading to different disease phenotypes. An increasing number of studies suggest that prion-like self-propagation may be a common feature of amyloid-like structures. Thus it is important to unravel every possible factor leading to the formation of different amyloid strains. Here we report on the formation of two types of insulin amyloid-like fibrils with distinct infrared spectroscopic features grown under slightly different pH conditions. Similar to prion strains, both insulin fibril types are able to self-propagate their conformational template under conditions, favoring spontaneous formation of different type fibrils. The low-pH-induced insulin amyloid strain is structurally very similar to previously reported strains formed either in the presence of 20% ethanol, or by modification of the amino acid sequence of insulin. A deeper analysis of literature data in the context of our current findings suggests a shift of the monomer-dimer equilibrium of insulin as a possible factor controlling the formation of different strains.

Introduction

Amyloid-like structures are associated with a number of pathological conditions including neurodegenerative diseases, such as Alzheimer's and Parkinson's, and infectious prion diseases, also a number of nonneuropathic systemic amyloidoses, and even type II diabetes [1]. In some cases amyloid-like folds can play a positive role as well: they have a structural function in spider silk and biofilm formation in bacteria, and a regulatory function in fungi or hormone storage in humans [2]. Experiments *in vitro* revealed even more amyloid-forming proteins and peptides, including proteins with no link to *in vivo* amyloids, such as polyaminoacids (e.g., polylysine, polythreonine and polyglutamic acid) [3], and short oligopeptides [4–6]. Finally, even an amyloid-like self-assembly of phenylalanine was recently reported [7]. All these findings support the idea that amyloid-like folds may be a generic property of all polypeptides, while the propensity of fibril formation would depend on the sequence of the polypeptide and on the environmental conditions (i.e., temperature, pressure, solution milieu, interaction with lipid interfaces, pH) [1].

Prions stand out among other amyloid-forming proteins as the only proteinaceous infectious pathogens [8]. Identical amino acid sequences of prion protein can adopt distinct pathogenic conformations, referred to as prion strains [9,10]. Different strains lead to distinct incubation periods and patterns of neuropathology in prion diseases [10]. Similar conformational variations were detected in other amyloid-forming proteins both *in vitro* [11–22] and i*n vivo* [23–25]. With growing evidence of the involvement of prion-like mechanisms in the progression of other amyloid-related diseases [23–33], it is indispensable to understand all the factors determining formation of different amyloid strains.

The new variant Creutzfeldt-Jakob disease (vCJD) is thought to be caused by a bovine spongiform encephalopathy (BSE) strain [34]. In this case, the determining factor for the formation of distinct prion strains is cross-species infection. Similar to prions, formation of distinct amyloid strains for two slightly different insulin forms was recently reported [19,35]. When protein sequences are identical, the environment plays the key role in straining of amyloid-like fibrils. The presence of co-solvents [11,14,15,20], different temperatures [36–38], different concentrations of denaturants [38,39] and salts [21], or different ways of agitation [12,40] may lead to distinct amyloid fibril strains. Here we report on the formation of distinct insulin amyloid strains at slightly different pH values.

As diagnostic tool, Fourier-transform infrared (FTIR) spectroscopy has been used, which has proven to be an important method for the characterization of secondary structural changes of prion and amyloid strains [11,19,41], supplemented by atomic force microscopy (AFM) measurements of the topology of amyloid fibrils and thioflavin T (ThT) fluorescence for recording the fibrillation kinetics.

Results and Discussion

In our recent work on potential inhibitors of insulin amyloid-like fibrillation, we followed the aggregation of insulin at pH 2 in the presence of 5% residual dimethylsulfoxide (DMSO) [42]. To test if the presence of a small amount of DMSO affects the fibrillation process, we compared the FTIR spectra of insulin amyloid-like fibrils spontaneously formed in D_2O in the presence (Fig 1A) and absence (Fig 1B) of 5% DMSO. To reveal possible changes upon using D_2O instead of H_2O, as required for the better quality FTIR measurements, and for looking into subtle pH changes on the fibrillation propensity of insulin, fibrils were prepared in heavy water samples at two pH* values (where pH* is the pH-meter readout uncorrected for isotopic effects, see Methods section), pH*1.6 to mimic similar concentrations of H^+ and D^+, and pH*2 to reach the same ionization state of the protein in the two solvents. The FTIR spectra look similar in the presence and absence of DMSO, but a rather small difference in pH* leads to significant differences in amide I' band contours (Fig 1A and 1B). Spectra of fibrils prepared at pH*2 exhibit maxima in the amide I' region at ~1628 cm^{-1} (with the main minimum of the second derivative at 1628 cm^{-1} and a weaker one at 1615 cm^{-1}), while spectra of fibrils grown at pH*1.6 exhibit maxima in the amide I' region at ~1621–22 cm^{-1} (with the main minimum of the second derivative at 1619 cm^{-1} and a weaker one at 1631 cm^{-1}), pointing toward predominantly beta-sheet structures but with a significantly different hydrogen-bonding patterns. A small band outside of the amide I' region at ~1728 cm^{-1} is present only in the spectra of fibrils grown at pH*1.6 and can be attributed to deuterated carboxyl groups [19]. Very similar spectral characteristics were recently described as a hallmark of two different insulin amyloid strains [19,35].

Fibrils grown at pH*1.6 in the presence of 5% DMSO are usually 2–4 nm in diameter and exhibit both a curved and straight morphology (Fig 1C), while fibrils grown at pH*2 both in the presence (Fig 1D) and absence (Fig 1E) of DMSO are thicker (4–16 nm) and usually

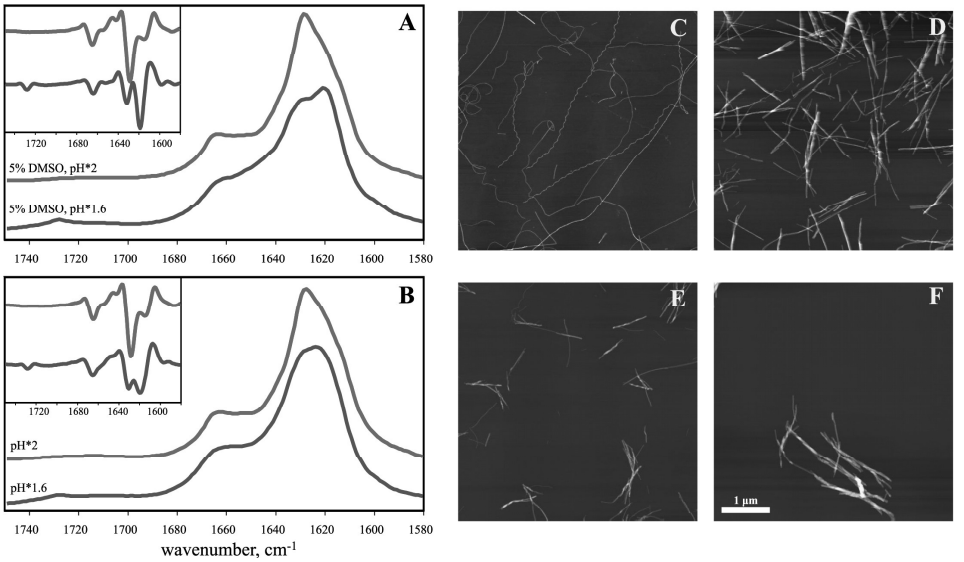

Fig 1. Polymorphism of insulin amyloid-like fibrils formed at different pH* values. FTIR absorption spectra (second derivative spectra in the inset) of fibrils grown in the presence (A), and absence (B) of 5% DMSO (spectra were repeated using different FTIR instruments in different labs, see S1 Fig). AFM images of fibrils prepared in the presence of DMSO at pH*1.6 (C), and pH*2 (D) or in absence of DMSO at pH*1.6 (E), and pH*2 (F). Fibril height measurements are shown in S2 Fig.

doi:10.1371/journal.pone.0136602.g001

straight. The structure of the fibrils at pH*1.6 in the absence of DMSO (Fig 1E) looks similar to the case at pH*2, suggesting no clear morphological differences between strains.

Both types of fibril seeds induce aggregation of insulin at either pH* and 37°C (Fig 2). Seeds grown at pH*1.6 fibrillate insulin at similar rates under both pH* conditions and faster than seeds grown at pH*2. The latter seeds elongate faster at solution conditions of the same pH*. As clearly visible, the fluorescence intensity of Thioflavin T (ThT), which marks formation of fibrillar amyloid states, is seed-dependent: pH*1.6-seed-induced aggregates result in an about double ThT intensity when compared to pH*2-seed-induced aggregates (Fig 2A). The light absorbance data at 600 nm—as measure of formation of larger insulin aggregates due to light scattering—show the reverse effect (Fig 2B). The pH*2-type fibrils induce aggregates which strongly absorb visible light (600 nm), the absorbance being ~25% lower in the case of seeding in the pH*1.6 environment. pH*1.6-type fibrils induce weakly absorbing aggregates (about 5 times lower than pH*2-type fibrils); however, the absorbance is strongly increased in the pH*2 solution.

The FTIR spectra of the seeded fibrils clearly demonstrate the superiority of the seed template versus the pH*-environment in controlling the fibrillar structure (Fig 3). The spectra of pH*2-seed-induced aggregates grown at pH*2 and pH*1.6 look identical. In case of the pH*1.6-seeded aggregates, the spectral signature is similar for both solution conditions; however, in pH*2, the intensity of the band at 1631 cm^{-1} is increased. These data confirm the ability

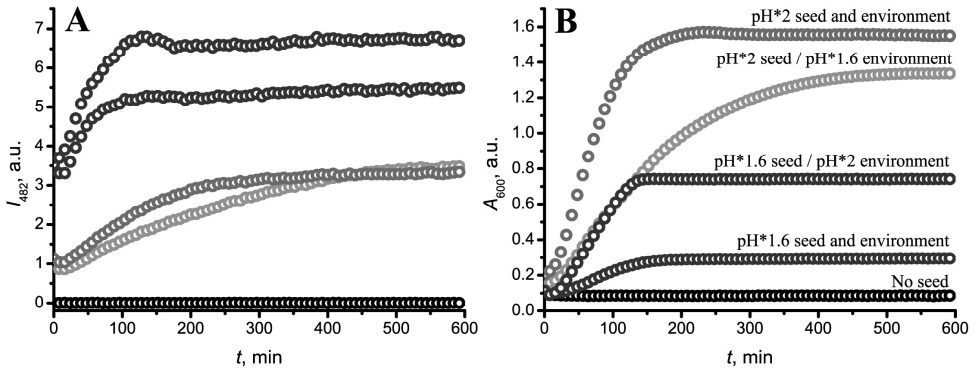

Fig 2. Kinetics of seed-induced aggregation of insulin; followed by ThT fluorescence intensity (A) as maker of fibril formation, and light absorbance at 600 nm (B). Measurements were repeated using 3 batch preparations showing similar results.

doi:10.1371/journal.pone.0136602.g002

of both types of insulin fibrils to self-propagate their conformational template in spite of unfavorable environmental factors (here different pH conditions), suggesting the existence of two different insulin amyloid strains.

Surprisingly, the FITR spectra of insulin amyloid-like fibrils spontaneously formed in H_2O at pH 1.6 and pH 2 look almost identical (Fig 4). Both spectra exhibit maxima in the amide I/I' region at ~1628 cm^{-1} (with the main minimum of the second derivative at 1628 cm^{-1} and a weaker one at 1641 cm^{-1}), and a small band outside of the amide I/I' region at ~1730 cm^{-1}. A different spectrum was obtained using fibrils spontaneously formed in H_2O at a slightly higher pH, at pH 2.4: it also exhibits a maximum in the amide I/I' region at ~1628 cm^{-1}, but the second derivative profile is different–two similar sized bands, at 1625 cm^{-1} and 1636 cm^{-1}, respectively. As the amyloid-like fibrils are highly protected from hydrogen/deuterium exchange, most of the amide hydrogens stay unchanged despite resuspension of the aggregates in D_2O. It reflects in the blue-shift of the spectra compared to insulin fibrils, prepared in D_2O.

Different types of insulin fibrils were first mentioned more than 60 years ago [43], however no structural or cross-seeding data were presented. In more recent studies, formation of different strains were reported in the presence and absence of 20% ethanol (at pH*1.5–1.8) [11,14,15], and using slightly different insulin forms (bovine insulin (BI) and recombinant Lys^{B31}-Arg^{B32} human insulin analog (KR)) at pH*1.9 [19,35]. Spectral characteristics of the latter strains are very similar to our data. The spectrum of the fibrils formed at pH*2 is similar to the spectrum of the BI strain, and the spectrum of the fibrils formed at pH*1.6 reminds us of the one of the KR strain. So the effect of two additional positively charged amino acids on the fibrillar structure is similar to the effect of ΔpH by -0.4 units. The change in net charge of the protein due to such ΔpH is minor, and taking into account that in normal water at pH 1.6 and pH 2 insulin aggregates into the same strain, we may conclude that ionization state of the protein is not the factor inducing formation of different strains. So what is the factor?

A possible answer to that question can be found by analyzing recent studies, which, at first sight, seem to contradict our findings [44–46]. In these works, no differences in the FTIR spectra of insulin fibrils formed at different pH values in the range between 1.3 and 3.1 are reported, however, a marked change of the vibrational circular dichroism (VCD) spectra are seen

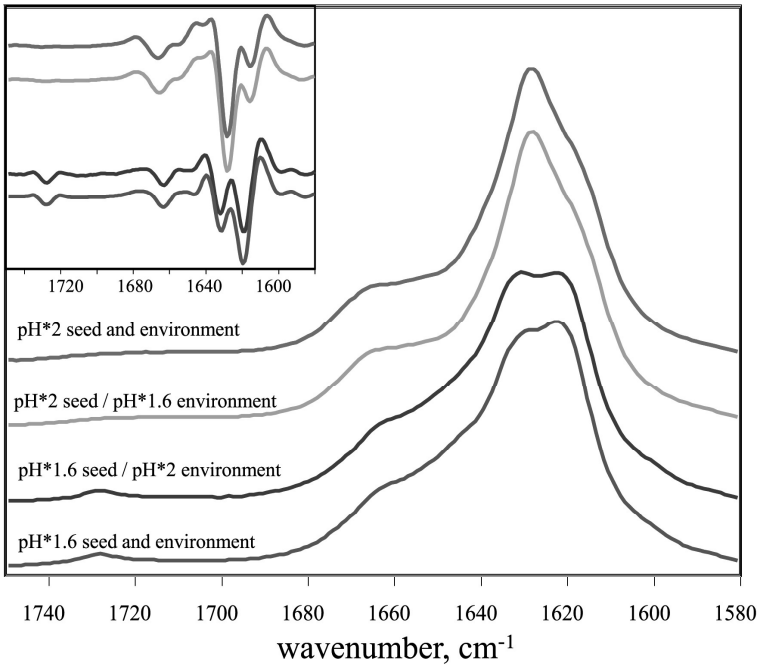

Fig 3. Infrared spectral features determined by the seeding template. Absorption and second derivative (inset) FTIR spectra.

doi:10.1371/journal.pone.0136602.g003

between pH 2.1 and 2.4, which is explained by a different supramolecular chirality [44,45]. Furthermore, it was shown that the chirality can be converted by incubation of preformed fibrils at different pH, thus excluding the possibility of different strains [46]. The reported FTIR spectra lack a detailed description, however, the shape of the amide I band looks very similar to the amide I' band of the pH*2 fibrils [44–46]. A closer inspection reveals one major experimental difference, which can affect the mechanism of insulin fibrillation. The concentration of insulin used in the aforementioned studies was 60 mg/mL (compared to 1 mM (~5.8 mg/mL) in our study), which means a strong shift towards a higher oligomeric state of insulin in solution, as even at much lower concentrations insulin tends to oligomerize [47–49]. Hence, the factor which determines the formation of different strains could be due to a shift in the monomer-oligomer equilibrium.

The spectral features of the insulin amyloid strain formed in the presence of 20% ethanol [11,14,15] are similar to those of the pH*1.6 and KR strain [19,35]. In all three cases the second derivative FTIR spectra in the amide I' region exhibit strong minima at 1619–1620 cm^{-1}, and a weaker one at 1630–31 cm^{-1}, plus a small band outside of amide I' region at 1728–30 cm^{-1}. Hence, it should be concluded that the same amyloid strain is present in all three cases. It is known that the presence of 20% ethanol strongly increases the dissociation of insulin dimers

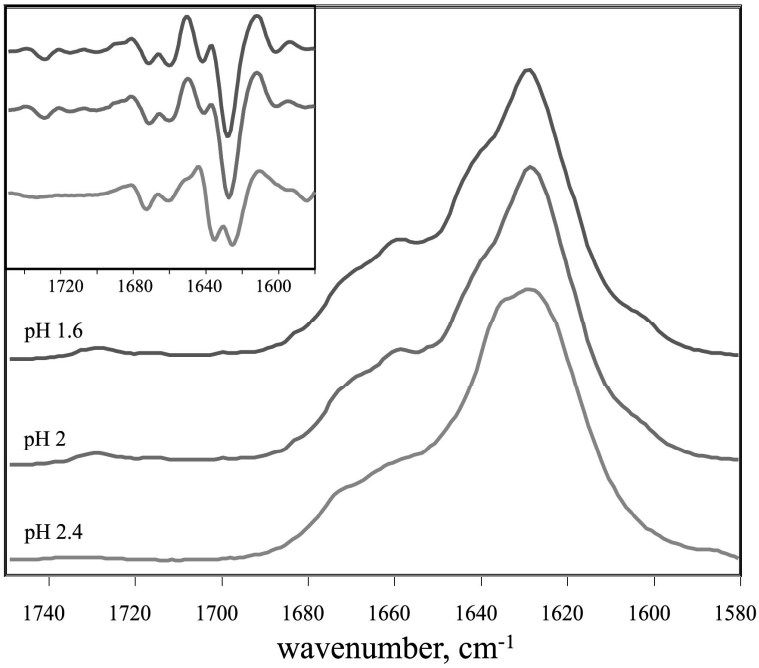

Fig 4. Infrared spectra of insulin amyloid-like fibrils formed in normal water (H_2O). Absorption and second derivative (inset) FTIR spectra.

doi:10.1371/journal.pone.0136602.g004

[50], leading to predominantly monomeric insulin at moderate concentrations [14,51]. The C-terminal part of the B-chain of insulin is involved in the formation of intramolecular antiparallel β-sheet that binds together native insulin dimers [19]. Thus there is a high probability that two additional charged amino acids would lead to dissociation of dimers in case of KR insulin. There is no data on the monomer-dimer equilibrium of insulin at pH* 1.6, but the fact that different strains can be formed not only with increasing pH*, but also with increased concentration of insulin, suggests a shift of the equilibrium to the monomeric state. We may hence hypothesize that the major factor which determines formation of different strains is a shift of the equilibrium between insulin monomers and dimers (oligomers) (Fig 5). If the equilibrium

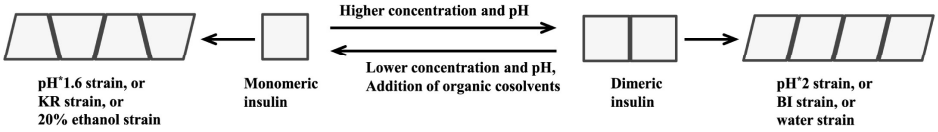

Fig 5. Proposed scheme of insulin amyloid straining.

doi:10.1371/journal.pone.0136602.g005

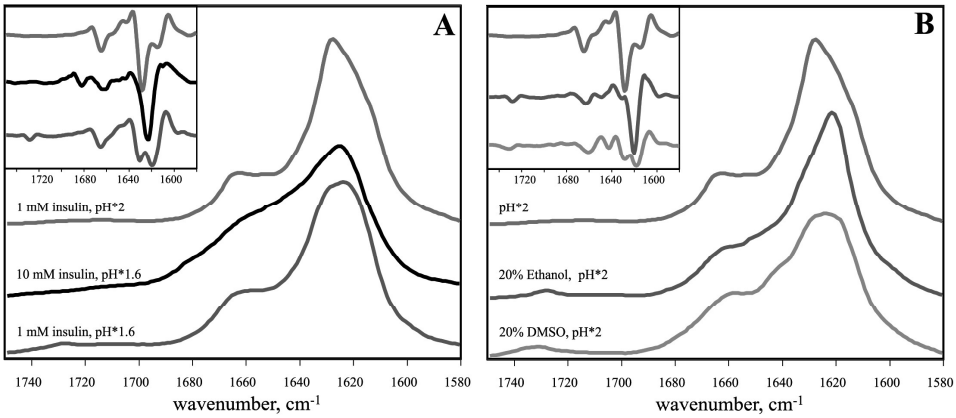

Fig 6. The effect of high insulin concentration (A), and organic cosolvents (B). Absorption and second derivative (inset) FTIR spectra.

doi:10.1371/journal.pone.0136602.g006

is shifted towards dimers (or higher oligomers), insulin aggregation would result in the pH*2-like strain, and in case that the equilibrium is shifted towards monomers, growth of the pH*1.6-like strain is fostered.

To further test the hypothesis we carried out several additional experiments. First we checked if an increased insulin concentration would explain the differences observed between the pH*1.6 and pH*2 data. As seen in Fig 6A, and Table 1, the spectrum of 10 mM insulin aggregates, prepared in the pH*1.6 environment, is slightly different from the other spectra. The blue shift of the amide I' maximum, when compared to the spectra of the pH*1.6 strain, and the absence of the band around 1728 cm^{-1} suggests that the increased protein

Table 1. Summary of FTIR band positions of insulin amyloid-like fibrils.

Insulin agregation conditions	Amide I/I' band (2nd derivative), cm^{-1}		Additional bands, cm^{-1}
	Beta-sheets	Turns/loops	Carboxyl groups[b]
1 mM insulin, pH*1.6	1619/1631[a]	1665	1728
1 mM insulin, pH*2	1628/1615	1665	absent
1 mM insulin, pH*1.6, 5% DMSO	1619/1631	1664	1728
1 mM insulin, pH*2, 5% DMSO	1628/1615	1665	absent
10 mM insulin, pH*1.6	1623	1662	absent
1 mM insulin, pH*2, 20% ethanol	1620/1631	1663	1728
1 mM insulin, pH*2, 20% DMSO	1619/1629	1661	1731
1 mM insulin, pH 1.6	1628/1641	1672/1661	1729
1 mM insulin, pH 2	1628/1641	1672/1661	1729
1 mM insulin, pH 2.4	1625/1636	1673/1661	absent

[a]All FTIR measurements were repeated at least three times showing similar results.
[b]Band assigned to carboxyl groups according to Surmacz-Chwedoruk et al [19]

doi:10.1371/journal.pone.0136602.t001

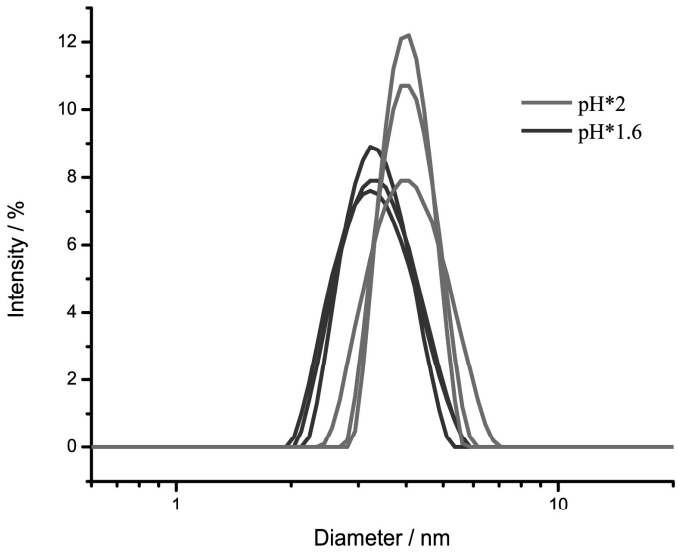

Fig 7. Size distribution of insulin in solution. DLS measurements were repeated using 3 batch preparations with similar results.

doi:10.1371/journal.pone.0136602.g007

concentration leads to formation of different strain. Nevertheless, the spectrum is also different from the pH*2 strain, so this data does not add much to strengthen our hypothesis. It is worth to mention that at high insulin concentration insulin aggregates form gel-like substance (which is not the case at lower insulin concentrations). It may point to the different aggregation mechanism thus explaining difference in FTIR spectra.

We also repeated previously described data on insulin aggregation in the presence of ethanol and examined the effect of higher DMSO concentrations. As seen in Fig 6B, the presence of 20% of both organic cosolvents during insulin aggregation in the pH*2 environment leads to formation of aggregates exhibiting pH*1.6-like IR spectra. This confirms that ethanol and, to a lower extent DMSO shifts the equilibrium towards formation of pH*1.6-like insulin amyloid strains.

Finally, we used dynamic light scattering (DLS) to determine the size distribution of insulin under the various solution conditions. The data reveal that average size of insulin, dissolved in pH*1.6 is lower than in pH*2 (Fig 7). The measured diameter of insulin in pH*1.6 is 3.4±0.7 nm, which is bigger than monomer, but smaller than dimer, while in pH*2, the diameter is 4.0±0.6, which is a little bigger than insulin dimer. Owing to the polydispersity of the sample, the method does not allow the exact estimation of the monomer and oligomer content, however the shift of the equilibrium towards dimeric/oligomeric species at higher pH* is unarguable, hence supporting our hypothesis.

Taken together, our data indicates different factors inducing polymorphism of insulin amyloid-like fibrils. However it seems that all the presented cases can be reduced to the formation

of two amyloid strains and possibly explained by the differences in the equilibrium between insulin monomers and dimers (oligomers).

Materials and Methods

Preparation of insulin fibrils

Recombinant human insulin was purchased from Sigma Aldrich (91077C). Insulin amyloid-like fibrils were prepared as described previously [52]. Briefly, fresh 1 mM insulin solution (in 100 mM phosphate buffer (PB), at different pH (in H_2O) and pH^* (in D_2O) values was incubated at 60°C for 24 hours with 300 rpm agitation (using a MHR 23 thermomixer, Ditabis, Germany). The secondary structures and morphological signatures of the aggregates obtained were tested using FTIR spectroscopy and AFM.

Seeds were prepared as described previously [52]. Briefly, 1 mL of fibrils were sonicated for 10 minutes using a Bandelin Sonopuls 3100 ultrasonic homogenizer equipped with a MS73 tip (using 50% of the power, cycles of 30 s/30 s sonication/rest, total energy applied to the sample per cycle, 0.56 kJ). The sample was kept on ice during the sonication procedure. Right after the treatment, one part of the fibrils was mixed with 9 parts of the fresh 1 mM insulin solution in the appropriate buffer and incubated at 37°C for 24 hours without agitation. The secondary structures of the aggregates obtained were tested using FTIR spectroscopy.

Elongation kinetics

To follow the seeding kinetics, samples were prepared as described above, with addition of 50 μM ThT. Right after the mixing the fresh insulin with seeds, samples were divided into 200 μL aliquots, in 96-well plates. The plates were sealed using clear polyolefin sealing tape. The aggregation kinetics was followed at constant 37°C temperature using a Biotek Synergy H4 plate reader without agitation. ThT fluorescence intensity upon fibril formation was observed using 440 nm excitation and 482 nm emission with simultaneous measurement of absorbance at 600 nm.

Infrared spectroscopy

To avoid overlapping of protein amide I and water bands, D_2O is used as solvent in FTIR measurements. At equal concentrations of D^+ and H^+, respectively, the pH-meter reading with a glass electrode is 0.4 pH units lower in D_2O than in H_2O [53]. However, isotopes affect the pK_a of protein ionizable groups, and for solutions of globular proteins the ΔpK_a was found to be 0.4 pH units in the acidic range, thus the isotope effect on the glass electrode and the ionization constant cancel each other, so that an identical pH-meter reading (in the acidic range) refers to an identical ionization state of the biopolymer in D_2O and H_2O solutions [54]. To prepare samples for the FTIR measurements, insulin fibrils prepared in H_2O were separated from water by centrifugation (30 min., 15000 *g*), and resuspended in D_2O, the procedure was repeated three times. All samples were sonicated for 1 minute using a Bandelin Sonopuls 3100 ultrasonic homogenizer equipped with a MS73 tip. The FTIR spectra were recorded using a Nicolet 5700 spectrometer from Thermo Scientific equipped with a liquid-nitrogen-cooled mercury-cadmium-telluride (MCT) detector, and using Bruker Alpha spectrometer equipped with deuterium triglycine sulfate (DTGS) detector. For all measurements, CaF_2 transmission windows and 0.05 mm Mylar spacers or 0.05 and 0.1 mm Teflon spacers (with Bruker instrument) were used. Spectra were recorded at room temperature. For each spectrum, 256 interferograms of 2 cm^{-1} resolution were co-added. A corresponding buffer spectrum was subtracted from each sample spectrum. All the spectra were baseline-corrected and normalized to the

same area of amide I/I' band (1700–1580 cm^{-1}) before further data processing. All data processing was performed using GRAMS software.

Dynamic light scattering

For DLS experiments, freshly prepared insulin solutions at different buffers were filtered using 0.22 μm syringe filter. The size measurements were performed using Zetasizer μV (Malvern instruments) with low-volume quartz batch cuvette at 60°C.

Atomic force microscopy

For AFM experiments, 1 mM insulin was diluted 100 times with deionized water, 30 μL of the sample were deposited on freshly cleaved mica and left to adsorb for 1 min, the sample was rinsed with 1 mL of water and dried gently using airflow. AFM images were recorded in the Tapping-in-Air mode at a drive frequency of approximately 300 kHz, using a MultiModee SPM microscope equipped with a NanoScope IIIa controller. PointProbe NCHR aluminium-coated silicon tips from Nanosensors were used as a probe.

Supporting Information

S1 Fig. Example of the repeatability of FTIR spectra. Red and blue spectra were collected using Thermo Nicolet instrument in TU Dortmund University, black and green–using Bruker Alpha instrument in Vilnius University.
(PDF)

S2 Fig. Fibril height measurements.
(PDF)

Author Contributions

Conceived and designed the experiments: VS. Performed the experiments: TS DD AB MG VS. Analyzed the data: TS DD VS. Contributed reagents/materials/analysis tools: RW VS. Wrote the paper: RW VS.

References

1. Chiti F, Dobson CM. Protein misfolding, functional amyloid, and human disease. Annu Rev Biochem. 2006; 75: 333–366. doi: 10.1146/annurev.biochem.75.101304.123901 PMID: 16756495
2. Pham CL, Kwan a H, Sunde M. Functional amyloid: widespread in Nature, diverse in purpose. Essays Biochem. 2014; 56: 207–219. doi: 10.1042/BSE0560207 PMID: 25131597
3. Fändrich M, Dobson CM. The behaviour of polyamino acids reveals an inverse side chain effect in amyloid structure formation. EMBO J. 2002; 21: 5682–5690. doi: 10.1093/emboj/cdf573 PMID: 12411486
4. Azriel R, Gazit E. Analysis of the minimal amyloid-forming fragment of the islet amyloid polypeptide. An experimental support for the key role of the phenylalanine residue in amyloid formation. J Biol Chem. 2001; 276: 34156–34161. doi: 10.1074/jbc.M102883200 PMID: 11445568
5. Sawaya MR, Sambashivan S, Nelson R, Ivanova MI, Sievers S a, Apostol MI, et al. Atomic structures of amyloid cross-beta spines reveal varied steric zippers. Nature. 2007; 447: 453–457. doi: 10.1038/nature05695 PMID: 17468747
6. Tamamis P, Adler-Abramovich L, Reches M, Marshall K, Sikorski P, Serpell L, et al. Self-assembly of phenylalanine oligopeptides: Insights from experiments and simulations. Biophys J. Biophysical Society; 2009; 96: 5020–5029. doi: 10.1016/j.bpj.2009.03.026
7. Adler-Abramovich L, Vaks L, Carny O, Trudler D, Magno A, Caflisch A, et al. Phenylalanine assembly into toxic fibrils suggests amyloid etiology in phenylketonuria. Nat Chem Biol. Nature Publishing Group; 2012; 8: 701–706. doi: 10.1038/nchembio.1002 PMID: 22706200
8. Prusiner SB. Prions. Proc Natl Acad Sci U S A. 1998; 95: 13363–13383. doi:VL—95 PMID: 9811807

9. Safar J, Wille H, Itri V, Groth D, Serban H, Torchia M, et al. Eight prion strains have PrP(Sc) molecules with different conformations. Nat Med. 1998; 4: 1157–1165. doi: 10.1038/2654 PMID: 9771749
10. Collinge J, Clarke AR. A general model of prion strains and their pathogenicity. Science. 2007; 318: 930–936. doi: 10.1126/science.1138718 PMID: 17991853
11. Dzwolak W, Smirnovas V, Jansen R, Winter R. Insulin forms amyloid in a strain-dependent manner: an FT-IR spectroscopic study. Protein Sci. 2004; 13: 1927–1932. doi: 10.1110/ps.03607204 PMID: 15169954
12. Petkova AT, Leapman RD, Guo Z, Yau W-M, Mattson MP, Tycko R. Self-propagating, molecular-level polymorphism in Alzheimer's beta-amyloid fibrils. Science. 2005; 307: 262–265. doi: 10.1126/science.1105850 PMID: 15653506
13. Heise H, Hoyer W, Becker S, Andronesi OC, Riedel D, Baldus M. Molecular-level secondary structure, polymorphism, and dynamics of full-length alpha-synuclein fibrils studied by solid-state NMR. Proc Natl Acad Sci U S A. 2005; 102: 15871–15876. doi: 10.1073/pnas.0506109102 PMID: 16247008
14. Dzwolak W, Grudzielanek S, Smirnovas V, Ravindra R, Nicolini C, Jansen R, et al. Ethanol-perturbed amyloidogenic self-assembly of insulin: Looking for origins of amyloid strains. Biochemistry. 2005; 44: 8948–8958. doi: 10.1021/bi050281t PMID: 15966720
15. Dzwolak W, Jansen R, Smirnovas V, Loksztejn A, Porowski S, Winter R. Template-controlled conformational patterns of insulin fibrillar self-assembly reflect history of solvation of the amyloid nuclei. Phys Chem Chem Phys. 2005; 7: 1349–1351. doi: 10.1039/b502255j PMID: 19787953
16. Paravastu AK, Leapman RD, Yau W-M, Tycko R. Molecular structural basis for polymorphism in Alzheimer's beta-amyloid fibrils. Proc Natl Acad Sci U S A. 2008; 105: 18349–18354. doi: 10.1073/pnas.0806270105 PMID: 19015532
17. Debelouchina GT, Platt GW, Bayro MJ, Radford SE, Griffin RG. Magic angle spinning NMR analysis of beta 2-microglobulin amyloid fibrils in two distinct morphologies. J Am Chem Soc. 2010; 132: 10414–10423. doi: 10.1021/ja102775u PMID: 20662519
18. Dinkel PD, Siddiqua A, Huynh H, Shah M, Margittai M. Variations in filament conformation dictate seeding barrier between three- and four-repeat tau. Biochemistry. 2011; 50: 4330–4336. doi: 10.1021/bi2004685 PMID: 21510682
19. Surmacz-Chwedoruk W, Nieznańska H, Wójcik S, Dzwolak W. Cross-seeding of fibrils from two types of insulin induces new amyloid strains. Biochemistry. 2012; 51: 9460–9469. doi: 10.1021/bi301144d PMID: 23127165
20. Chatani E, Yagi H, Naiki H, Goto Y. Polymorphism of beta 2-microglobulin amyloid fibrils manifested by ultrasonication-enhanced fibril formation in trifluoroethanol. J Biol Chem. 2012; 287: 22827–22837. doi: 10.1074/jbc.M111.333310 PMID: 22566695
21. Bousset L, Pieri L, Ruiz-Arlandis G, Gath J, Jensen PH, Habenstein B, et al. Structural and functional characterization of two alpha-synuclein strains. Nat Commun. 2013; 4: 2575. doi: 10.1038/ncomms3575 PMID: 24108358
22. Tycko R. Physical and structural basis for polymorphism in amyloid fibrils. Protein Sci. 2014; 23: 1528–39. doi: 10.1002/pro.2544 PMID: 25179159
23. Aguzzi A. Neurodegeneration: Alzheimer's disease under strain. Nature. 2014; 512: 32–4. doi: 10.1038/512032a PMID: 25100477
24. Stöhr J, Condello C, Watts JC, Bloch L, Oehler A, Nick M, et al. Distinct synthetic Aβ prion strains producing different amyloid deposits in bigenic mice. Proc Natl Acad Sci U S A. 2014; 111: 2–7. doi: 10.1073/pnas.1408968111
25. Watts JC, Condello C, Stöhr J, Oehler A, Lee J, DeArmond SJ, et al. Serial propagation of distinct strains of Aβ prions from Alzheimer's disease patients. Proc Natl Acad Sci. 2014; 111: 10323–10328. doi: 10.1073/pnas.1408900111 PMID: 24982139
26. Westermark GT, Westermark P. Prion-like aggregates: Infectious agents in human disease. Trends Mol Med. Elsevier Ltd; 2010; 16: 501–507. doi: 10.1016/j.molmed.2010.08.004 PMID: 20870462
27. Brundin P, Melki R, Kopito R. Prion-like transmission of protein aggregates in neurodegenerative diseases. Nat Rev Mol Cell Biol. Nature Publishing Group; 2010; 11: 301–307. doi: 10.1038/nrm2873 PMID: 20308987
28. Frost B, Diamond MI. Prion-like mechanisms in neurodegenerative diseases. Nat Rev Neurosci. Nature Publishing Group; 2010; 11: 155–159. doi: 10.1038/nrm2786 PMID: 20029438
29. Angot E, Steiner J a., Hansen C, Li JY, Brundin P. Are synucleinopathies prion-like disorders? Lancet Neurol. Elsevier Ltd; 2010; 9: 1128–1138. doi: 10.1016/S1474-4422(10)70213-1 PMID: 20846907
30. Prusiner SB. A Unifying Role for Prions in Neurodegenerative Diseases. Science (80-). 2012; 336: 1511–1513. doi: 10.1126/science.1222951

31. Eisele YS. From soluble Abeta to progressive Abeta aggregation: Could prion-like templated misfolding play a role? Brain Pathol. 2013; 23: 333–341. doi: 10.1111/bpa.12049 PMID: 23587139

32. Masuda-Suzukake M, Nonaka T, Hosokawa M, Oikawa T, Arai T, Akiyama H, et al. Prion-like spreading of pathological α-synuclein in brain. Brain. 2013; 136: 1128–1138. doi: 10.1093/brain/awt037 PMID: 23466394

33. Goedert M, Falcon B, Clavaguera F, Tolnay M. Prion-like Mechanisms in the Pathogenesis of Tauopathies and Synucleinopathies. Curr Neurol Neurosci Rep. 2014; 14: 495. doi: 10.1007/s11910-014-0495-z PMID: 25218483

34. Hill a F, Desbruslais M, Joiner S, Sidle KC, Gowland I, Collinge J, et al. The same prion strain causes vCJD and BSE. Nature. 1997; 389: 448–450, 526. doi: 10.1016/S0887-7963(98)80051-5 PMID: 9333232

35. Surmacz-Chwedoruk W, Babenko V, Dzwolak W. Master and Slave Relationship Between Two Types of Self-Propagating Insulin Amyloid Fibrils. J Phys Chem B. 2014; 118: 13582–13589. doi: 10.1021/jp510980b PMID: 25373010

36. Tanaka M, Chien P, Naber N, Cooke R, Weissman JS. Conformational variations in an infectious protein determine prion strain differences. Nature. 2004; 428: 323–328. doi: 10.1038/nature02392 PMID: 15029196

37. Tanaka M, Collins SR, Toyama BH, Weissman JS. The physical basis of how prion conformations determine strain phenotypes. Nature. 2006; 442: 585–589. doi: 10.1038/nature04922 PMID: 16810177

38. Colby DW, Giles K, Legname G, Wille H, Baskakov I V., DeArmond SJ, et al. Design and construction of diverse mammalian prion strains. Proc Natl Acad Sci U S A. 2009; 106: 20417–20422. doi: 10.1073/pnas.0910350106 PMID: 19915150

39. Cobb NJ, Apostol MI, Chen S, Smirnovas V, Surewicz WK. Conformational stability of mammalian prion protein amyloid fibrils is dictated by a packing polymorphism within the core region. J Biol Chem. 2014; 289: 2643–2650. doi: 10.1074/jbc.M113.520718 PMID: 24338015

40. Ostapchenko VG, Sawaya MR, Makarava N, Savtchenko R, Nilsson KPR, Eisenberg D, et al. Two amyloid states of the prion protein display significantly different folding patterns. J Mol Biol. Elsevier Ltd; 2010; 400: 908–921. doi: 10.1016/j.jmb.2010.05.051 PMID: 20553730

41. Caughey B, Raymond GJ, Bessen R a. Strain-dependent differences in beta-sheet conformations of abnormal prion protein. J Biol Chem. 1999; 273: 32230–32235. doi: 10.1074/jbc.273.48.32230

42. Malisauskas R, Botyriute A, Cannon JG, Smirnovas V. Flavone Derivatives as Inhibitors of Insulin Amyloid-Like Fibril Formation. PLoS One. 2015; 10: e0121231. doi: 10.1371/journal.pone.0121231 PMID: 25799281

43. Waugh DF, Wilhelmson DF, Commerford SL, Sackler ML. Studies of the nucleation and growth reactions of selected types of insulin fibrils. J Am Chem Soc. 1952; 75: 2592–2600. doi: 10.1021/ja01107a013

44. Kurouski D, Lombardi R a, Dukor RK, Lednev IK, Nafie L a. Direct observation and pH control of reversed supramolecular chirality in insulin fibrils by vibrational circular dichroism. Chem Commun (Camb). 2010; 46: 7154–7156. doi: 10.1039/c0cc02423f

45. Kurouski D, Dukor RK, Lu X, Nafie L a., Lednev IK. Normal and reversed supramolecular chirality of insulin fibrils probed by vibrational circular dichroism at the protofilament level of fibril structure. Biophys J. Elsevier; 2012; 103: 522–531. doi: 10.1016/j.bpj.2012.04.042 PMID: 22947868

46. Kurouski D, Dukor RK, Lu X, Nafie L a., Lednev IK. Spontaneous inter-conversion of insulin fibril chirality. Chem Commun. 2012; 48: 2837. doi: 10.1039/c2cc16895b

47. Bryant C, Spencer DB, Miller a, Bakaysa DL, McCune KS, Maple SR, et al. Acid stabilization of insulin. Biochemistry. 1993; 32: 8075–8082. doi: 10.1021/Bi00083a004 PMID: 8394123

48. Nielsen L, Frokjaer S, Brange J, Uversky VN, Fink a. L. Probing the mechanism of insulin fibril formation with insulin mutants. Biochemistry. 2001; 40: 8397–8409. doi: 10.1021/bi0105983 PMID: 11444987

49. Nettleton EJ, Tito P, Sunde M, Bouchard M, Dobson CM, Robinson C V. Characterization of the oligomeric states of insulin in self-assembly and amyloid fibril formation by mass spectrometry. Biophys J. Elsevier; 2000; 79: 1053–1065. doi: 10.1016/S0006-3495(00)76359-4 PMID: 10920035

50. Kim SK, Ha T, Schermann J-P. Biomolecular structures: from isolated molecules to the cell crowded medium. Phys Chem Chem Phys. 2010; 12: 3334–3335. doi: 10.1039/c004156b PMID: 20336242

51. Grudzielanek S, Jansen R, Winter R. Solvational tuning of the unfolding, aggregation and amyloidogenesis of insulin. J Mol Biol. 2005; 351: 879–894. doi: 10.1016/j.jmb.2005.06.046 PMID: 16051271

52. Milto K, Botyriute A, Smirnovas V. Amyloid-Like Fibril Elongation Follows Michaelis-Menten Kinetics. Baskakov I V., editor. PLoS One. 2013; 8: e68684. doi: 10.1371/journal.pone.0068684 PMID: 23874721

53. Glasoe PK, Long FA. Use of glass electrodes to measure acidities in deuterium oxide. J Phys Chem. 1960; 64: 188–190. doi: 10.1021/j100830a521

54. Bundi A, Wüthrich K. 1H-nmr parameters of the common amino acid residues measured in aqueous solutions of the linear tetrapeptides H-Gly-Gly-X-L-Ala-OH. Biopolymers. 1979; 18: 285–297. doi: 10.1002/bip.1979.360180206

PeerJ

Polymorphism of amyloid-like fibrils can be defined by the concentration of seeds

Tomas Sneideris*, Katažyna Milto* and Vytautas Smirnovas

Department of Biothermodynamics and Drug Design, Vilnius University, Institute of Biotechnology, Vilnius, Lithuania
* These authors contributed equally to this work.

ABSTRACT

Prions are infectious proteins where the same protein may express distinct strains. The strains are enciphered by different misfolded conformations. Strain-like phenomena have also been reported in a number of other amyloid-forming proteins. One of the features of amyloid strains is the ability to self-propagate, maintaining a constant set of physical properties despite being propagated under conditions different from those that allowed initial formation of the strain. Here we report a cross-seeding experiment using strains formed under different conditions. Using high concentrations of seeds results in rapid elongation and new fibrils preserve the properties of the seeding fibrils. At low seed concentrations, secondary nucleation plays the major role and new fibrils gain properties predicted by the environment rather than the structure of the seeds. Our findings could explain conformational switching between amyloid strains observed in a wide variety of *in vivo* and *in vitro* experiments.

Subjects Biochemistry, Biophysics
Keywords Amyloid, Prion, Protein misfolding, Protein aggregation, Amyloid-like fibrils, Prion strain, Polymorphism, Elongation, Nucleation

Submitted 19 May 2015
Accepted 1 August 2015
Published 20 August 2015

Corresponding author
Vytautas Smirnovas,
vytautas.smirnovas@bti.vu.lt

Academic editor
Vladimir Uversky

Additional Information and Declarations can be found on page 9

DOI 10.7717/peerj.1207

INTRODUCTION

Prions are infectious particles which play the main role in a group of fatal neurodegenerative disorders, also known as the transmissible spongiform encephalopaties (TSE's). Prion diseases propagate by self-replication of a pathogenic prion isoform (PrP^{Sc}) using cellular prion protein (PrP^{C}) as a substrate (*Prusiner, 1998*; *Collinge, 2001*). Although structures of infectious forms of PrP are still only partially defined, it is known that PrP^{Sc} is rich in beta-sheet structure and demonstrates fibrillar morphology (*Sim & Caughey, 2009*; *Colby & Prusiner, 2011*). Different conformations of PrP^{Sc} are responsible for variations in prion disease phenotypes and are usually referred to as strains (*Safar et al., 1998*). For a long time, prion protein was the only suspected infective protein in humans; however, recently there is growing evidence that proteins in other amyloid-related diseases may spread via prion-like mechanisms (*Lundmark et al., 2002*; *Soto, Estrada & Castilla, 2006*; *Frost & Diamond, 2010*; *Brundin, Melki & Kopito, 2010*; *Eisele et al., 2010*; *Angot et al., 2010*; *Westermark & Westermark, 2010*; *Masuda-Suzukake et al., 2013*; *Eisele, 2013*; *Goedert et al., 2014*). Moreover, the most recent data suggest that variants of Alzheimer's disease are encoded by different strains (*Stöhr et al., 2014*; *Watts et al., 2014*; *Aguzzi, 2014*).

How to cite this article Sneideris et al. (2015), Polymorphism of amyloid-like fibrils can be defined by the concentration of seeds. **PeerJ 3:e1207; DOI 10.7717/peerj.1207**

A lot of information on possible mechanisms of amyloid-like fibril formation comes from *in vitro* studies of the aggregation kinetics (*Knowles et al., 2009*; *Arosio et al., 2014*; *Meisl et al., 2014*). It is thought that four major steps are involved in fibril formation (*Meisl et al., 2014*). In the case of spontaneous aggregation, everything starts from primary nucleation. It takes time for a group of soluble protein molecules to get together and misfold into an amyloid-like structure, which serves as a nucleus for fibrillation. Once nuclei are formed, they start elongation into fibrils by attaching soluble protein at the ends and refolding it into an amyloid-like structure. Although nucleation and elongation could be sufficient for describing fibrillation, in many cases secondary processes, such as fibril fragmentation and secondary nucleation are extremely important (*Knowles et al., 2009*; *Meisl et al., 2014*). Fibril fragmentation increases the number of fibril ends, which leads to faster elongation. The presence of fibrils can induce formation of new nuclei with much shorter lag times compared to primary nucleation; this is referred to as secondary nucleation (*Meisl et al., 2014*).

How would such a mechanism of fibril formation work in the case of different amyloid strains? Strain-like structural polymorphism was observed in a number of different amyloid-forming proteins (*Tanaka et al., 2004*; *Tanaka et al., 2005*; *Yamaguchi et al., 2004*; *Dzwolak et al., 2004*; *Petkova et al., 2005*; *Jones & Surewicz, 2005*; *Heise et al., 2005*; *Paravastu et al., 2008*; *Makarava et al., 2009*; *Colby et al., 2009*; *Dinkel et al., 2011*; *Jones et al., 2011*; *Chatani et al., 2012*; *Bousset et al., 2013*; *Ghaemmaghami et al., 2013*; *Cobb et al., 2014*; *Tycko, 2014*; *Surmacz-Chwedoruk, Babenko & Dzwolak, 2014*). To form different amyloid strains *de novo* using the same protein, different environmental conditions, such as temperature (*Tanaka et al., 2005*), shear forces (*Makarava et al., 2009*), concentration of denaturants (*Cobb et al., 2014*) or co-solvents (*Dzwolak et al., 2004*) are involved. Once nuclei are formed, they are able to carry strain-specific properties even in unfavorable environments (*Dzwolak et al., 2004*; *Petkova et al., 2005*; *Makarava et al., 2009*; *Cobb et al., 2014*; *Surmacz-Chwedoruk, Babenko & Dzwolak, 2014*). This indicates that environment defines different strains during primary nucleation, but affects only kinetics, not the structure, of fibrils formed via elongation. In the case of secondary nucleation, formation of new nuclei is induced by existing fibrils, but there is no experimental evidence if the structure of these nuclei is determined by the environment conditions, or by structure of the fibrils. Or in other words, can secondary nucleation be responsible for conformational switching in amyloid-like fibril strains?

MATERIALS AND METHODS

Recombinant mouse prion protein fragment (rMoPrP(89-230)) used in this study was purified and stored as described previously (*Milto, Michailova & Smirnovas, 2014*). Protein grade guanidine hydrochloride (GuHCl) was purchased from Carl Roth GmbH, guanidine thiocyanate (GuSCN) and other chemicals were purchased from Fisher Scientific UK.

To prepare different fibril strains, monomeric protein from a stock solution was diluted to a concentration of 0.5 mg/mL in 50 mM phosphate buffer (pH 6) containing 2 M or 4 M GuHCl, and incubated for one week at 37 °C with 220 rpm shaking (in shaker incubator

IKA KS 4000i). For seeding experiments rPrP-A^{4M} fibrils were treated for 10 min using Bandelin Sonopuls 3100 ultrasonic homogenizer equipped with MS72 tip (using 20% power, cycles of 30 s/30 s sonication/rest, total energy applied to the sample per cycle—0.36 kJ). The sample was kept on ice during the sonication. Right after the treatment, fibrils were mixed with 0.5 mg/ml of mouse prion solution in 2 M GuHCl in 50 mM phosphate buffer, pH 6, containing 50 μM ThT. Elongation kinetics at 60 °C temperature was monitored by ThT fluorescence assay (excitation at 470 nm, emission at 510 nm) using Qiagen Rotor-Gene Q real-time analyzer (*Milto, Michailova & Smirnovas, 2014*). ThT fluorescence curves were normalized by dividing each point by the maximum intensity of the curve.

For denaturation assays, amyloid fibrils were resuspended to a concentration of 25 μM in 50 mM phosphate buffer, pH 6, containing 0.5 M GuSCN and homogenized by sonication (same way as in preparation of seeds). These solutions were diluted 1:4 in a buffer containing varying concentrations of GuSCN, and incubated for 60 min at 25 °C in Maxymum Recovery™ microtubes (Axygen Scientific, Inc., Union City, California, USA). 150 μL of samples were mixed with 850 μL of 100 mM phosphate buffer, pH 7, containing ThT (final concentration after dilution was 50 μM), then each mixture was sonicated for 15 s (same conditions as described above). Fluorescence was measured at 480 nm using the excitation wavelength of 440 nm. Denaturation curves were normalized by dividing each point by the average intensity of the points in the plateau region. Fractional loss of signal at increasing denaturant concentrations corresponds to the fraction of rPrP dissociated from amyloid fibrils.

For AFM experiments, 30 μL of the sample were deposited on freshly cleaved mica and left to adsorb for 1 min, the sample was rinsed with several mL of water and dried gently using airflow. AFM images were recorded in the Tapping-in-Air mode at a drive frequency of approximately 300 kHz, using a Dimension Icon (Bruker, Santa Barbara, California, USA) scanning probe microscope system. Aluminium-coated silicon tips (RTESPA-300) from Bruker were used as a probe.

To prepare samples for the FTIR measurements, rMoPrP aggregates were separated from the buffer by centrifugation (30 min, 15,000 g), and resuspended in D_2O, sedimentation and resuspension was repeated three times to minimize the amount of GuHCl and H_2O. After resuspension samples were homogenized by 1 min sonication (same conditions as described above). The FTIR spectra were recorded using Bruker Alpha spectrometer equipped with deuterium triglycine sulfate (DTGS) detector. For all measurements, CaF_2 transmission windows and 0.1 mm Teflon spacers were used. Spectra were recorded at room temperature. For each spectrum, 256 interferograms of 2 cm^{-1} resolution were co-added. A corresponding buffer spectrum was subtracted from each sample spectrum. All the spectra were normalized to the same area of amide I/I' band. All data processing was performed using GRAMS software.

RESULTS

Conformational stability of PrP^{Sc} as defined by resistance to chemical denaturation has been one of the key parameters used to define differences between strains (*Colby et al.,*

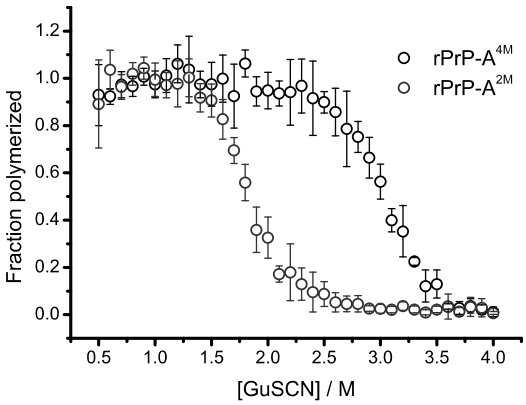

Figure 1 Denaturation profiles of rPrP-A^{2M} and rPrP-A^{4M} fibrils in GuSCN reveal different conformational stabilities. Standard errors calculated from 6 measurements using Student's *t*-distribution at $P = 0.05$.

2009). Different strains of recombinant mammalian prion protein amyloid-like fibrils made in 2 and 4 M guanidine hydrochloride (rPrP-A^{2M} and rPrP-A^{4M}, respectively) were thoroughly characterized by Surewicz group (*Cobb et al., 2014*). We used recombinant N-terminally truncated mouse prion protein (rMoPrP(89-230)) to create rPrP-A^{2M} and rPrP-A^{4M} strains of amyloid-like fibrils. Similar to recent data on recombinant human PrP (*Cobb et al., 2014*), rMoPrP fibrils formed in 2 and 4 M guanidine hydrochloride (GuHCl) have different conformational stability (Fig. 1). Due to the fact that rPrP-A^{4M} fibrils could not be fully denatured using even 7.5 M GuHCl (*Cobb et al., 2014*), a denaturation assay using a more strongly chaotropic salt, guanidine thiocynate (GuSCN) was performed. Midpoint of denaturation of rPrP-A^{2M} is at ∼1.8 M GuSCN and rPrP-A^{4M} is at ∼3 M GuSCN, respectively. This difference served as a simple, unbiased marker of different strains in further experiments.

In our previous work we have described elongation kinetics at different temperatures and GuHCl concentrations, using rPrP-A^{2M} as a seed (*Milto, Michailova & Smirnovas, 2014*). It was not possible to get reliable data above 2.5 M GuHCl due to depolymerization of rPrP-A^{2M}. Thus only one way cross-seeding is possible for rPrP-A^{2M} and rPrP-A^{4M} strains. We followed cross-seeding kinetics using different concentrations of seeds. As seen in Fig. 2A, five percent seeds led to fast growth of amyloid-like fibrils from the very beginning, suggesting fast fibril elongation. At 1% seed volume (Fig. 2B) elongation is slower, but after some time the rate of aggregation explodes. At a lower concentration of seeds (Fig. 2C) elongation is very slow and the curve looks sigmoidal, as usually seen in case of spontaneous fibrillation; however in absence of seeds no aggregation was detected within the experimental timeframe. Fitting data suggests that the observed process can be

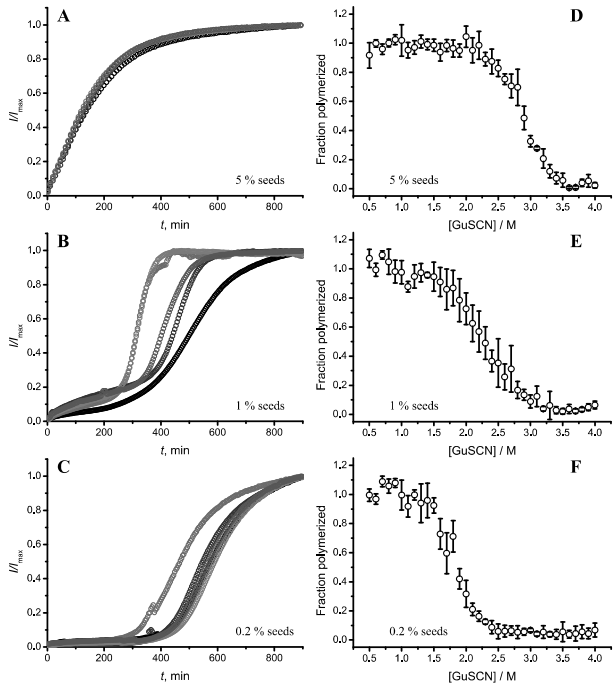

Figure 2 Concentration of seeds determines the mechanism of aggregation and stability of the final strain. Different amounts of rPrP-A^{4M} fibrils (sonicated for 300 s) were added to the solution of rMoPrP, prepared in 2 M GuHCl, 50 mM phosphate buffer, pH6. The kinetics was followed at 60 °C using Thioflavin T (ThT) fluorescence assay, five data repeats at each seed concentration plotted in (A–C). No change of ThT fluorescence was observed in samples without seeds. Denaturation profiles in GuSCN reveal different conformational stabilities of formed fibrils (D–F). Standard errors calculated from 6 measurements using Student's *t*-distribution at $P = 0.05$.

attributed to fibril-induced secondary nucleation (see Supplemental Information). The fibril denaturation assay (Fig. 2D) revealed that stability of fibrils formed in the presence of 5% seeds (midpoint at ∼2.9 M GuSCN) is very similar to rPrP-A^{4M} strain, which was used as a seed. At 1% seed volume (Fig. 2E), stability of fibrils is lower (midpoint at ∼2.2 M GuSCN), and at 0.2% of seeds (Fig. 2F) it is the same (midpoint at ∼1.8 M GuSCN) as the rPrP-A^{2M} strain. This allows hypothesizing that fibrils initiated by secondary nucleation do not follow the seeding template, despite using template fibrils as nucleation sites.

AFM analysis did not reveal any major differences between rPrP-A^{4M} and rPrP-A^{2M} strains (Figs. 3A and 3B). In both cases fibril diameters range from 4 to 16 nm, however thicker fibrils are more often in samples of rPrP-A^{2M} strains. This difference is more

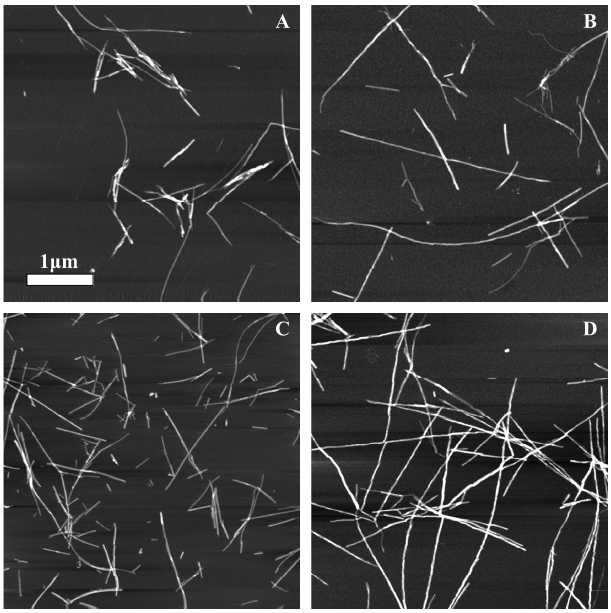

Figure 3 AFM images of rMoPrP amyloid-like aggregates. (A) and (B) show fibrils of rPrP-A^{4M} and rPrP-A^{2M} strains, (C) and (D) show fibrils formed during cross-seeding in the presence of 5% and 0.2% seeds, respectively.

obvious when comparing fibrils formed in presence of 5% and 0.2% seeds (Figs. 3C and 3D). The majority of fibrils formed in presence of high amount of seeds are 4–8 nm in diameter, while these formed at low seed concentration are usually 8–16 nm.

FTIR spectra of rMoPrP amyloid-like fibrils display major band in the amide I/I' region, corresponding to beta-sheet structure with subtle difference in band frequencies between rPrP-A^{4M} and rPrP-A^{2M} strains (Fig. 4). The spectrum of rPrP-A^{4M} strain is very similar to the spectrum of fibrils, prepared in the presence of 5% seeds; both show peak maxima at ~1,620 cm^{-1}. The spectrum of rPrP-A^{2M} strain and the spectrum of fibrils, prepared in the presence of 0.2% seeds show peak maxima at ~1,624 cm^{-1}. This data serve as additional confirmation that propagation of the strain-specific structure depends on the amount of seeds and possibly on the mechanism of aggregation.

In our previous work we have demonstrated the impact of sonication on the elongation kinetics of PrP fibrils (*Milto, Michailova & Smirnovas, 2014*). Comparison of microscopy data before (Fig. 3A) and after (Fig. 5) sonication suggests that the main effect of sonication is breaking fibrils into shorter pieces, thus increasing number of fibril ends.

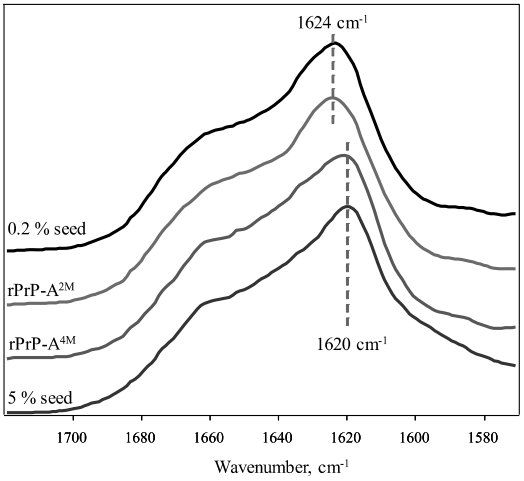

Figure 4 **FTIR spectra of rPrP amyloid-like fibrils.**

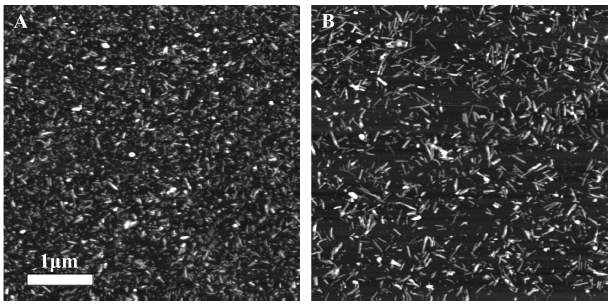

Figure 5 **AFM images of rPrP-A^{4M} fibrils after 300 s (A) and 30 s (B) sonication.**

As seen in Figs. 6A and 6B, in case of shorter (or in the absence of) sonication, kinetic curves have sigmoidal shapes, similar as in case of lower amount of longer-sonicated seeds. Fibrils formed in the presence of 30 s sonicated seeds (Fig. 6C) are more stable (midpoint at ~2.8 M GuSCN) compared to the fibrils formed in presence of unsonicated seeds (midpoint at ~2.3 M GuSCN).

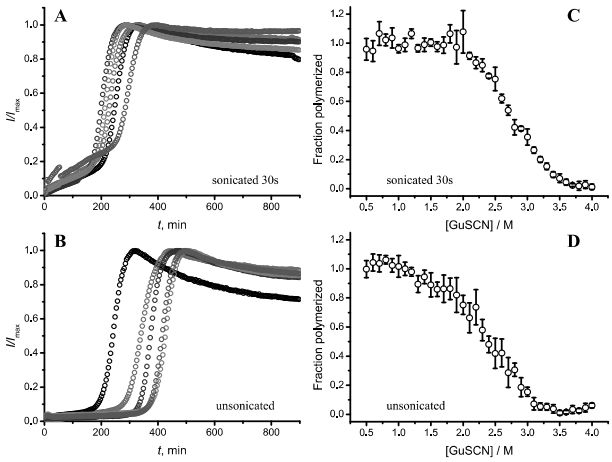

Figure 6 Effect of sonication on the kinetics of aggregation (A–B) and stability of formed fibrils (C–D). The same amount of seeds (5%) was used in all experiments. Five data repeats plotted in (A) and (B). Standard errors calculated from 6 measurements using Student's *t*-distribution at $P = 0.05$.

DISCUSSION

Taken together the data with different seed concentrations (Fig. 2), and sonication times (Fig. 6), show that stability of fibrils is dependent on the kinetics. Different processes in fibril formation leads to the mixture of rPrP-A^{4M} and rPrP-A^{2M} fibril populations in all samples, and different proportions of two strains determine their denaturation profiles. Increase of fibril ends leads to shorter lag times and faster elongation rates, and to the bigger proportion of more stable fibrils. In fact, we cannot exclude the impact of fibril surface as a catalyzer of secondary nucleation. Larger super-structures can be disrupted by sonication thus releasing more fibril surface. We haven't found large clumps using microscopy, but the possibility of larger aggregates is suggested by the decline of final fluorescence in samples where mild or no sonication was used. Larger aggregates used as seeds grow further and may settle out of solution leading to the decrese of ThT fluorescence.

It is interesting to compare reproducibility of kinetic curves at different conditions. At highest amount of seeds the data is extremely reproducible (Fig. 2A), which is common for fibril elongation reactions. In case of lowest seed concentration (Fig. 2C) it is also relatively good; however it is poor at moderate seed concentration (Fig. 2B) or in case of unsonicated seeds (Fig. 6B). Nucleation is a stochastic event and the reproducibility goes down with the decrease of the monomer concentration. Due to the elongation of fibrils, average monomer concentration available for nucleation in the presence of 1% seeds is lower than in case of 0.2% seeds, thus it can serve as an explanation of the worse reproducibility.

Amyloid strain switching has been observed in animal studies (*Bartz et al., 2000*; *Asante et al., 2002*; *Lloyd et al., 2004*; *Ghaemmaghami et al., 2013*), cell culture (*Li et al., 2010*), and experiments *in vitro* (*Castilla et al., 2008*; *Makarava et al., 2009*; *Surmacz-Chwedoruk, Babenko & Dzwolak, 2014*). Two possibilities are suggested to explain this phenomenon (*Collinge & Clarke, 2007*; *Cobb & Surewicz, 2009*). The first one describes coexistence of multiple structures in the infective material, when only the dominant type would be recognized experimentally; however, upon transmission to different host, the minor population may self-propagate much better and become dominant, reflected in the change of strain properties. Recently this way of amyloid strain switching was demonstrated for insulin fibrils *in vitro* (*Surmacz-Chwedoruk, Babenko & Dzwolak, 2014*). The second possibility suggested that sometimes host protein can adopt amyloid conformations distinct from the heterologous template. The Baskakov group demonstrated adaptive conformational switching within individual fibrils as a possible mechanism for such change (*Makarava et al., 2009*). Our data suggests a possibility of strain switching via secondary nucleation pathways. Moreover, secondary nucleation could explain switching of strains in absence of species barrier, for example in case of recently described Darwinian evolution of prions in cell culture, which showed strain mutations within a single host protein (*Li et al., 2010*) or in case of protein misfolding cyclic amplification (PMCA) of recombinant PrP (*Smirnovas et al., 2009*). In summary, we hypothesize that continuous propagation or switching between amyloid strains may be determined by the mechanism of replication in addition to the environment. In cases when a species barrier or environmental barrier stops or slows down fibril elongation, there is the possibility of secondary nucleation events to seed the formation of different strains. The mechanism is dependent on the concentration of fibrils, which opens up a new dimension in cross-species and cross-environment seeding/infection experiments.

We would like to acknowledge that part of the described kinetic profiles differs from the general fibrillation kinetics, normally observed in the field. Thus, in the absence of supporting investigations of different systems, we would like to stress that all our findings may be limited to the described system and any extrapolation to other amyloid proteins and/or other conditions of fibrillation needs an additional experimental evidence.

ACKNOWLEDGEMENTS

The authors thank Prof. Witold Surewicz for sharing MoPrP(89-230) plasmid, Dr. Marija Jankunec for help with AFM, and Dr. Jonathan G. Cannon for critical reading of the manuscript.

ADDITIONAL INFORMATION AND DECLARATIONS

Funding

This research was funded by a grant (No. MIP-030/2012) from the Research Council of Lithuania. VS was supported by a Marie Curie Career Integration Grant 293476. The funders had no role in study design, data collection and analysis, decision to publish, or preparation of the manuscript.

Grant Disclosures

The following grant information was disclosed by the authors:
Research Council of Lithuania: MIP-030/2012.
Marie Curie Career Integration Grant: 293476.

Competing Interests

The authors declare there are no competing interests.

Author Contributions

- Tomas Sneideris and Katažyna Milto conceived and designed the experiments, performed the experiments, analyzed the data, prepared figures and/or tables, reviewed drafts of the paper.
- Vytautas Smirnovas conceived and designed the experiments, analyzed the data, contributed reagents/materials/analysis tools, wrote the paper, prepared figures and/or tables, reviewed drafts of the paper.

Supplemental Information

Supplemental information for this article can be found online at http://dx.doi.org/10.7717/peerj.1207#supplemental-information.

REFERENCES

Aguzzi A. 2014. Neurodegeneration: alzheimer's disease under strain. *Nature* **512**:32–34 DOI 10.1038/512032a.

Angot E, Steiner JA, Hansen C, Li JY, Brundin P. 2010. Are synucleinopathies prion-like disorders? *The Lancet Neurology* **9**:1128–1138 DOI 10.1016/S1474-4422(10)70213-1.

Arosio P, Cukalevski R, Frohm B, Knowles TPJ, Linse S. 2014. Quantification of the concentration of Abeta42 propagons during the lag phase by an amyloid chain reaction assay. *Journal of the American Chemical Society* **136**:219–225 DOI 10.1021/ja408765u.

Asante EA, Linehan JM, Desbruslais M, Joiner S, Gowland I, Wood AL, Welch J, Hill AF, Lloyd SE, Wadsworth JDF, Collinge J. 2002. BSE prions propagate as either variant CJD-like or sporadic CJD-like prion strains in transgenic mice expressing human prion protein. *EMBO Journal* **21**:6358–6366 DOI 10.1093/emboj/cdf653.

Bartz JC, Bessen RA, McKenzie D, Marsh RF, Aiken JM. 2000. Adaptation and selection of prion protein strain conformations following interspecies transmission of transmissible mink encephalopathy. *Journal of Virology* **74**:5542–5547 DOI 10.1128/JVI.74.12.5542-5547.2000.

Bousset L, Pieri L, Ruiz-Arlandis G, Gath J, Jensen PH, Habenstein B, Madiona K, Olieric V, Böckmann A, Meier BH, Melki R. 2013. Structural and functional characterization of two alpha-synuclein strains. *Nature Communications* **4**:Article 2575 DOI 10.1038/ncomms3575.

Brundin P, Melki R, Kopito R. 2010. Prion-like transmission of protein aggregates in neurodegenerative diseases. *Nature Reviews. Molecular Cell Biology* **11**:301–307 DOI 10.1038/nrm2873.

Castilla J, Gonzalez-Romero D, Saá P, Morales R, De Castro J, Soto C. 2008. Crossing the species barrier by PrPSc replication *in vitro* generates unique infectious prions. *Cell* **134**:757–768 DOI 10.1016/j.cell.2008.07.030.

Chatani E, Yagi H, Naiki H, Goto Y. 2012. Polymorphism of beta 2-microglobulin amyloid fibrils manifested by ultrasonication-enhanced fibril formation in trifluoroethanol. *Journal of Biological Chemistry* **287**:22827–22837 DOI 10.1074/jbc.M111.333310.

Cobb NJ, Apostol MI, Chen S, Smirnovas V, Surewicz WK. 2014. Conformational stability of mammalian prion protein amyloid fibrils is dictated by a packing polymorphism within the core region. *Journal of Biological Chemistry* **289**:2643–2650 DOI 10.1074/jbc.M113.520718.

Cobb NJ, Surewicz WK. 2009. Prion diseases and their biochemical mechanisms. *Biochemistry* **48**:2574–2585 DOI 10.1021/bi900108v.

Colby DW, Giles K, Legname G, Wille H, Baskakov IV, DeArmond SJ, Prusiner SB. 2009. Design and construction of diverse mammalian prion strains. *Proceedings of the National Academy of Sciences of the United States of America* **106**:20417–20422 DOI 10.1073/pnas.0910350106.

Colby DW, Prusiner SB. 2011. Prions. *Cold Spring Harbor Perspectives in Biology* **3**:1–22 DOI 10.1101/cshperspect.a006833.

Collinge J. 2001. Prion diseases of humans and animals: their causes and molecular basis. *Annual Review of Neuroscience* **24**:519–550 DOI 10.1146/annurev.neuro.24.1.519.

Collinge J, Clarke AR. 2007. A general model of prion strains and their pathogenicity. *Science* **318**:930–936 DOI 10.1126/science.1138718.

Dinkel PD, Siddiqua A, Huynh H, Shah M, Margittai M. 2011. Variations in filament conformation dictate seeding barrier between three- and four-repeat tau. *Biochemistry* **50**:4330–4336 DOI 10.1021/bi2004685.

Dzwolak W, Smirnovas V, Jansen R, Winter R. 2004. Insulin forms amyloid in a strain-dependent manner: an FT-IR spectroscopic study. *Protein Science: a Publication of the Protein Society* **13**:1927–1932 DOI 10.1110/ps.03607204.

Eisele YS, Obermüller U, Heilbronner G, Baumann F, Kaeser SA, Wolburg H, Walker LC, Staufenbiel M, Heikenwalder M, Jucker M. 2010. Peripherally applied Abeta-containing inoculates induce cerebral beta-amyloidosis. *Science* **330**:980–982 DOI 10.1126/science.1194516.

Eisele YS. 2013. From soluble Abeta to progressive Abeta aggregation: could prion-like templated misfolding play a role? *Brain Pathology* **23**:333–341 DOI 10.1111/bpa.12049.

Frost B, Diamond MI. 2010. Prion-like mechanisms in neurodegenerative diseases. *Nature Reviews. Neuroscience* **11**:155–159 DOI 10.1038/nrn2786.

Ghaemmaghami S, Colby DW, Nguyen HOB, Hayashi S, Oehler A, Dearmond SJ, Prusiner SB. 2013. Convergent replication of mouse synthetic prion strains. *American Journal of Pathology* **182**:866–874 DOI 10.1016/j.ajpath.2012.11.038.

Goedert M, Falcon B, Clavaguera F, Tolnay M. 2014. Prion-like mechanisms in the pathogenesis of tauopathies and synucleinopathies. *Current Neurology and Neuroscience Reports* **14**:Article 495 DOI 10.1007/s11910-014-0495-z.

Heise H, Hoyer W, Becker S, Andronesi OC, Riedel D, Baldus M. 2005. Molecular-level secondary structure, polymorphism, and dynamics of full-length alpha-synuclein fibrils studied by solid-state NMR. *Proceedings of the National Academy of Sciences of the United States of America* **102**:15871–15876 DOI 10.1073/pnas.0506109102.

Jones EM, Surewicz WK. 2005. Fibril conformation as the basis of species- and strain-dependent seeding specificity of mammalian prion amyloids. *Cell* **121**:63–72 DOI 10.1016/j.cell.2005.01.034.

Jones EM, Wu B, Surewicz K, Nadaud PS, Helmus JJ, Chen S, Jaroniec CP, Surewicz WK. 2011. Structural polymorphism in amyloids: new insights from studies with Y145Stop prion protein fibrils. *Journal of Biological Chemistry* **286**:42777–42784 DOI 10.1074/jbc.M111.302539.

Knowles TPJ, Waudby CA, Devlin GL, Cohen SIA, Aguzzi A, Vendruscolo M, Terentjev EM, Welland ME, Dobson CM. 2009. An analytical solution to the kinetics of breakable filament assembly. *Science* **326**:1533–1537 DOI 10.1126/science.1178250.

Li J, Browning S, Mahal SP, Oelschlegel AM, Weissmann C. 2010. Darwinian evolution of prions in cell culture. *Science* **327**:869–872 DOI 10.1126/science.1183218.

Lloyd SE, Linehan JM, Desbruslais M, Joiner S, Buckell J, Brandner S, Wadsworth JDF, Collinge J. 2004. Characterization of two distinct prion strains derived from bovine spongiform encephalopathy transmissions to inbred mice. *Journal of General Virology* **85**:2471–2478 DOI 10.1099/vir.0.79889-0.

Lundmark K, Westermark GT, Nyström S, Murphy CL, Solomon A, Westermark P. 2002. Transmissibility of systemic amyloidosis by a prion-like mechanism. *Proceedings of the National Academy of Sciences of the United States of America* **99**:6979–6984 DOI 10.1073/pnas.092205999.

Makarava N, Ostapchenko VG, Savtchenko R, Baskakov IV. 2009. Conformational switching within individual amyloid fibrils. *Journal of Biological Chemistry* **284**:14386–14395 DOI 10.1074/jbc.M900533200.

Masuda-Suzukake M, Nonaka T, Hosokawa M, Oikawa T, Arai T, Akiyama H, Mann DMA, Hasegawa M. 2013. Prion-like spreading of pathological α-synuclein in brain. *Brain* **136**:1128–1138 DOI 10.1093/brain/awt037.

Meisl G, Yang X, Hellstrand E, Frohm B, Kirkegaard JB, Cohen SIA, Dobson CM, Linse S, Knowles TPJ. 2014. Differences in nucleation behavior underlie the contrasting aggregation kinetics of the Aβ40 and Aβ42 peptides. *Proceedings of the National Academy of Sciences of the United States of America* **111**:9384–9389 DOI 10.1073/pnas.1401564111.

Milto K, Michailova K, Smirnovas V. 2014. Elongation of mouse prion protein amyloid-like fibrils: effect of temperature and denaturant concentration. *PLoS ONE* **9**:e94469 DOI 10.1371/journal.pone.0094469.

Paravastu AK, Leapman RD, Yau W-M, Tycko R. 2008. Molecular structural basis for polymorphism in Alzheimer's beta-amyloid fibrils. *Proceedings of the National Academy of Sciences of the United States of America* **105**:18349–18354 DOI 10.1073/pnas.0806270105.

Petkova AT, Leapman RD, Guo Z, Yau W-M, Mattson MP, Tycko R. 2005. Self-propagating, molecular-level polymorphism in alzheimer's beta-amyloid fibrils. *Science* **307**:262–265 DOI 10.1126/science.1105850.

Prusiner SB. 1998. Prions. *Proceedings of the National Academy of Sciences of the United States of America* **95**:13363–13383 DOI 10.1073/pnas.95.23.13363.

Safar J, Wille H, Itri V, Groth D, Serban H, Torchia M, Cohen FE, Prusiner SB. 1998. Eight prion strains have PrP(Sc) molecules with different conformations. *Nature Medicine* **4**:1157–1165 DOI 10.1038/2654.

Sim VL, Caughey B. 2009. Ultrastructures and strain comparison of under-glycosylated scrapie prion fibrils. *Neurobiology of Aging* **30**:2031–2042 DOI 10.1016/j.neurobiolaging.2008.02.016.

Smirnovas V, Kim J Il, Lu X, Atarashi R, Caughey B, Surewicz WK. 2009. Distinct structures of scrapie prion protein (PrPSc)-seeded versus spontaneous recombinant prion protein fibrils revealed by hydrogen/deuterium exchange. *Journal of Biological Chemistry* **284**:24233–24241 DOI 10.1074/jbc.M109.036558.

Soto C, Estrada L, Castilla J. 2006. Amyloids, prions and the inherent infectious nature of misfolded protein aggregates. *Trends in Biochemical Sciences* **31**:150–155 DOI 10.1016/j.tibs.2006.01.002.

Stöhr J, Condello C, Watts JC, Bloch L, Oehler A, Nick M, DeArmond SJ, Giles K, DeGrado WF,

Prusiner SB. 2014. Distinct synthetic Aβ prion strains producing different amyloid deposits in bigenic mice. *Proceedings of the National Academy of Sciences of the United States of America* **111**:2–7 DOI 10.1073/pnas.1408968111.

Surmacz-Chwedoruk W, Babenko V, Dzwolak W. 2014. Master and slave relationship between two types of self-propagating insulin amyloid fibrils. *The Journal of Physical Chemistry B* **118**:13582–13589 DOI 10.1021/jp510980b.

Tanaka M, Chien P, Naber N, Cooke R, Weissman JS. 2004. Conformational variations in an infectious protein determine prion strain differences. *Nature* **428**:323–328 DOI 10.1038/nature02392.

Tanaka M, Chien P, Yonekura K, Weissman JS. 2005. Mechanism of cross-species prion transmission: an infectious conformation compatible with two highly divergent yeast prion proteins. *Cell* **121**:49–62 DOI 10.1016/j.cell.2005.03.008.

Tycko R. 2014. Physical and structural basis for polymorphism in amyloid fibrils. *Protein Science: a Publication of the Protein Society* **23**:1528–1539 DOI 10.1002/pro.2544.

Watts JC, Condello C, Stöhr J, Oehler A, Lee J, DeArmond SJ, Lannfelt L, Ingelsson M, Giles K, Prusiner SB. 2014. Serial propagation of distinct strains of Aβ prions from alzheimer's disease patients. *Proceedings of the National Academy of Sciences* **111**:10323–10328 DOI 10.1073/pnas.1408900111.

Westermark GT, Westermark P. 2010. Prion-like aggregates: infectious agents in human disease. *Trends in Molecular Medicine* **16**:501–507 DOI 10.1016/j.molmed.2010.08.004.

Yamaguchi KI, Katou H, Hoshino M, Hasegawa K, Naiki H, Goto Y. 2004. Core and heterogeneity of β2-microglobulin amyloid fibrils as revealed by H/D exchange. *Journal of Molecular Biology* **338**:559–571 DOI 10.1016/j.jmb.2004.02.067.

PCCP

PAPER

View Article Online
View Journal | View Issue

Cite this: *Phys. Chem. Chem. Phys.*, 2018, **20**, 27638

Received 30th July 2018,
Accepted 22nd October 2018

DOI: 10.1039/c8cp04838j

rsc.li/pccp

Self-inhibition of insulin amyloid-like aggregation†

Mantas Ziaunys, Tomas Sneideris and Vytautas Smirnovas *

Protein misfolding and amyloid formation are related to multiple diseases. Besides its relation to injection-localized amyloidosis, insulin is also often used as a model protein to study amyloid aggregation *in vitro*. Possible mechanisms for aggregation of insulin monomers into amyloid-like fibrils are described in several publications, but the role of native-like oligomers, which are present in solution above pH 2, is poorly understood. Here we show that the addition of sodium chloride shifts the equilibrium from monomers towards oligomers without affecting the secondary structure of insulin. Initial analysis of the aggregation kinetics showed unusual dependence of aggregation half-times on the initial insulin concentration, suggesting the possibility of self-inhibition. Global fitting of the kinetic data revealed possible capping of fibril ends by insulin tetramers, leading to the inhibition of fibril elongation.

Introduction

Amyloids are self-assembled, highly ordered and closely packed peptide or protein aggregates, which are usually rich in β-sheet structures.[1,2] Formation of insoluble amyloid aggregates is associated with multiple disorders,[3,4] including currently incurable and fatal neurodegenerative diseases such as Alzheimer's, Parkinson's or infective prion diseases. A proper understanding of the aggregation process, including the molecular pathways leading to the formation of amyloid structures, is crucial for the development of effective medicine and treatment methods of amyloid diseases.

The process of amyloid formation is very complex and consists of multiple microscopic events. Different combinations and rates of these events can determine distinct aggregation pathways.[5] The amyloid aggregation mechanism consists of a combination of four microscopic events: spontaneous formation of nuclei, which act as aggregation centers; elongation of existing fibrils by the addition of monomers to the ends of fibrils; fragmentation of fibrils, which results in generation of new fibril ends (aggregation centers); and secondary nucleation – fibril-surface-catalysed formation of aggregation nuclei.[5,6]

Protein aggregation is influenced by the environment. Factors, such as different pH,[7–12] temperature,[8,12–14] agitation,[12,15,16] pressure,[17] ionic strength,[17–19] protein concentration[12,14,19–26] and the presence of different co-solvents,[27,28] other additives[12,14,29,30] or preformed protein aggregates,[12,31,32] were shown to affect protein amyloid formation. A wide variety of environmental conditions suggest the possible existence of different aggregation mechanisms that may lead towards formation of distinct amyloid structures (polymorphs) of the same protein, which makes the aggregation process notoriously difficult to study and understand.

Insulin is a peptide hormone that is involved in the regulation of carbohydrate, fat and protein metabolism. Despite its main use in medicine, it is also extensively used as a model protein to study amyloid-like fibril formation *in vitro*. It was shown that changes in the environment may affect insulin aggregation and induce formation of polymorphs. Several sets of conditions leading to distinct structures of insulin amyloid-like fibrils include the presence/absence of 20% ethanol,[27,28,33] slightly different pH/pD ($\leq$2 and 2.4),[34] and using different insulin forms (bovine insulin *versus* recombinant LysB31–ArgB32 human insulin analogue).[32,35] The most recent study suggested that all three cases lead to the same pair of structures.[34] However, for deeper understanding of insulin amyloid-like fibril polymorphism, mechanistic studies of insulin aggregation at different conditions are necessary. A series of studies demonstrated the power of global fitting of kinetic models to elucidate molecular mechanisms of amyloid aggregation.[5,6,16,36–40] Global fitting of insulin fibrillation kinetics at pH 1.6 suggested a "classic" amyloid aggregation mechanism with a saturated elongation step.[5] In order to reveal mechanistic differences leading towards the pH-induced polymorphism of insulin amyloid-like fibrils, we used global fitting on the data of insulin aggregation at pH 2.4.

Results and discussion

It is known that the presence of NaCl may affect aggregation kinetics, induce structural changes of proteins and aggregates or even alter formation of on- and off-pathway oligomeric species, subsequently changing the pathway of aggregation

Institute of Biotechnology, Life Sciences Center, Vilnius University, Saulėtekio 7, LT-10257 Vilnius, Lithuania. E-mail: vytautas.smirnovas@bti.vu.lt

† Electronic supplementary information (ESI) available. See DOI: 10.1039/c8cp04838j

Therefore we followed insulin aggregation under a range of NaCl concentrations.

State of insulin before and after aggregation

Fourier transform infrared (FTIR) spectra of 5.0 mg ml^{-1} insulin at pD 2.4 (pH-meter readout +0.4),[34,41] in the range from zero to 100 mM NaCl, exhibit maxima in the amide I/I′ band region at 1653 cm^{-1} and corresponding major minima of the second derivative at 1656 cm^{-1} (Fig. 1A), which can be interpreted as a predominantly α-helical structure, typical for native insulin.[18] Almost identical profiles of second derivative spectra in the presence or absence of NaCl suggest that the secondary structure of insulin is not affected by salt in the examined range. The circular dichroism (CD) spectra of insulin with and without salt are also nearly identical (Fig. 1B) and experience no noticeable changes during the lag time of aggregation (Fig. S1, ESI†).

The FTIR spectra of insulin amyloid-like fibrils, prepared at pH 2.4, exhibit maxima in the amide I/I′ band region at 1628 cm^{-1} and two major minima of the second derivative at 1636 cm^{-1} and 1627 cm^{-1} (Fig. 1C) typical for β-sheets. Again, the profiles of second derivative spectra in the presence or absence of NaCl look nearly identical.

Analysis of the insulin aggregate morphology using atomic force microscopy (AFM) revealed straight fibrils of 0.5–3 μm in length and 6–12 nm in diameter, both in the presence or absence of NaCl (Fig. 1D), and no significant differences were observed.

It was recently shown that elevated NaCl and protein (amyloid-β and hen egg-white lysozyme) concentrations may induce formation of metastable oligomers.[19,26] Dynamic light scattering (DLS) revealed that the concentration of salt affects the average size of insulin particles (Fig. 1E and F). The maximum scattering intensity of the insulin sample in the absence of salt is at 3.7 ± 0.1 nm, which is slightly lower than the size of insulin dimers.[42] In the presence of 50 mM NaCl, the maximum scattering intensity is at 3.9 ± 0.3 nm; this value rises with increasing salt concentration up to 4.3 ± 0.1 nm at 100 mM NaCl, suggesting the formation of larger oligomers as the ionic strength of the solution increases. At lower NaCl concentrations (up to 75 mM) no scattering signal of particles above 5 nm was observed, while at 100 mM of salt, the DLS signal suggests the possibility of larger oligomers. However, given the exponential signal-to-size dependence in DLS measurements, the majority of insulin would be distributed within monomers–dimers–tetramers in all the cases. Such an occurrence can be explained by electrostatic interactions. Low pH values in solution result in strong electrostatic repulsive forces between protein molecules, which hinder the assembly of oligomeric forms. The addition of salt mitigates such effects by shielding positively charged insulin molecules with chloride ions and leads to the formation of larger oligomers.[43] According to Nielsen *et al.*,[12] over the pH 2–8 range, zinc-free insulin should be in dimeric form at lower protein concentrations, shifting towards tetramers at protein concentrations above 1.5 mg ml^{-1}, while our data suggest dimers even at 5.0 mg ml^{-1} concentration. It seems that the Nielsen *et al.* assumption is based on SAXS measurements, which were performed in the presence of 100 mM NaCl, and on the data from analytical ultracentrifugation, which was performed at pH 3.7 and 8.0.[12,44] According to our DLS data, both the addition of salt (Fig. 1E) and increased pH[34] may shift the equilibrium towards tetramers.

The particle size distribution is dependent also on the concentration of insulin. In the absence of salt, we observed a minor increase in the insulin hydrodynamic radius as the protein concentration rises. In the presence of salt, however, the change in radius is a lot more apparent, leading to a greater divergence from particle sizes without salt at higher insulin concentrations (Fig. 1F). The data suggest a monomer–dimer equilibrium (with a possible small number of tetramers) throughout the entire range of insulin concentrations in the absence, and at low insulin concentrations (up to 1.5–2 mg ml^{-1}) in the presence, of NaCl. Further increase of the protein concentration in the presence of NaCl shifts the equilibrium towards tetramers.

Kinetics of insulin aggregation

Thioflavin T (ThT) fluorescence assay was employed to follow the kinetics of insulin (concentration range 0.5–5.0 mg ml^{-1}) aggregation at pH 2.4 under five different NaCl concentrations from 0 to 100 mM. Due to the complexity of the aggregation process, determination of suitable models for fitting experimental data is difficult, however, the number of model choices can be narrowed down by applying constraints on possible mechanisms, as described by Meisl *et al.*[6] The curvature of the aggregation half-time (t_{50}) plot *versus* the monomer concentration can help to determine if the aggregation process is monomer dependent and the slope of the logarithmic plot can be used to calculate the reaction order, which makes aggregation half-time plots a good starting point in the selection of the appropriate model.[6]

In the case of our data, a discontinuity in the half-time plot of insulin aggregation in the absence of NaCl was observed (Fig. 2A), which suggests the presence of a saturation effect,[5,6] while the low value of the slope, which becomes ∼0 for insulin concentrations >3.0 mg ml^{-1}, points towards saturated elongation and fragmentation.[5,6]

In the presence of NaCl, an unusual dependence of t_{50} on the initial insulin concentration was observed (Fig. 2B and Fig. S2, ESI†). Following the point of discontinuity, there is a gradual increase of the t_{50} values. This could not be associated with the presence of a saturation effect as the t_{50} starts to grow at different insulin concentrations, depending on the concentration of salt in the sample. The point of discontinuity in t_{50} values shifts from 3.0 mg ml^{-1} at 0 mM NaCl to 1.5 mg ml^{-1} at 100 mM NaCl. The positive slope is observed even at the lowest NaCl concentration. The steepness of the slopes increases from ∼0 to 0.3–0.4 with the increase of salt concentration. The differences in t_{50} values between these samples appear to be the result of competition between the aggregation-enhancing effects of salt (easier insulin interactions due to positive charge shielding) and the formation of off-pathway oligomers, which may affect certain steps of the aggregation.

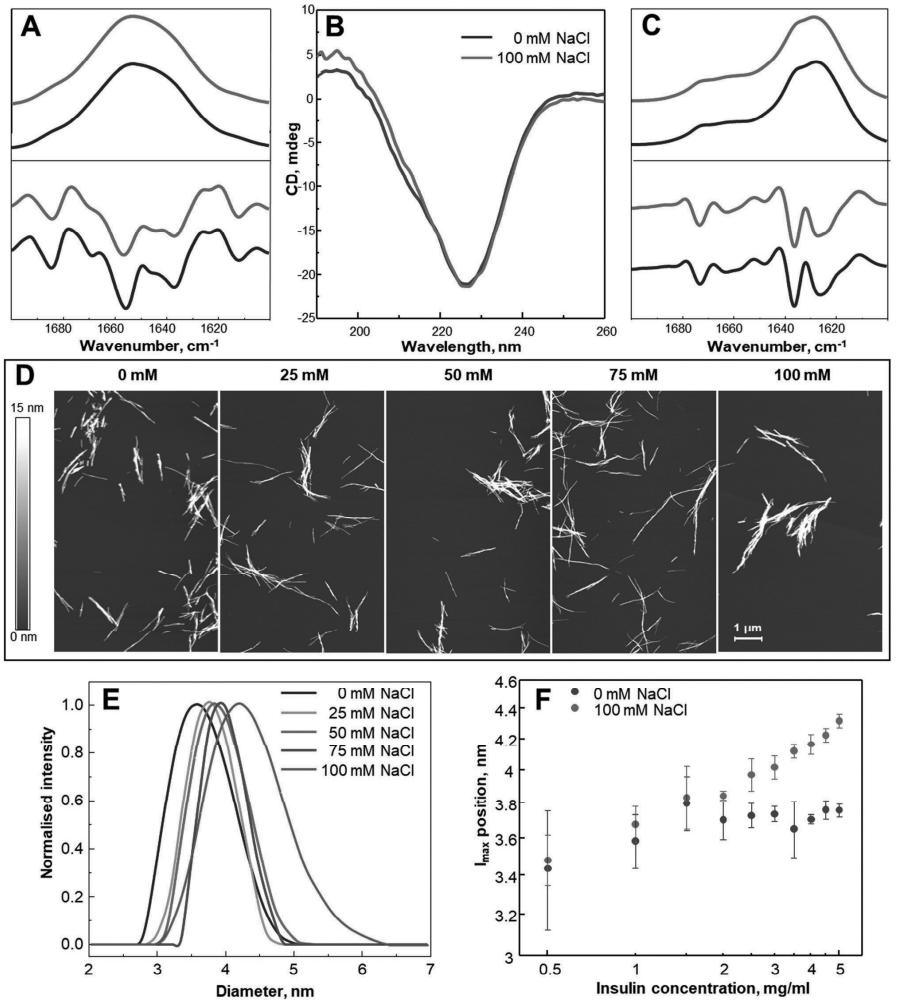

Fig. 1 Characterization of initial and final forms of insulin. FTIR spectra with the second derivative (A) and CD (B) spectra of the initial form of insulin (5 mg ml^{-1}, 60 °C) and FTIR spectra with the second derivative of the aggregated (C) form of insulin. AFM images of insulin amyloid-like aggregates prepared in different NaCl concentration solutions (D). Scattering intensity distribution of insulin (5 mg ml^{-1}) in initial solutions (E) (average of 3 repeats for each sample). Dependence of the maximum scattering intensity position on protein concentration in the presence and absence of 100 mM NaCl (average of 9 repeats for each sample) (F).

Possible models for global fitting

The model containing four major steps of amyloid fibril formation (primary nucleation, fibril elongation, secondary nucleation and fibril fragmentation (Fig. 3)) became the classic model used to describe amyloid aggregation, however, in some cases the modification of existent or introduction of additional microscopic events is necessary for a model to fit experimental data.[5,6,36,45] None of the current modifications of the model

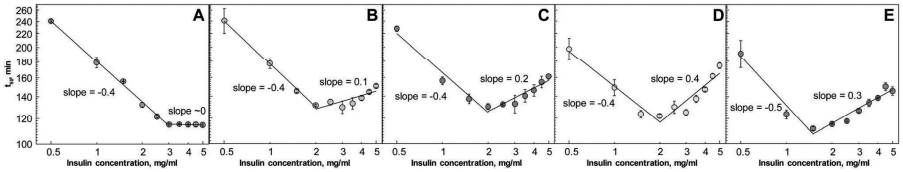

Fig. 2 Dependence of insulin aggregation half-times on concentration under conditions with 0 mM (A), 25 mM (B), 50 mM (C), 75 mM (D) and 100 mM (E) NaCl. Error bars are standard deviations estimated from three repeats.

consider the possible existence of oligomers that might be present in the initial sample (as shown in Fig. 1E and F), but would not directly participate in the aggregation reaction (Fig. 3). The formation of off-pathway oligomers alone would only result in proportional reduction of the initial monomer concentration, which can't explain an increase of t_{50} with increasing concentration of monomers. However, it can be explained by oligomer-induced inhibition, as we see a divergence in the insulin hydrodynamic radius for samples over 1.5 mg ml^{-1} in the presence and absence of 100 mM NaCl (Fig. 1F), which matches with the point where the linear fit slope changes (Fig. 2E). Notably, inhibition of fibril formation by metastable off-pathway assemblies was recently suggested for aggregation of lysozyme and amyloid beta at elevated NaCl concentrations.[26] However, the lysozyme and amyloid beta oligomer formation was detectable by changes in FTIR and CD spectra, as well as increased ThT emissions, none of which are seen in the case of insulin.

According to Arosio *et al.*[36,45] inhibition of primary nucleation would affect the lag phase (but not the growth rate); inhibition of secondary nucleation would mostly affect the growth rate; and inhibition of elongation would affect both the lag phase and the growth rate. According to our experimental data, the lag time follows a similar tendency as t_{50} values. While the higher NaCl concentration leads to increased apparent growth rates at low protein concentrations, at high protein concentrations the effect of salt is opposite (Fig. S2, ESI†). Therefore, we hypothesize that the unusual dependence of t_{50} on the initial insulin concentration in the presence of salt (Fig. 2B–E) may be altered by the formation of off-pathway oligomers (tetramers) that bind to nuclei/fibril ends ("capping" them). This would not only reduce the number of viable monomers, but also actively inhibit fibril elongation.

Global fitting of the experimental data

We used four previously described aggregation models to fit experimental data obtained at five different ionic strength conditions. The only model not sufficient to fit the data obtained in the absence of salt was the "classic" one (Fig. 4A), suggesting a need for either a saturation effect (Fig. 4B) or formation of intermediate species (Fig. 4C and D). Despite a fairly good global fit, more than half of t_{50} values calculated from the fit curves of the saturated elongation model do not overlap with the experimental ones. Both models which account for a loss of viable monomers due to oligomer formation lead to better overlaps of t_{50}. Capping does not add much (and it shouldn't, if insulin is

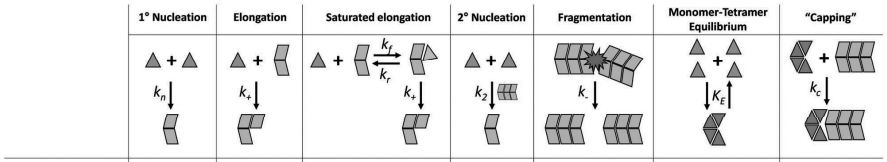

Fig. 3 A schematic representation of microscopic steps involved in fibrillary aggregation for each of the four models. The rate constants are k_n (primary nucleation), k_+ (elongation), k_2 (secondary nucleation), k_- (fragmentation), and k_f and k_r (intermediate association and dissociation) as well as two additional steps, which include K_E (monomer–tetramer equilibrium) and k_c (aggregation center "capping").

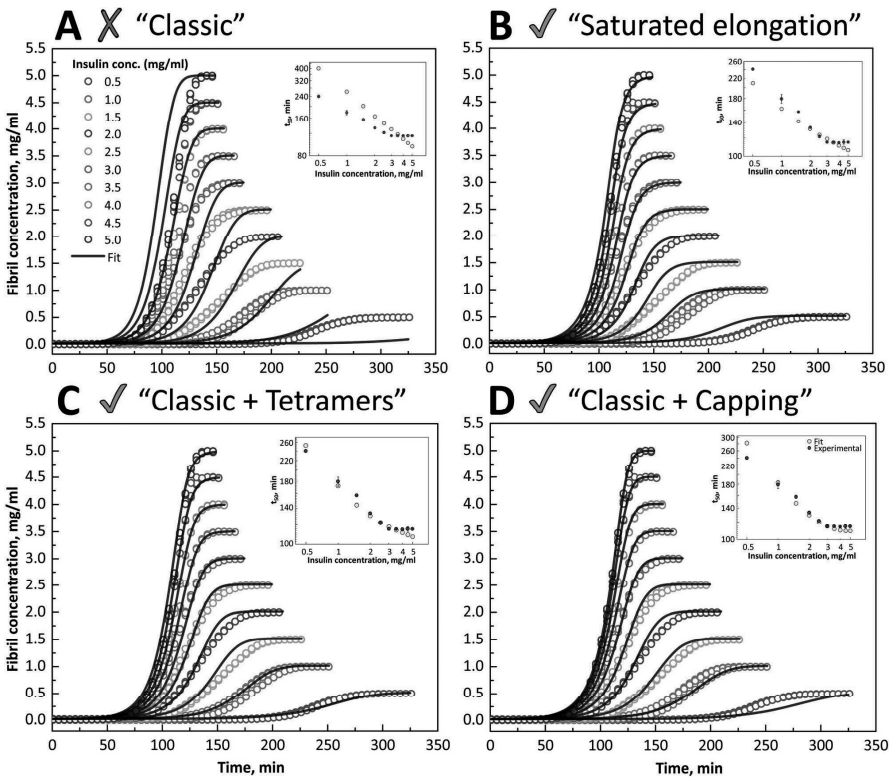

Fig. 4 Global fits of experimental data without salt. The global fit of the "Classic" (A), "Saturated elongation" (B), "Classic + Tetramers" (C) and "Classic + Capping" (D) model to the experimental data with comparison inserts of experimental and fit t_{50} values. In each case the primary and secondary nucleus size was set to 2. Open circles represent normalised experimental data (3 repeats for each protein concentration).

mainly monomeric/dimeric) apart from the better fit at the highest insulin concentrations, which can be explained by the presence of small amounts of tetramers.

In the presence of NaCl, models which do not include an inhibitory step were unable to account for the increase in aggregation half-times as the concentration of insulin increased (Fig. 5A–C and Fig. S3A–C; S4A–C, S5A–C, ESI†). As expected, the only model which includes inhibition was suitable to accurately fit aggregation data (Fig. 5D and Fig. S3D, S4D, S5D, ESI†). According to DLS data, the equilibrium may be shifted towards tetramers at higher insulin concentrations in the presence of 100 mM NaCl, while only a small number of tetramers may be present in the absence of salt. It explains both a good fit of the data in the absence of salt by models involving a monomer–oligomer equilibrium step and only the capping model being able to fit the data in the presence of salt. If it is assumed that the addition of salt does not change the mechanism of insulin aggregation, but rather just affects the rates of microscopic events, then we can conclude that the tetramer-inhibition model is the one explaining the mechanism of insulin aggregation at pH 2.4.

The comparison of rate constants (Table 1) obtained from global fitting of all data sets revealed that all association events are accelerated by salt (it affects not only oligomerization and aggregation, but also leads to more effective inhibition as a result of an increased "capping" rate), which can be easily explained by the salt-induced reduction of electrostatic repulsion between positively charged protein molecules. Oppositely, the fibril breaking rate decreases upon the increase of NaCl concentration, which is not surprising, as higher ionic strength may lead to clustered fibrils,[18] which should be harder to break. Interestingly, the rate of secondary nucleation is affected by salt more than any other event. It is known that insulin can exist in

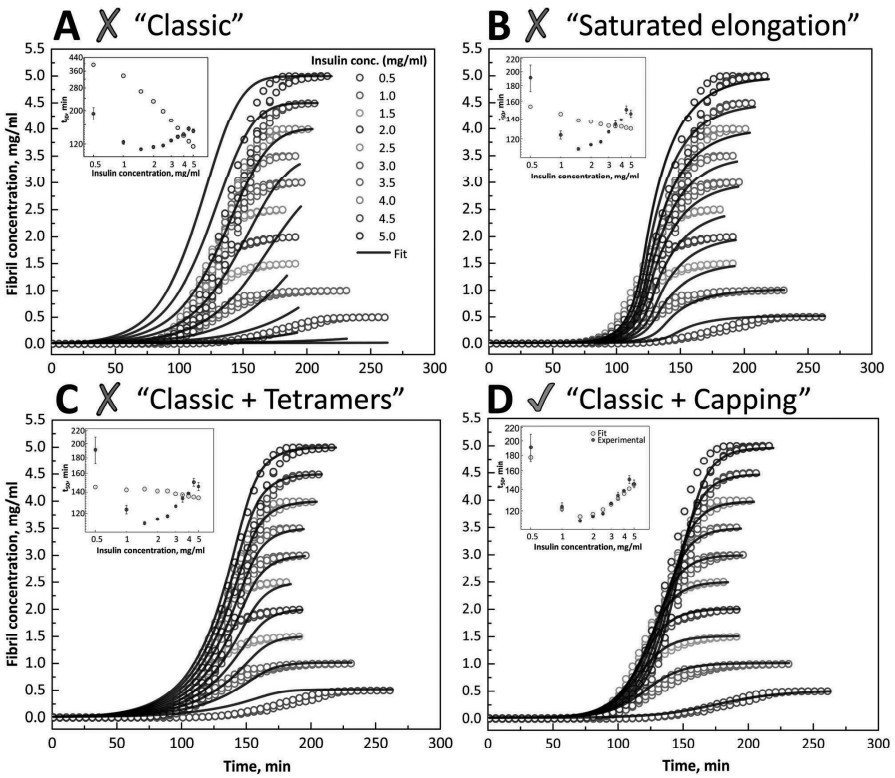

Fig. 5 Global fits of experimental data with 100 mM NaCl. The global fit of the "Classic" (A), "Saturated elongation" (B), "Classic + Tetramers" (C) and "Classic + Capping" (D) model to the experimental data with comparison inserts of experimental and fit t_{50} values. In each case the primary and secondary nucleus size was set to 2. Open circles represent normalised experimental data (3 repeats for each protein concentration).

Table 1 Reaction rate constants at different salt concentrations, where $k_n k_+$ is the multiplicative rate constant of primary nucleation and elongation, $k_+ k_2$ – elongation and secondary nucleation, and $k_+ k_-$ – elongation and fragmentation. K_E is the monomer–tetramer equilibrium constant and k_c is the "capping" rate constant. The standard deviations were estimated by fitting three different subsets of the replicates at each concentration

Conditions	0 mM NaCl	25 mM NaCl	50 mM NaCl	75 mM NaCl	100 mM NaCl
$k_n k_+$	$(8.6 \pm 0.5) \times 10^{-7}$	$(4.1 \pm 0.7) \times 10^{-7}$	$(4.1 \pm 0.8) \times 10^{-7}$	$(4.3 \pm 1.8) \times 10^{-6}$	$(1.4 \pm 0.2) \times 10^{-5}$
$k_+ k_2$	$(1.1 \pm 0.5) \times 10^{-6}$	$(3.1 \pm 0.4) \times 10^{-6}$	$(1.5 \pm 1.4) \times 10^{-4}$	$(4.0 \pm 1.5) \times 10^{-3}$	$(2.2 \pm 0.2) \times 10^{-2}$
$k_+ k_-$	$(2.2 \pm 0.1) \times 10^{-3}$	$(2.8 \pm 0.1) \times 10^{-3}$	$(3.9 \pm 0.3) \times 10^{-3}$	$(9.8 \pm 8.4) \times 10^{-4}$	$(3.6 \pm 1.6) \times 10^{-5}$
K_E	$(7.8 \pm 0.5) \times 10^{-3}$	$(6.8 \pm 0.6) \times 10^{-3}$	$(2.2 \pm 1.2) \times 10^{-2}$	$(2.7 \pm 2.1) \times 10^{-2}$	$(3.2 \pm 0.2) \times 10^{-1}$
k_c	$(5.3 \pm 0.3) \times 10^{-2}$	$(2.1 \pm 0.1) \times 10^{-1}$	$(2.4 \pm 0.5) \times 10^{-1}$	$(1.9 \pm 1.1) \times 10^{-0}$	$(8.7 \pm 0.3) \times 10^{-1}$

monomeric, dimeric, tetrameric, and (in the presence of Zn ions) hexameric forms and it is still not clear what role different oligomers may play in the pathway of amyloid-like fibril formation.[12] Usually these forms are seen just as an off-pathway storage of insulin monomers, which are the main actors in the show.[12,17,18] In fact, often insulin aggregation was studied at pH <2 or in the presence of 20% acetic acid, which favours the monomeric form,[5,12,46] which is probably the main reason why there was no clear evidence of the possible direct role of oligomeric insulin forms in the amyloid formation pathway. Our work supports the role of tetramers and adds one more piece to the global picture of the insulin aggregation mechanism.

Keeping in mind that insulin fibrils formed at pH 2.4 are structurally distinct from the ones formed at pH <2[34] one can suspect that oligomeric forms of insulin play a role in the polymorphism of amyloid-like fibrils.

Conflicts of interest

There are no conflicts to declare.

Acknowledgements

The authors acknowledge Prof. G. Niaura from the Center of Physical Sciences and Technology for the access to FTIR.

Notes and references

1 A. W. P. Fitzpatrick, G. T. Debelouchina, M. J. Bayro, D. K. Clare, M. A. Caporini, V. S. Bajaj, C. P. Jaroniec, L. Wang, V. Ladizhansky, S. A. Muller, C. E. MacPhee, C. A. Waudby, H. R. Mott, A. De Simone, T. P. J. Knowles, H. R. Saibil, M. Vendruscolo, E. V. Orlova, R. G. Griffin and C. M. Dobson, Atomic structure and hierarchical assembly of a cross-amyloid fibril, *Proc. Natl. Acad. Sci. U. S. A.*, 2013, **110**, 5468–5473.

2 D. Eisenberg and M. Jucker, The amyloid state of proteins in human diseases, *Cell*, 2012, **148**, 1188–1203.

3 F. Chiti and C. M. Dobson, Protein misfolding, functional amyloid, and human disease, *Annu. Rev. Biochem.*, 2006, **75**, 333–366.

4 T. P. J. Knowles, M. Vendruscolo and C. M. Dobson, The amyloid state and its association with protein misfolding diseases, *Nat. Rev. Mol. Cell Biol.*, 2014, **15**, 384–396.

5 G. Meisl, L. Rajah, S. A. I. Cohen, M. Pfammatter, A. Šarić, E. Hellstrand, A. K. Buell, A. Aguzzi, S. Linse, M. Vendruscolo, C. M. Dobson and T. P. J. Knowles, Scaling behaviour and rate-determining steps in filamentous self-assembly, *Chem. Sci.*, 2017, **8**, 7087–7097.

6 G. Meisl, J. B. Kirkegaard, P. Arosio, T. C. T. Michaels, M. Vendruscolo, C. M. Dobson, S. Linse and T. P. J. Knowles, Molecular mechanisms of protein aggregation from global fitting of kinetic models, *Nat. Protoc.*, 2016, **11**, 252–272.

7 J. L. Whittingham, D. J. Scott, K. Chance, A. Wilson, J. Finch, J. Brange and G. Guy Dodson, Insulin at pH 2: structural analysis of the conditions promoting insulin fibre formation, *J. Mol. Biol.*, 2002, **318**, 479–490.

8 A. Noormägi, K. Valmsen, V. Tõugu and P. Palumaa, Insulin Fibrillization at Acidic and Physiological pH Values is Controlled by Different Molecular Mechanisms, *Protein J.*, 2015, **34**, 398–403.

9 S. Kobayashi, Y. Tanaka, M. Kiyono, M. Chino, T. Chikuma, K. Hoshi and H. Ikeshima, Dependence pH and proposed mechanism for aggregation of Alzheimer's disease-related amyloid-beta(1–42) protein, *J. Mol. Struct.*, 2015, **1094**, 109–117.

10 W. Hoyer, T. Antony, D. Cherny, G. Heim, T. M. Jovin and V. Subramaniam, Dependence of α-synuclein aggregate morphology on solution conditions, *J. Mol. Biol.*, 2002, **322**, 383–393.

11 Y. Su and P. T. Chang, Acidic pH promotes the formation of toxic fibrils from beta-amyloid peptide, *Brain Res.*, 2001, **893**, 287–291.

12 L. Nielsen, R. Khurana, A. Coats, S. Frokjaer, J. Brange, S. Vyas, V. N. Uversky and A. L. Fink, Effect of environmental factors on the kinetics of insulin fibril formation: elucidation of the molecular mechanism, *Biochemistry*, 2001, **40**, 6036–6046.

13 A. Noormägi, J. Gavrilova, J. Smirnova, V. Tõugu and P. Palumaa, Zn(II) ions co-secreted with insulin suppress inherent amyloidogenic properties of monomeric insulin, *Biochem. J.*, 2010, **430**, 511–518.

14 A. Tiiman, J. Krishtal, P. Palumaa and V. Tõugu, *In vitro* fibrillization of Alzheimer's amyloid-β peptide (1–42), *AIP Adv.*, 2015, **5**, 092401.

15 K. M. Batzli and B. J. Love, Agitation of amyloid proteins to speed aggregation measured by ThT fluorescence: a call for standardization, *Mater. Sci. Eng., C*, 2015, **48**, 359–364.

16 S. I. a Cohen, S. Linse, L. M. Luheshi, E. Hellstrand, D. a White, L. Rajah, D. E. Otzen, M. Vendruscolo, C. M. Dobson and T. P. J. Knowles, Proliferation of amyloid-β42 aggregates occurs through a secondary nucleation mechanism, *Proc. Natl. Acad. Sci. U. S. A.*, 2013, **110**, 9758–9763.

17 S. Grudzielanek, V. Smirnovas and R. Winter, Solvation-assisted pressure tuning of insulin fibrillation: from novel aggregation pathways to biotechnological applications, *J. Mol. Biol.*, 2006, **356**, 497–509.

18 V. Smirnovas and R. Winter, Revealing Different Aggregation Pathways of Amyloidogenic Proteins by Ultrasound Velocimetry, *Biophys. J.*, 2008, **94**, 3241–3246.

19 T. Miti, M. Mulaj, J. D. Schmit and M. Muschol, Stable, metastable, and kinetically trapped amyloid aggregate phases, *Biomacromolecules*, 2015, **16**, 326–335.

20 F. Librizzi and C. Rischel, The kinetic behavior of insulin fibrillation is determined by heterogeneous nucleation pathways, *Protein Sci.*, 2005, **14**, 3129–3134.

21 V. Foderà, F. Librizzi, M. Groenning, M. van de Weert and M. Leone, Secondary nucleation and accessible surface in insulin amyloid fibril formation, *J. Phys. Chem. B*, 2008, **112**, 3853–3858.

22 V. Foderà, S. Cataldo, F. Librizzi, B. Pignataro, P. Spiccia and M. Leone, Self-organization pathways and spatial heterogeneity in insulin amyloid fibril formation, *J. Phys. Chem. B*, 2009, **113**, 10830–10837.

23 A. Nayak, M. Sorci, S. Krueger and G. Belfort, A universal pathway for amyloid nucleus and precursor formation for insulin, *Proteins: Struct., Funct., Bioinf.*, 2009, **74**, 556–565.

24 S. Saha and S. Deep, Glycerol inhibits the primary pathways and transforms the secondary pathway of insulin aggregation, *Phys. Chem. Chem. Phys.*, 2016, **18**, 18934–18948.

25 E. Hellstrand, B. Boland, D. M. Walsh and S. Linse, Amyloid β-protein aggregation produces highly reproducible kinetic

data and occurs by a two-phase process, *ACS Chem. Neurosci.*, 2010, **1**, 13–18.
26 F. Hasecke, T. Miti, C. Perez, J. Barton, D. Schölzel, L. Gremer, C. S. R. Grüning, G. Matthews, G. Meisl, T. P. J. Knowles, D. Willbold, P. Neudecker, H. Heise, G. Ullah, W. Hoyer and M. Muschol, Origin of metastable oligomers and their effects on amyloid fibril self-assembly, *Chem. Sci.*, 2018, **9**, 5937–5948.
27 W. Dzwolak, S. Grudzielanek, V. Smirnovas, R. Ravindra, C. Nicolini, R. Jansen, A. Loksztejn, S. Porowski and R. Winter, Ethanol-perturbed amyloidogenic self-assembly of insulin: looking for origins of amyloid strains, *Biochemistry*, 2005, **44**, 8948–8958.
28 W. Dzwolak, V. Smirnovas, R. Jansen and R. Winter, Insulin forms amyloid in a strain-dependent manner: an FT-IR spectroscopic study, *Protein Sci.*, 2004, **13**, 1927–1932.
29 E. Chatani, R. Inoue, H. Imamura, M. Sugiyama, M. Kato, M. Yamamoto, K. Nishida and T. Kanaya, Early aggregation preceding the nucleation of insulin amyloid fibrils as monitored by small angle X-ray scattering, *Sci. Rep.*, 2015, **5**, 15485.
30 S. Saha, A. Sharma and S. Deep, Differential influence of additives on the various stages of insulin aggregation, *RSC Adv.*, 2016, **6**, 28640–28652.
31 V. Foderà, M. van de Weert and B. Vestergaard, Large-scale polymorphism and auto-catalytic effect in insulin fibrillogenesis, *Soft Matter*, 2010, **6**, 4413.
32 W. Surmacz-Chwedoruk, V. Babenko and W. Dzwolak, Master and slave relationship between two types of self-propagating insulin amyloid fibrils, *J. Phys. Chem. B*, 2014, **118**, 13582–13589.
33 W. Dzwolak, R. Jansen, V. Smirnovas, A. Loksztejn, S. Porowski and R. Winter, Template-controlled conformational patterns of insulin fibrillar self-assembly reflect history of solvation of the amyloid nuclei, *Phys. Chem. Chem. Phys.*, 2005, **7**, 1349–1351.
34 T. Sneideris, D. Darguzis, A. Botyriute, M. Grigaliunas, R. Winter and V. Smirnovas, pH-driven polymorphism of insulin amyloid-like fibrils, *PLoS One*, 2015, **10**, e0136602.
35 W. Surmacz-Chwedoruk, H. Nieznańska, S. Wójcik and W. Dzwolak, Cross-seeding of fibrils from two types of insulin induces new amyloid strains, *Biochemistry*, 2012, **51**, 9460–9469.
36 P. Arosio, M. Vendruscolo, C. M. Dobson and T. P. J. Knowles, Chemical kinetics for drug discovery to combat protein aggregation diseases, *Trends Pharmacol. Sci.*, 2014, **35**, 127–135.
37 P. Arosio, R. Cukalevski, B. Frohm, T. P. J. Knowles and S. Linse, Quantification of the concentration of Aβ42 propagons during the lag phase by an amyloid chain reaction assay, *J. Am. Chem. Soc.*, 2014, **136**, 219–225.
38 T. P. J. Knowles, C. A. Waudby, G. L. Devlin, S. I. A. Cohen, A. Aguzzi, M. Vendruscolo, E. M. Terentjev, M. E. Welland and C. M. Dobson, An analytical solution to the kinetics of breakable filament assembly, *Science*, 2009, **326**, 1533–1537.
39 S. I. A. Cohen, M. Vendruscolo, C. M. Dobson and T. P. J. Knowles, From macroscopic measurements to microscopic mechanisms of protein aggregation, *J. Mol. Biol.*, 2012, **421**, 160–171.
40 G. Meisl, X. Yang, E. Hellstrand, B. Frohm, J. B. Kirkegaard, S. I. A. Cohen, C. M. Dobson, S. Linse and T. P. J. Knowles, Differences in nucleation behavior underlie the contrasting aggregation kinetics of the Aβ40 and Aβ42 peptides, *Proc. Natl. Acad. Sci. U. S. A.*, 2014, **111**, 9384–9389.
41 G. I. Makhatadze, G. M. Clore and A. M. Gronenborn, Solvent isotope effect and protein stability, *Nat. Struct. Biol.*, 1995, **2**, 852–855.
42 A. Banga, *Therapeutic Peptides and Proteins*, CRC Press, 2nd edn, 2005.
43 V. Babenko, W. Surmacz-Chwedoruk and W. Dzwolak, On the function and fate of chloride ions in amyloidogenic self-assembly of insulin in an acidic environment: salt-induced condensation of fibrils, *Langmuir*, 2015, **31**, 2180–2186.
44 C. Bryant, D. B. Spencer, A. Miller, D. L. Bakaysa, K. S. McCune, S. R. Maple, A. H. Pekar and D. N. Brems, Acid stabilization of insulin, *Biochemistry*, 1993, **32**, 8075–8082.
45 P. Arosio, T. C. T. Michaels, S. Linse, C. Månsson, C. Emanuelsson, J. Presto, J. Johansson, M. Vendruscolo, C. M. Dobson and T. P. J. Knowles, Kinetic analysis reveals the diversity of microscopic mechanisms through which molecular chaperones suppress amyloid formation, *Nat. Commun.*, 2016, **7**, 10948.
46 O. M. Selivanova, M. Y. Suvorina, N. V. Dovidchenko, I. A. Eliseeva, A. K. Surin, A. V. Finkelstein, V. V. Schmatchenko and O. V. Galzitskaya, How to determine the size of folding nuclei of protofibrils from the concentration dependence of the rate and lag-time of aggregation. II. Experimental application for insulin and LysPro insulin: aggregation morphology, kinetics, and sizes of nuclei, *J. Phys. Chem. B*, 2014, **118**, 1198–1206.

biomolecules

MDPI

Article

The Environment Is a Key Factor in Determining the Anti-Amyloid Efficacy of EGCG

Tomas Sneideris [1,†], Andrius Sakalauskas [1,†], Rebecca Sternke-Hoffmann [2,†], Alessia Peduzzo [2], Mantas Ziaunys [1], Alexander K. Buell [2,3,*] and Vytautas Smirnovas [1,*]

1 Institute of Biothechnology, Life Sciences Center, Vilnius University, LT-10257 Vilnius, Lithuania; sneideris.t@gmail.com (T.S.); sakalauskas.and@gmail.com (A.S.); mantas.ziaunys@gmail.com (M.Z.)

2 Institute of Physical Biology, Heinrich-Heine-University, 40225 Düsseldorf, Germany; Rebecca.Sternke-Hoffmann@uni-duesseldorf.de (R.S.-H.); alessia.peduzzo@uni-duesseldorf.de (A.P.)

3 Department of Biotechnology and Biomedicine, Technical University of Denmark, DK-2800 Kgs Lyngby, Denmark

* Correspondence: alebu@dtu.dk (A.K.B.); vytautas.smirnovas@bti.vu.lt (V.S.)

† These authors contributed equally to this work.

Received: 16 October 2019; Accepted: 6 December 2019; Published: 11 December 2019

Abstract: Millions of people around the world suffer from amyloid-related disorders, including Alzheimer's and Parkinson's diseases. Despite significant and sustained efforts, there are still no disease-modifying drugs available for the majority of amyloid-related disorders, and the overall failure rate in clinical trials is very high, even for compounds that show promising anti-amyloid activity in vitro. In this study, we demonstrate that even small changes in the chemical environment can strongly modulate the inhibitory effects of anti-amyloid compounds. Using one of the best-established amyloid inhibitory compounds, epigallocatechin-3-gallate (EGCG), as an example, and two amyloid-forming proteins, insulin and Parkinson's disease-related α-synuclein, we shed light on the previously unexplored sensitivity to solution conditions of the action of this compound on amyloid fibril formation. In the case of insulin, we show that the classification of EGCG as an amyloid inhibitor depends on the experimental conditions select, on the method used for the evaluation of the efficacy, and on whether or not EGCG is allowed to oxidise before the experiment. For α-synuclein, we show that a small change in pH value, from 7 to 6, transforms EGCG from an efficient inhibitor to completely ineffective, and we were able to explain this behaviour by the increased stability of EGCG against oxidation at pH 6.

Keywords: insulin; α-synuclein; inhibition; EGCG; amyloid aggregation

1. Introduction

The onset and progression of more than 50 human disorders, including the neurodegenerative Alzheimer's and Parkinson's diseases (AD and PD), is associated with the failure of peptides and proteins to adopt or remain in their native functional and soluble states, and their subsequent conversion into amyloid fibrils [1,2]. Millions of people around the world suffer from these disorders; AD alone affects 40 million patients worldwide and is projected to rise steadily to afflict 135 million people by 2050 [3,4]. Distinct peptides and proteins are associated with these particular human disorders; however, the formation and accumulation of insoluble fibrillar aggregates are common among these diseases [1,2]. Whether extracted from patients or generated in vitro, amyloid fibrils formed from different proteins seem to be remarkably similar in overall morphology. Mature amyloid fibrils tend to appear as unbranched, thread-like, elongated structures, several nanometres in diameter and with lengths of the order of micrometres [1,2]. In addition, the corresponding fibrils all contain a β-sheet-rich structure, termed "cross-β," according to the pattern in X-ray fibre diffraction studies [5].

Several therapeutic approaches, such as a reduction in the production of amyloidogenic peptides, the increase of the native state stability of amyloidogenic proteins, an enhancement in the clearance rates of misfolded proteins, and a direct inhibition of the self-assembly process, have been suggested for treatment of amyloid-related disorders [6–12]. Numerous small molecular weight compounds, short peptides, and antibodies have been suggested as potential modulators and inhibitors of toxic oligomeric and fibrillar species' assemblies [6,8,9,12–15]. Despite significant and persistent efforts, there are still no effective disease-modifying drugs or treatment modalities available for the majority of amyloid-related disorders (overall success rate of clinical trials is <0.5%) [16–21].

The formation of amyloid fibrils is a complex process, which involves several microscopic steps (e.g., nucleation, growth, fragmentation, and secondary nucleation) [1,2]. Alterations in environmental conditions can modulate these microscopic steps, resulting in different pathways and leading to the formation of structurally distinct amyloid aggregates [1,22–25]. Such conformational variability, also known as polymorphism, is thought to be a generic property of amyloid proteins, and has been proposed to be able to cause distinct disease phenotypes [1,26,27]. Moreover, the effects of potential therapeutic agents can vary depending on the conditions in which they are assayed (i.e., pH, temperature, buffer, interfaces, agitation, and others) [12], possibly due to chemical modifications of potential therapeutic molecules [28–30]. Since the environmental conditions under which aggregation of amyloid proteins is performed can vary between distinct studies, the search and assessment of potential inhibitors becomes extremely challenging, as the results may lead to diverse conclusions.

An ideal amyloid assembly inhibitor should act as broadly as possible and be capable of interacting with different species along the pathway of aggregation. The desired outcome of such an interaction is to block the formation of toxic oligomeric species and to possibly dissociate preformed fibrillar aggregates into non-toxic species [31]. Epigallocatechin-3-gallate (EGCG), the main polyphenol found in green tea, has been reported to effectively inhibit the aggregation of a number of amyloidogenic peptides and proteins, including amyloid-β (related to AD) [32,33], α-synuclein (related to PD) [33–36], islet amyloid polypeptide (related to type-II diabetes) [37,38], huntingtin exon 1 (related to Huntington's disease) [39], tau (related to AD and tauopathies) [40], superoxide dismutase (related to amyotrophic lateral sclerosis) [41], prion proteins (related to prion diseases) [42], and others. In addition, it has been shown that EGCG can induce remodeling and/or dissociation of pre-existing aggregate species [33,34,36,43,44]. Taken together, EGCG appears to be a "universal" inhibitor of amyloid fibril formation, suggesting that this molecule could be used as a therapeutic agent for the prevention and treatment of amyloid-related disorders. However, EGCG is not stable at neutral or alkaline pH [45–48], where it is susceptible to auto-oxidation, resulting in the formation of numerous products [28] which may differently affect amyloid aggregation [29,30,49].

In this study, we set out to explore whether or not the universal nature of EGCG as an inhibitor is robust against variation in solution conditions. We chose two amyloid forming protein systems, a model system (insulin) and a disease-related protein (α-synuclein), which form amyloid fibrils under very different solution conditions. This choice allowed us to separately probe the influence of EGCG oxidation and the interplay between the solution conditions and the action of EGCG.

The formation of insulin amyloid fibrils in vivo is associated with the clinical syndrome injection-localised amyloidosis, which was observed in diabetes patients after continuous subcutaneous injections of insulin [50,51]. Despite its main application in medicine, recombinant human insulin is also extensively used as a model protein to study pathways and mechanisms of amyloid fibril formation in vitro. It has been demonstrated that several sets of conditions, including the presence of ethanol [52–54]; different pHs [22,55] or salt concentrations [23,55]; and agitation [55,56], can alter insulin aggregation pathways and even lead to the formation of structurally different amyloid fibrils. The majority of insulin aggregation studies were performed at low pHs, which do not reflect the physiological environment, but serve to significantly accelerate amyloid fibril formation through a destabilisation of the native state. At the same time, acidic conditions are known to lead to higher EGCG stability against oxidation. We demonstrate the different effects of EGCG and its auto-oxidation

products ($EGCG_{ox}$) on insulin aggregation. Furthermore, we show that even under the acidic reaction conditions where EGCG is stable, the exact solvent conditions determine whether or not EGCG is able to modulate the kinetics of insulin amyloid fibril formation.

The strong pH-dependence of EGCG's stability against oxidation in the proximity of neutral pH enabled us to probe the interplay of protein aggregation and EGCG oxidation, using the protein α-synuclein, associated with Parkinson's disease [57]. By comparing α-synuclein amyloid fibril formation at pH 7, where EGCG rapidly oxidises, and pH 6, where it is much more stable, we found that EGCG converts from an efficient inhibitor at pH 7 to being completely ineffective at pH 6. On the other hand, pre-oxidised EGCG is a very powerful inhibitor at pH 6 as well. Taken together, in this study we demonstrate that even an inhibitor candidate as well-characterised as EGCG can display a dramatically different inhibitory efficiency depending on the solution conditions, and hence a systematic exploration of the interplay of solution conditions and compound stability and efficacy is crucial.

2. Results

We first performed insulin amyloid fibril formation experiments under different acidic solution conditions. When the insulin aggregation reaction was performed in 100 mM phosphate buffer, pH 2.4 (PB), under quiescent conditions, the presence of EGCG increased the half-time (t_{50}), i.e., the time to reach half the maximal Thioflavin-T (ThT) fluorescence intensity, by almost two-fold, while at the same time decreasing the maximum fluorescence intensity (I_{max}) nearly two-fold, when compared to the control (Figures 1 and S1). The effect of $EGCG_{ox}$ (see Methods section for experimental protocol to generate oxidised EGCG) is stronger, and leads to an almost four times longer t_{50} and almost four times lower I_{max}. In the Supplementary Material, we show time-resolved UV–Vis data of EGCG that demonstrates the lack of oxidation under the conditions of these kinetic experiments (Figure S2). Under agitated conditions in PB, EGCG has no inhibitory effect, while $EGCG_{ox}$ has a minor effect on the insulin aggregation process (Figures 1 and S1).

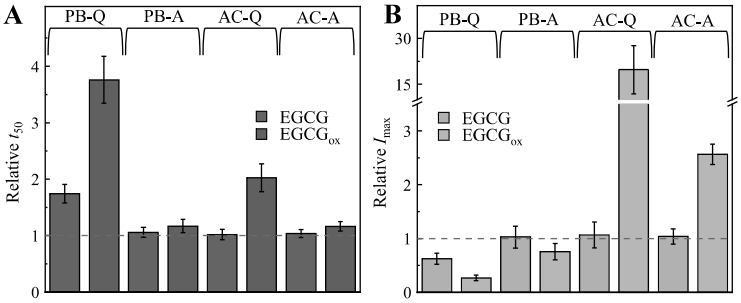

Figure 1. Effects of EGCG and $EGCG_{ox}$ on insulin aggregation kinetics (**A**) and maximum ThT fluorescence intensity (**B**). Abbreviations PB and AC represent environmental conditions (100 mM phosphate buffer and 20% acetic acid, respectively), while Q and A denote the agitation conditions (quiescent and agitated, respectively), under which the insulin aggregation reactions were performed. Error bars represent standard deviations.

The presence of $EGCG_{ox}$ results in a two times longer t_{50} and 20 times higher I_{max} effect, when the aggregation reaction is performed in 20% acetic acid (AC), under quiescent conditions (Figure 1). When agitation is applied, the presence of $EGCG_{ox}$ results in a three times higher I_{max} and has a minor effect on t_{50} (Figures 1 and S1). The presence of non-oxidised EGCG has no effect on t_{50} or I_{max}, when the aggregation reaction is performed under either quiescent or agitated conditions (Figures 1 and S1) in AC. Taken together, these results suggest that under these sets of solution conditions, EGCG has only a weak effect on insulin amyloid fibril formation, which is reinforced by oxidation of EGCG.

Furthermore, the results also suggest that the absolute fluorescence intensity of ThT bound to insulin amyloid fibrils is strongly influenced by the presence of $EGCG_{ox}$.

Sample analysis using atomic force microscopy (AFM) confirmed the formation of insulin amyloid fibrils within 15 h under all test conditions (Figure 2, Figures S3–S6). Typically, individual fibrils are 3–10 nm in height and their lengths range from several hundred nm to several µm. In PB, insulin amyloid fibrils tend to cluster, and larger bundles were apparent when the reaction was performed under agitated conditions. In the presence of $EGCG_{ox}$, the fibrils seem to be more dispersed (Figure 2, Figures S3 and S4). In AC more fibrils can be seen in the presence of $EGCG_{ox}$, when compared to the control sample (Figure 2, Figures S5 and S6), even though care must be taken when quantitatively comparing AFM images and correlating these results with the composition of the solution. Fibrils formed in the presence of EGCG under all environmental conditions are similar in morphology to their respective control samples; i.e., the absence of EGCG or $EGCG_{ox}$.

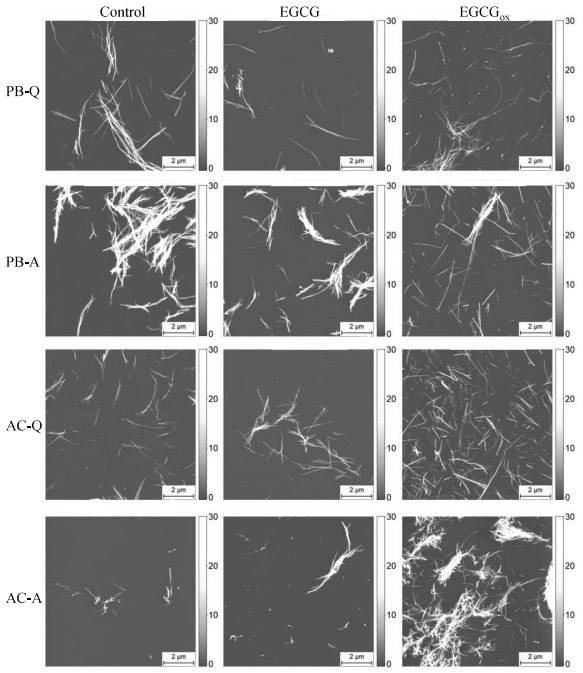

Figure 2. AFM images of insulin amyloid fibrils formed in PB or AC in the absence and presence of EGCG or $EGCG_{ox}$. Abbreviations Q and A denote agitation conditions (quiescent and agitated, respectively), under which the insulin aggregation reactions were performed. The height scale (*z*) is in nm.

The secondary structure of insulin amyloid fibrils was assessed using Fourier-transform infrared (FTIR) spectroscopy (Figure 3). Second derivative FTIR spectra of fibrils formed in AC under quiescent and agitated conditions are almost identical, both showing a major minimum at 1627 cm^{-1} and a minor one at 1641 cm^{-1} in the amide I/I′ region, attributed to β-sheet structure and an additional band at 1729 cm^{-1} (Figure 3), which was assigned to the stretching vibrations of a deuterated carboxyl group (-COOD) [58]. Similarly, a major minimum at 1627 cm^{-1} in the amide I/I′ region, is present in case of PB under agitated conditions; however, the other two minima observed in AC are missing. The second

derivative FTIR spectrum of insulin amyloid fibrils formed in PB under quiescent conditions has two minima at 1625 cm^{-1} and 1637 cm^{-1} in the Amide I/I′ region. It confirms that fibrils formed without agitation in PB are structurally different from fibrils formed in AC, while the fibrils formed in PB with agitation seem to have a secondary structure profile, which looks like an intermediate between PB and AC. These results suggest that despite the very similar morphology, as judged from AFM images, the insulin amyloid fibrils formed under different solvent conditions have some structural differences.

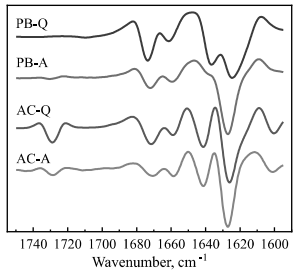

Figure 3. Second derivative FTIR spectra of insulin amyloid-like aggregates formed in PB and AC under quiescent and agitated conditions. Abbreviations PB and AC represent environmental conditions (100 mM phosphate buffer and 20% acetic acid, respectively), while Q and A denote agitation conditions (quiescent and agitated, respectively), under which the insulin aggregation reaction was performed.

The insulin aggregation experiments under acidic conditions described above allow one to isolate the oxidation of EGCG from the protein aggregation. However, in many cases, amyloid fibril formation is studied under conditions under which EGCG is highly unstable. We therefore performed additional amyloid fibril formation experiments with α-synuclein, the aggregation of which is associated with Parkinson's disease [57]. α-synuclein forms amyloid fibrils at both neutral and mildly acidic pH [25], which provides an ideal paradigm to study the inhibition by EGCG, because the latter compound displays a dramatic change in stability between neutral and slightly acidic pH (Figure S2). We incubated monomeric α-synuclein in polystyrene plates under shaking, and in the presence of glass beads. Under these conditions, the surface-catalysed nucleation [59] and subsequent amplification through fragmentation [25] of α-synuclein amyloid fibrils is very efficient. We compared the time course of ThT fluorescence at pH 7, where it has been shown that EGCG is an efficient inhibitor of α-synuclein amyloid fibril formation [33], and at the slightly more acidic pH of 6 (Figure 4A,B). We found that, based on ThT intensity alone, at pH 7, EGCG completely inhibits the formation of α-synuclein amyloid fibrils at a stoichiometric ratio of 1:1, whereas at pH 6, the maximal ThT intensity is merely reduced by a factor of two, while the half time is very similar compared to the absence of EGCG.

AFM images (Figure 5) show amyloid fibrils at pH 7 without EGCG and at pH 6 both in the presence and absence of EGCG. At pH 7 in the presence of EGCG, AFM imaging reveals some amorphous aggregates together with very short fibrillar structures, and in the presence of $EGCG_{ox}$, almost no fibrils are found. The situation is dramatically different at pH 6, where fibrils can clearly be seen under all conditions, albeit very few in the presence of $EGCG_{ox}$, where ThT fluorescence is completely suppressed. In order to obtain an independent measure for the degree of inhibition of aggregation by EGCG and $EGCG_{ox}$, we centrifuged the samples after the aggregation experiment and quantified the average size and concentration (Figure 4C) of the soluble protein by microfluidic diffusional sizing (MDS) [60,61] (see Methods section for details). We found that in the absence of EGCG, both at pH 7 and pH 6, the protein converts near-quantitatively into aggregates, whereas in the presence of EGCG and $EGCG_{ox}$, nearly all of the protein remains soluble, and display average hydrodynamic radii of ∼2.3 nm at pH 6 and ∼2.7 nm at pH 7, indistinguishable from measurements of

pure monomeric protein and in close agreement with previous measurements under similar solution conditions [62]. Interestingly, at pH 6, MDS reveals that EGCG has no effect on the conversion efficiency into aggregates, and even in the presence of $EGCG_{ox}$, inhibition is only partial, despite the fact that ThT fluorescence is completely quenched. We also accompanied these experiments by UV–Vis spectroscopic stability studies of EGCG under the same solution conditions, and we found that while the EGCG absorption spectrum undergoes substantial changes at pH 7 already after 1 h, almost no change is observed at pH 6 after almost 1 day of incubation (Figure S2).

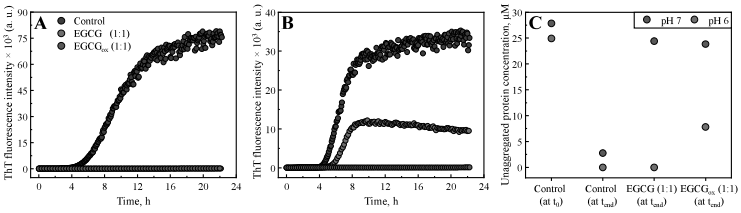

Figure 4. The effects of EGCG and $EGCG_{ox}$ on the aggregation kinetics of α-synuclein monitored at pH 7 (**A**) and pH 6 (**B**). (**C**) α-synuclein concentration measured in the supernatant after centrifuging the end product of the aggregation reactions at pH 7 and pH 6, respectively.

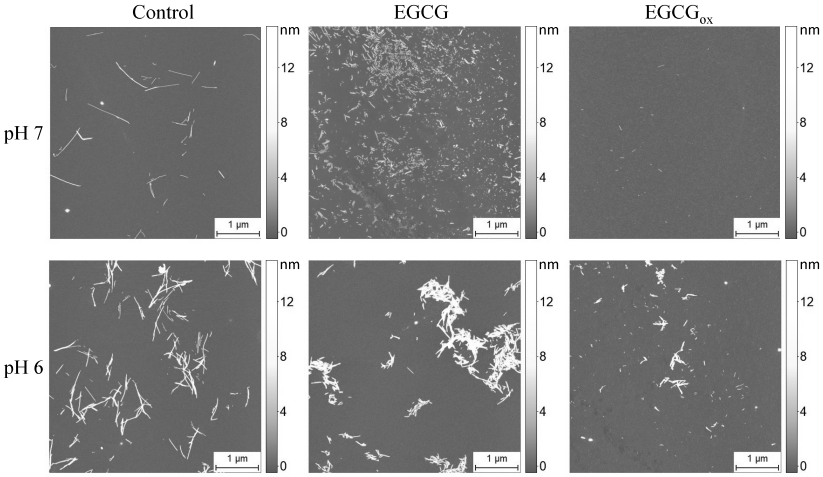

Figure 5. AFM images of α-synuclein aggregates formed at pH 7 or pH 6 in the absence and presence of EGCG or $EGCG_{ox}$.

3. Discussion and Conclusions

The effects of potential inhibitor compounds on the process of amyloid fibril formation are often determined by analysing the kinetics of aggregation [15,29,30,32,33,63–68] and/or the maximum ThT intensity [29,30,32,33,65,67–71] in the absence and presence of the compound. The effects of EGCG and $EGCG_{ox}$ on the process of amyloid fibril formation by both insulin and α-synuclein performed under distinct environmental conditions were assessed using both aforementioned approaches (Figures 1 and S7), and the conclusions are presented in (Table 1). In the case of insulin, if t_{50} and/or I_{max} were used as the main criteria, EGCG could be defined as an inhibitor of amyloid formation

only if the screening was performed in PB under quiescent conditions. In case of $EGCG_{ox}$ the picture is more complex. In PB, $EGCG_{ox}$ was found to be an inhibitor independently of the assessment criteria, whereas in AC, t_{50} points towards an inhibitory effect, while I_{max} suggests an enhancement of aggregation. In the case of α-synuclein amyloid fibril formation, on the other hand, both criteria suggest EGCG to be a strong inhibitor at pH 7, whereas only I_{max} indicates inhibition at pH 6. In the latter case, only the inclusion of the soluble protein at the end of the reaction as an additional measured parameter allows to correctly evaluate the inhibitory effect. These results suggest that depending on aggregation conditions and the screening criteria, the same compound could be defined as a hit or a failure. This raises the question as to the origin of such variable results.

Table 1. Evaluation of EGCG and $EGCG_{ox}$'s effects on the insulin aggregation process.

Assessed by Change in t_{50}			
Protein	**Conditions**	**EGCG**	**$EGCG_{ox}$**
Insulin	PB-Q	Inhibitory [1]	Inhibitory
	PB-A	No Effect	Inhibitory
	AC-Q	No Effect	Inhibitory
	AC-A	No Effect	Inhibitory
α-synuclein	pH 7	Inhibitory	Inhibitory
	pH 6	No Effect	Inhibitory
Assessed by Change in I_{max}			
Protein	**Conditions**	**EGCG**	**$EGCG_{ox}$**
Insulin	PB-Q	Inhibitory	Inhibitory
	PB-A	No Effect	Inhibitory
	AC-Q	No Effect	Enhancing
	AC-A	No Effect	Enhancing
α-synuclein	pH 7	Inhibitory	Inhibitory
	pH 6	Inhibitory	Inhibitory

[1] Established by comparing experimental values of t_{50} or I_{max} of control samples with the ones determined in the presence of EGCG or $EGCG_{ox}$ using one-way ANOVA (See Figure S7). $p < 0.01$ was accepted as statistically significant.

First, alterations in environmental conditions can modulate protein aggregation pathways and result in the formation of structurally distinct amyloid aggregates (Figure 6A) [22–24,26,27]. Thus, it is plausible that species targeted by the compound might exist only under certain environmental conditions. Indeed, EGCG inhibits the insulin aggregation reaction only when the latter is performed in PB under quiescent conditions. AFM analysis did not reveal any major differences between fibrils formed in the absence or presence of EGCG (Figure 2). However, differences in the secondary structure of fibrils, determined using FTIR (Figure 3), suggest the possibility of distinct pathways and intermediates involved in the process of insulin fibril formation in PB under quiescent or agitated conditions or in AC under both the presence and absence of agitation. It is possible that the molecular species targeted by EGCG or its oxidation products are only present under certain environmental conditions. A similar explanation can be valid for the different relative t_{50} values in PB and AC in the presence of $EGCG_{ox}$. The strong increase in ThT fluorescence intensity in the presence of $EGCG_{ox}$ in AC, on the other hand, requires an alternative explanation. A simple increase in the quantity of fibrils formed is not sufficient to explain the observed several-fold increase in I_{max}. It has been demonstrated before that amyloid fibrils formed under distinct environmental conditions may possess different ThT binding sites, affinities for ThT, and ThT quantum yields [72–74]. Thus, since the secondary structure of insulin amyloid fibrils formed in PB and AC was found to be different (Figure 3), it is possible that $EGCG_{ox}$ induces slight conformational changes in the amyloid fibrils formed in AC, which results in an increase in quantum yield in the bound ThT, and therefore, in increased ThT fluorescence intensity. However, no obvious differences in morphology or secondary structure (Figures S5, S6 and S8), of

insulin fibrils formed in AC in the absence or presence of $EGCG_{ox}$ were observed. Therefore, it is also possible that the change in ThT intensity stems from a direct interaction between bound ThT and $EGCG_{ox}$. The fact that extrinsic compounds can dramatically change the ThT fluorescence quantum yield has sometimes led to false interpretation of a given compound as an inhibitor (Figure 6B). It has, for example, been shown that the two amyloid dyes, Congo red (CR) and ThT, have an affinity for each other and that CR strongly quenches ThT fluorescence, rather than inhibiting amyloid fibril growth [75]. Therefore, absolute fluorescence intensity is often not a reliable readout for the extent of inhibition by any given compound. This conclusion is further supported by the results obtained for α-synuclein at pH 6, where the final ThT intensity in the presence of EGCG suggests a significant inhibition, but measurement of soluble protein and AFM show that the sample has quantitatively been converted into fibrils. The nature of the surfaces involved (cuvette, plate surface, stir bar, and air-water-interface), in combination with the physico-chemical properties of the protein can also have a large impact on the protein aggregation process [59,76–79]. Indeed, additional experiments showed that the strong increase in I_{max} observed in the presence of $EGCG_{ox}$ depends on the type of surface of the microplate used (Figure S9). Under agitated conditions the effect of $EGCG_{ox}$ on insulin aggregation was found to be weaker when compared to the one under quiescent conditions. Agitation in general speeds up amyloid fibril formation, mostly because of its effect on fibril fragmentation, and the detachment of species from the air-water or solid-water interface, where proteins have a strong tendency to accumulate and where in many cases the nucleation step of amyloid fibril formation is likely to occur. By selectively enhancing individual steps, such as fragmentation or nucleation, the concentrations of species that can be targeted by EGCG may be decreased, and hence, its inhibitory effect diminished.

Second, specific environmental conditions may induce modifications of compounds (Figure 6C) [28–30,80]. For example, EGCG is not stable at neutral pH and oxidises within several hours. In general, the effect of $EGCG_{ox}$ on insulin aggregation, is stronger when compared to its non-oxidised form. A further striking example of the effect of the solution conditions on the inhibitory effects of EGCG is given by our findings that a change in pH by only one unit dramatically changes the inhibition of α-synuclein amyloid fibril formation. At the most often employed neutral pH of 7, where EGCG is highly unstable, almost complete inhibition is observed by stoichiometric amounts of EGCG, as evaluated by ThT fluorescence and microfluidic diffusional sizing (MDS). At the same time, UV–Vis experiments with EGCG under equivalent conditions show that EGCG undergoes rapid and quantitative oxidation within a similar time scale as the aggregation process itself (Figures S2 and 6C). This leads to the fact that mostly oxidised EGCG is available to inhibition. The effect of EGCG and $EGCG_{ox}$ at pH 7 is to keep the protein in its monomeric form, as has recently also been reported [81]. The amorphous aggregates that have been observed to be formed by α-synuclein in the presence of EGCG at neutral pH could stem in part from monomeric protein that clusters into amorphous structures during sample preparation for AFM or electron microscopy. We note that even under these conditions of near complete inhibition, as evaluated by ThT fluorescence and MDS, some short fibrils can be seen in AFM images, stressing the importance of the use of multiple experimental methods in order to obtain a complete picture of the inhibitory action. A change to pH 6, however, leads to an increased stability of EGCG (as confirmed by UV–Vis spectroscopy, Figure S2), which is paralleled by a strongly decreased inhibitory effect on α-synuclein aggregation. Indeed, despite the fact that ThT fluorescence intensity is decreased by approximately 50% in the presence of stoichiometric amounts of EGCG and quantitatively suppressed in the presence of stoichiometric amounts of $EGCG_{ox}$, MDS and AFM suggest no inhibition by EGCG and only partial inhibition by $EGCG_{ox}$. These results not only suggest an influence of EGCG and $EGCG_{ox}$ on ThT fluorescence intensity (Figure 6B), but most notably a dramatic pH dependence of the inhibitory effect of EGCG, most likely related to EGCG stability, as discussed above. This finding is highly relevant and interesting, as α-synuclein experiences environments with reduced pH during its life cycle, such as endosomes and lysosomes [82,83]. Furthermore, it has been shown that the aggregation of α-synuclein is strongly enhanced at mildly acidic pH values [25], as found in such microenvironments, whereas at the same time EGCG appears to lose its inhibitory effect. In conclusion,

we demonstrate here that the environmental conditions and the methods used for assessments of the effects of inhibitory compounds play an important role in the reliable identification of anti-amyloid compounds. Under certain circumstances the study design may define whether a given compound is found to be a hit or a failure. Therefore, assessing the effects and the intrinsic stability of compounds under a range of environmental conditions in vitro is essential for the further development of the lead compounds resulting in increased success rates for in vivo studies and clinical trials.

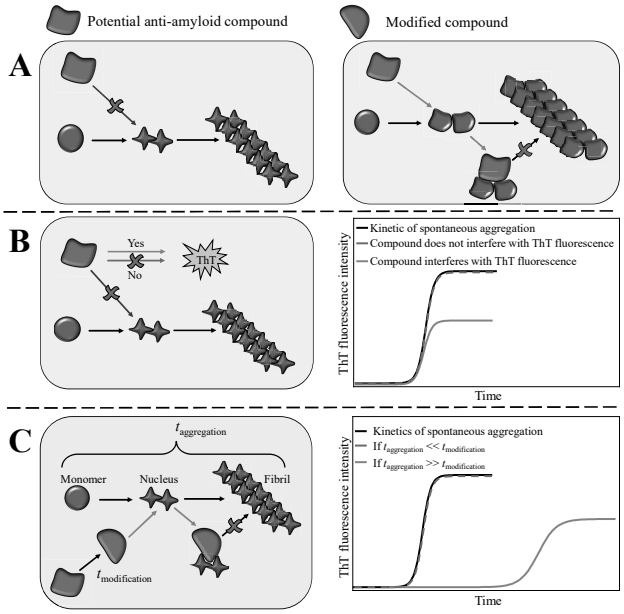

Figure 6. Schematic depiction of possible effects of potential anti-amyloid compounds on the amyloid aggregation reaction performed under distinct environmental conditions. Different environmental conditions can lead to the formation of distinct aggregate species of which only some are targeted by the compound (**A**), as in case of insulin aggregation in PB-Q and AC-Q. Certain compounds can also interfere with ThT's fluorescence intensity (**B**), suggesting inhibition, which was not confirmed by other experiments, such as the quantification of soluble protein at the final plateau of ThT intensity. An example is EGCG and α-synuclein at pH 6. Moreover, specific environmental conditions can induce modifications of the compound, which results in the generation of products that target aggregation prone species (**C**), as in the case of α-synuclein aggregation at neutral pH. The compound modification can only manifest itself if it occurs with kinetics comparable to, or faster than the kinetics of aggregation. Distinct background colours represent different environmental conditions. Different shapes of aggregates represent distinct pathways reflecting the observed polymorphism of amyloid fibrils.

4. Materials and Methods

4.1. Materials and Solutions

Initial solutions of insulin (Sigma Aldrich, St. Louis, MO, USA, number 91077C) were prepared by dissolving 2 mg of dry insulin powder in 0.5 mL of 100 mM sodium phosphate buffer, pH 2.4, supplemented with 100 mM NaCl (PB) or 20% acetic acid, supplemented with 100 mM NaCl (AC).

Concentration of insulin (M.W.—5808 Da, ε_{280}—6335 M^{-1} cm^{-1}) was determined by measuring UV-absorption at 280 nm using NanoDrop 2000 (Thermo Fisher Scientific, Wolsom, MA, USA). Subsequently, insulin solutions were diluted to a final concentration of 2 mg/mL (344 μM) using PB or AC and supplemented with 200 μM of Thioflavin-T (ThT; Sigma Aldrich, number T3516) from a 10 mM ThT stock solution (in MilliQ water). For the insulin inhibition experiments, fresh solutions of 344 μM of EGCG (Sigma Aldrich, number 989-51-5) were prepared by dissolving EGCG in 100 mM sodium phosphate buffer pH 2.4, supplemented with 100 mM NaCl or in 20% acetic acid, supplemented with 100 mM NaCl, just before the experiment. $EGCG_{ox}$ was prepared by dissolving 10 mM of EGCG in 10 mM phosphate buffer solution, pH 7.4, and incubation for 8 h at 60 °C in a thermomixer MHR 23 (Ditabis, Pforzheim, Germany). Subsequently, it was diluted to a final concentration of 344 μM using PB or AC.

The α-synuclein in the pT7-7 vector was expressed in *Escherichia coli* BL21 (DE3) and purified as previously described [25]. As a last step, α-synuclein was purified by size-exclusion chromatography on an ÄKTA pure chromatography system (GE Healthcare) using a Superdex 200 Increase 10/300 GL (GE Healthcare) and 20 mM citric acid, pH 7, as an elution buffer. α-synuclein concentration was determined by measuring UV-absorption at 275 nm (extinction coefficient of 5600 M^{-1} cm^{-1}). For the α-synuclein inhibition experiments, 5 mM solutions of EGCG (Tocris, Abingdon, UK, number 4524) were prepared by dissolving EGCG in dH_2O. The solutions were frozen and stored at –20 °C, after monitoring no difference between fresh and thawed EGCG. $EGCG_{ox}$ was prepared by dissolving 10 mM of EGCG in 20 mM citric acid, pH 7, and incubation for 6 h at 60 °C in a thermomixer. Subsequently, it was diluted to a final concentration of 5 mM, frozen and stored at –20 °C.

4.2. Measurements of Aggregation Kinetics

Insulin: For the inhibition experiments, 344 μM solutions of EGCG or $EGCG_{ox}$ were mixed with 344 μM insulin solutions in a 1:1 ratio. Three replicates of each solution were then pipetted into a nonbinding surface plate (NBS; Corning, Corning, NY, USA, number 3881). The plate was sealed using sealing tape (Nunc, Roskilde, Denmark, number 232701). Kinetics of insulin aggregation was monitored at 60 °C without (quiescent conditions) and with continuous shaking (960 rpm; agitated conditions) by measuring ThT fluorescence emission intensity (excitation—440 nm; emission—480 nm) through the bottom of the plate using a Synergy H4 Hybrid Multi-Mode (Biotek, Winooski, VT, USA) microplate reader for 15 h (readouts were taken every 5 min under quiescent conditions and every 2 min under agitated conditions). Three independent measurements were performed for each sample.

α-synuclein: To study the effect of EGCG on the α-synuclein fibril formation, solutions of 25 μM of α-synuclein were prepared with EGCG or $EGCG_{ox}$ solutions in a 1:1 ratio, 20 μM ThT and 150 mM citric acid at the wanted pH-value (pH 6 or pH 7). Three replicates of each solution were then pipetted into a high binding surface plate Costar (Corning, number 3601) and glass beads were added into the wells. The plate was sealed using SealPlate film (Sigma-Aldrich, number Z369667). Kinetics of amyloid formation were monitored at 37 °C under continuous shaking (300 rpm) by measuring ThT fluorescence intensity through the bottom of the plate using FLUOstar (BMG LABTECH, Ortenberg, Germany) microplate reader (readouts were taken every 5 min).

The highest ThT fluorescence emission value within each curve was assumed to be I_{max}. Half-times (t_{50}) of the aggregation process were obtained as described by Nielsen et al. [55]. Briefly, experimental data was fitted using the following sigmoidal equation:

$$Y = y_i + m_i t + \frac{y_f + m_f t}{1 + e^{-\left(\frac{t - t_{50}}{\tau}\right)}}, \quad (1)$$

where Y is the ThT fluorescence emission intensity, t is the time, and t_{50} is the time when 50% of maximum ThT fluorescence intensity is reached. The initial baseline is described by $y_i + m_i t$ and the final baseline is described by $y_f + m_f t$.

4.3. Evaluation of EGCG and $EGCG_{ox}$ Effects on the Insulin Aggregation Process.

The effects of EGCG and $EGCG_{ox}$ on the insulin aggregation process were determined by comparing experimental values of t_{50} or I_{max} of control samples with the ones determined in the presence of EGCG or $EGCG_{ox}$ using one-way the one-way analysis of variance (ANOVA). $p < 0.01$ was accepted as statistically significant. The analysis was performed using OriginPro software.

4.4. Atomic Force Microscopy (AFM)

Insulin: Directly after the kinetic measurements, the samples were collected, and 20 µL of each sample was deposited on freshly cleaved mica and incubated for 1 min. Subsequently, the samples were rinsed with 1 mL of MilliQ water and dried under gentle airflow. Three-dimensional AFM maps were acquired using a Dimension Icon (Bruker) atomic force microscope operating in tapping mode, equipped with a silicon cantilever Tap300AI-G (40 N m^{-1}, Budget Sensors) with a typical tip radius of curvature of 8 nm. High-resolution (1024 × 1024 pixels) images were acquired. The scan rate was 0.5 Hz. AFM images were flattened using SPIP (Image Metrology, Hessholm, Denmark) or NanoScope Analysis (Bruker, Billerica, MA, USA) software.

α-synuclein: AFM images were acquired directly after the aggregation kinetic measurements. In total, 10 µL of each sample was deposited onto freshly cleaved mica. After drying, the samples were washed 5 times with 100 µL of dH_2O and dried under gentle flow of nitrogen. Three-dimensional AFM maps were obtained using a NanoScope V (Bruker) atomic force microscope equipped with a silicon cantilever ScanAsyst-Air (Bruker) with a tip radius of 2–12 nm. High-resolution (1024 × 1024 pixels) images were acquired. The scan rate was 0.9 Hz. AFM images were flattened using SPIP (Image Metrology) software.

4.5. Fourier-Transform Infrared (FTIR) Spectroscopy

Insulin fibrils were separated from buffer solution by centrifugation at 10,000× *g* for 30 min and subsequently resuspended in 1 mL of D_2O; the procedure was repeated three times. Finally, fibrils were resuspended in 0.3 mL of D_2O and sonicated for 1 min using Sonopuls 3100 (Bandelin, Berlin, Germany) ultrasonic homogeniser equipped with MS73 tip (using 50% of the power; total energy applied to the sample ∼1.12 kJ). Samples were deposited between two CaF_2 transmission windows separated by 0.05 mm teflon spacers. The FTIR spectra were recorded using a Vertex 80v (Bruker) IR spectrometer equipped with a mercury cadmium telluride detector, at room temperature under vacuum (∼2 mBar) conditions. A total of 256 interferograms of 2 cm^{-1} resolution were averaged for each spectrum. The spectrum of D_2O was subtracted from the spectrum of each sample. All spectra were normalised to the same area of amide I/I' band (1700–1595 cm^{-1}). All data processing was performed using GRAMS software.

4.6. Microfluidic Diffusional Sizing and Concentration Measurements

To measure the concentration of the soluble α-synuclein, the samples were centrifuged for 60 min at 16,100× *g* at 25 °C using a centrifuge 5415 R (Eppendorf) directly after the kinetic measurements. The supernatant was taken, and 6 µL was pipetted onto a disposable microfluidic chip and measured with the FluidityOne (Fluidic Analytics, Cambridge, UK). FluidityOne is a microfluidic diffusional sizing (MDS, [60]) device, which measures the rate of diffusion under steady state, laminar flow. The protein concentration is determined by fluorescence intensity, as the protein is mixed with ortho-phthalaldehyde (OPA) after the diffusion, a compound which reacts with primary amines, producing a fluorescent compound [61].

4.7. Time Course of EGCG Oxidation

The oxidation of EGCG was followed by UV–Vis spectroscopy. Solutions of EGCG were prepared as described above. In total, 10 mM EGCG solutions were dissolved in 10 mM sodium phosphate

buffer pH 7.4, corresponding to the conditions under which a stock solution of $EGCG_{ox}$ for insulin experiments was produced, and in 20 mM citric acid, pH 7, corresponding to the conditions under which a stock solution of $EGCG_{ox}$ for the α-synuclein experiments was produced. The oxidation of EGCG was carried out by incubating the solutions at 60 °C for 0–22 h. Subsequently, the solutions were diluted and the spectra were recorded in the wavelength range between 250 nm and 500 nm in a UV-transparent plate (Corning, Corning, NY, USA, number 3679) using a Spark (Tecan, Mannedorf, Switzerland) microplate reader. To monitor the stability of EGCG under the used aggregation experiments, 172 µM EGCG in 100 mM NaCl, 100 mM sodium phosphate buffer, pH 2.4, 172 µM EGCG in 20% acetic acid, and 100 mM NaCl were incubated at 60 °C for 0–22h, corresponding to the conditions of the insulin aggregation experiments, and 125 µM EGCG in 150 mM citric acid at pH 6 and pH 7 were incubated at 37 °C for 0–22 h, corresponding to the conditions of the α-synuclein aggregation experiments.

Supplementary Materials: The following are available online at http://www.mdpi.com/2218-273X/9/12/855/s1 , Figure S1: Representative curves of insulin aggregation kinetics in the absence and presence of EGCG or $EGCG_{ox}$ under different environmental conditions. Figure S2: EGCG oxidation followed by UV–Vis spectroscopy. Figure S3: AFM images of insulin fibrils formed in PB under quiescent conditions in the absence and presence of EGCG or $EGCG_{ox}$. Figure S4: AFM images of insulin fibrils formed in PB under agitated conditions in the absence and presence of EGCG or $EGCG_{ox}$. Figure S5: AFM images of insulin fibrils formed in AC under quiescent conditions in the absence and presence of EGCG or $EGCG_{ox}$. Figure S6: AFM images of insulin fibrils formed in AC under agitated conditions in the absence and presence of EGCG or $EGCG_{ox}$. Figure S7: Evaluation of EGCG and $EGCG_{ox}$ effects on t_{50} and I_{max} using one-way ANOVA. Figure S8: Second derivative FTIR spectra of insulin amyloid-like aggregates formed in AC in the absence and presence of $EGCG_{ox}$. Figure S9: Effect of $EGCG_{ox}$ on t_{50} and I_{max} in AC assessed in NBS-plates and untreated-plates. Raw data of insulin and α-synuclein aggregation kinetics; microfluidic diffusional sizing and concentration measurements; UV–Vis spectra of EGCG oxidation; FTIR spectra of insulin aggregates.

Author Contributions: Conceptualisation, T.S. A.S., R.S.-H., A.K.B., and V.S.; funding acquisition, A.K.B. and V.S.; Supervision; A.K.B. and V.S.; investigation, T.S., A.S., R.S.-H., A.P., and M.Z.; Resources, A.K.B. and V.S.; writing—original draft preparation, T.S., A.K.B., and V.S.; writing—review and editing, T.S., A.S., R.S.-H., M.Z., A.K.B., and V.S.

Funding: This research was funded by the Marie Curie Career Integration Grant 293476. A.K.B. and R.S.H. thank the Manchot Foundation for funding. A.K.B. thanks the Novo Nordisk Foundation for funding through a Novo Nordisk Foundation Professorship.

Acknowledgments: The authors acknowledge G. Niaura from the Center of Physical Sciences and Technology for the access to FTIR.

Conflicts of Interest: The authors declare no conflict of interest.

References

1. Chiti, F.; Dobson, C.M. Protein misfolding, amyloid formation, and human disease: A summary of progress over the last decade. *Annu. Rev. Biochem.* **2017**, *86*, 27–68, doi:10.1146/annurev-biochem-061516-045115. [CrossRef] [PubMed]
2. Knowles, T.P.J.; Vendruscolo, M.; Dobson, C.M. The amyloid state and its association with protein misfolding diseases. *Nat. Rev. Mol. Cell Biol.* **2014**, *15*, 384–396, doi:10.1038/nrm3810. [CrossRef] [PubMed]
3. Selkoe, D.J.; Hardy, J. The amyloid hypothesis of Alzheimer's disease at 25 years. *EMBO Mol. Med.* **2016**, *8*, 595–608, doi:10.15252/emmm.201606210. [CrossRef] [PubMed]
4. Wisniewski, T.; Goñi, F. Immunotherapeutic approaches for Alzheimer's disease. *Neuron* **2015**, *85*, 1162–1176, doi:10.1016/j.neuron.2014.12.064. [CrossRef]
5. Fitzpatrick, A.W.P.; Debelouchina, G.T.; Bayro, M.J.; Clare, D.K.; Caporini, M.A.; Bajaj, V.S.; Jaroniec, C.P.; Wang, L.; Ladizhansky, V.; Muller, S.A.; et al. Atomic structure and hierarchical assembly of a cross-beta amyloid fibril. *Proc. Natl. Acad. Sci. USA* **2013**, *110*, 5468–5473, doi:10.1073/pnas.1219476110. [CrossRef]
6. Porat, Y.; Abramowitz, A.; Gazit, E. Inhibition of amyloid fibril formation by polyphenols: Structural similarity and aromatic interactions as a common inhibition mechanism. *Chem. Biol. Drug Des.* **2006**, *67*, 27–37, doi:10.1111/j.1747-0285.2005.00318.x. [CrossRef]
7. Doig, A.J.; Derreumaux, P. Inhibition of protein aggregation and amyloid formation by small molecules. *Current Opin. Struct. Biol.* **2015**, *30*, 50–56, doi:10.1016/j.sbi.2014.12.004. [CrossRef]

8. Mangialasche, F.; Solomon, A.; Winblad, B.; Mecocci, P.; Kivipelto, M. Alzheimer's disease: Clinical trials and drug development. *Lancet Neurol.* **2010**, *9*, 702–716, doi:10.1016/S1474-4422(10)70119-8. [CrossRef]
9. Castellani, R.J.; Plascencia-Villa, G.; Perry, G. The amyloid cascade and Alzheimer's disease therapeutics: Theory versus observation. *Lab. Investig.* **2019**, *99*, 958–970, doi:10.1038/s41374-019-0231-z. [CrossRef]
10. Cheng, B.; Gong, H.; Xiao, H.; Petersen, R.B.; Zheng, L.; Huang, K. Inhibiting toxic aggregation of amyloidogenic proteins: A therapeutic strategy for protein misfolding diseases. *Biochim. Biophys. Acta Gen. Subj.* **2013**, *1830*, 4860–4871, doi:10.1016/j.bbagen.2013.06.029. [CrossRef]
11. Lao, K.; Ji, N.; Zhang, X.; Qiao, W.; Tang, Z.; Gou, X. Drug development for Alzheimer's disease: Review. *J. Drug Target.* **2019**, *27*, 164–173, doi:10.1080/1061186X.2018.1474361. [CrossRef]
12. Stefani, M.; Rigacci, S. Protein folding and aggregation into amyloid: The interference by natural phenolic compounds. *Int. J. Mol. Sci.* **2013**, *14*, 12411–12457, doi:10.3390/ijms140612411. [CrossRef]
13. Molino, S.; Dossena, M.; Buonocore, D.; Ferrari, F.; Venturini, L.; Ricevuti, G.; Verri, M. Polyphenols in dementia: From molecular basis to clinical trials. *Life Sci.* **2016**, *161*, 69–77, doi:10.1016/j.lfs.2016.07.021. [CrossRef]
14. Goyal, D.; Shuaib, S.; Mann, S.; Goyal, B. Rationally designed peptides and peptidomimetics as inhibitors of amyloid-β (Aβ) aggregation: Potential therapeutics of Alzheimer's disease. *ACS Comb. Sci.* **2017**, *19*, 55–80. doi:10.1021/acscombsci.6b00116. [CrossRef] [PubMed]
15. Agerschou, E.D.; Flagmeier, P.; Saridaki, T.; Galvagnion, C.; Komnig, D.; Nagpal, A.; Gasterich, N.; Heid, L.; Prasad, V.; Shaykhalishahi, H.; et al. An engineered monomer binding-protein for α-synuclein efficiently inhibits the proliferation of amyloid fibrils. *eLife* **2019**, *8*, e46112. [CrossRef] [PubMed]
16. Mehta, D.; Jackson, R.; Paul, G.; Shi, J.; Sabbagh, M. Why do trials for Alzheimer's disease drugs keep failing? A discontinued drug perspective for 2010–2015. *Expert Opin. Investig. Drugs* **2017**, *26*, 735–739, doi:10.1080/13543784.2017.1323868. [CrossRef] [PubMed]
17. Mathur, S.; Dewitte, S.; Robledo, I.; Isaacs, T.; Stamford, J. Rising to the challenges of clinical trial improvement in Parkinson's disease. *J. Parkinson's Dis.* **2015**, *5*, 263–268, doi:10.3233/JPD-150541. [CrossRef] [PubMed]
18. Athauda, D.; Foltynie, T. Challenges in detecting disease modification in Parkinson's disease clinical trials. *Parkinsonism Relat. Disord.* **2016**, *32*, 1–11, doi:10.1016/j.parkreldis.2016.07.019. [CrossRef]
19. Al-Ansari, A.; Robertson, N.P. Creutzfeldt-Jacob disease: New directions in diagnosis and therapeutics. *J. Neurol.* **2017**, *264*, 1029–1031, doi:10.1007/s00415-017-8473-4. [CrossRef]
20. Yaari, R.; Hake, A. Alzheimer's disease clinical trials: Past failures and future opportunities. *Clin. Investig.* **2015**, *5*, 297–309, doi:10.4155/cli.14.127. [CrossRef]
21. Cummings, J.L.; Morstorf, T.; Zhong, K. Alzheimer's disease drug-development pipeline: Few candidates, frequent failures. *Alzheimer's Res. Ther.* **2014**, *6*, 37, doi:10.1186/alzrt269. [CrossRef] [PubMed]
22. Sneideris, T.; Darguzis, D.; Botyriute, A.; Grigaliunas, M.; Winter, R.; Smirnovas, V. pH-driven polymorphism of insulin amyloid-like fibrils. *PLoS ONE* **2015**, *10*, e0136602, doi:10.1371/journal.pone.0136602. [CrossRef] [PubMed]
23. Ziaunys, M.; Sneideris, T.; Smirnovas, V. Self-inhibition of insulin amyloid-like aggregation. *Phys. Chem. Chem. Phys.* **2018**, *20*, 27638–27645, doi:10.1039/C8CP04838J. [CrossRef] [PubMed]
24. Sneideris, T.; Milto, K.; Smirnovas, V. Polymorphism of amyloid-like fibrils can be defined by the concentration of seeds. *PeerJ* **2015**, *3*, e1207, doi:10.7717/peerj.1207. [CrossRef] [PubMed]
25. Buell, A.K.; Galvagnion, C.; Gaspar, R.; Sparr, E.; Vendruscolo, M.; Knowles, T.P.J.; Linse, S.; Dobson, C.M. Solution conditions determine the relative importance of nucleation and growth processes in α-synuclein aggregation. *Proc. Natl. Acad. Sci. USA* **2014**, *111*, 7671–7676, doi:10.1073/pnas.1315346111. [CrossRef] [PubMed]
26. Guo, J.L.; Lee, V.M.Y. Cell-to-cell transmission of pathogenic proteins in neurodegenerative diseases. *Nat. Med.* **2014**, *20*, 130–138, doi:10.1038/nm.3457. [CrossRef] [PubMed]
27. Adamcik, J.; Mezzenga, R. Amyloid polymorphism in the protein folding and aggregation energy landscape. *Angew. Chem. Int. Ed.* **2018**, *57*, 8370–8382, doi:10.1002/anie.201713416. [CrossRef]
28. Wei, Y.; Chen, P.; Ling, T.; Wang, Y.; Dong, R.; Zhang, C.; Zhang, L.; Han, M.; Wang, D.; Wan, X.; et al. Certain (-)-epigallocatechin-3-gallate (EGCG) auto-oxidation products (EAOPs) retain the cytotoxic activities of EGCG. *Food Chem.* **2016**, *204*, 218–226, doi:10.1016/j.foodchem.2016.02.134. [CrossRef]

29. An, T.T.; Feng, S.; Zeng, C.M. Oxidized epigallocatechin gallate inhibited lysozyme fibrillation more strongly than the native form. *Redox Biol.* **2017**, *11*, 315–321, doi:10.1016/j.redox.2016.12.016. [CrossRef]
30. Palhano, F.L.; Lee, J.; Grimster, N.P.; Kelly, J.W. Toward the molecular mechanism(s) by which EGCG treatment remodels mature amyloid fibrils. *J. Am. Chem. Soc.* **2013**, *135*, 7503–7510, doi:10.1021/ja3115696. [CrossRef]
31. Attar, A.; Rahimi, F.; Bitan, G. Modulators of amyloid protein aggregation and toxicity: EGCG and CLR01. *Transl. Neurosci.* **2013**, *4*, 385–409, doi:10.2478/s13380-013-0137-y. [CrossRef]
32. Liu, Y.; Liu, Y.; Wang, S.; Dong, S.; Chang, P.; Jiang, Z. Structural characteristics of (-)-epigallocatechin-3-gallate inhibiting amyloid Aβ42 aggregation and remodeling amyloid fibers. *RSC Adv.* **2015**, *5*, 62402–62413, doi:10.1039/c5ra09608a. [CrossRef]
33. Bieschke, J.; Russ, J.; Friedrich, R.P.; Ehrnhoefer, D.E.; Wobst, H.; Neugebauer, K.; Wanker, E.E. EGCG remodels mature α-synuclein and amyloid-β fibrils and reduces cellular toxicity. *Proc. Natl. Acad. Sci. USA* **2010**, *107*, 7710–7715, doi:10.1073/pnas.0910723107. [CrossRef] [PubMed]
34. Zhao, J.; Liang, Q.; Sun, Q.; Chen, C.; Xu, L.; Ding, Y.; Zhou, P. (-)-Epigallocatechin-3-gallate (EGCG) inhibits fibrillation, disaggregates amyloid fibrils of α-synuclein, and protects PC12 cells against α-synuclein-induced toxicity. *RSC Adv.* **2017**, *7*, 32508–32517, doi:10.1039/c7ra03752j. [CrossRef]
35. Qing, H.; McGeer, P.L.; Zhang, Y.; Yang, Q.; Dai, R.; Zhang, R.; Guo, J.; Wong, W.; Xu, Y.; Quan, Z. Epigallocatechin gallate (EGCG) inhibits alpha-synuclein aggregation: A potential agent for Parkinson's disease. *Neurochem. Res.* **2016**, *41*, 2788–2796, doi:10.1007/s11064-016-1995-9. [CrossRef]
36. Roy, S.; Bhat, R. Suppression, disaggregation, and modulation of γ-Synuclein fibrillation pathway by green tea polyphenol EGCG. *Protein Sci.* **2019**, *28*, 382–402. doi:10.1002/pro.3549. [CrossRef]
37. Lee, Y.H.; Lin, Y.; Cox, S.J.; Kinoshita, M.; Sahoo, B.R.; Ivanova, M.; Ramamoorthy, A. Zinc boosts EGCG's hIAPP amyloid Inhibition both in solution and membrane. *Biochim. Biophys. Acta (BBA) Proteins Proteom.* **2019**, *1867*, 529–536. [CrossRef]
38. Xu, Z.X.; Ma, G.L.; Zhang, Q.; Chen, C.H.; He, Y.M.; Xu, L.H.; Zhou, G.R.; Li, Z.H.; Yang, H.J.; Zhou, P. Inhibitory mechanism of epigallocatechin gallate on fibrillation and aggregation of amidated human islet amyloid polypeptide. *ChemPhysChem* **2017**, *18*, 1611–1619. doi:10.1002/cphc.201700057. [CrossRef]
39. Ehrnhoefer, D.E.; Duennwald, M.; Markovic, P.; Wacker, J.L.; Engemann, S.; Roark, M.; Legleiter, J.; Marsh, J.L.; Thompson, L.M.; Lindquist, S.; et al. Green tea (-)-epigallocatechin-gallate modulates early events in huntingtin misfolding and reduces toxicity in Huntington's disease models. *Hum. Mol. Genet.* **2006**, *15*, 2743–2751, doi:10.1093/hmg/ddl210. [CrossRef]
40. Wobst, H.J.; Sharma, A.; Diamond, M.I.; Wanker, E.E.; Bieschke, J. The green tea polyphenol (-)-epigallocatechin gallate prevents the aggregation of tau protein into toxic oligomers at substoichiometric ratios. *FEBS Lett.* **2015**, *589*, 77–83, doi:10.1016/j.febslet.2014.11.026. [CrossRef]
41. Srinivasan, E.; Rajasekaran, R. Probing the inhibitory activity of epigallocatechin-gallate on toxic aggregates of mutant (L84F) SOD1 protein through geometry based sampling and steered molecular dynamics. *J. Mol. Graph. Model.* **2017**, *74*, 288–295, doi:10.1016/j.jmgm.2017.04.019. [CrossRef] [PubMed]
42. Roberts, B.E.; Duennwald, M.L.; Wang, H.; Chung, C.; Lopreiato, N.P.; Sweeny, E.A.; Knight, M.N.; Shorter, J. A synergistic small-molecule combination directly eradicates diverse prion strain structures. *Nat. Chem. Biol.* **2009**, *5*, 936–946, doi:10.1038/nchembio.246. [CrossRef] [PubMed]
43. Townsend, D.; Hughes, E.; Akien, G.; Stewart, K.L.; Radford, S.E.; Rochester, D.; Middleton, D.A. Epigallocatechin-3-gallate remodels apolipoprotein A-I amyloid fibrils into soluble oligomers in the presence of heparin. *J. Biol. Chem.* **2018**, *293*, 12877–12893, doi:10.1074/jbc.RA118.002038. [CrossRef] [PubMed]
44. Andrich, K.; Bieschke, J., The effect of (-)-epigallo-catechin-(3)-gallate on amyloidogenic proteins suggests a common mechanism. In *Natural Compounds as Therapeutic Agents for Amyloidogenic Diseases*; Vassallo, N., Ed.; Springer International Publishing: Cham, Switzerland, 2015; pp. 139–161, doi:10.1007/978-3-319-18365-7_7. [CrossRef]
45. Zhu, Q.Y.; Zhang, A.; Tsang, D.; Huang, Y.; Chen, Z.Y. Stability of green tea catechins. *J. Agric. Food Chem.* **1997**, *45*, 4624–4628, doi:10.1021/jf9706080. [CrossRef]
46. Hatano, T.; Ohyabu, T.; Yoshida, T. The structural variation in the incubation products of (-)-epigallocatechin gallate in neutral solution suggests its breakdown pathways. *Heterocycles* **2005**, *65*, doi:10.3987/COM-04-10259. [CrossRef]

47. Sang, S.; Lee, M.J.; Hou, Z.; Ho, C.T.; Yang, C.S. Stability of tea polyphenol (-)-epigallocatechin-3-gallate and formation of dimers and epimers under common experimental conditions. *J. Agric. Food Chem.* **2005**, *53*, 9478–9484. doi:10.1021/jf0519055. [CrossRef] [PubMed]
48. Zeng, L.; Ma, M.; Li, C.; Luo, L. Stability of tea polyphenols solution with different pH at different temperatures. *Int. J. Food Prop.* **2017**, *20*, 1–18, doi:10.1080/10942912.2014.983605. [CrossRef]
49. Hirohata, M.; Hasegawa, K.; Tsutsumi-Yasuhara, S.; Ohhashi, Y.; Ookoshi, T.; Ono, K.; Yamada, M.; Naiki, H. The anti-amyloidogenic effect is exerted against Alzheimer's β-amyloid fibrils in vitro by preferential and reversible binding of flavonoids to the amyloid fibril structure. *Biochemistry* **2007**, *46*, 1888–1899, doi:10.1021/bi061540x. [CrossRef]
50. Haas, J.; Vohringer-Martinez, E.; Bogehold, A.; Matthes, D.; Hensen, U.; Pelah, A.; Abel, B.; Grubmuller, H. Primary steps of pH-dependent insulin aggregation kinetics are governed by conformational flexibility. *ChemBioChem* **2009**, *10*, 1816–1822, doi:10.1002/cbic.200900266. [CrossRef]
51. Dische, F.E.; Wernstedt, C.; Westermark, G.T.; Westermark, P.; Pepys, M.B.; Rennie, J.A.; Gilbey, S.G.; Watkins, P.J. Insulin as an amyloid-fibril protein at sites of repeated insulin injections in a diabetic patient. *Diabetologia* **1988**, *31*, 158–161, doi:10.1007/BF00276849. [CrossRef]
52. Dzwolak, W.; Grudzielanek, S.; Smirnovas, V.; Ravindra, R.; Nicolini, C.; Jansen, R.; Loksztejn, A.; Porowski, S.; Winter, R. Ethanol-perturbed amyloidogenic self-assembly of insulin: Looking for origins of amyloid strains. *Biochemistry* **2005**, *44*, 8948–8958, doi:10.1021/bi050281t. [CrossRef] [PubMed]
53. Dzwolak, W.; Smirnovas, V.; Jansen, R.; Winter, R. Insulin forms amyloid in a strain-dependent manner: An FT-IR spectroscopic study. *Protein Sci. Publ. Protein Soc.* **2004**, *13*, 1927–1932, doi:10.1110/ps.03607204. [CrossRef] [PubMed]
54. Dzwolak, W.; Jansen, R.; Smirnovas, V.; Loksztejn, A.; Porowski, S.; Winter, R. Template-controlled conformational patterns of insulin fibrillar self-assembly reflect history of solvation of the amyloid nuclei. *Phys. Chem. Chem. Phys. PCCP* **2005**, *7*, 1349–1351, doi:10.1039/B502255J. [CrossRef] [PubMed]
55. Nielsen, L.; Khurana, R.; Coats, A.; Frokjaer, S.; Brange, J.; Vyas, S.; Uversky, V.N.; Fink, A.L. Effect of environmental factors on the kinetics of insulin fibril formation: Elucidation of the molecular mechanism. *Biochemistry* **2001**, *40*, 6036–6046. [CrossRef]
56. Nielsen, L.; Frokjaer, S.; Carpenter, J.F.; Brange, J. Studies of the structure of insulin fibrils by Fourier transform infrared (FTIR) spectroscopy and electron microscopy. *J. Pharm. Sci.* **2001**, *90*, 29–37, doi:10.1002/1520-6017(200101)90:1<29::AID-JPS4>3.0.CO;2-4. [CrossRef]
57. Spillantini, M.G.; Schmidt, M.L.; Lee, V.M.; Trojanowski, J.Q.; Jakes, R.; Goedert, M. Alpha-synuclein in Lewy bodies. *Nature* **1997**, *388*, 839–840, doi:10.1038/42166. [CrossRef]
58. Surmacz-Chwedoruk, W.; Babenko, V.; Dzwolak, W. Master and slave relationship between two types of self-propagating insulin amyloid fibrils. *J. Phy. Chem. B* **2014**, *118*, 13582–13589. [CrossRef]
59. Vácha, R.; Linse, S.; Lund, M. Surface effects on aggregation kinetics of amyloidogenic peptides. *J. Am. Chem. Soc.* **2014**, *136*, 11776–11782, doi:10.1021/ja505502e. [CrossRef]
60. Arosio, P.; Müller, T.; Rajah, L.; Yates, E.V.; Aprile, F.A.; Zhang, Y.; Cohen, S.I.; White, D.A.; Herling, T.W.; De Genst, E.J.; et al. Microfluidic diffusion analysis of the sizes and interactions of proteins under native solution conditions. *ACS Nano* **2015**, *10*, 333–341, doi:10.1021/acsnano.5b04713. [CrossRef]
61. Yates, E.V.; Müller, T.; Rajah, L.; De Genst, E.J.; Arosio, P.; Linse, S.; Vendruscolo, M.; Dobson, C.M.; Knowles, T.P.J. Latent analysis of unmodified biomolecules and their complexes in solution with attomole detection sensitivity. *Nat. Chem.* **2015**, *7*, 802–809, doi:10.1038/nchem.2344. [CrossRef]
62. Gang, H.; Galvagnion, C.; Meisl, G.; Müller, T.; Pfammatter, M.; Buell, A.K.; Levin, A.; Dobson, C.M.; Mu, B.; Knowles, T.P.J. Microfluidic Diffusion Platform for Characterizing the Sizes of Lipid Vesicles and the Thermodynamics of Protein-Lipid Interactions. *Anal. Chem.* **2018**, *90*, 3284–3290, doi:10.1021/acs.analchem.7b04820. [CrossRef]
63. Arosio, P.; Vendruscolo, M.; Dobson, C.M.; Knowles, T.P.J. Chemical kinetics for drug discovery to combat protein aggregation diseases. *Trends Pharmacol. Sci.* **2014**, *35*, 127–135, doi:10.1016/j.tips.2013.12.005. [CrossRef]
64. Arosio, P.; Michaels, T.C.T.; Linse, S.; Månsson, C.; Emanuelsson, C.; Presto, J.; Johansson, J.; Vendruscolo, M.; Dobson, C.M.; Knowles, T.P.J. Kinetic analysis reveals the diversity of microscopic mechanisms through which molecular chaperones suppress amyloid formation. *Nat. Commun.* **2016**, *7*, 10948, doi:10.1038/ncomms10948. [CrossRef]

65. Joshi, P.; Chia, S.; Habchi, J.; Knowles, T.P.; Dobson, C.M.; Vendruscolo, M. A fragment-based method of creating small-molecule libraries to target the aggregation of intrinsically disordered proteins. *ACS Comb. Sci.* **2016**, *18*, 144–153, doi:10.1021/acscombsci.5b00129. [CrossRef]
66. Andrich, K.; Hegenbart, U.; Kimmich, C.; Kedia, N.; Bergen, H.R.; Schönland, S.; Wanker, E.; Bieschke, J. Aggregation of full-length immunoglobulin light chains from systemic light chain amyloidosis (AL) patients is remodeled by epigallocatechin-3-gallate. *J. Biol. Chem.* **2017**, *292*, 2328–2344, doi:10.1074/jbc.M116.750323. [CrossRef]
67. Sneideris, T.; Baranauskiene, L.; Cannon, J.G.; Rutkiene, R.; Meskys, R.; Smirnovas, V. Looking for a generic inhibitor of amyloid-like fibril formation among flavone derivatives. *PeerJ* **2015**, *3*, e1271, doi:10.7717/peerj.1271. [CrossRef]
68. Malisauskas, R.; Botyriute, A.; Cannon, J.G.; Smirnovas, V. Flavone Derivatives as Inhibitors of Insulin Amyloid-Like Fibril Formation. *PLoS ONE* **2015**, *10*, 1–14, doi:10.1371/journal.pone.0121231. [CrossRef]
69. Aarabi, M.H. The role of two natural flavonoids on human amylin aggregation. *Afr. J. Pharm. Pharmacol.* **2012**, *6*, 2374–2379, doi:10.5897/ajpp12.616. [CrossRef]
70. Chaudhury, S.; Dutta, A.; Bag, S.; Biswas, P.; Das, A.K.; Dasgupta, S. Probing the inhibitory potency of epigallocatechin gallate against human γB-crystallin aggregation: Spectroscopic, microscopic and simulation studies. *Spectrochim. Acta Part A Mol. Biomol. Spectrosc.* **2018**, *192*, 318–327. [CrossRef]
71. Jayamani, J.; Shanmugam, G. Gallic acid, one of the components in many plant tissues, is a potential inhibitor for insulin amyloid fibril formation. *Eur. J. Med. Chem.* **2014**, *85*, 352–358, doi:10.1016/j.ejmech.2014.07.111. [CrossRef]
72. Biancalana, M.; Koide, S. Molecular mechanism of Thioflavin-T binding to amyloid fibrils. *Biochim. Biophys. Acta (BBA) Proteins Proteom.* **2010**, *1804*, 1405–1412, doi:10.1016/j.bbapap.2010.04.001. [CrossRef] [PubMed]
73. Sulatskaya, A.I.; Kuznetsova, I.M.; Belousov, M.V.; Bondarev, S.A.; Zhouravleva, G.A.; Turoverov, K.K. Stoichiometry and affinity of thioflavin T binding to Sup35p amyloid fibrils. *PLoS ONE* **2016**, *11*, 1–14, doi:10.1371/journal.pone.0156314. [CrossRef] [PubMed]
74. Ziaunys, M.; Smirnovas, V. Additional thioflavin-T binding mode in insulin fibril inner core region. *J. Phys. Chem. B* **2019**, doi:10.1021/acs.jpcb.9b08652. [CrossRef] [PubMed]
75. Buell, A.K.; Dobson, C.M.; Knowles, T.P.J.; Welland, M.E. Interactions between Amyloidophilic Dyes and Their Relevance to Studies of Amyloid Inhibitors. *Biophys. J.* **2010**, *99*, 3492–3497, doi:10.1016/j.bpj.2010.08.074. [CrossRef] [PubMed]
76. Campioni, S.; Carret, G.; Jordens, S.; Nicoud, L.; Mezzenga, R.; Riek, R. The presence of an air-water interface affects formation and elongation of α-synuclein fibrils. *J. Am. Chem. Soc.* **2014**, *136*, 2866–2875, doi:10.1021/ja412105t. [CrossRef] [PubMed]
77. Linse, S. Mechanism of amyloid protein aggregation and the role of inhibitors. *Pure Appl. Chem.* **2019**, *91*, 211–229, doi:10.1515/pac-2018-1017. [CrossRef]
78. Murray, A.N.; Palhano, F.L.; Bieschke, J.; Kelly, J.W. Surface adsorption considerations when working with amyloid fibrils in multiwell plates and Eppendorf tubes. *Protein Sci.* **2013**, *22*, 1531–1541, doi:10.1002/pro.2339. [CrossRef]
79. Risor, M.W.; Juhl, D.W.; Bjerring, M.; Mathiesen, J.; Enghild, J.J.; Nielsen, N.C.; Otzen, D.E. Critical influence of cosolutes and surfaces on the assembly of serpin-derived amyloid fibrils. *Biophys. J.* **2017**, *113*, 580–596. [CrossRef]
80. Zhu, M.; Han, S.; Fink, A. Oxidized quercetin inhibits α-synuclein fibrillization. *Biochim. Biophys. Acta* **2013**, *1830*, 2872–2881. [CrossRef]
81. Daniels, M.J.; Nourse, J.B.; Kim, H.; Sainati, V.; Schiavina, M.; Murrali, M.G.; Pan, B.; Ferrie, J.J.; Haney, C.M.; Moons, R.; et al. Cyclized NDGA modifies dynamic α-synuclein monomers preventing aggregation and toxicity. *Sci. Rep.* **2019**, *9*, 2937, doi:10.1038/s41598-019-39480-z. [CrossRef]

82. Mak, S.K.; McCormack, A.L.; Manning-Bog, A.B.; Cuervo, A.M.; Monte, D.A.D. Lysosomal degradation of alpha-synuclein in vivo. *J. Biol. Chem.* **2010**, *285*, 13621–13629, doi:10.1074/jbc.M109.074617. [CrossRef] [PubMed]
83. Bourdenx, M.; Bezard, E.; Dehay, B. Lysosomes and α-synuclein form a dangerous duet leading to neuronal cell death. *Front. Neuroanat.* **2014**, *8*, 83, doi:10.3389/fnana.2014.00083. [CrossRef] [PubMed]

Notes

Vilniaus universiteto leidykla
Saulėtekio al. 9, III rūmai, LT-10222 Vilnius
El. p. info@leidykla.vu.lt,
www.leidykla.vu.lt
Tiražas 15 egz.